X-ray Transitions in Broad Band Materials

A Thesis Submitted to the

College of Graduate Studies and Research

in Partial Fulfillment of the Requirements

for the degree of Doctor of Philosophy

in the Department of Physics and Engineering Physics

University of Saskatchewan

Saskatoon

By

John A. McLeod

Permission to Use

In presenting this thesis in partial fulfilment of the requirements for a Postgraduate degree from the University of Saskatchewan, I agree that the Libraries of this University may make it freely available for inspection. I further agree that permission for copying of this thesis in any manner, in whole or in part, for scholarly purposes may be granted by the professor or professors who supervised my thesis work or, in their absence, by the Head of the Department or the Dean of the College in which my thesis work was done. It is understood that any copying or publication or use of this thesis or parts thereof for financial gain shall not be allowed without my written permission. It is also understood that due recognition shall be given to me and to the University of Saskatchewan in any scholarly use which may be made of any material in my thesis.

Requests for permission to copy or to make other use of material in this thesis in whole or part should be addressed to:

Head of the Department of Physics and Engineering Physics
116 Science Place
University of Saskatchewan
Saskatoon, Saskatchewan
Canada
S7N 5E2

Abstract

The general application of soft X-ray spectroscopy in the study of the electronic structure of materials is discussed, with particular emphasis on broad band materials. Several materials are studied using both soft X-ray spectroscopy and density functional theory to provide experimental and theoretical electronic structures, respectively. In particular, bonding, cation hybridization, and band gaps for several binary oxides (the alkali oxides: BeO, MgO, CaO, SrO, BaO; the post-transition metal oxides: ZnO, CdO, HgO; and the period 5 oxides In_2O_3, SnO, SnO_2, Sb_2O_3, Sb_2O_5, and TeO_2) are studied. The technique of using the peaks in the second derivatives of an X-ray emission and an X-ray absorption spectrum to estimate the band gap of a material is critically analyzed, and a more accurate "semi-empirical" method that involves both measured spectra and theoretical calculations is proposed.

The techniques used in the study of binary oxides are then applied to a more interesting (and industrially relevant) group of ternary oxides based on TiO_2 ($PbTiO_3$, Sn_2TiO_4, $Bi_2Ti_4O_{11}$, $Bi_4Ti_3O_{12}$, and $ZnTiO_3$), and a general rule for the band gaps of these materials is suggested based on empirical data. This research may help direct efforts in synthesizing a hydrogen-producing photocatalyst with a band gap that can efficiently harness the bulk of the solar spectrum.

Finally, several layered pnictide superconductors and related compounds ($CaFe_2As_2$, Co-, Ni- and Cu-doped $BaFe_2As_2$, LiFeAs, LiMnAs, $CaCu_{1.7}As_2$, $SrCu_2As_2$, $SrCu_2(As_{0.84}Sb_{0.16})_2$, $SrCu_2Sb_2$, and $BaCu_2Sb_2$) are studied. The X-ray spectra provide rather strong evidence that these materials lack strong on-site Hubbard-like correlations, and that their electronic structures are almost entirely like those of a broad band metal. In particular, it is shown that the notion that the transition metals are all divalent is completely wrong for copper in a layered pnictide, and that at best in these systems the copper is monovalent.

Acknowledgements

I would like to thank my faculty advisor, Prof. Alexander Moewes, for his help and support during the course of my degree, and our frequent visitor from Russia, Dr. Ernst Kurmaev, for providing a great deal of direction to my studies. I also owe thanks to the beamline scientists at the Canadian Light Source — David Muir, Tom Regier, and Lucia Zuin in particular — and Wanli Yang at the Advanced Light Source. The other students in Prof. Alexander Moewes' research group are due both thanks and rebukes in equal parts for simulating discussion both on- and off-topic.

I would also like to thank my collaborators who graciously provided materials for me to study; without their help I would have little research to report, especially Prof. Paul Canfield, Dr. Alexei Belik, and Prof. Hideo Hosono (and their respective research groups), all of whom have provide many different materials on different occasions. Thanks are also due to Prof. Manfred Neumann and Dr. Anna Buling for supporting my data with their XPS measurements.

Finally I would like to thank Dr. Lijia Liu for many things, including making sure this thesis was finally written.

I gratefully acknowledge support from the Natural Sciences and Engineering Research Council of Canada (NSERC) and the Canada Research Chair program. The Advanced Light Source, at which much of my measurements were conducted, is supported by the Director, Office of Science, Office of Basic Energy Sciences, of the U. S. Department of Energy under Contract No. DE-AC02-05CH11231. The Canadian Light Source, at which the remainder of my measurements were conducted, is supported by NSERC, the National Research Council (NSC) Canada, the Canadian Institute of Health Research (CIHR), the Province of Saskatchewan, Western Economic Deversification Canada, and the University of Saskatchewan. Finally, a large portion of my computational studies were enabled by the use of computing resources provided by WestGrid and Compute/Calcul Canada.

Contents

List of Tables

List of Figures

List of Abbreviations

AFM	Antiferromagnet
ALS	Advanced Light Source
APW	Augmented Planewave
BL8	Beamline 8.0.1
CLS	Canadian Light Source
DFT	Density Functional Theory
DOS	Density Of States
FM	Ferromagnetic
GGA	Generalized Gradient Approximation
HF	Hybrid Functional
HOPG	Highly Oriented Planar Graphite
IPFY	Inverse Partial Fluorescence Yield
LAPW	Linearized Augmented Planewave
LDA	Local Density Approximation
LSDA	Local Spin Density Approximation
LCAO	Linear Combination of Atomic Orbitals
LO	Local Orbital
mBJ	Modified Becke Johnson
PBE	Perdew, Burke, and Ernzerhof
RIXS	Resonant Inelastic X-ray Scattering
RXES	Resonant X-ray Emission Spectroscopy
SGM	Spherical Grating Monochromator
TEY	Total Electron Yield
TFY	Total Fluorescence Yield
UHV	Ultra High Vacuum
VLS-PGM	Variable Line Spacing - Planar Grating Monochromator
XAS	X-ray Absorption Spectroscopy
XES	X-ray Emission Spectroscopy
XPS	X-ray Photoemission Spectroscopy
XRD	X-ray Diffraction

Chapter 1

Introduction

High performance materials are essential to the modern world, and there is almost no facet of our society that could not be improved with access to better and cheaper materials. To list a few suggestions; buildings could be made stronger, roads could be made more durable, aircraft could be made lighter without sacrificing structural integrity, computers could be made faster and more efficient, medical drugs could be delivered directly to target areas of the body, bones could be repaired with artificial splints, and solar power could be made cheaper and more efficient.

The keys to developing the next generation of high performance materials obviously rests in materials science and condensed matter, and here the problem is not just one of *synthesizing* advanced materials but also accurately *characterizing* their properties. For one thing, a novel substance can usually only be synthesized with great difficulty and in small amounts, and knowing whether the new material substantially improves upon commonplace materials (perhaps the new material has improved structural, electronic, optical, or magnetic properties compared to an existing industry standard) is essential when deciding whether to devote considerable time and money into devising cheaper and better ways of synthesizing that material. There is little point in putting a great deal of effort into efficiently making a new material if it offers poorer performance than the current industry standard. Secondly, knowing the properties of novel substances helps determine how the new substances relate to similar materials (say with the similar atomic compositions or crystal structures). The "holy grail" of materials science is to be able to start from a list of desired material properties and work backwards to identify the appropriate chemical composition necessary to realize those properties. For this reason, novel materials are useful for testing the applicability of existing theory, even if these materials may not promise useful practical applications.

The electronic structure of a material is almost solely responsible for practically all the properties that make a material relevant to industry. Hardness, electrical conductivity, optical transparency, luminescence, and magnetism are all driven entirely by the arrangement of electrons within a material [3], and consequently directly measuring the electronic structure is very useful. When synthesizing a novel material is very difficult and/or expensive, it is useful to have techniques of characterizing the electronic structure of that material that are:

- Unambiguous and directly comparable to existing standards,
- Non-destructive but still bulk-sensitive, and
- Insensitive to phase (i.e. powder, polycrystalline, or single crystal) and trace impurities.

In addition to these practical needs, it should not be forgotten that measuring and providing a suitable theoretical description of the spin and charge distributions in a material, especially in the context of magnetic and orbital ordering near quantum critical points, is one of the largest open questions in condensed matter physics today.

X-ray spectroscopy is currently one of the best techniques to realize these goals. X-ray spectroscopy has been recognized as a valuable tool in studying the electronic structure of materials for decades [4, 5], indeed for almost as long as the concept of band structure in periodic solids has been known [6]. After the discovery of synchrotron radiation, X-ray spectroscopists had access to unprecedented X-ray brightness, and X-ray spectroscopy became a truly indispensable technique in materials science.

All spectroscopic techniques measure transitions between different states (usually electronic or vibrational) in a material. The aspect of X-ray spectroscopy that sets it apart from other spectroscopic techniques (such as optical spectroscopy) is that it probes electronic transitions between a state that is well-known and relatively universal, and a state that is highly dependent on the specific material [4, 7]. The former is either a tightly bound core level that depends only on the atomic species — not the material structure (used in X-ray absorption or emission spectroscopy), or a continuum state (used in X-ray photoelectron spectroscopy), and the latter is a valence or conduction band state. In fact, because most types of X-ray spectroscopy involve electronic transitions to or from a core level, the resulting X-ray spectrum is a probe of the electronic structure *local* to a particular atomic species.

This thesis is a summary of my efforts to study various materials with X-ray spectroscopy. I have limited the discussion herein to "broad band" materials; materials whose electronic structure is adequately described by band theory [6], and accurately calculated with density functional theory [8, 9]. Over the course of my research I have used X-ray spectroscopy to measure the electronic structure and gain insight into very *specific* properties of certain materials; whether the iron surplus in $FeSe_x$ (where $x < 1$) is due to interstitial iron or vacant selenium sites [10], what drives the metal-insulator transition in $NiS_{2-x}Se_x$ [11], whether the electride $12(CaO)\cdot 7(Al_2O_3)$ conducts electricity through lattice hopping or a "cage conduction band" [12], and how porous silicon might act as a selective detector for airborne explosives [13], to cite some examples. However in an effort to present a coherent narrative I have focussed on using X-ray spectroscopy to study more *general* properties of materials in this thesis.

With that in mind, the text is organized as follows:

- A brief outline of X-ray spectroscopy from a practical experimental standpoint is given. This section is short on specific technical details because these tend to vary considerably depending on the specific equipment used. The research contained herein was typically conducted on more than one type of experimental apparatus, and I was responsible for neither the design, construction, nor maintenance of the equipment. Technical details can be found in the references noted in this section, and in the documentation provided by the specific laboratory that hosts the equipment.

- A brief outline of density functional theory is given. I use a commercially available software package (WIEN2k [14]) for my electronic structure calculations, so again the technical intricacies of the code are omitted. However I do provide technical details on the parameters used in my calculations.

- The theoretical basis for X-ray transitions is derived, in particular within the scope of density functional theory.

- The technique of using X-ray spectroscopy to determine the electronic structure of a material is discussed using some simple binary oxides as model compounds. Particular

attention is paid to methods of determining the band gap, which is possibly the most important single parameter of the electronic structure of a material. The research discussed herein has been published in References [15–17].

- The techniques of studying electronic structure and band gaps with X-ray spectroscopy and density functional theory are applied to the more interesting (and practical) case of band gap engineering in photocatalysts. The research discussed herein has been published in References [18, 19].

- The relatively novel iron pnictide superconductors, and some related materials, are studied with X-ray spectroscopy and theoretical methods. These materials are shown to be broad band materials, and not strongly correlated systems like cuprate superconductors. The research discussed herein has been published in References [20–23].

Ultimately, while X-ray spectroscopy is a well-established experimental technique, there are still challenges in interpreting the resulting spectra in manners more rigorous than simply comparing the spectral shapes to that of reference compounds. My research identifies a few ways that X-ray spectra can be interpreted without relying on extensively calculating the electronic structure of a material, but there is still much progress to be made before relevant physical parameters can be unambiguously extracted from X-ray spectra.

Chapter 2

Experimental Techniques

X-rays are an excellent tool for probing the properties of matter. Every atom, except for H and He, has a distinct set of core electrons which are well-separated in energy, and these energies are within the X-ray energy range. By tuning a monochromatized X-ray beam to the appropriate energy, one can excite a specific set of core electrons. Coupled with the fact that X-ray penetration depths range from hundreds of nanometres to millimetres, X-ray spectroscopy provides a bulk-sensitive element specific probe of the properties of matter, and can be used to obtain *in situ* non-destructive measurements.

My research outlined in this thesis is entirely based on soft X-ray spectroscopy. Soft X-rays span an energy range of about 50 eV to about 2000 eV, and are important for materials research because the core levels of many elements found in novel materials or used in practical applications fall within this range; most notably the organic (C, N, and O) $1s$ core levels, and the transition metal (Sc, Ti, V, Cr, Mn, Fe, Co, Ni, Cu, and Zn) $2p$ core levels. This chapter briefly outlines the equipment required for a soft X-ray spectroscopy measurement, and explains the X-ray spectroscopic techniques I use in my research. The theory behind X-ray transitions in matter is developed more thoroughly in Chapter 4.

2.1 Synchrotron Radiation

To perform X-ray spectroscopy efficiently and effectively, a monochromatic source of X-rays is necessary, and while some techniques can use laboratory sources to obtain publication-quality data, for most types of X-ray spectroscopy there is no substitute for a synchrotron. In a synchrotron, relativistic bunches of electrons travel along a pipe in vacuum, tracing the perimeter of a polyhedron. At each corner of the polyhedron the electrons emit a fan-like

distribution of intense electromagnetic radiation over a broad energy range. Electromagnetic radiation can also be generated in the straight sections by having the electron bunches pass through an array of alternating magnets, called "insertion devices". The dimensionless figure of merit for an insertion device, K, is defined as [24]:

$$K = \frac{eB_0\lambda_u}{2\pi m_e c}, \tag{2.1}$$

where e is the charge of the particles (these are almost always electrons), B_0 is the magnetic field of the insertion device, λ_u is the length of the magnetic period, m_e is the mass of the particles (again, typically an electron), and c is the speed of light. The insertion devices with $K \leq 1$ are called "undulators", while those with $K \gg 1$ are called "wigglers".

A synchrotron is essential for X-ray spectroscopy not only because it provides a very bright source of X-rays, but also because it provides a tunable source of X-ray energy. All the measurements reported in this thesis were obtained from the Advanced Light Source synchrotron (ALS) at the Lawrence National Berkeley Laboratory, in Berkeley CA, and the Canadian Light Source synchrotron (CLS) at the University of Saskatchewan in Saskatoon, SK. The former normally operates with a ring energy of 1.9 GeV (the mass-energy of the relativistic electrons), while the latter normally operates at 2.9 GeV. More information on synchrotrons can be found in Chapter 2 of my Master's thesis [25].

2.2 Soft X-ray Beamlines

The X-rays are generated by bending magnets or insertion devices inside the synchrotron ring; these X-rays are then piped outside the ring, through some X-ray optics (such as focussing mirrors) towards an experimental endstation; this arrangement is called a "beamline". Most of the spectra reported herein were acquired at Beamline 8.0.1 (BL8) at the ALS, others were collected at the Spherical Grating Monochromator beamline (SGM) at the CLS.

BL8 has a soft X-ray fluorescence endstation, and is suitable for both X-ray absorption spectroscopy (XAS) and X-ray emission spectroscopy (XES). The X-rays are generated with an undulator made of permanent magnets with a periodicity of 50 mm, and a spherical grating monochromator is used to select the X-ray energy with a resolving power (E/ΔE) of

about 10^4. BL8 has an energy range of 70 to 1200 eV, and when optimized for maximum flux can deliver on the order of 10^{13} photons per second focussed to a 100 μm $\times$ 100 μm spot on the sample plate [26].

BL8 has a graphite channeltron total fluorescence detector and a picoammeter to obtain XAS specta in both the bulk sensitive total fluorescence yield (TFY) and the surface sensitive total electron yield (TEY) modes. BL8 also has a large spherical grating spectrometer, using a Rowland circle geometry, to measure high resolution XES spectra. For the measurements reported herein, the spectrometer's resolving power was between 500 and 1000. Because soft X-rays are readily absorbed by the atmosphere, the entire spectroscopy apparatus is within ultrahigh vacuum (UHV) chambers; at the point of measurement the pressure is 10^{-7} torr or better.

The samples are affixed to a steel plate with carbon tape (an electrically conducting, vacuum compatible adhesive). This plate is screwed onto a copper holder, and the holder is transferred into the main measurement chamber under vacuum. More information on the technical details of BL8 can be found in Reference [26].

The SGM is a soft X-ray absorption beamline, and as such is suitable for XAS spectroscopy. The SGM also uses a spherical grating monochromator (obvious, given the name of the beamline) and a permanent magnet undulator with a periodicity of 45 mm. The SGM operates over an energy range of 250 to 2000 eV, and below 800 eV the resolving power of the monochromator is better than 10^4. Because of the higher resolution (and often better signal-to-noise), I often try to remeasure XAS spectra that were originally acquired with BL8 with the SGM, but otherwise the operation of the SGM is quite similar to that of BL8. More information on the technical details of the SGM can be found in References [27] and [28].

Finally, the Resonant Elastic/Inelastic X-ray Scattering (REIXS) beamline at the CLS was open for commissioning during the last few months of my thesis reseach. This beamline uses a grating spectrometer similar in design and energy range to the one at BL8, but promising higher resolution. It also has an elliptical polarizing undulator, so the polarization of the incident X-ray beam can be tuned based on the experimentalist's needs. The REIXS beamline will probably play a prominent role in my future research, but at this time I have acquired only a few emission spectra using this beamline. Therefore, unless explicitly noted,

all XES spectra were taken at BL8.

2.3 X-ray Absorption Spectroscopy

When an incident X-ray has an energy greater than the binding energy of a core electron, there is the possibility that the core electron will absorb the X-ray and be promoted to an excited state. Most of these transitions are uninteresting, since the X-ray absorption cross-section of a given edge varies slowly and smoothly over a broad energy range [29]. The exception to this is when the incident X-ray energy is resonant, or close to resonant, with the the binding energy of a core electron. In this case the electron can be promoted to a bound state within the conduction band of the material, and in this regime the X-ray absorption cross-section varies considerably over a small energy range. For historical reasons, the type of XAS spectrum is labelled according to the core level that is close to resonance; when the $1s$ electrons are excited a K edge spectrum is acquired, when the $2s$, $2p_{1/2}$, or $2p_{3/2}$ electrons are excited an L_1, L_2, or L_3 edge spectrum is acquired, respectively, and so on.

The near resonant regime is where where XAS provides useful information about the material. By monitoring the quantity of X-rays absorbed by a material with respect to the incident X-ray energy over a range close to the binding energy of a core electron, the density of states (DOS) of the conduction band can be investigated. As shown schematically in Figure 2.1, conduction band states of energy E can be probed by exciting an electron from a known core level of energy E_{bind} with incident X-rays of energy $h\nu = E - E_{bind}$. The best way of measuring X-ray absorption is by measuring the intensity of the X-ray beam before and after passing through the sample, referred to as a "transmission measurement". This technique is routinely used when the incident X-rays have energies well in excess of 2000 eV, but in the soft X-ray regime the X-rays have very short penetration depths and consequently samples for soft X-ray transmission measurements must be only a few nanometres thin. Therefore other methods of measuring soft X-ray absorption are more common.

During the X-ray absorption transition, a core electron is excited to a conduction band state, and a vacant core level (a "core hole") is left behind. This core hole is filled almost immediately with an electron from a state higher in energy (either another core level or a

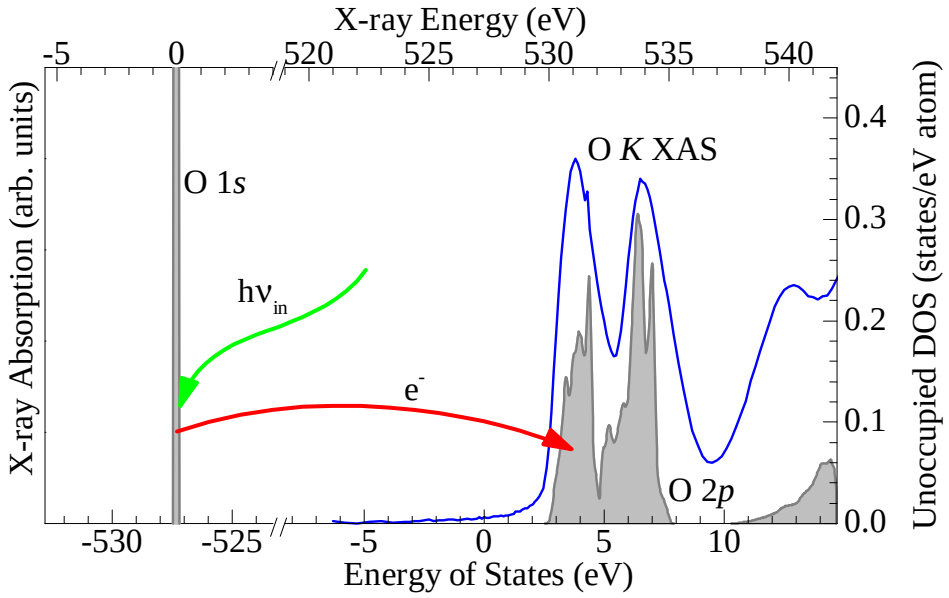

Figure 2.1: An example of an X-ray absorption transition. An incident X-ray of energy $h\nu_{in}$ excites an electron with a binding energy of E_{bind} to a conduction band state of energy $E = h\nu_{in} + E_{bind}$. This figure shows an O K XAS spectrum (taken in TEY mode) and calculated DOS for rutile TiO_2.

valence state), and the resulting energy released can be absorbed by other electrons or emitted as an X-ray. In the former process, excited electrons near the surface of a sample in UHV can be ejected, leaving the surface with a net electric charge. If the sample plate is grounded, the current drawn from the ground to balance the surface charge can be measured with a picoammeter, and the magnitude of this current is related to the magnitude of the X-ray absorption. This XAS technique is called "total electron yield" (TEY). Since electrons have a very short penetration depth this technique is quite surface sensitive (TEY probes only 10 nm deep or less [30]), and if the surface of the sample is oxidized or otherwise contaminated a TEY XAS spectrum may not be representative of the true XAS spectrum of the bulk sample.

For TFY, the emitted X-rays can be measured with a spectrometer or a non-energy dispersive detector like a channeltron. In this process, the total intensity of emitted X-rays is related to the magnitude of the X-ray absorption. This XAS technique is called "total fluorescence yield" (TFY). X-rays have a much longer penetration depth (TFY can probe hundreds of nanometres [29]) so this technique is bulk sensitive, but there is always

the possibility that emitted X-rays can be reabsorbed by the sample before reaching the detector. This "self-absorption" of X-ray fluorescence can suppress or distort features in the XAS spectrum. If an energy dispersive detector is available, often only a small energy range of the X-ray fluorescence will be integrated in a XAS measurement; this technique is called "partial fluorescence yield" (PFY) but is otherwise very similar to to TFY.

When a TFY (and/or PFY) spectrum matches the TEY spectrum, then the surface of the sample is free from contamination, self-absorption is not a significant problem, and the surface electronic states are representative of those in the bulk. In this situation the XAS spectra can be trusted to be representative of the true sample; however often this is not the case. Self-absorption is typically not a significant problem with light non-metal K edge spectra (i.e. those from B, C, N, O, and F), so TFY mode is often used when measuring those edges. However self-absorption is a major problem with transition metal $L_{2,3}$ edge spectra, as is surface oxidation, so great care must be taken to get a trustworthy XAS measurement [31].

One final method of measuring an XAS spectrum is to use "inverse partial fluorescence yield" (IPFY). With this method, the PFY of a *non-resonant* edge that has an energy less than the edge of interested is monitored. As the edge of interest begins to absorb photons, the PFY of the other edge is reduced (since those photons are no longer available for absorption). When the PFY of this non-resonant edge is inverted, the absorption spectrum of the edge in question is revealed. This technique is both bulk sensitive and free from self-absoprtion, [31] but it can only be done on materials with low energy edges that produce lots of X-ray emission. IPFY is typically used when one wants to measure the transition metal $L_{2,3}$ XAS of a material containing oxygen. For most of the materials I study herein, IPFY is not a viable option for measuring XAS.

2.4 X-ray Emission Spectroscopy

As mentioned above, after the X-ray absorption process has occurred a core hole exists that is quickly filled by an electron from a higher energy state. Sometimes the energy gained from this transition is released as an X-ray, and when the X-ray fluorescence intensity is integrated as a function of incident X-ray energy, a TFY mode XAS spectrum is acquired. If

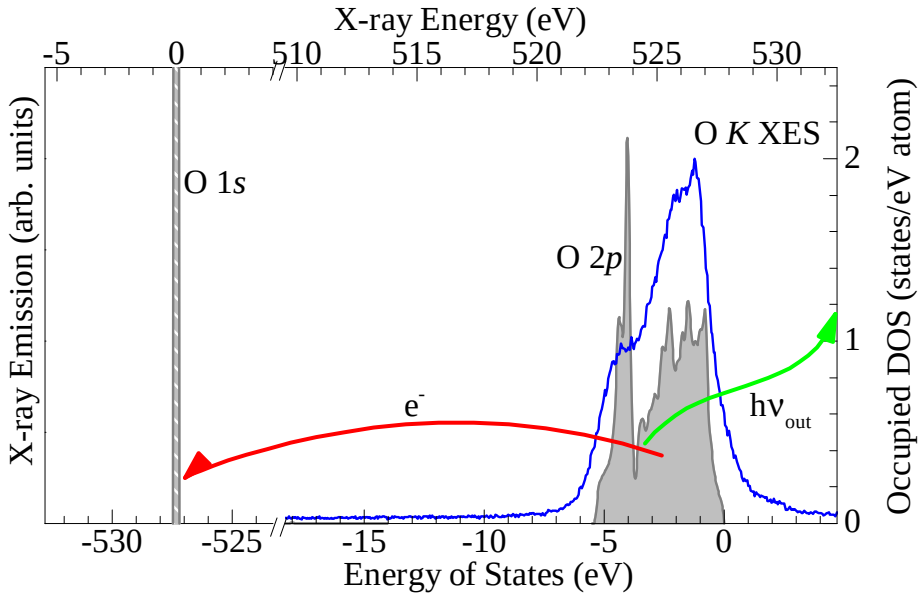

Figure 2.2: An example of an X-ray emission transition. A valence band electron of energy E decays to fill an unoccupied core level of energy E_{bind}. This releases an outgoing incident X-ray of energy $h\nu_{out} = E - E_{bind}$. This figure shows an O K XES spectrum and calculated DOS for rutile TiO_2.

a high resolution spectrometer is available (like the one at BL8), then an XES spectrum can be acquired: the incident X-ray energy is fixed, and the intensity of the X-ray fluorescence is measured as a function of emission energy. An XES spectrum can be acquired from the decay of another core state to fill the deeper core hole, but the most interesting spectra (and certainly the spectra most relevant to material properties) are when a weakly bound valence electron decays to fill the core hole. This process is shown schematically in Figure 2.2, note that the same nomenclature (K, $L_{2,3}$, etc.) is used to describe XES spectra as is used for XAS spectra: Since there is often more than one transition in which an electron can fill a core hole with via fluorescence decay, often an XES spectrum is described by the same letters and numbers as an XAS spectrum but followed by a Greek letter indexing the fluorescence decay (Siegbahn notation). For example, a Cu $2p_{3/2}$ core hole could be filled by a "semi-core" $3s$ state, resulting in $L_3\ell$ emission, or by a valence state, resulting in $L_3\alpha_{1,2}$ emission [32]. However, since all of my XES measurements are of valence to core level transitions, I have omitted the Greek letters in my labels for XES spectra.

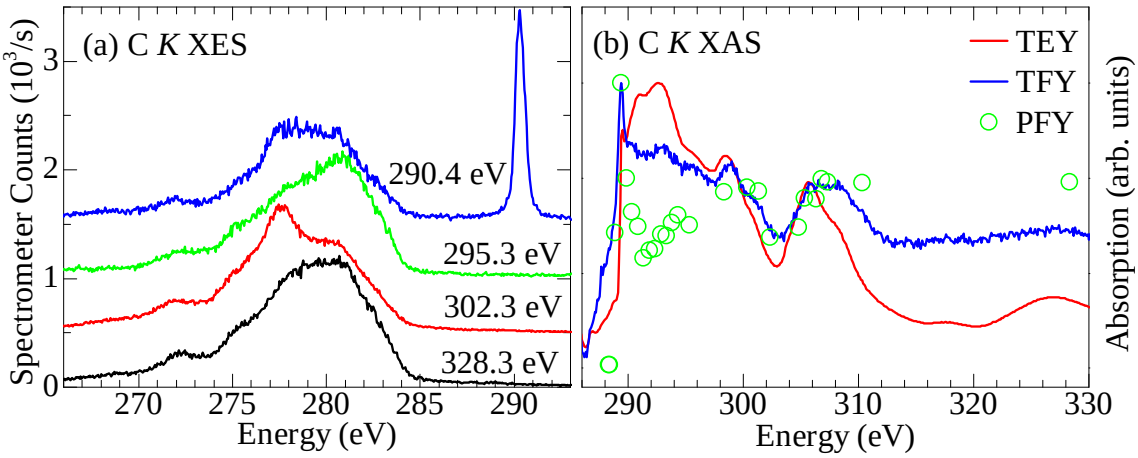

Figure 2.3: An example of some RXES measurements on commercial nanodiamond (Sigma Aldrich, measured at the REIXS beamline at the CLS): (a) Various C *K* XES spectra at different energies, note the changes in the shape of the spectrum. The elastic scatter is clearly visible in the top-most spectrum. (b) The C *K* XAS spectra, in both TEY and TFY modes. Also shown are the normalized integrated intensities of each XES spectrum (only 4 of which are shown in (a)).

By probing the occupied states, XES is an excellent compliment to XAS for studying a material. Since XES relies on emitted X-rays, it is bulk sensitive in the same manner that TFY (or PFY) mode XAS is. Since XES has a fixed incident X-ray energy, and the emitted X-rays have energies below the absorption threshold, an XES spectrum is rarely significantly distorted by self-absorption. Strong or weak self-absorption will change the total amplitude of the XES spectrum, but since the total amplitude is rarely quantitatively meaningful, self-absorption is usually not a problem with XES measurements. The main difficulty with XES is technical: the only high resolution detectors available at present are rather large and expensive grating spectrometers, so there are far fewer beamlines practising XES than XAS.

Typically an XES spectrum is acquired when the incident X-ray energy is well above resonance, this effectively decouples the absorption transition from the emission transition. However XES spectra can also be acquired when the incident X-ray energy is resonant with a particular absorption feature (RXES), this can reveal many interesting properties, most notably inelastic scattering from charge transfer, *dd*, or magnetic transitions [33], or momentum-preserving transitions within the band structure [34]. An example of this is shown in Figure

2.3, note how the shape of the XES spectrum changes as the excitation energy changes.

2.5 X-ray Photoemission Spectroscopy

One final X-ray spectroscopic technique is X-ray photoemission spectroscopy (XPS). Just like XES is related to TFY mode XAS, XPS is related to TEY mode XAS. In an XPS measurement, the incident X-ray energy is fixed and the kinetic energy of the electrons ejected from the sample is measured. The number of electrons measured with a given kinetic energy E_{kin} excited with a known X-ray energy $h\nu_{in}$ is related to the number of occupied states at energy $E = E_{kin} - h\nu_{in} + \phi$ (where ϕ is the correction for the work functions of both the sample and the detector). XPS therefore requires an energy dispersive detector of electrons; these can be much smaller and are much more commonplace than X-ray spectrometers.

Since XPS does not, strictly speaking, require a tunable X-ray source, nor a particularly bright X-ray source (since electron detectors have much higher efficiencies than X-ray detectors), XPS is often measured in laboratory systems, typically sourced with X-rays from a Mg or Al target, however there are many synchrotron XPS beamlines as well. XPS can probe core states as well as the valence level, as shown in Figure 2.4. Since XPS relies on emitted electrons, it is highly surface sensitive. However when an uncontaminated surface can be provided (typically by cleaving a sample in vacuum), XPS is a valuable technique that is complementary to XAS and XES, as the former probes the total occupied states while the latter two probe partial unoccupied or occupied states, respectively.

I have only performed a few XPS measurements personally, and none of those data are reported herein. In my published work the XPS data I have analysed has been measured by Dr. Anna Buling of the University of Osnabrück, Osnabrück, Germany and some more recent spectra have been measured by Dr. Dmitry Zatsepin of Ural Federal University, Yekaterinburg, Russia.

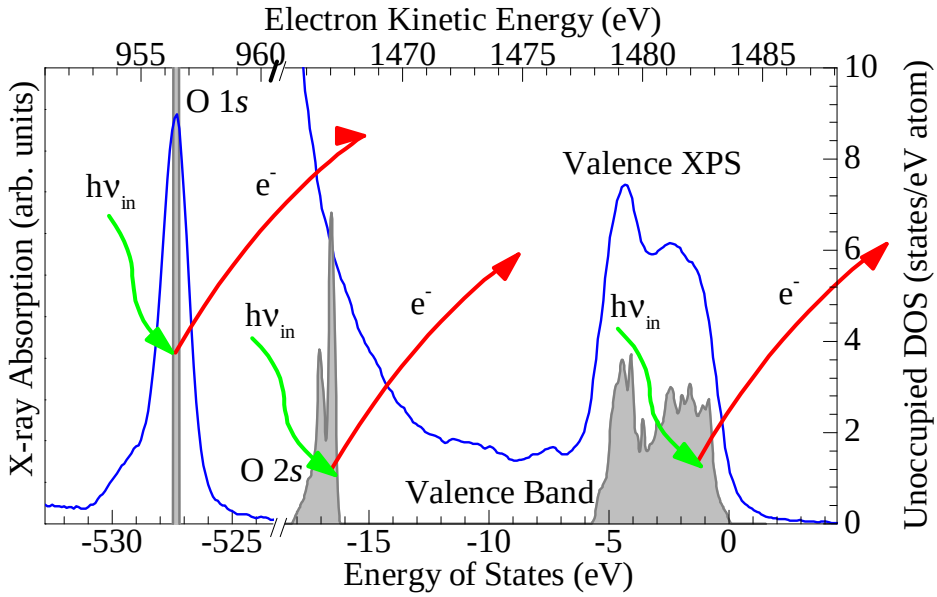

Figure 2.4: An example of an X-ray photoelectron transition. An incident X-ray of energy $h\nu_{in}$ excites an electron of energy E_{bind} to a continuum state, the electron ends up at a detector with kinetic energy $E_{kin} = h\nu_{in} + E_{bind} - \phi$ where *phi* is the correction for the work functions of both the sample and the detector. This figure shows an O 1s and a valence band XPS spectrum and calculated DOS for rutile TiO_2. XPS measurements were performed by Dr. Dmitry Zatsepin, Ural Federal University, Yekaterinburg, Russia.

2.6 Measurement Details

Unless explicitly noted, all samples reported herein were prepared for XES and XAS measurements by affixing them to a metallic sample holder with carbon tape. All measurements were conducted near 10^{-7} torr at ambient temperature with linearly polarized incident X-rays. All SGM XAS spectra were acquired with the incident X-rays at normal incidence to the sample, while all BL8 XAS spectra were acquired with the incident X-rays 30° from normal incidence. The BL8 XES spectrometer is orthogonal to the incident beam, so the XES spectra were acquired with the emitted X-rays at 60° from normal incidence.

Chapter 3

Density Functional Theory

While the many-body Hamiltonian that describes a crystal lattice is easy to write down, it is an extremely challenging task to solve that Hamiltonian to obtain the ground state many-body wavefunction so that ground state properties of the system can be calculated. Density functional theory (DFT) is an increasingly common and powerful theoretical approach for studying material properties by finding approximate solutions to the many-body Hamiltonian of a periodic solid or an isolated cluster (such as a molecule of a nanoparticle), and despite the inherent simplifications, DFT often yields accurate predictions on the properties of many materials.

In the context of my research I almost exclusively use the WIEN2k software package for DFT calculations. WIEN2k is a "full potential, all electron" code, meaning that the behaviour of every electron in the system is calculated — including the tightly bound core states — and the true potential of the atomic nuclei is used [14]. This is in contrast to "pseudopotential" codes, such as SIESTA, that replace the Coulomb potential of the atomic nuclei with a specially constructed potential that already includes the contribution from the core states [35–37]. A well-constructed pseudopotential can describe ground state properties with the same accuracy as a full potential approach, but is often much faster to calculate. On the other hand, since my experimental data is all obtained from X-ray spectroscopy which involves transitions from core levels, for my purposes it is advantageous to have explicitly calculated core state wavefunctions.

There are several textbooks outlining the DFT method (see, for example, References [35, 38, 39]), this chapter will just briefly outline the theory behind DFT.

3.1 The Many-Body Hamiltonian

Solving the many-body Hamiltonian is the central problem in solid state physics. For n atomic nuclei, and n_e electrons, the many-body Hamiltonian in the Schrödinger picture of quantum mechanics is [40]:

$$\begin{aligned}\mathbb{H} &= -\frac{\hbar^2}{2}\sum_i^n \frac{\nabla^2_{\vec{R}_i}}{M_i} - \frac{\hbar^2}{2}\sum_i^{n_e}\frac{\nabla^2_{\vec{r}_i}}{m_e} - \frac{1}{4\pi\epsilon_0}\sum_{i,j}^{n,n_e}\frac{e^2 Z_i}{\vec{R}_i - \vec{r}_j} \\ &\quad + \frac{1}{8\pi\epsilon_0}\sum_{i\neq j}^{n_e}\frac{e^2}{|\vec{r}_i - \vec{r}_j|} + \frac{1}{8\pi\epsilon_0}\sum_{i\neq j}^{n}\frac{e^2 Z_i Z_j}{\left|\vec{R}_i - \vec{R}_j\right|},\end{aligned} \tag{3.1}$$

where $\vec{R}_i$, M_i, and Z_i are the position, mass, and atomic number of nuclei i, respectively, and $\vec{r}_i$ is the position of electron i. This Hamiltonian is analytically intractable because of the Coulomb interaction terms between the nuclei and the electrons, given by the last three terms in the above equation.

In order to simplify this Hamiltonian, we first make the approximation that the atomic nuclei have infinite mass. This is called the "Born Oppenheimer approximation" [39], and as a result the first term (the kinetic energy of the atomic nuclei) and the last term (the Coulomb interaction between nuclei) drop out of the equation since the atomic cores are no longer free to move. A second important consequence is that the third term (the Coulomb interaction between nuclei and electrons) becomes separable since the atomic cores now provide a fixed Coulomb potential that each electron interacts with individually. Therefore the Coulomb potential of the atomic cores is treated as an "external potential" acting on a self-interacting electron gas, and the many-body Hamiltonian is simplified to:

$$\mathbb{H} = -\frac{\hbar^2}{2}\sum_i^{n_e}\frac{\nabla^2_{\vec{r}_i}}{m_e} + \frac{1}{8\pi\epsilon_0}\sum_{i\neq j}^{n_e}\frac{e^2}{|\vec{r}_i - \vec{r}_j|} + V_{ext}(\vec{r}) \tag{3.2}$$

$$\text{where } V_{ext}(\vec{r}) = -\frac{1}{4\pi\epsilon_0}\sum_{i,j}^{n,n_e}\frac{e^2 Z_i}{\left|\vec{R}_i - \vec{r}_j\right|},$$

The key to *density* functional theory, as was noted by Hohenberg and Kohn, is that the ground state electron density $\rho(\vec{r})$ of a system is uniquely defined by the external potential $V_{ext}(\vec{r})$ and vice versa [8]. This is easy to prove by contradiction:

1. Assume that $\rho(\vec{r})$) is the ground state electron density for two *different* $V_{ext}(\vec{r})$, say V_1 and V_2.

2. Assume the systems $\mathbb{H}_1$ and $\mathbb{H}_2$, corresponding to the two external potentials, V_1 and $V_2(\vec{r})$, respectively, have ground state wavefunctions $\psi_1(\vec{r})$ and $\psi_2(\vec{r})$, respectively.

3. Since $\psi_1(\vec{r})$ is the ground state wavefunction of the system $\mathbb{H}_1$, the ground state energy energy $E_1 = \langle\psi_1|\,\mathbb{H}_1\,|\psi_1\rangle$ is the minimum energy for this system.

4. The same is true for system $\mathbb{H}_2$; $E_2 = \langle\psi_2|\,\mathbb{H}_2\,|\psi_2\rangle$ is the lowest energy.

5. Therefore $E_1 < \langle\psi_2|\,\mathbb{H}_1\,|\psi_2\rangle$.

6. However the only difference between $\mathbb{H}_1$ and $\mathbb{H}_2$ is the external potential, so $E_1 < \langle\psi_2|\,\mathbb{H}_2 + V_1 - V_2\,|\psi_2\rangle$, or $E_1 < E_2 + \langle\psi_2|\,(V_1 - V_2)\,|\psi_2\rangle$.

7. Likewise, $E_2 < E_1 - \langle\psi_1|\,(V_1 - V_2)\,|\psi_1\rangle$.

8. We also have $\langle\psi_2|\,(V_1 - V_2)\,|\psi_2\rangle = \int dV_{\vec{r}}(V_1 - V_2)|\psi_2|^2 = \int dV_{\vec{r}}(V_1 - V_2)\rho(\vec{r}) = \Delta E_{ext}$.

9. Since we assumed the ground state electron density was the same for each system, we also have $\langle\psi_1|\,(V_1 - V_2)\,|\psi_1\rangle = \Delta E_{ext}$.

10. Therefore, $E_1 < E_2 + \Delta E_{ext}$ and $E_2 < E_1 - \Delta E_{ext}$.

11. Adding these equations together, we have $E_1 + E_2 < E_1 + E_2$, an obvious contradiction.

This shows that any observable (some operator $\mathbb{A}$) is a unique *functional* of the ground state electron density, i.e. $\langle\psi|\,\mathbb{A}\,|\psi\rangle = A(\rho)$. Hohenberg and Kohn also showed that the Hamiltonian functional, $H(\rho)$, providing the ground state energy (E_0);

$$\begin{aligned} E_0 = H(\rho) &= \langle\psi|\left[-\frac{\hbar^2}{2}\sum_i^{n_e}\frac{\nabla^2_{\vec{r}_i}}{m_e} + \frac{1}{8\pi\epsilon_0}\sum_{i\neq j}^{n_e}\frac{e^2}{|\vec{r}_i - \vec{r}_j|}\right]|\psi\rangle + \langle\psi|\,V_{ext}(\vec{r})\,|\psi\rangle \\ &= F_{HK}(\rho) + \int dV_{\vec{r}}\rho(\vec{r})V_{ext}(\vec{r}), \end{aligned} \tag{3.3}$$

exhibits two important properties [8]:

1. The "Hohenberg-Kohn" functional $F_{HK}(\rho)$, involves terms dealing solely with the electrons, not the atomic nuclei. Therefore this functional is *universal* for describing the self-interacting and kinetic behaviour of electrons in any many-body system, and

2. The ground state energy functional $H(\rho)$ reaches a global minimum when ρ is the ground state electron density of V_{ext}.

I should note that due to the electron-electron Coulomb interaction, the functional $F_{HK}(\rho)$ is intractable. However the first property shows that if $F_{HK}(\rho)$ can be found (or suitably approximated) it can be applied to *every* many-electron system. The second property shows that if $F_{HK}(\rho)$ can be found (or suitably approximated), a simple variational scheme can be used to find the true ground state electron density $\rho(\vec{r})$ by minimizing the energy [40]. One of the nice things about Hohenberg and Kohn's theory is that to some degree it separates the work of theorists from experimentalists; the former can toil away attempting to find better solutions for $F_{HK}(\rho)$ using abstract systems without worrying about whether these systems are physical, while the latter can use these (approximate) solutions to predict the properties of real materials with little concern for how they were obtained. (Although, obviously, since $F_{HK}(\rho)$ can only be approximately solved this separation between theory and practice is not entirely complete.)

3.2 The Kohn-Sham Equations

The work of Hohenberg and Kohn on a self-interacting electron gas in an external potential provide important insight on what is necessary to determine the ground state properties of a periodic lattice or cluster of atoms, but did not provide a means of finding the ground state density. It was Kohn and Sham who later determined a method for finding $\rho(\vec{r})$ [9]. The key step was to rewrite the functional $F_{HK}(\rho)$ as:

$$\begin{aligned} F_{HK}(\rho) &= K(\rho) + V(\rho) \\ &= K_0(\rho) + V_H(\rho) + (V(\rho) - V_H(\rho)) + (K(\rho) - K_0(\rho)) \\ &= K_0(\rho) + V_H(\rho) + V_x(\rho) + V_c(\rho) \end{aligned} \tag{3.4}$$

Here $K(\rho)$ and $V(\rho)$ are the kinetic energy and self-interaction Coulomb potentials of the many-electron system (see above, where $F_{HK}(\rho)$ is explicitly defined). $K_0(\rho)$ is the kinetic energy of a *non-interacting* electron gas, and $V_H(\rho)$ is the Hartree potential [35], defined by:

$$V_H(\rho) = \frac{e^2}{4\pi\epsilon_0}\int dV_{\vec{r}}\, dV_{\vec{r}'}\, \frac{\rho(\vec{r})\rho(\vec{r}')}{|\vec{r}-\vec{r}'|} \tag{3.5}$$

Finally, $V_x(\rho)$ is the "exchange potential" functional, given by the difference between the exact many-electron Coulomb potential functional and the Hartree potential functional, and $V_c(\rho)$ is the "correlation potential" functional, given by the difference between the exact many-electron kinetic energy functional and the non-interacting electron gas functional. Typically the exchange and correlation potential functionals are treated as a single "exchange correlation" functional, $V_{xc}(\rho) = V_x(\rho) + V_c(\rho)$.

When the Hamiltonian functional is written as above, Kohn and Sham showed that the ground state electron density of an n electron system was [9]:

$$\rho(\vec{r}) = \sum_i^n |\phi_i(\vec{r})|^2 , \tag{3.6}$$

where $\{\phi_i(\vec{r})\}$ are the n eigenfunctions solutions to [35, 40]:

$$\begin{aligned} \mathbb{H}_{KS}\phi_i(\vec{r}) &= \varepsilon_i\phi_i(\vec{r}) \\ \text{where } \mathbb{H}_{KS} &= \mathbb{K}_0 + \mathbb{V}_H + \mathbb{V}_{xc} \\ \mathbb{V}_{xc} &= \frac{d}{d\rho}V_{xc}(\rho) \end{aligned} \tag{3.7}$$

Kohn and Sham's theory therefore reduces a problem involving n self-interacting particles to an analogous one involving n independent particles. While each of these analogous independent particles, described by the single particle wavefunctions $\phi(\vec{r})$, have absolutely no physical meaning, all of these particles together reproduce the true ground state electron density (within the limits of the approximations made to obtain $V_{xc}(\rho)$) and consequently the true ground state wavefunction (by Hohenberg and Kohn's theory as described above) [40].

3.3 Exchange Correlation Potential

With Kohn-Sham theory, what was seemingly the insurmountable problem of solving the n-electron Schrödinger equation was reduced to the far more approachable problem of finding

n independent solutions to the Kohn-Sham Hamiltonian. Fortunately, due to Hohenberg-Kohn theory, whether or not DFT can be a useful theoretical tool rests with whether or not theorists can come up with approximations to the true exchange correlation potential V_{xc} that produce accurate results.

Fortunately there are many such solutions available, and consequently DFT is a very popular and powerful theoretical tool [35]. Since Hohenberg-Kohn theory assures us that a good approximation for V_{xc} will be independent of any specific material (i.e. any specific crystal lattice), experimentalists like myself can more or less freely choose an exchange correlation potential for the material under study without worrying about the specific theoretical details of that potential. Therefore this section will just provide a brief overview of the exchange correlation potentials used in my work.

The simplest exchange correlation functional is the "local density approximation" (LDA) functional, wherein the potential energy at a point $\vec{r}$ depends only on the electron density $\rho(\vec{r})$. This is written as [35]:

$$V_{xc}(\rho) \quad = \quad \int dV_{\vec{r}} \rho(\vec{r}) \epsilon_{xc}(\rho(\vec{r})), \tag{3.8}$$

where $\epsilon_{xc}(\rho(\vec{r}))$ is the solution to the exchange correlation energy calculated for a self-interacting electron gas (calculated for a variety of possibilities of $\rho(\vec{r})$ by Quantum Monte Carlo methods) [40]. Again, the usefulness of DFT relies on the fact that some theorist need calculated $\epsilon_{xc}(\rho(\vec{r}))$ only *once*, the resulting function can then be used in *every* subsequent DFT calculation for an arbitrary system.

The LDA exchange correlation functional is quite useful, but it can be improved upon by using a functional that depends not only on the local electron density, but also on the gradient of the local electron density. These are called "generalized gradient approximation" (GGA) functionals. Unlike the LDA functional, GGA functionals depend on specific parameters addressing how the gradient $\nabla\rho(\vec{r})$ is incorporated [41], and therefore there are many different GGA functionals (see, for example, References [42–44]). In a sense, because GGA functionals use specific parameters, calculations involving these functionals are not truly *ab initio* [40]. However in actual practice one particular GGA functional, that of Perdew, Burke, and Ernzerhof (the "PBE" functional) [44] is overwhelmingly used for almost every material.

Finally, I should mention that for non-magnetic, or collinear magnetic situations the DFT calculation can be split into separate spin channels (for LDA this is often called the "local spin density approximation", or LSDA; the GGA term applies to both non-spin polarized and spin polarized calculations).

GGA functionals have been shown to improve many material parameters over LDA functionals [35, 44], but tend to overestimate magnetic moments [35]. On the other hand, both GGA and LDA functionals are known to significantly underestimate the band gaps of insulators [45]. Recently a modification of a GGA developed by Becke and Johnson [46] was shown to greatly improve the band gap predictions (the "modified Becke Johnson", or mBJ functional) [47].

Band gaps are underestimated in DFT because the exchange part of the exchange correlation functional significant underestimates the influence of the Pauli exclusion principle (in contrast, the Hartree-Fock method, which calculates the exact exchange, often significantly overestimates band gaps [48]). The mBJ functional uses both a generalized gradient and a term involving the kinetic energy of each single particle state; this essentially produces an "effective potential" which mimics the influence of exact exchange on the single particle wavefunctions [46, 47].

In the DFT calculations described herein, I often start with the PBE functional. In the case of insulators I often follow up with an mBJ calculation using the ground state calculated with PBE (at present, the mBJ functional "corrects" the electronic structure already calculated with an LDA or GGA functional). However LDA and GGA functionals only work well for systems where an averaged electron density is a good approximation, i.e. systems where the electron-electron interactions do not manifest as localized increases in electron density. [49]

For certain systems it is necessary to modify the LDA or a GGA functional with some additional potential that is localized to a particular atomic site and often a particular orbital symmetry (typically d- or f-states). These calculations are definitely not *ab initio*, since the modifications to the exchange correlation functional are made in a material specific manner, but are sometimes necessary to obtain an electronic structure that agrees with experimental measurements. There are two types of modifications that I have used; the first is to mix

in partial amounts of the exact Fock (or Hartree-Fock) exchange-correlation functional — applied only to the charge local to a particular site and possessing a particular angular symmetry — to the over-all LDA or GGA function [50]. The second method is to add a Hubbard-like localized Coulomb potential of a specified energy U — again only to the charge local to a particular site and possessing a particular angular symmetry — to the over-all LDA or GGA function (this is the LDA+U or GGA+U approach) [49, 51].

This latter approach derives from the Hubbard model, which in mean field theory, adds an interaction Hamiltonian to specific orbitals (as noted above, usually valence d- or f-states of transition metals, lanthanides, or actinides) defined as [49]:

$$\begin{aligned} H_U &= \frac{1}{2}\sum_i U\left[\left(\langle n_i^{\uparrow}\rangle + \langle n_i^{\downarrow}\rangle\right)\left(n_i^{\uparrow} + n_i^{\downarrow}\right)\right. \\ &\quad \left. -\left(\langle n_i^{\uparrow}\rangle - \langle n_i^{\downarrow}\rangle\right)\left(n_i^{\uparrow} - n_i^{\downarrow}\right)\right] \\ &\quad -\frac{1}{4}\sum_i U\left[\left(\langle n_i^{\uparrow}\rangle + \langle n_i^{\downarrow}\rangle\right)^2 - \left(\langle n_i^{\uparrow}\rangle - \langle n_i^{\downarrow}\rangle\right)^2\right], \end{aligned} \tag{3.9}$$

where $n_i^{\uparrow}$ ($n_i^{\downarrow}$) is the number operator of spin up (spin down) states. This expression will tend to create a separation energy of U between the occupied and unoccupied orbitals, this expression also includes a correction for the double counting error (or self interaction correction) that is inherent in mean field approximations.

3.4 DFT Basis Sets

Hohenberg-Kohn and Kohn-Sham theory, combined with an appropriate approximation to the exchange correlation potential, provide a means of solving the many-electron Schrödinger equation in terms of "quasi"-single particle wavefunctions $\phi_i(\vec{r})$. In practice, these wavefunctions are expressed in terms of a known basis set. One of the first practical basis sets used was the "augmented planewave" (APW) basis set, originally described by Slater [6]. In this basis set the single particle wavefunctions are composed of planewaves in the spatial regions that were predetermined to be "interstitial" (i.e. sufficiently far from an atomic nuclei) and atomic-like wavefunctions consisting of solutions to the radial Schödinger (or Dirac, for scalar relativistic systems) equations and spherical harmonics in regions predetermined to be

within an appropriate radius of an atomic sphere. In this basis set, the planewaves ensure the periodicity conditions dictated by Bloch's theorem are met, while the use of atomic-like wavefunctions close to atomic nuclei greatly reduce the number of planewaves needed to describe the significant localization of charge that occurs in this region. Appropriate scaling factors are included for the atomic-like wavefunctions so they smoothly match the planewaves at the boundaries of the atomic spheres.

In practice, Slater's APW basis is rarely used because each single particle wavefunction depends on the as-yet undetermined eigen-energy ε_i. The "linearized augmented planewave" (LAPW) basis, developed by Andersen [52], improves on this by using a pre-determined fixed energy (or sometimes a separate energy for each choice of angular momentum ℓ) for all of the radial parts of the wavefunction within a given atomic sphere, and including an additional energy derivative of the radial part of the wavefunction. These two components (with two appropriate scaling factors) typically allow the atomic-like wavefunction to match the interstitial planewave in amplitude and spatial derivative at the sphere boundary; while the number of scaling factors is doubled (since one is needed for both the radial wavefunction and the energy derivative of that wavefunction) the problem is greatly simplified since the energy at which that the wavefunction is evaluated does not depend on the as-yet unknown eigen-energy solution to the Kohn-Sham Hamiltonian [40].

Finally, while Andersen's LAPW basis is much more computationally expedient than Slater's APW basis, it has problems accurately accounting for "semi-core" states, that is states considered to be inside the valence energy range but well separated from the topmost part of the valence band (most top-row transition metal $3s$- and $3p$-states fall into this category). To fix this problem, often "local orbitals" (LOs) are added to the LAPW basis; these orbitals are chosen only for specific atomic species and angular momenta, and the energies are centred on the expected energy of the "semi-core" states [40]. Because these states are only weakly influenced by the crystal structure, the appropriate LO angular momenta and energies can be chosen almost entirely based on the atomic species, rather than the specific crystal lattice in question. These LOs are defined such that their amplitudes go to zero outside the atomic sphere.

In fact, WIEN2k uses a heavily mixed basis consisting of LAPW states, LAPW + LO

states, "APW + lo" states (using Slater's APW basis with a fixed radial wavefunction energy and a single local orbital, as defined above, to improve the charge distribution across multiple bands), and "APW + lo + LO" states (that use both the previously defined APW-like local orbital and an additional local orbital to define "semi-core" states). The definitions of these states and the appropriate coefficients may be found in Appendix B.

In closing, I should mention that the choice of atomic sphere size is very important in pseudopotential and "muffin-tin" calculations (where the nuclei potential is only used up to the atomic sphere size, and in the interstitial region a constant average potential is used). However in "full potential" codes, like WIEN2k, the atomic sphere size only defines where the atomic-like basis set is traded for the planewave basis set. Since the basis sets are defined so the amplitude of the wavefunction is continuous across the sphere boundary, a judicious choice of atomic sphere size may improve the speed and convergence of a calculation but will not significantly affect the ground state density. However the atomic sphere size will strongly influence what is considered to be the "local" DOS (for example, the O $2p$ DOS is only the p-symmetry DOS within the O atomic sphere, not the projection of the entire electronic charge onto a basis of spherical harmonics centred on the O atomic site). Since X-ray spectroscopy involves transitions to and from a core wavefunction, any atomic sphere size which sufficiently contains that core wavefunction (i.e. the core wavefunction is sufficiently close to zero for any point beyond the atomic sphere) is appropriate.

3.5 Calculation Details

Unless explicitly noted, all calculations were conducted with the PBE exchange-correlation functional, all calculations involved discretizing the first Brillouin zone into a k-point mesh of 1000 points per fundamental unit cell, and a cut-off of -6.0 Ryd (measured with respect to the average interstitial potential) was used to discriminate between core and valence (or "semi-core") states. All calculations were extended to outer Brillouin zones such that $R_{MT}^{min} K_{max} = 7$; that is the product of the smallest atomic sphere and the largest reciprocal lattice vector was 7. All ground state electron densities were calculated self-consistently from initial guesses until the calculated electron density converged within margins of less than 0.0001 Ryd in

energy and 0.001 e^- in charge (both per unit cell).

The zero for the energy scale of the calculated DOS is always placed at the top of the valence band, i.e. the energy of highest occupied state. All states at negative energies are therefore occupied in the ground state, while all states a positive energies are unoccupied. I also refer to this energy as the "Fermi level"; this is rigorously accurate for metallic systems (since the DFT calculations are implicitly performed at temperatures of 0 K), for insulators and semiconductors this should be considered just a naming convention. Strictly speaking the Fermi level is undefined in insulators and semiconductors, [3] but it is also common to call the chemical potential the "Fermi level" in insulators and semiconductors, in contrast to the notation used in this thesis.

Finally, unless explicitly noted, the experimental crystal structures determined by X-ray diffraction (XRD) were used.

Chapter 4

X-ray Transitions

The X-ray transitions discussed here will all involve excitations from, or to, a core level. Because a core electron is extremely spatially localized compared to the wavelength of an X-ray with sufficient energy to promote that core electron to an unoccupied state, the operator governing this transition can be simplified considerably without significantly affecting the accuracy of the result. This not only simplifies the mathematics involved in calculating a soft X-ray spectrum; it also provides the selection rules which dominate a soft X-ray spectrum.

X-ray transitions are governed by the Fermi golden rule; consequently all of these X-ray transitions discussed here are equivalent to the probability amplitude of the projection of a valence (or conduction) band state on a transition-operator modified core level state.

4.1 Transition Operator for Electrons in a Radiation Field

From time-dependent perturbation theory, the interaction between electrons and classical radiation field is [53]:

$$T = -\frac{e}{mc}\exp\left(i\frac{E_f - E_i}{\hbar c}\hat{n}\cdot\vec{r}\right)\vec{p}\cdot\vec{A}. \tag{4.1}$$

Here E_f is the energy of the final state, E_i is the energy of the initial state, $\hat{n}$ is the propagation direction of the radiation, $\vec{r}$ is the position of the electron, $\vec{p}$ is the momentum of the electron, $\vec{A}$ is the vector potential of the radiation field, m is the mass of an electron, c is the speed of light, e is the charge of an electron, and $\hbar$ is the reduced Planck's constant. For linearly polarized light we have $\vec{A} = A\hat{e}$ for polarization direction $\hat{e}$.

The exponential $\exp\left(i\frac{E_f-E_i}{\hbar c}\hat{n}\cdot\vec{r}\right)$ represents the retardation of the field across the atom. Since the X-ray energies are typically less than 2000 eV, and the distance r is less than 1 Å, the argument for the exponent is less than 1 (for the C K-edge with $r = 0.5$ Å the argument is about 0.07). Therefore we can expand the exponent in a McLauren series:

$$\exp\left(i\frac{E_f-E_i}{\hbar c}\hat{n}\cdot\vec{r}\right) \simeq 1 + i\frac{E_f-E_i}{\hbar c}\hat{n}\cdot\vec{r} - \left(\frac{E_f-E_i}{\hbar c}\hat{n}\cdot\vec{r}\right)^2 + \cdots . \tag{4.2}$$

We typically only retain the first term in this expansion, which limits the transitions to those allowed by dipole selection rules. We therefore use the transition operator:

$$T_{if} \simeq -\frac{eA}{mc}\vec{p}\cdot\hat{e}. \tag{4.3}$$

From quantum mechanics we know that for a ground state Hamiltonian $\mathbb{H}_0 = \frac{\vec{p}^2}{2m} + V(\vec{r})$ we have the commutation relation:

$$\begin{aligned}
[\vec{r}, \mathbb{H}_0] &= \vec{r}\mathbb{H}_0 - \mathbb{H}_0\vec{r} \\
&= \vec{r}\left(\frac{\vec{p}^2}{2m}\right) - \left(\frac{\vec{p}^2}{2m}\right)\vec{r} \\
&= \frac{i\hbar}{m}\vec{p},
\end{aligned} \tag{4.4}$$

and we can therefore also write the transition operator as:

$$\mathbb{T}_{if} \simeq \frac{eA}{i\hbar c}[\vec{r}, H_0]\cdot\hat{e}. \tag{4.5}$$

The probability, $\Gamma_{if}(\hat{e})$, of a given X-ray transition is then:

$$\begin{aligned}
\Gamma_{if}(\hat{e}) &= \frac{2\pi}{\hbar}\left|\langle\psi_f|\mathbb{T}_{if}|\psi_i\rangle\right|^2\delta(E_f - E_i - h\nu) \\
&\simeq \frac{2\pi e^2A^2}{\hbar^3c^2}\left|\langle\psi_f|[\vec{r}, \mathbb{H}_0]\cdot\hat{e}|\psi_i\rangle\right|^2\delta(E_f - E_i - h\nu) \\
&\simeq \frac{2\pi e^2A^2}{\hbar^3c^2}\left|\langle\psi_f|\left(\vec{r}\mathbb{H}_0 - \mathbb{H}_0\vec{r}\right)\cdot\hat{e}|\psi_i\rangle\right|^2\delta(E_f - E_i - h\nu) \\
&\simeq \frac{2\pi e^2A^2}{\hbar^3c^2}\left|\langle\psi_f|\left(E_i - E_f\right)\vec{r}\cdot\hat{e}|\psi_i\rangle\right|^2\delta(E_f - E_i - h\nu) \\
&\simeq \frac{2\pi e^2A^2}{\hbar^3c^2}\left(E_f - E_i\right)^2\left|\langle\psi_f|\vec{r}\cdot\hat{e}|\psi_i\rangle\right|^2\delta(E_f - E_i - h\nu).
\end{aligned}$$

We can expand the dot-product $\vec{r}\cdot\hat{e}$ using the addition theorem for spherical harmonics [54]:

$$\begin{aligned} P_\ell(\hat{x}\cdot\hat{y}) &= \frac{4\pi}{2\ell+1}\sum_m Y_{\ell m}(\hat{x})Y^\dagger_{\ell m}(\hat{y}) \\ \vec{r}\cdot\hat{e} &= rP_1(\hat{r}\cdot\hat{e}) \qquad (4.6) \\ &= \frac{4\pi}{3}r\sum_{q=-1}^{1} Y^\dagger_{1q}(\hat{e})Y_{1q}(\hat{r}), \qquad (4.7) \end{aligned}$$

where $P_\ell(x)$ is a Legendre polynomial of degree ℓ, and $Y_{\ell m}(\hat{x})$ is a spherical harmonic of degree ℓ and order m. If we take into account that the delta function will set $(E_f - E_i) = h\nu$, the X-ray transition probability is now:

$$\Gamma_{if}(\hat{e}) \simeq \frac{4(2\pi)^6 e^2 A^2 \nu^2}{9hc^2}\left|\sum_q Y^\dagger_{1q}(\hat{e})\langle\psi_f|rY_{1q}(\hat{r})|\psi_i\rangle\right|^2 \delta(E_f - E_i - h\nu). \qquad (4.8)$$

4.2 The Dipole Matrix Elements

Evaluating an X-ray transition involves solving the matrix elements of $\langle\psi_f|rY_{1q}(\hat{r})|\psi_i\rangle$. We can express the many-body wavefunctions as the product of the single particles involved in the transition with the remainder of the system:

$$\begin{aligned} |\psi_i\rangle &= |\phi_i\rangle\,|\Phi_i\rangle \\ |\psi_f\rangle &= |\phi_f\rangle\,|\Phi_f\rangle \qquad (4.9) \\ \langle\psi_f|\,rY_{1q}(\hat{r})\,|\psi_i\rangle &= \langle\phi_i|\,rY_{1q}\,|\phi_f\rangle\,\langle\Phi_f|\Phi_i\rangle\,, \end{aligned}$$

where here $\phi_{i,f}$ represents the single particle wavefunction in the initial and final states, respectively, and $\Phi_{i,f}$ represents the wavefunction of the (many) remaining particles in the system in the initial and final states. Since X-ray transitions are highly spatially localized and the transitions occur very rapidly [55], it is common to assume $\langle\Phi_f|\Phi_i\rangle = 1$, and this approximation is usually sufficient to explain the majority of the features in any X-ray spectrum from a broad-band material [56].

Since X-ray transitions typically involve a core state which is tightly bound to an atomic site, it is convenient to express the single particle wavefunctions in terms of spherical harmonics centred on that site. A core state would then be defined simply as:

$$\phi_{core} = u_\ell(r,E)Y_{\ell m}(\hat{r}), \qquad (4.10)$$

where $u_\ell(r, E)$ is the radial solution to the Schrödinger equation for the atomic potential at energy E, while a band state would be defined as (refer to Appendix B for the specifics of an APW, LAPW, LAPW+LO, or APW+lo+LO band state):

$$\phi_{band} = \sum_{\ell m} f_{\ell m}(r, E) Y_{\ell m}(\hat{r}) \tag{4.11}$$

for some radial expression $f_{\ell m}(r, E)$ which would in general depend on the energy of the band state, as well as the crystal momentum.

Even for systems that provide a more rigourous description of core states than is found in Hydrogen-like wavefunctions (i.e. take spin-orbit splitting and other many-body effects into account) the wavefunctions for electrons would still consist of the sum of one or more radial functions and spherical harmonics [57].

The general matrix element for an X-ray transition therefore involves a radial integral and an integral over spherical harmonics:

$$\langle \phi_i | \, r Y_{1q} \, | \phi_f \rangle \;\; \simeq \;\; \int r^2 dr f_i(r, E_i) r f_f(r, E_f) \int d\Omega_r Y^\dagger_{\ell_i m_i}(\hat{r}) Y_{1q}(\hat{r}) Y_{\ell_f m_f}(\hat{r}). \tag{4.12}$$

Integrals of three spherical harmonics over a complete sphere, like the one shown above, have analytic solutions. These can conveniently be expressed in terms of Wigner 3j symbols [57], and are discussed in more detail in Appendix C. Since outside of the simple Hydrogen-like atom the radial wavefunctions do not have an analytic solution, the radial integral shown above must be evaluated numerically (and the radial wavefunctions contributing to this integral must be solved by numerically integrating the radial Schödinger or Dirac equation).

It is important to stress that because the core level radial wavefunction is spatially confined to a particular atomic site, the radial integral for any core level X-ray transition can be limited to a finite radius from the particular atomic nucleus. Since WIEN2k requires the regions local to an atomic site be defined as part of that "atomic sphere" (refer back to Section 3.4), the integral described above can be evaluated fairly expediently. As long as the atomic sphere is large enough to essentially enclose the core level wavefunction (and this condition is, in fact, necessary for a well-converged calculation, because otherwise core charge can "leak" out and not be properly accounted for), an X-ray transition can be completely evaluated within that atomic sphere.

Referring back to Equation 4.8, we can consider the situation where either the initial state (for an absorption transition) or the final state (for an emission transition) is a core state, and the incoming (or outgoing) photons are unpolarized (or, alternatively, the sample is polycrystalline). If the core state is a solution to the Dirac equation (note that relativistic considerations are important for core states in heavy atoms) [58], then m for the core state is not a good quantum number and should be summed over (since a specific m cannot be selected experimentally). If the photons are unpolarized, or the sample consists of randomly oriented grains, then all possible polarization states should be integrated. In this situation (consider the core state as the initial state) we therefore have:

$$\begin{aligned}
\Gamma_{if} &\propto \sum_{m_i} \int d\Omega_{\hat{e}} \left| \sum_q Y_{1q}^{\dagger}(\hat{e}) \langle \psi_f | r Y_{1q}(\hat{r}) | \psi_i \rangle \right|^2 \delta(E_f - E_i - h\nu) \\
&\propto \sum_{m_i} \sum_{qq'} \int d\Omega_{\hat{e}} Y_{1q}^{\dagger}(\hat{e}) Y_{1q'}(\hat{e}) \langle \psi_f | r Y_{1q}(\hat{r}) | \psi_i \rangle \langle \psi_i | r Y_{1q'}^{\dagger}(\hat{r}) | \psi_f \rangle \delta(E_f - E_i - h\nu) \\
&\propto \sum_{m_i} \sum_{q} \langle \psi_f | r Y_{1q}(\hat{r}) | \psi_i \rangle \langle \psi_i | r Y_{1q'}^{\dagger}(\hat{r}) | \psi_f \rangle \delta(E_f - E_i - h\nu). \qquad (4.13)
\end{aligned}$$

Referring back to the general expressions for core states (Equation 4.10) and band states (Equation 4.11), and using the notation for spherical harmonic integrals given in Appendix C, we have:

$$\begin{aligned}
\Gamma_{if} &\propto \sum_{\ell_f m_f} \sum_{\ell'_f m'_f} \int r^2 dr f_{\ell_f m_f}(r, E_f) r u_{\ell_i}(r, E_i) \int r^2 dr f_{\ell'_f m'_f}(r, E_f) r u_{\ell_i}(r, E_i) \\
&\quad \times \sum_{m_i, q} \Omega\left(\ell_i m_i, 1q, \ell_f m_f\right) \Omega\left(\ell_i m_i, 1q, \ell'_f m'_f\right) \delta(E_f - E_i - h\nu) \\
&\propto \sum_{\ell_f m_f} \left[\int r^2 dr f_{\ell_f m_f}(r, E_f) r u_{\ell_i}(r, E_i) \right]^2 W(\ell_1, 1, \ell_f) \delta(E_f - E_i - h\nu). \qquad (4.14)
\end{aligned}$$

This leads to an X-ray transition probability of:

$$\begin{aligned}
\Gamma_{if} &\propto \sum_{\ell_f m_f} W(\ell_i, 1, \ell_f) \left[\int r^2 dr f_{\ell_f m_f}(r, E_f) r u_{\ell_i}(r, E_i) \right]^2 \delta(E_f - E_i - h\nu), \\
\text{where :} \qquad W(\ell_i, 1, \ell_f) &= \left(\left(\frac{\ell_i}{2\ell_i + 1} \right) \delta_{\ell_i - 1, \ell_f} + \left(\frac{\ell_i + 1}{2\ell_i + 3} \right) \delta_{\ell_i + 1, \ell_f} \right). \qquad (4.15)
\end{aligned}$$

This form of the X-ray transition probability works for both emission and absorption transitions in broad band materials, since the only difference between the two is whether the core

state is the initial or final state, and whether the band state is a nominally occupied or unoccupied state. This simpler expression obtained by averaging the polarizations is widely used when calculating X-ray spectra using the WIEN2k code [59–61], but when using a computer code it is still relatively simple to include the influence of photon polarization.

Finally, it should be stressed that since X-ray transitions are governed by the Fermi golden rule; the "final state" of the transition has a dominant influence on the spectrum. For an X-ray emission transition, the final state is a full core level, a hole in the valence band, and an excited electron. The perturbation from a single valence hole and an excited electron on the ground state electronic structure is very minor, and consequently the ground state electronic structure often provides a very accurate description of the XES spectrum. However the final state in an X-ray absorption transition has a hole in a deep core level, and an excited electron. The perturbation from this "core hole" can be quite significant [62], and it is often necessary to explicitly include a vacancy in a core level to accurately calculate an XAS spectrum [63, 64].

4.3 Practical Polarized X-ray Spectra

The dependence of the X-ray transition probability in Equation 4.8 on the polarization vector $\hat{e}$ allows one to use the results of a band structure calculation to obtain the X-ray spectrum for an arbitrary polarization with respect to the coordinates of the unit cell. However this is not usually an experimentally realizable situation; typical samples will have less than perfect ordering. In fact, since many samples are polycrystalline, the unpolarized formula derived in the previous section is appropriate even for measurements obtained with highly polarized synchrotron light.

In between the extremes of perfect polarization in a perfect crystal, and a completely polycrystalline or amorphous material, there are several possibilities of intermediate disorder that present different methods of treating the polarization. Some possibilities that I considered are shown in Figure 4.1. The first case (part **a** of Figure 4.1) is the aforementioned situation of a perfect crystal exposed to linearly polarized light. In this case the polarization vector, defined relative to the crystal axes, sufficiently describes the situation. The second

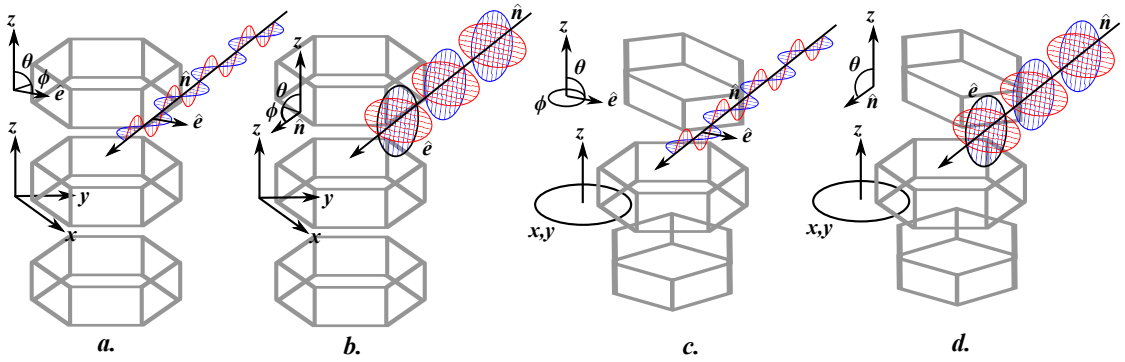

Figure 4.1: Some different ways of partially averaging the polarization vector, due to partial disorder in the sample or the light. The grey hexagons represent small crystalline pieces of material, with the coordinate system labelled $\{x, y, z\}$. The normal vector of the incident light is shown (labelled $\hat{n}$), and the polarization (labelled $\hat{e}$) is either fixed or consists of all possibilities normal to $\hat{n}$. For X-ray emission, simply treat the incident light as outgoing (emitted) light.

case (part **b** of Figure 4.1) is the situation where a perfect crystal is exposed to unpolarized light with a known incidence vector. This is a useful description of X-ray emission from perfect crystals, where the vector of the emitted light is known (by the geometry of the sample with the X-ray detector), but the detector is unable to measure X-ray polarization. This situation can be treated by integrating the polarization over all angles (θ,ϕ) that are normal to the incident vector $\hat{n}$. This form of polarization is completely described by specifying the direction of the incident light ($\hat{n} = \{\theta, \phi\}$).

The third case (part **c** of Figure 4.1) is the situation where the sample consists of polycrystalline pieces that have a preferred orientation (in this case in the z direction), and the sample is exposed to linearly polarized light. Thin films or highly-oriented planar graphite (HOPG) are good examples of these types of systems. In this situation there is no clear x and y axes of the crystal, and this is effectively treated by integrating the polarization over all angles that change the projection of the polarization in the plane of the sample. In situations where the z axes is the preferred orientation, the integration is over the longitudinal angles ($\phi \in \{0, 2\pi\}$), and can be performed analytically. However the preferred orientation of a system does not always correspond to the z axis of the maximum-symmetry coordinates of an atomic site, so in general the integration must be done numerically. This form of polarization

is completely described by specifying the azimuthal angle of the polarization with respect to the preferred orientation of the sample (i.e. the θ angle of $\hat{e}$ if the preferred orientation is z).

The fourth and final case (part **d** of Figure 4.1) is a combination of the previous two situations; here the sample has a preferred orientation (again shown here for the z direction), and the light is unpolarized but has a known incident (or outgoing) direction $\hat{n}$. This is an appropriate treatment for angle-resolved X-ray emission spectra from HOPG, for example. This situation is treated by integrating the polarization over all angles (θ,ϕ) that are normal to the incident (outgoing) vector $\hat{n}$, and also integrating over all incident (outgoing) vectors $\hat{n}$ that have different projections in the plane of the sample. As before, in situations where the z axes is the preferred orientation, this corresponds to integrating over all longitudinal angles (ϕ-component of $\hat{n}$). This form of polarization is completely described by specifying the azimuthal angle of the incident vector with respect to the preferred orientation of the sample (i.e. the θ angle of $\hat{n}$ if the preferred orientation is z).

An example of polarized XES and XAS spectra is shown in Figure 4.2 for perfect graphite; this compares favourably with measured spectra (see, for example, Reference [65]). The linear and circular polarizations in Figure 4.2 refer to methods (c) and (d), respectively, shown schematically in Figure 4.1. Of course actually measuring linearly polarized XES measurements would require a X-ray spectrometer capable of detecting and discriminating incoming X-ray polarizations. It should also perhaps be mentioned that while the *formalism* for calculating polarized X-ray spectra within a DFT framework is not new, I *implemented* these algorithms for the WIEN2k code myself.

4.4 Resonant X-ray Transitions

The concept of RXES was briefly mentioned in Section 2.4 as a spectroscopic technique that essentially couples the X-ray absorption and X-ray emission transitions together. In the context of a broad band material, where the XES and XAS measurements are close to probing the ground state electronic structure, RXES measurements can be thought of as "momentum selective" XES spectra. Because the absorption and emission transitions are linked, and because an X-ray can carry negligible crystal momentum, the X-ray emission can

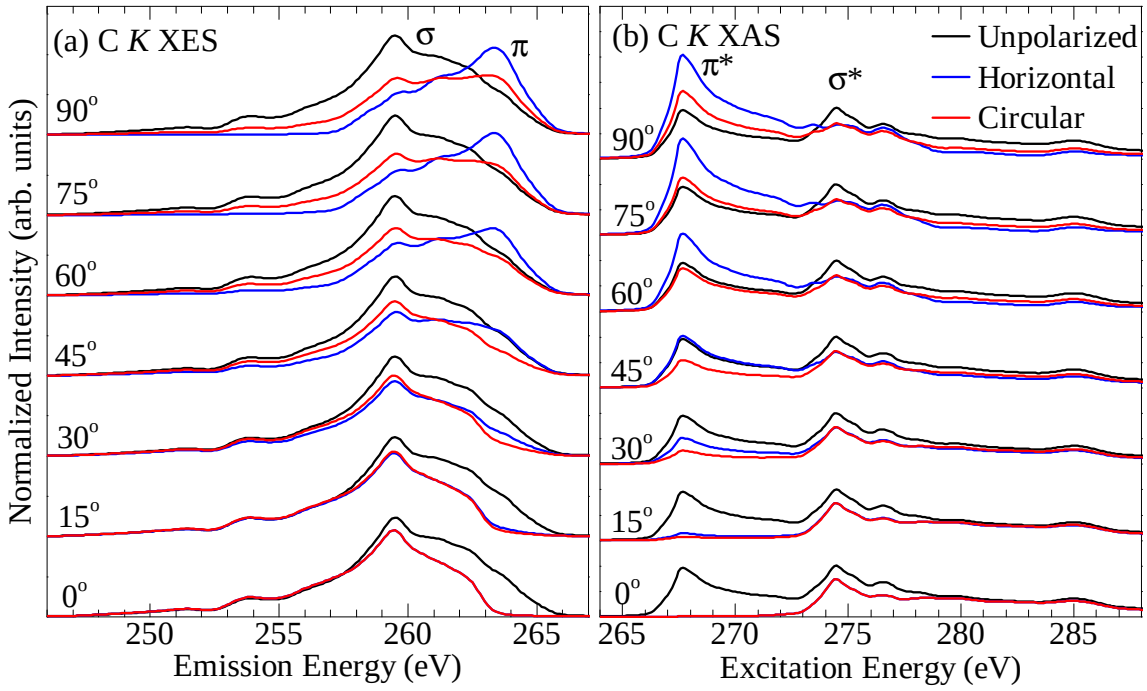

Figure 4.2: Calculated linearly and circularly polarized spectra from graphite: (a) the C K XES spectra (polarization is given for the *emitted* X-rays), where the angle between the sample normal (crystalline c axis) and the spectrometer is given, and (b) the C K XAS spectra (polarization is given for the *incident* X-rays), where the angle between the sample normal (crystalline c axis) and the incident X-ray beam is given.

only occur from sites within the band structure that have the same crystal momentum as the unoccupied bound states that were involved in the X-ray absorption transition.

Resonant X-ray emission is best described as a second order effect (compared to non-resonant X-ray emission or X-ray absorption, both first order effects) of the perturbation of an electromagnetic field on a system of electrons. To describe this, it is perhaps better to use the interaction Hamiltonian between electrons and an electromagnetic field (rather than just the simple classical electromagnetic field from Equation 4.1), which is (neglecting spin) [33]:

$$H_{int} = \sum_i \left[\frac{e}{m} \vec{A} \cdot \vec{p} + \frac{e^2}{2m} \vec{A}^2 \right], \tag{4.16}$$

where e and m are the usual charge and mass of an electron, $\vec{A}$ is the vector potential of the radiation field (in the gauge $\nabla \cdot \vec{A} = 0$), and $\vec{p}$ is the electron momentum operator [33]. To second order, the Fermi golden rule for this interaction Hamiltonian is then:

$$\Gamma_{if} = \frac{2\pi}{\hbar} \sum_f \left| \langle \psi_f | H_{int} | \psi_i \rangle + \sum_m \frac{\langle \psi_f | H_{int} | \psi_m \rangle \langle \psi_m | H_{int} | \psi_i \rangle}{E_i + h\nu - E_m + i\gamma_m} \right|^2 \delta(E_f - E_i - h\nu), \tag{4.17}$$

where there is a sum over all final states f, and all intermediate states m (and γ_m is the lifetime of the intermediate state). The first term in the square is just the regular X-ray emission, already describe in Section 4.1, while the second term is the resonant X-ray emission. In the interaction potential the $\vec{A}^2$ term describes Thompson scattering, which is not very sensitive to resonant excitation. [33] If the first term (the regular X-ray emission) in Equation 4.17 and the Thompson scattering from the interaction Hamiltonian are neglected, we obtain the the Kramers-Heisenberg formula [33, 53, 66], which reduces to (by the same procedure used to derive Equation 4.8):

$$I(\nu_{in}, \nu_{out}) = \sum_f \left| \sum_m \frac{\langle \Psi_f | \vec{r}_f \cdot \hat{e}_f | \Psi_m \rangle \langle \Psi_m | \vec{r}_i \cdot \hat{e}_i | \Psi_i \rangle}{E_m - E_i - h\nu_{in} - i\frac{\Gamma}{2}} \right|^2 \delta \left(E_f + h\nu_{out} - E_i - h\nu_{in} \right), \tag{4.18}$$

where Ψ_f is the final state, Ψ_m is the intermediate state, and Ψ_i is the initial state. Γ is the lifetime of the intermediate state, and $\hat{e}_1$ is the polarization of the incident light.

Since the Kramers-Heisenberg Formula involves two-particle interactions, in a single-particle band structure each wavefunction is the product of two single particle wavefunctions.

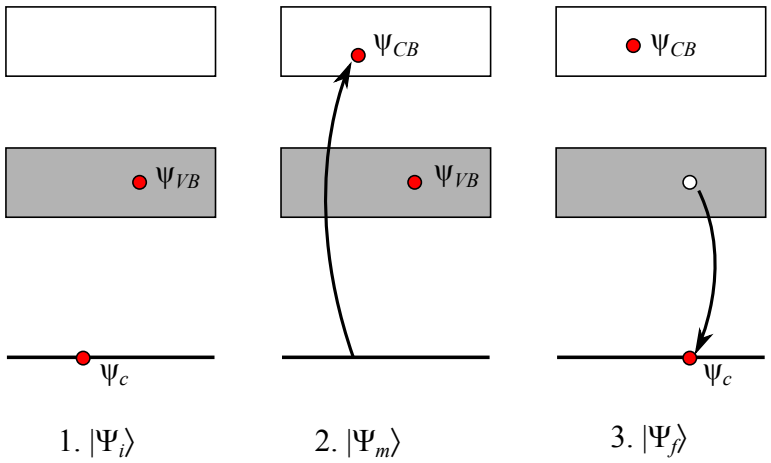

Figure 4.3: The initial, intermediate, and final wavefunctions for a Kramers-Heisenberg X-ray transition in a single particle band structure.

For a core state ψ_c, a valence band state ψ_{VB}, and a conduction band state ψ_{CB} we have:

$$\begin{aligned} |\Psi_i\rangle &= |\psi_c(\vec{r}_i)\rangle\,|\psi_{VB}(\vec{r}_f)\rangle \\ |\Psi_m\rangle &= |\psi_{CB}(\vec{r}_i)\rangle\,|\psi_{VB}(\vec{r}_f)\rangle \\ |\Psi_f\rangle &= |\psi_{CB}(\vec{r}_i)\rangle\,|\psi_c(\vec{r}_f)\rangle \end{aligned} \tag{4.19}$$

These wavefunctions are shown schematically in Figure 4.3. Note that there is only one final state core level available, and it is the same as the initial state core level (assuming only radiative decay).

With single particle wavefunctions the two transitions matrix elements are therefore:

$$\begin{aligned} \langle\Psi_m|\,\vec{r}_i\cdot\hat{e}_i\,|\Psi_i\rangle\rangle &= \langle\psi_{CB}(\vec{r}_i)|\,\langle\psi_{VB}(\vec{r}_f)|\,\vec{r}_i\cdot\hat{e}_i\,|\psi_c(\vec{r}_i)\rangle\,|\psi_{VB}(\vec{r}_f)\rangle \\ &= \langle\psi_{CB}(\vec{r}_i)|\,\vec{r}_i\cdot\hat{e}_i\,|\psi_c(\vec{r}_i)\rangle\,\langle\psi_{VB}(\vec{r}_f)|\psi_{VB}(\vec{r}_f)\rangle \\ &= \langle\psi_{CB}(\vec{r}_i)|\,\vec{r}_i\cdot\hat{e}_i\,|\psi_c(\vec{r}_i)\rangle \\ \text{and}\qquad \langle\Psi_f|\,\vec{r}_f\cdot\hat{e}_f\,|\Psi_m\rangle &= \langle\psi_c(\vec{r}_f)|\,\vec{r}_f\cdot\hat{e}_f\,|\psi_{VB}(\vec{r}_f)\rangle \end{aligned} \tag{4.20}$$

With these definitions for the valence and conduction band states, the choice of initial and final state completely determines the intermediate state, and therefore there is only one state Ψ_m to sum over (this is in contrast to model-Hamiltonian RIXS calculations that have multiple intermediate states). Using the definitions of core and band states given above in

Equations 4.10 and 4.11, and the expansion of $\vec{r}\cdot\hat{e}$ in terms of spherical harmonics [54], we have:

$$\begin{aligned}
I(\nu_{in},\nu_{out}) &= \left(\frac{4\pi}{3}\right)^4 \sum_{m_c m_c'}\sum_{q_i q_i'} Y^{\dagger}_{1q_i}(\hat{e}_i)Y_{1q_i'}(\hat{e}_i)\sum_{q_f q_f'} Y^{\dagger}_{1q_f'}(\hat{e}_f)Y_{1q_f}(\hat{e}_f)\frac{\delta\left(E_f+h\nu_{out}-E_i-h\nu_{in}\right)}{\left|E_m-E_i-h\nu_{in}-i\frac{\Gamma}{2}\right|^2} \\
&\times \sum_{\ell_{VB}m_{VB}}\left[\int r^2 dr f_{\ell_{VB}m_{VB}}(r,E_{VB})ru_{\ell_c}(r,E_c)\right]\Omega\left(\ell_c m_c,1q_i,\ell_{VB}m_{VB}\right) \\
&\times \sum_{\ell'_{VB}m'_{VB}}\left[\int r^2 dr f_{\ell'_{VB}m'_{VB}}(r,E_{VB})ru_{\ell_c}(r,E_c)\right]\Omega\left(\ell_c m_c,1q_i',\ell'_{VB}m'_{VB}\right) \\
&\times \sum_{\ell_{CB}m_{CB}}\left[\int r^2 dr f_{\ell_{CB}m_{CB}}(r,E_{CB})ru_{\ell'_c}(r,E_{c'})\right]\Omega\left(\ell'_c m'_c,1q_f,\ell_{CB}m_{CB}\right) \\
&\times \sum_{\ell'_{CB}m'_{CB}}\left[\int r^2 dr f_{\ell'_{CB}m'_{CB}}(r,E_{CB})ru_{\ell'_c}(r,E_{c'})\right]\Omega\left(\ell'_c m'_c,1q_f',\ell'_{CB}m'_{CB}\right) \quad (4.21)
\end{aligned}$$

In the case of polycrystalline or powder samples, we can integrate over all incoming and outgoing polarizations to obtain:

$$\begin{aligned}
I(\nu_{in},\nu_{out}) &= \left(\frac{4\pi}{3}\right)^4 \frac{\delta\left(E_f+h\nu_{out}-E_i-h\nu_{in}\right)}{\left|E_m-E_i-h\nu_{in}-i\frac{\Gamma}{2}\right|^2}\sum_{\ell_{VB}m_{VB}}\left[\int r^2 dr f_{\ell_{VB}m_{VB}}(r,E_{VB})ru_{\ell_c}(r,E_c)\right] \\
&\times \sum_{\ell'_{VB}m'_{VB}}\left[\int r^2 dr f_{\ell'_{VB}m'_{VB}}(r,E_{VB})ru_{\ell_c}(r,E_c)\right]\sum_{m_c q_i} \\
&\times\Omega\left(\ell_c m_c,1q_i,\ell_{VB}m_{VB}\right)\Omega\left(\ell_c m_c,1q_i,\ell'_{VB}m'_{VB}\right) \\
&\times \sum_{\ell_{CB}m_{CB}}\left[\int r^2 dr f_{\ell_{CB}m_{CB}}(r,E_{CB})ru_{\ell'_c}(r,E_{c'})\right] \\
&\times \sum_{\ell'_{CB}m'_{CB}}\left[\int r^2 dr f_{\ell'_{CB}m'_{CB}}(r,E_{CB})ru_{\ell'_c}(r,E_{c'})\right] \\
&\times \sum_{m'_c q_f}\Omega\left(\ell'_c m'_c,1q_f,\ell_{CB}m_{CB}\right)\Omega\left(\ell'_c m'_c,1q_f,\ell'_{CB}m'_{CB}\right) \\
&= \left(\frac{4\pi}{3}\right)^4 \frac{\delta\left(E_f+h\nu_{out}-E_i-h\nu_{in}\right)}{\left|E_m-E_i-h\nu_{in}-i\frac{\Gamma}{2}\right|^2} \\
&\times \sum_{\ell_{VB}m_{VB}}\left[\int r^2 dr f_{\ell_{VB}m_{VB}}(r,E_{VB})ru_{\ell_c}(r,E_c)\right]^2 W(\ell_c,1,\ell_{VB}) \\
&\times \sum_{\ell_{CB}m_{CB}}\left[\int r^2 dr f_{\ell_{CB}m_{CB}}(r,E_{CB})ru_{\ell'_c}(r,E_{c'})\right]^2 W(\ell'_c,1,\ell_{CB}) \quad (4.22)
\end{aligned}$$

In other words, a non-polarized RXES spectrum from a band structure material is just the product of the non-polarized XES and XAS spectra, subject to both energy conservation and

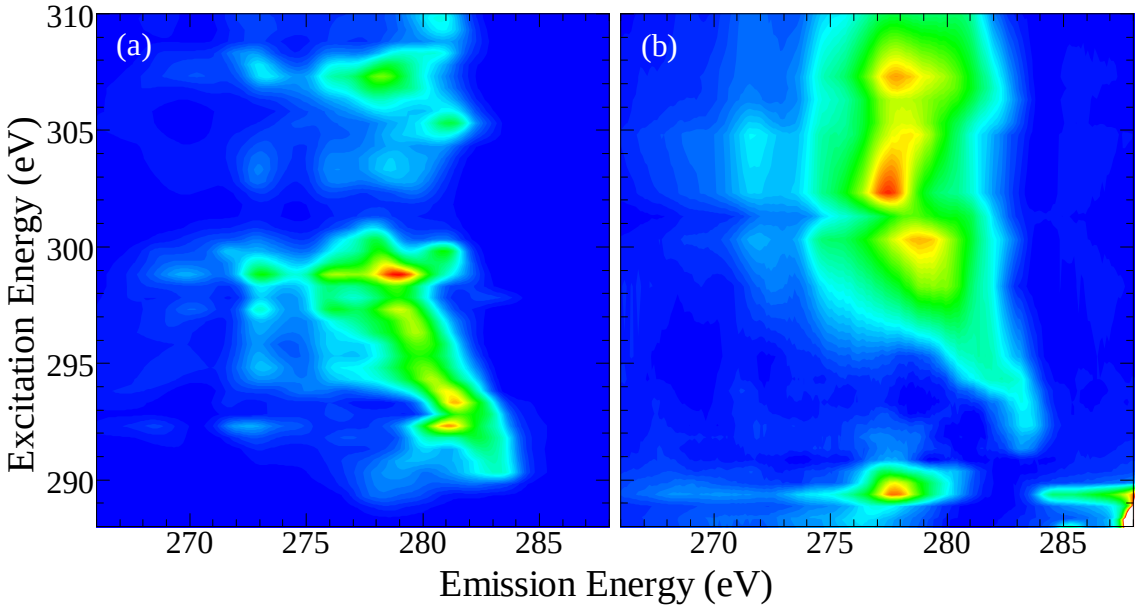

Figure 4.4: A photon-in, photon-out map of the C K edge of diamond: (a) calculated, (b) measured (using a nanodiamond sample, on the REIXS beamline at CLS). Each horizontal line corresponds to an emission spectrum at a given energy. The non-resonant portion of the spectrum has been subtracted, as described in Reference [34].

that the valence and conduction band states have the same crystal momentum. Note also that in most practical cases the core level in the final state will be the same as the core level in the initial state (i.e. $E_c = E_{c'}$, $\ell_c = \ell_{c'}$).

As an example, a "RXES map", or 2D image consisting of a RXES spectrum for every point in a XAS spectrum, is shown in Figure 4.4 for nanodiamond. It is clear that near the conduction band onset (in the energy range from around 290 eV to 300 eV) the calculated and measured spectral shapes are in reasonably good agreement. There is also some elastic scatter in the bottom right corner of the measured map (Figure 4.4(b)) that the calculation did not attempt to reproduce (no elastic scatter was calculated), and there is also a strong emission feature near 277 eV when excited at 290 eV that is not part of the ground state band structure (it is a resonance feature and is related to the core hole perturbation). Above 290 eV the agreement between the calculated and measured spectra is less accurate, it is possible that the momentum selectivity of the measured spectra is too weak to manifest in dramatic changes in the emission line shape.

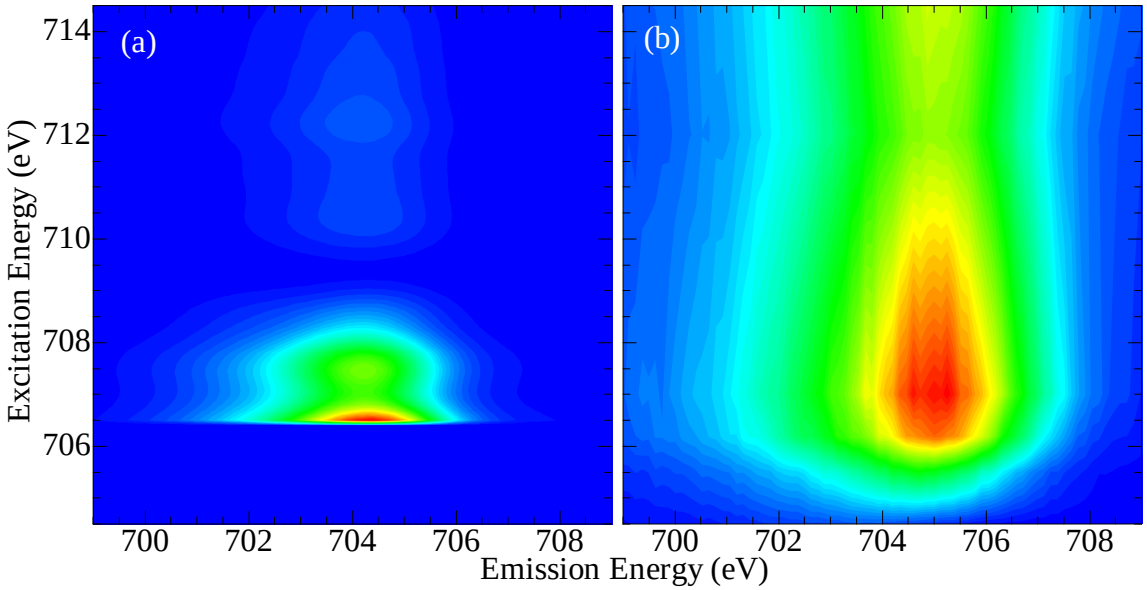

Figure 4.5: A photon-in, photon-out map of the Fe L_3 edge of LiFeAs: (a) calculated, (b) measured. Each horizontal line corresponds to an emission spectrum at a given energy.

Unfortunately this type of spectroscopic mapping to determine band structure is useful only in broad band materials that contain only a few bands with relatively large curvatures. Diamond, graphite, and silicon carbide, among a few others, have been successfully studied with this approach (see Reference [34] for a review). However in many other broad band materials, the band structure is too "flat" to provide much contrast between RXES spectra excited at different energies.

The iron pnictides are an excellent example of this; while it could be argued that a Fe L_3 RXES is not a good probe of band structure (due to the possible influence from LS-coupling multiplets and on-site correlation effects), it is certainly clear that the calculated Fe L_3 RXES map of the iron pnictide LiFeAs (see Figure 4.5(a)) provides no readily apparent band structure information, and looks similar to the measured RXES map (see Figure 4.5(b)). This is because the bands in LiFeAs are relatively flat: for a given excitation energy, certain conduction bands are populated with electrons. Because the bands are relatively flat, an electron in each conduction band can access almost the entire valence band by a momentum-conserving transition, so the RXES spectra are essentially the same as the non-resonant XES

(which probes the entire valence band because it is not restricted by momentum conservation). The electronic structure of LiFeAs is analysed in greater detail in Section 7.4.

Chapter 5

Electronic Structure of Binary Oxides

While chemically simple, binary oxides are interesting materials in their own right; even the very simple alkaline oxides (BeO, MgO, CaO, SrO, BaO) are useful materials in catalysis [67–69], while transition metal oxides may be used as photocatalysts (such as TiO_2) [70–72], exhibit metal-insulator transitions (like V_2O_3, Fe_3O_4, etc.) [73], or are strongly correlated systems (FeO, NiO, etc.) [49,62,74–76]. Finally the post-transition metal oxides (ZnO, CdO, HgO) and several non-metal oxides (such Ga_2O_3, In_2O_3, SnO, SnO_2, etc.) are semiconductors used in optoelectronics [77–88].

Secondly, binary oxides are a useful class of test materials for comparing measured X-ray spectra and calculated electronic structure, because these materials are cheap, stable, and often have simple crystal structures. Further, the oxygen-cation bonding in these materials can range from ionic to covalent, so a variety of hybridization strengths can be expected.

This chapter details my research into probing the electronic structure of binary oxides with X-ray spectroscopy. Three groups of oxides are studied here; the alkaline oxides (BeO, MgO, CaO, SrO, and BaO), the post-transition metal oxides (ZnO, CdO, HgO), and several period 5 oxides (In_2O_3, SnO, SnO_2, Sb_2O_3, Sb_2O_5, TeO_2). These findings are also reported in my published work on the subject, see References [15–17].

5.1 Alkaline Oxides

The alkaline oxides are extremely simple materials; in all cases they have only 8 valence electrons per formula unit and are very ionic. Since these systems have no d- or f-states, DFT should be able to accurately calculate the electronic structure of these systems. The crystal structures of BeO, MgO, CaO, SrO, and BaO are listed in Table 5.1. Apart from BeO,

Table 5.1: Crystal structures for the alkaline oxides. BeO is the only compound with a non-cubic structure; so for this compound the a and c lattice constants are listed here as well as the z coordinate for the atomic sites.

	Space Group	Lattice Constant (Å)	Atomic Sites Cation, O	Bond Length (Å)	Reference
BeO	$P6_3mc$	2.698, 4.380	(2b) (2b) $z = 0, 0.378$	1.65	[89]
MgO	$Fm\bar{3}m$	4.211	(4a), (4b)	2.10	[90]
CaO	$Fm\bar{3}m$	4.815	(4a), (4b)	2.41	[91]
SrO	$Fm\bar{3}m$	5.160	(4a), (4b)	2.58	[92]
BaO	$Fm\bar{3}m$	5.523	(4a), (4b)	2.76	[92]

all of the other materials have the same cubic space group; structurally the only difference between the non-BeO alkaline oxides is the species of cation and the lattice constant of the unit cell.

These materials make an ideal series to study with oxygen K-edge XES and XAS: oxygen K-edge XES and XAS will probe the local occupied or unoccupied $2p$-states, respectively, which represent the primary bonding states for oxygen. Secondly, since these samples are studied from the same X-ray edge, the energy scale and experimental resolution is consistent. Finally, since MgO, CaO, SrO, and BaO have the same crystal structure, any differences in the spectra (or electronic structure) must be due to the different cations and bond lengths, rather than related to the point group symmetry of the oxygen site.

These oxides were obtained from a commercial vendor in powder form (Alfa Aesar, 99% purity or higher). The O K-edge XES and XAS spectra for the alkaline oxides is shown in Figure 5.1. The O K XES spectrum for these compounds consists mainly of a single Gaussian-shaped feature that is around 526 eV above the binding energy of the oxygen $1s$ core level and has a relatively consistent width. Since these systems are highly ionic, one might expect this feature to be representative of a full $2p^6$ shell that is highly localized to the oxygen site. There is, however, obviously some hybridization evident in the O K XES spectrum of BeO, MgO, CaO, and BaO. In the two former compounds this is due to

hybridization with the cation states (at an energy of about 523 eV for both), while in the latter two this is due to hybridization with carbon *sp*-states and is indicative of a surface carbonate layer (noted by the arrows on the O K-edge XES spectrum of CaO and BaO in Figure 5.1, indicative of $CaCO_3$ and $BaCO_3$, respectively) [15].

In contrast to the O K XES, the O K XAS shown in Figure 5.1 for these samples are all quite distinct from each other. This is again expected since the systems are highly ionic; any unoccupied O $2p$-states occur almost entirely from hybridizations with unoccupied cation states. Since each system has a different cation, it is not unexpected that these hybridizations with the cation unoccupied s-, p-, and d-states should occur at different energies and have different spectral intensities.

Finally, since the O K XES and XAS provide *independent* probes of the occupied and unoccupied states, the energy separation between the two should be related to the band gap of the material. Of course an X-ray transition can, in principle, represent a rather drastic perturbation from the ground state. As mentioned in Chapter 4, for X-ray transitions that can be expressed in terms of the Fermi golden rule, the final state of the transition dominates [64]. In an XES spectrum the final state is a filled core level with a hole in the valence band, while in an XAS spectrum the final state is a hole in a deep core level and an electron in the conduction band. It is pretty clear that the latter state is much further from the ground state than the former, and therefore we expect an XES spectrum (in the absence of strong many-body effects) to be a much closer representation of the ground state valence band than an XAS spectrum is of the ground state conduction band. However, despite these caveats, a cursory analysis of the XAS is still possible. In particular, a core hole represents an increase in the local potential (i.e. the nuclear charge is less screened than in the ground state), and due to this greater attractive potential one can expect the onset of an XAS spectrum would be lower in energy than the onset of the true ground state conduction band, but not higher [63], and therefore the separation between the XES and XAS spectra from the same edge should provide a lower limit on the band gap in the material. From the spectra in Figure 5.1 we can anticipate that the band gap of BeO is by far the largest of these materials, the band gap of MgO is perhaps the next largest and the remaining three compounds have rather similar band gaps.

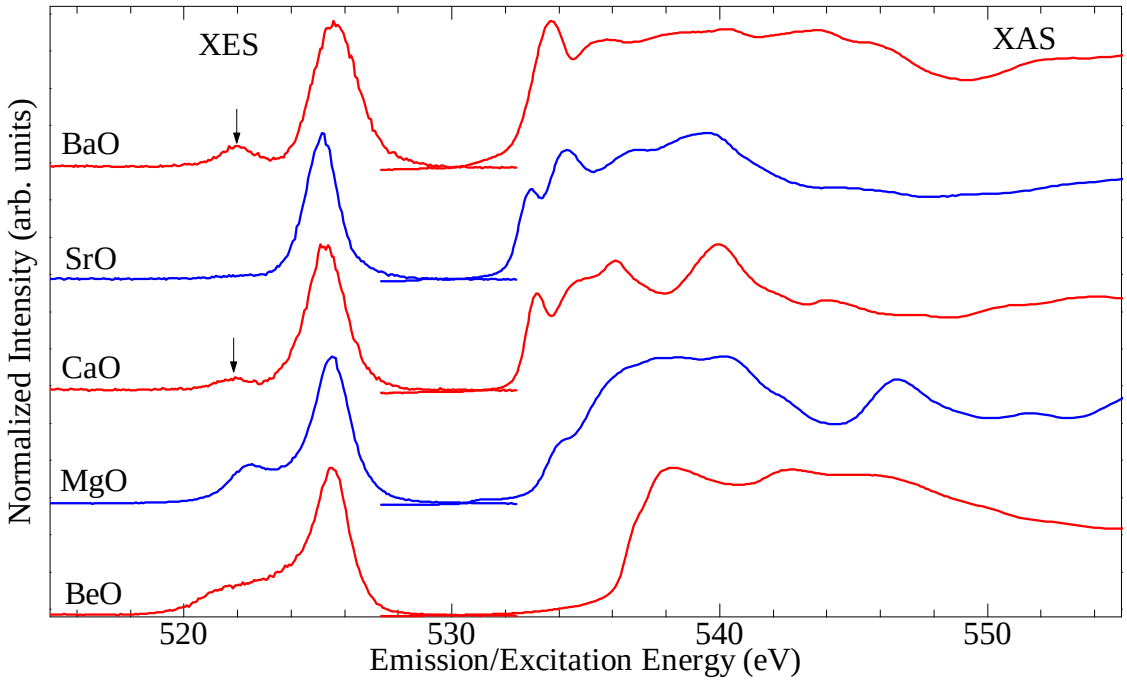

Figure 5.1: The measured O K XES and XAS (TFY mode) spectra for the alkaline oxides. The XES spectra were excited near 540 eV. The arrow points to the spectral signature of a carbonate species ($BaCO_3$ in the XES spectrum of BaO and $CaCO_3$ in the XES spectrum of CaO) indicating some surface contamination. This figure is adapted from data published in Reference [15].

The calculated DOS of these alkaline oxides is shown in Figure 5.2. These DOSes were all calculated using the Perdew, Burke, and Ernzerhof's generalized gradient approximation (PBE) exchange-correlation functional [44]. It is reasonably clear that the O K XES is an accurate probe of the ground state O $2p$ occupied DOS; the O $2p$ valence band of BeO is considerably wider than in the other compounds, with a distinct broad low energy shoulder, qualitatively the same trends are apparent in the BeO O K XES spectrum. The O $2p$ valence band in MgO is the second broadest, this band also has a distinct secondary peak at lower energies, again in qualitative agreement with the trends in the measured O K XES spectra. Finally, the remaining three compounds all have rather sharp and narrow valence bands (less than 3 eV wide).

The onset of the conduction bands in BaO, SrO, and CaO, shown in Figure 5.2, are dominated by the unoccupied $5d$-, $4d$-, and $3d$-states, respectively. In MgO and BeO, on the other hand, there is a rather weak weighting of d-like states (as one might expect), in fact it is O $2p$-states that dominate the onset of the conduction band. The cation $2s$, $2p$- and $3s$,$3p$-states do not become dominant until some 10 eV above the edge in BeO and MgO, respectively. This is again in qualitative agreement with the O K XAS spectra shown in Figure 5.1, suggesting that even with the perturbative influence of a core hole some ground state properties may be deduced from a XAS spectrum.

In an effort to provide a quantitative estimate of the band gap from a XES and XAS spectrum, our group often uses peaks in the second derivative of each spectrum [62]. This method is without any real theoretical justification, but it does provide a consistent and repeatable empirical method of estimating the onsets of the valence and conduction bands (although, of course, the latter may be perturbed by the core hole). The band gap is arguably the most important single parameter in the electronic structure of a material, and any bulk sensitive technique of estimating the band gap is valuable [16]. In fact, the exact band gap is controversial for many materials because it can depend greatly on the probing depth of the measurement [93]. An example of applying this method to the O K XES and XAS spectra of MgO and CaO is shown in Figure 5.3. For a thorough treatment of all materials in this series please refer to Reference [16]. The second derivative method can also provide a consistent and repeatable estimate of the width of the valence band, as shown in Figure 5.3. This is

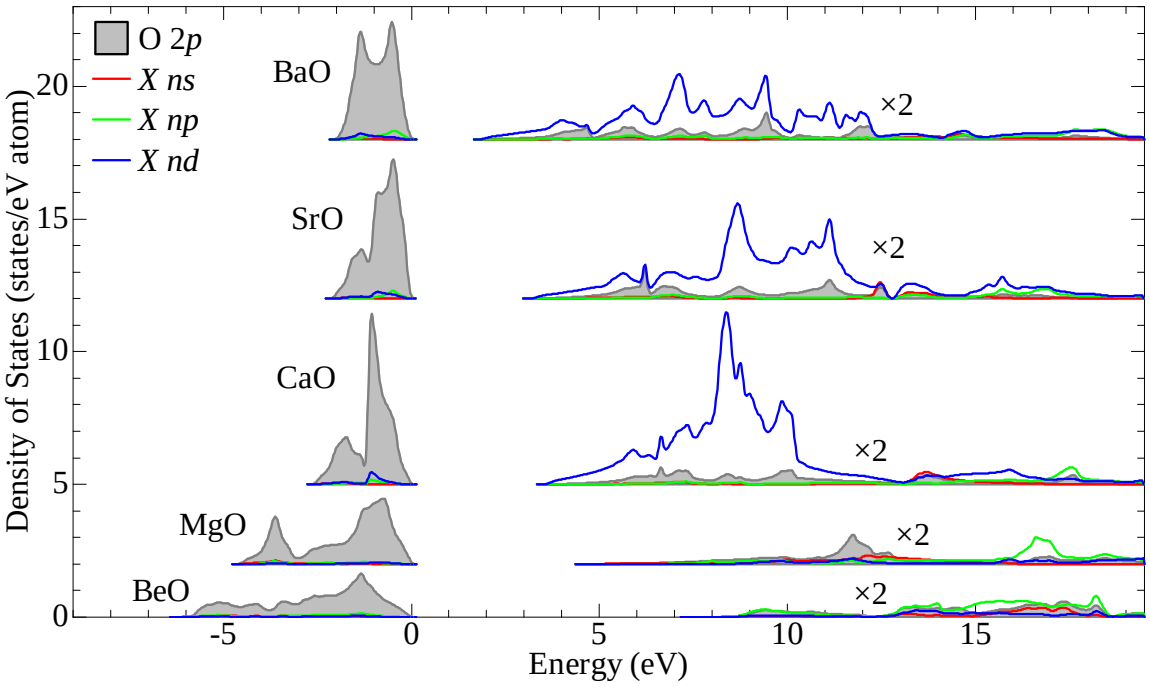

Figure 5.2: The calculated partial DOS for the alkaline oxides. The top of the valence band is at 0 eV. In the legend, X refers to the cation (Ba, Sr, Ca, Mg, or Be, as appropriate). Note that the all of the unoccupied partial DOSes have been scaled by a factor of 2. This figure is adapted from data published in Reference [15].

another value that can be directly compared to the results from a theoretical calculation, and since DFT calculations typically underestimate the band gap by a significant amount [45], any disagreement between measured and calculated band widths may be a more accurate indication of a problem with the calculation (or perhaps a contaminated measurement) than a disagreement between band gaps. Although not relevant for these compounds, the valence band width is also important in judging the correlation strength in materials with a large on-site Hubbard potential [49, 74].

As shown in Figure 5.3, the O K XES spectrum is in reasonable agreement with the (broadened) O $2p$ occupied DOS of MgO and CaO, and the second derivative of the O K XES gives a reasonably accurate estimate (error of ± 0.5 eV or less) of the valence band width. The O K XAS spectrum, on the other hand, is in only qualitative agreement with the calculated unoccupied O $2p$-states. It is reasonably clear that the calculated band gap is too small, as expected. However because of the core hole in the final state of the measured XAS spectrum, we should not expect the ground state conduction band to be the same as the measured XAS spectrum.

The XES and XAS spectra can be calculated from the DOS, using the procedure for calculating the transition matrix elements outlined in Chapter 4. The calculated O K XES and XAS spectra for the alkaline oxides is shown in Figure 5.4. The XAS spectra shown here were calculated using the "ground state" of a system with an explicit core hole in a single O $1s$ level and a background charge of +1 e in a $2 \times 2 \times 2$ supercell (see Reference [15] for details). This method is also called the "full core hole" approach, but I will use the label "core hole" (or CH for short) in this thesis. The XES spectra are accurately described by the ground state of the system, sometimes this is described as "no core hole" but I will use the terminology "ground state" (or GS for short) in this thesis.

The top of the valence band was aligned with the highest energy peak in the second derivative of the measured O K XES (as shown in Figure 5.3). The alignment between the calculated and measured O K XES shows nicely the caveats of the second derivative method; since BaO, SrO, and CaO have very narrow valence bands, and very sharp onsets at the top and bottom of the valence band (especially BaO), as shown in Figure 5.2, the peak in the second derivative is in the low or high energy tails of the lifetime- and instrumentally-

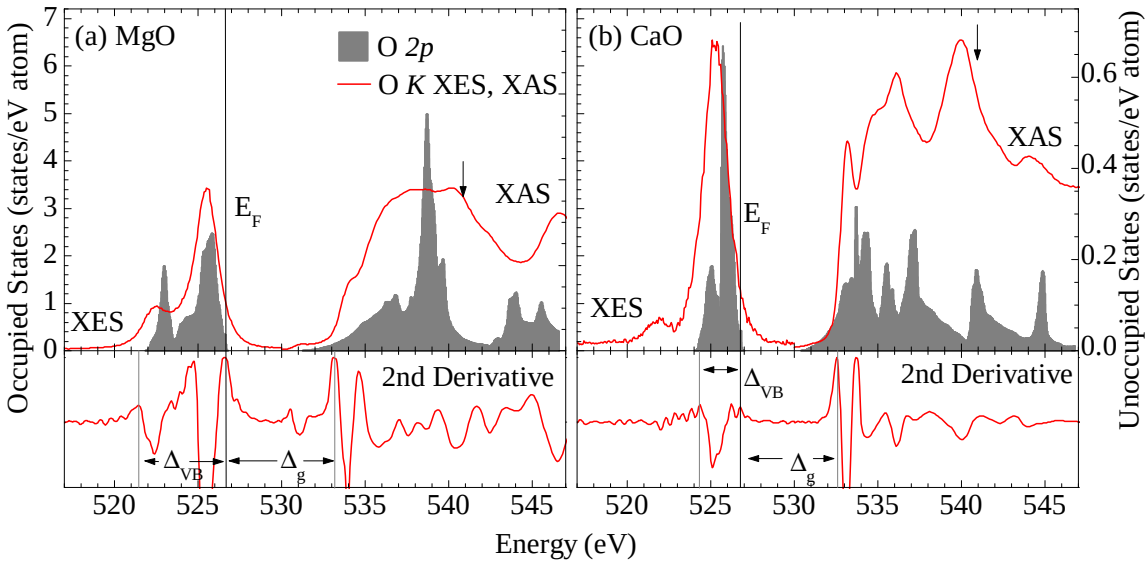

Figure 5.3: The calculated O $2p$ DOS and measured O K XES and XAS (TFY mode) spectra for (a) MgO and (b) CaO. The second derivatives of these spectra are shown in the bottom panels, the peaks are used to estimate the widths of the valence bands (Δ_{VB}) and the band gaps (Δ_{g}) as shown. The excitation energy for the XES spectrum is indicated by the arrow on the XAS spectrum. The calculated DOS have been aligned with the measured spectra using the high energy peak in the second derivative of the XES spectrum as an indication of the top of the valence band. Note the occupied and unoccupied DOS have different vertical scales, but these scales are consistent for (a) and (b). This figure is a modification of one published in Reference [15].

broadened spectrum. In contrast, since BeO has a relatively broad valence band, and the bottom and top of the valence band have much more gradual onsets than in the other compounds, it seems that the peaks in the second derivative of the O K XES are at points that are within the valence band. Only in situations where the intensity in the onset of the valence band is "just right" does this method accurately line up the peaks of the calculated and measured spectra, as is the case for MgO.

This alignment also makes it clear that the band gaps in the calculated DOS are too small in all cases (except perhaps MgO), as can be seen by comparing the calculated and measured XAS spectra in Figure 5.4. The calculated XAS spectra shapes are only in qualitative agreement with the measured XAS spectra, if the calculated XAS spectra is shifted appropriately, features in the calculated XAS spectra can be tentatively identified in the measured XAS spectra but the relative intensities are often poorly reproduced. The general influence of the core hole provides more important information; however, in comparison to the ground state unoccupied O $2p$-states, the calculated XAS show that in addition to shifting to lower energies the core hole also greatly increases the intensity of features near the onset of the conduction band [16,63,64]. The poor agreement between the calculated and measured XAS can be attributed partly to the size of the supercell (a larger supercell, such as a $3 \times 3 \times 3$ cell is better), and more importantly to the failings of calculating the effect of a core hole perturbation using time *independent* DFT. In all of the core-hole perturbed calculations discussed herein, the electronic structure is fully relaxed; essentially the core hole lifetime is taken as being infinite. This is likely why the core hole perturbed calculated XAS spectrum is in such poor agreement with the measured XAS spectrum for BeO — since Be is so light compared to O, a fully relaxed O $1s$ core hole introduces a much more significant perturbation to the ground state band structure than in a system with a heavier cation.

5.2 Post-Transition Metal Oxides

The post-transition metal oxides (ZnO, CdO, and HgO) have the same formal valencies as the alkaline oxides; however unlike the alkaline cations the post-transition metals have a nominally full d^{10} shell that is very close to the valence level. It is of interest to determine

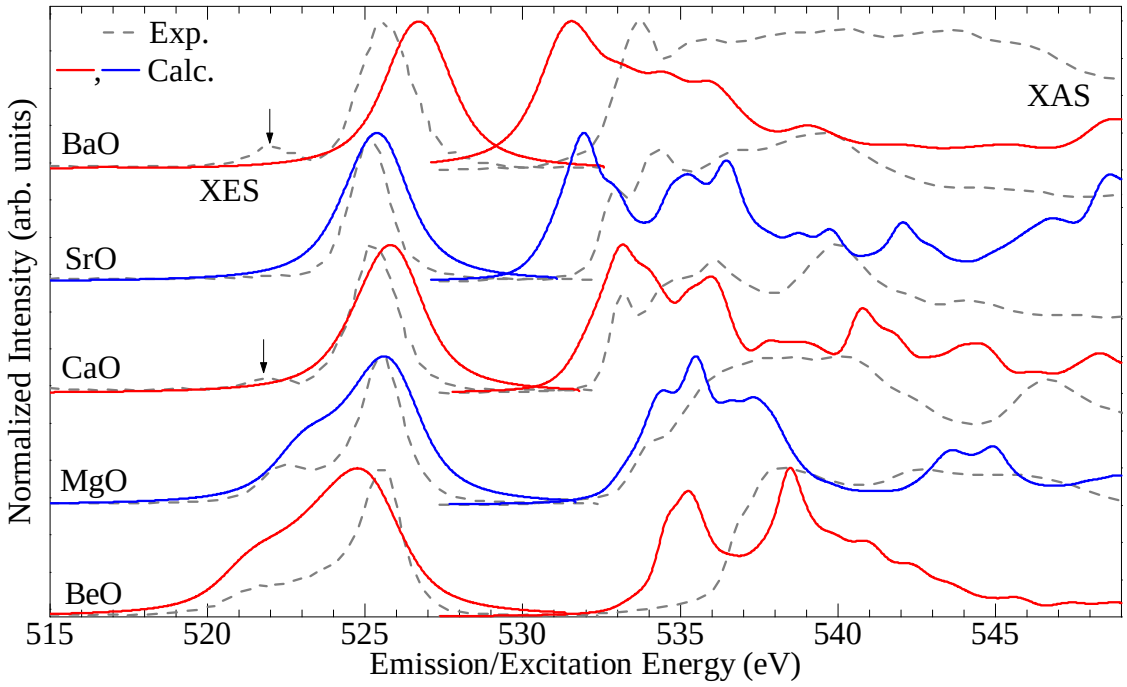

Figure 5.4: The calculated O K XES and XAS spectra for the alkaline oxides, compared with the measured spectra from Figure 5.1. The arrow points to the spectral signature of a carbonate species in the measured O K spectrum; no attempt was made to calculate the spectrum of the contamination phase. This figure is adapted from data published in Reference [15].

Table 5.2: Crystal structures for the post-transition metal oxides. The z coordinates of the Zn and O sites are given for ZnO, as are the x and z coordinates for the Hg and O sites in HgO, respectively.

	Space Group	Lattice Constant (Å)	Atomic Sites Cation, O	Bond Length (Å)	Reference
ZnO	$P6_3mc$	3.2494, 5.2038	(2b) (2b), $z = 0, 0.3821$	1.98	[94]
CdO	$Fm\bar{3}m$	4.70	(4a) (4b)	2.35	[95]
HgO	$Pnma$	6.6129, 5.5208, 3.5219	(4c) (4c),	1.89	[96]
			$z = 0.2456, 0.5955,$	2.05	
			$x = 0.1136, 0.3592$		

how chemically active this shell is, and whether it plays a key role in the optoelectronic properties of these materials. Fortunately the most common phase of ZnO, wurtzite [94], is isostructural to BeO [89], and CdO has the same rocksalt structure as the other alkaline oxides [95]. This again helps with the analysis of the O K-edge X-ray spectra, because any differences between spectra from isostructural systems can be attributed directly to the different chemical properties of the cations rather than to the point group symmetry of the oxygen site. The structures of ZnO, CdO, and HgO are summarized in Table 5.2.

These oxides were obtained from a commercial vendor in powder form (Alfa Aesar, 99% purity or higher). The O K XES spectra of the post-transition metal oxides has a great deal more structure than those from the alkaline oxides, as shown in Figure 5.1. Like the alkaline oxides, all of these XES spectra have a rather sharp peak at 526 eV, this seems to be a general characteristic of bonding $2p$-states in oxides. All of these XES spectra also have a low energy shoulder around 524 eV. The O K XES spectrum from both BeO and MgO had a low energy shoulder as well, since it appears in cubic (MgO, CdO), hexagonal (BeO, ZnO), and orthorhombic (HgO) structures, and does not appear in other cubic (CaO, SrO, BaO) structures, this feature is probably due to the specific species of cation, rather than driven by the particular point group symmetry of any one structure. Finally, all of the post transition metal compounds have a secondary low energy peak between 520 and 522 eV in the O K

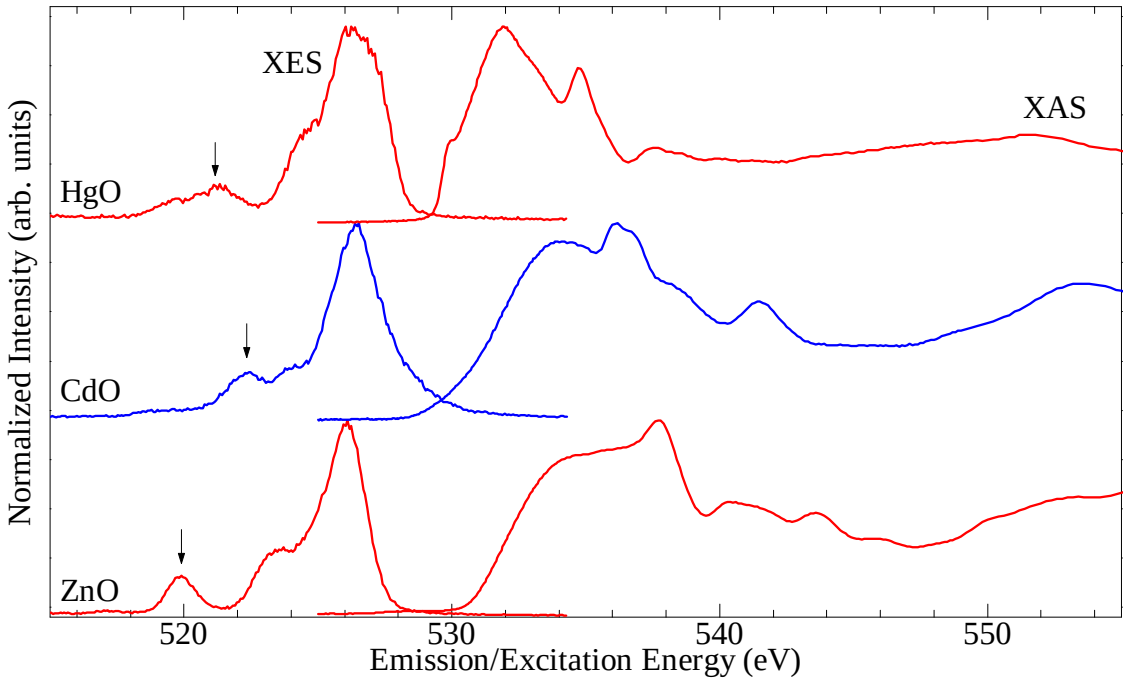

Figure 5.5: The measured O K XES and XAS (TFY mode) spectra for the post-transition metal oxides. The XES spectra were excited near 540 eV. Note the low energy features, indicated by the arrows, due to hybridization between the O $2p$ and cation full-shell nd^{10} states. This figure is adapted from data published in Reference [15].

XES spectrum. This peak is not related to a carbonate phase or any other contaminant, rather it is due to hybridization between the O $2p$-states and the cation d^{10} shell [15].

Secondly, the O K XAS spectra of the post-transition metal oxides are all rather smooth and lack sharp features, especially close to the edge; qualitatively these spectra are closer to those from BeO and MgO than the other alkaline oxides (refer back to Figure 5.1). This is also expected because the sharp near-edge features in CaO, SrO, and BaO are due to hybridization between the unoccupied O *2p*-states and the unoccupied cation nd-states. In terms of simple atomic orbitals, the cations in neither BeO (with an atomic valence state of $1s^2$) nor MgO (with an atomic valence state of $2s^2$) are expected to have vacant d-like states right at the edge of the conduction band, so we expect the major hybridizations present in the O K XAS to be between unoccupied the cation ns- and possibly np-states. Likewise, ZnO, CdO, and HgO all have a full nd^{10} shell so we expect the next unoccupied d-like states to be reasonable high in energy — and not appear near the edge of an XAS spectrum.

This description of the X-ray spectra is supported by the calculated DOS, shown in Figure 5.6. These DOS were all calculated with a "hybrid functional" consisting of the local spin density approximation (LSDA) exchange functional mixed with 35% of the exact Fock potential [50] (hereafter, this is labelled as "LSDA+αHF"). This is necessary because a simple GGA or LSDA functional does not localize the full-shell nd^{10} states sufficiently [16]. It is clear from Figure 5.6 that the O K XES should show three features; a main peak a close to the top of the valence band, a secondary shoulder due to hybridization between O $2p$- and cation s-,p-, and d-states (at -4 eV in these systems), and a secondary peak due to O $2p$-states weakly hybridizing with a the localized cation nd^{10} shell (below -5 eV in these systems). Secondly, as anticipated by the O K XAS, the conduction band has very weak cation d-character; the near edge is predominantly unoccupied O $2p$- and cation ns-states, and cation np-states start to become prevalent several eV above the edge of the conduction band.

As discussed, X-ray spectra can be predicted from the electronic structure. The calculated O K XES and XAS spectra for ZnO, CdO, and HgO are shown in Figure 5.7. As was the case for the binary oxides, the XAS spectrum was calculated with an explicit $1s$ core hole at a single O atom in a $2 \times 2 \times 2$ supercell. As expected, the calculated O K XES spectra show

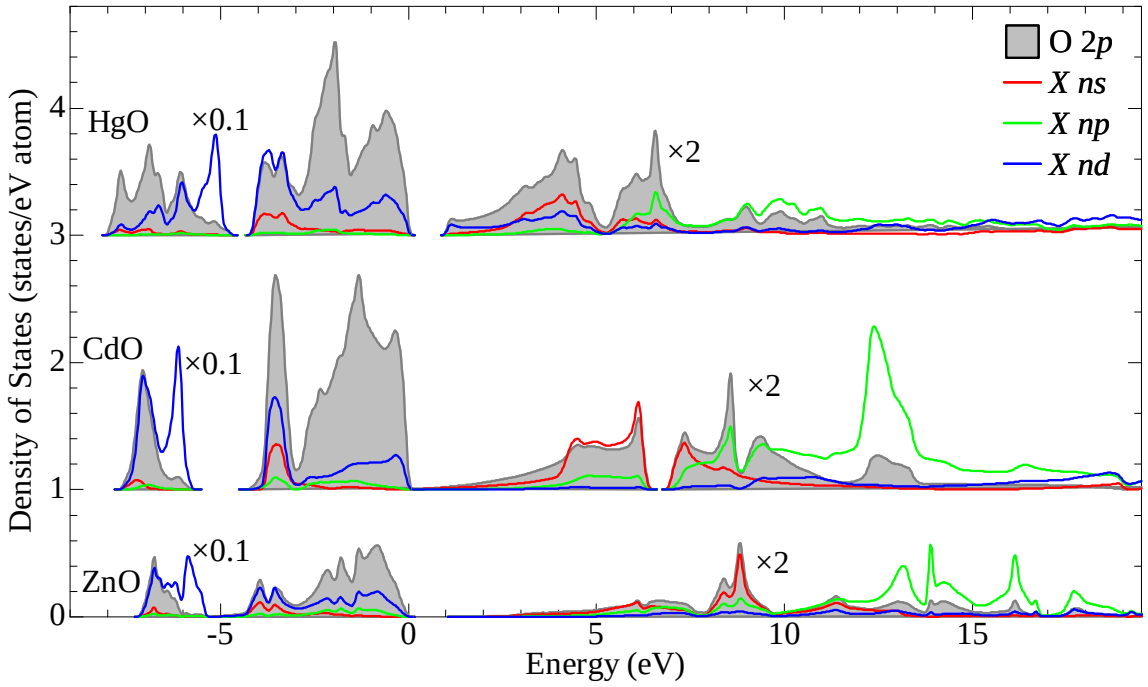

Figure 5.6: The calculated partial DOS for the post-transition metal oxides. The top of the valence band is at 0 eV. The cation full-shell nd^{10} states (i.e. those below -5 eV) have been reduced in intensity by a factor of 10, and the all the unoccupied partial DOSes have been scaled by a factor of 2. This figure is adapted from data published in Reference [15].

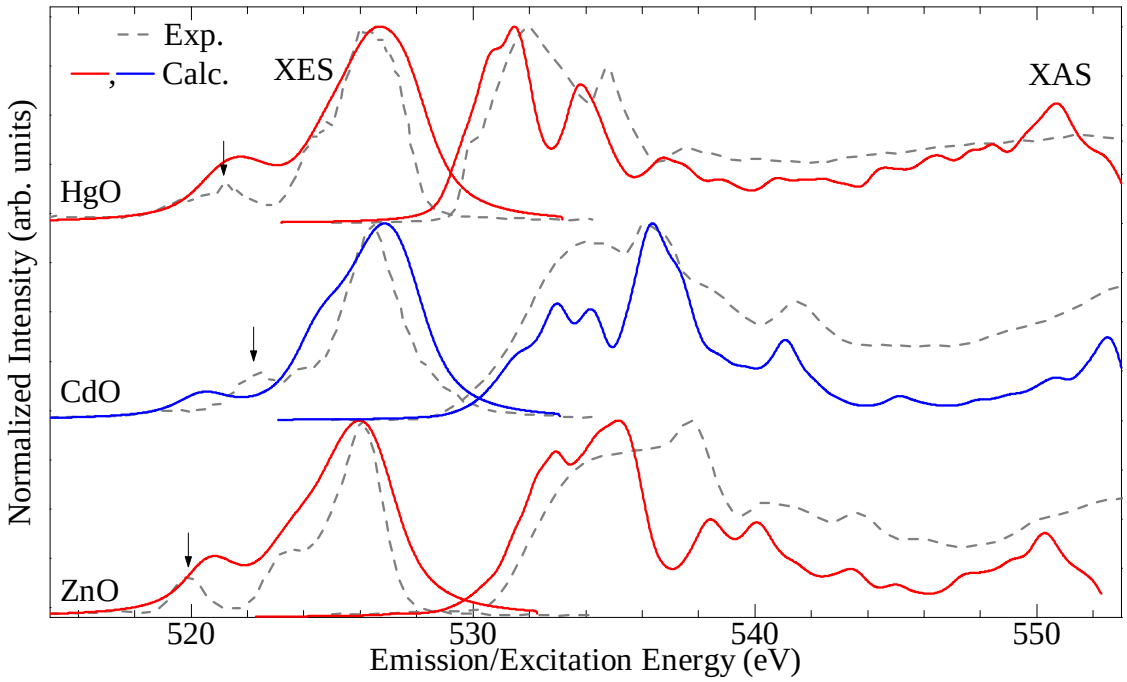

Figure 5.7: The calculated O K XES and XAS spectra for the post-transition metal oxides, compared with the measured spectra from Figure 5.5. This figure is adapted from data published in Reference [15].

the same three features identified in the measured spectra, however the energy alignment of these is not entirely consistent with the measured spectra (see Figure 5.7). This discrepancy is likely due to the simple choice of the Fock mixing in the hybrid functional; I chose a mixing of 35% simply because this was previously shown to be a "good" generic value [50]. In fact because a partial weight of the exact on-site Fock exchange correlation energy was used these calculations are no longer *ab initio* and better agreement could be reached by tuning the mixing factor.

Interestingly, the calculated XAS spectra of these post-transition metal oxides are closer to the experimental spectra than was the case in the alkaline oxides (refer back to Figure 5.4). I believe the reason is two-fold: as previously mentioned the near edge of the conduction band is dominated by O $2p$ — cation ns hybridization; this near edge region is also the area most significantly influenced by the core hole perturbation. Because s- and p-like states are more accurately treated with DFT than d- and f-like states, one can expect that the influence of the local core hole perturbation will be more accurately treated as well. This is also the case for BeO and MgO, but the cations in ZnO, CdO, and HgO are all much more massive relative to O than the cations in BeO and MgO: Since I expect the influence of the O $1s$ core hole on cation states to be inversely related to the size of the cation potential, this means that the core hole should have a weaker perturbative effect on ZnO, CdO, and HgO compared to BeO and MgO, and consequently the approximations inherent in the calculated core hole perturbed XAS spectrum to be less significant [15].

To readdress a point brought up above, I have attempted to match the experimental XES spectra of ZnO with the electronic structure of ZnO calculated using several different functionals, as shown in Figure 5.8. This approach is hardly *ab initio*, indeed since adding an on-site Hubbard potential U for the Zn $3d$ will simply reduce the average energy of these states by $U/2$ from that in a regular GGA calculation [49], I specifically chose a value of $U = 8$ eV because the bulk of the Zn $3d$-states in the GGA calculation were 4 eV too high [16]. The weakly correlated calculation the using the PBE potential clearly fails to localize the Zn $3d$-states sufficiently (see Figure 5.8(b)); this localization, at 8 eV or so below the edge of the valence band, is clearly apparent in the O K and Zn L_3 XES shown in Figure 5.8(a). One important aspect of this study is that the "modified Becke Johnson" functional

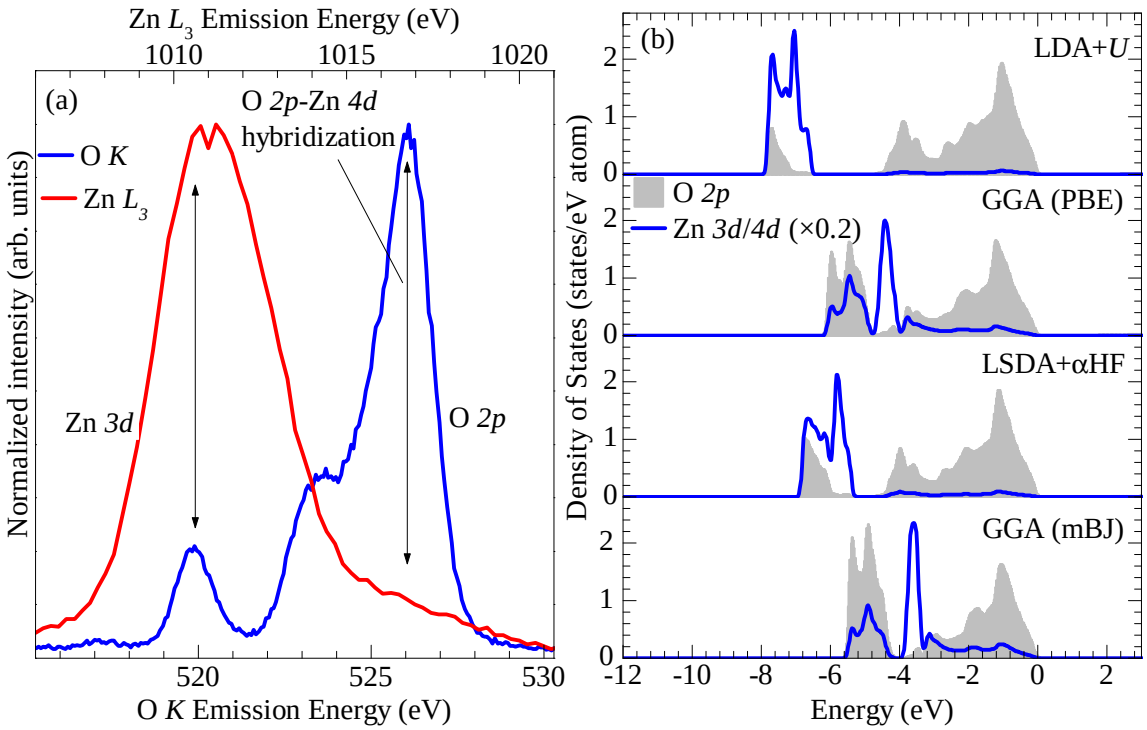

Figure 5.8: A detailed look at the behaviour of the Zn $3d^{10}$ in ZnO. (a) Reconstructing the valence band of ZnO from O K and Zn L_3 XES. The vertical arrows indicate the regions of hybridization; the low energy feature in the O K XES was used to align the Zn L_3 XES. (b) The partial DOS for ZnO calculated using a variety of functionals. Note how a hybrid HF or $+U$ method is necessary to get the correct localization of these states. This figure is a modification of one published in Reference [16].

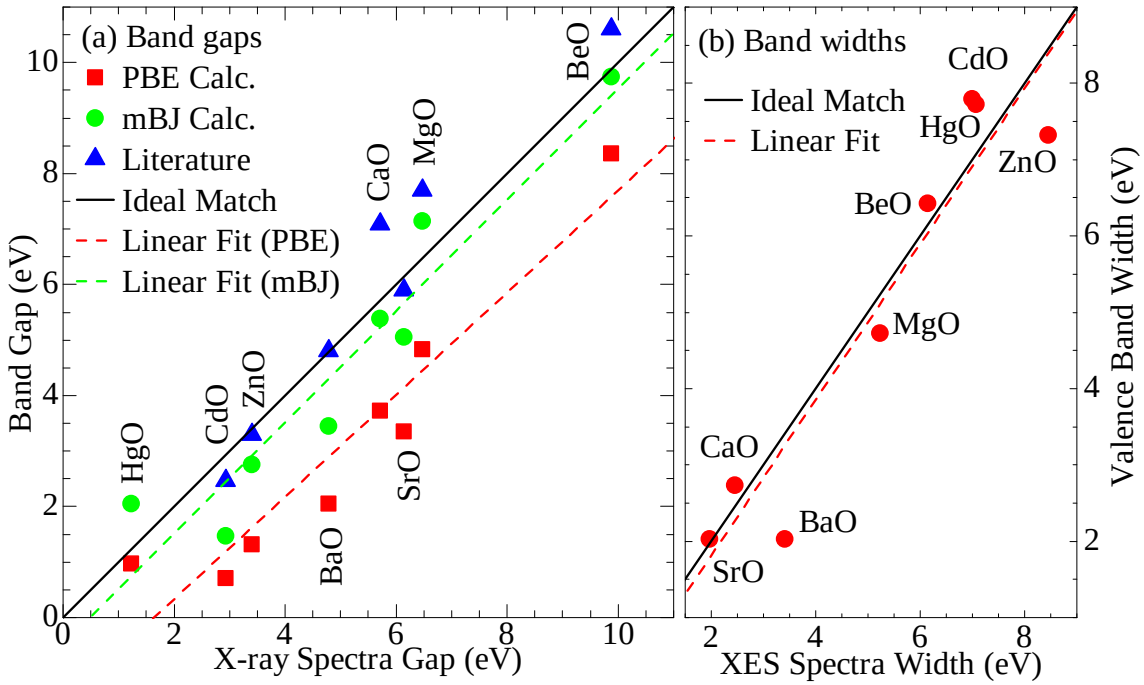

Figure 5.9: The band gaps and band widths of the alkaline and post-transition metal oxides. (a) The band gaps calculated with both PBE and mBJ functionals as well as the band gap measurements found in the literature (all optical gaps except for HgO which was determined from XPS + XAS) [78,97–103], as a function of the gap estimated from the peaks in the second derivatives of the O K XES and XAS (refer back to Figure 5.3 for an example). The diagonal line indicates perfect agreement. The dotted lines represent linear fits of the PBE and mBJ band gaps to the estimated gaps. (b) The valence band widths calculated with PBE as a function of the band widths estimated from the peaks in the second derivative of the O K XES (refer back to Figure 5.3 for an example). This figure is adapted from data published in References [15, 16].

(mBJ), a recently developed GGA exchange-correlation functional which greatly improves the calculated band gaps [47], still fails to properly localize the Zn $3d^{10}$ states, in contrast to initial claims that the mBJ functional would also accurately reproduce the DOS in these types of systems [50].

Despite the caveats mentioned above, the practice of using the peaks in the second derivative of the XES and XAS spectra is a reasonable empirical approach in general, especially if no theoretical electronic structures are available. Figure 5.9(a) plots the band gaps calculated with the PBE and mBJ exchange correlation functionals and the band gaps obtained from optical experiments available in the literature, all with respect to the band gaps estimated

from the second derivatives of the XES and XAS. Although the band gap of any single material may not be accurately described by the second derivatives of the XES and XAS, the linear fits of the calculated band gaps with respect to gaps estimated from the second derivatives have a slope very close to unity; so the band gaps estimated from the second derivative method are rather close to the calculated gaps for these materials within an energy shift that is constant for all materials in this series. For the PBE and mBJ calculated gaps the best fit lines are (where G_{sxs} is the second derivative estimate of the band gap):

$$\begin{aligned} G_{PBE} &= (0.92 \pm 0.12) G_{sxs} - (1.51 \pm 0.67) \text{ eV}; \qquad R^2 = 0.89 \\ G_{mBJ} &= (1.00 \pm 0.13) G_{sxs} - (0.48 \pm 0.75) \text{ eV}; \qquad R^2 = 0.89 \end{aligned}$$

It is also worth pointing out that the valence band widths estimated from the second derivative method and obtained from the PBE calculation are even more accurate, as shown in Figure 5.9(b). Again, although the second derivative estimate of the valence band width for any single material may be too large or too small compared to the calculated value, the average from all of these materials is very close to a perfect fit. As previously mentioned, using peaks in the second derivative of a spectrum to determine the energy of the band edges has little theoretical justification. However, based on the linear fits of the calculated band gaps and band widths as a function of the second derivative estimates, the using the "second derivative method" to estimate the band gaps is justifiable if no deeper insight or accurate theoretical electronic structures of the material in question is available. The same argument holds when comparing the second derivative estimate to the optical band gaps found in the literature, as shown in Figure 5.9(a) (the optical gaps are obtained from References [78, 97–102], also see References [15, 16] for more discussion).

5.3 Period 5 Oxides

The alkaline and post-transition metal oxides were notable because the cations, all with the same nominal 2+ oxidation state, did not contribute significant occupied states to the valence band (with the exception of the localized nd^{10} shell in the post-transition metal

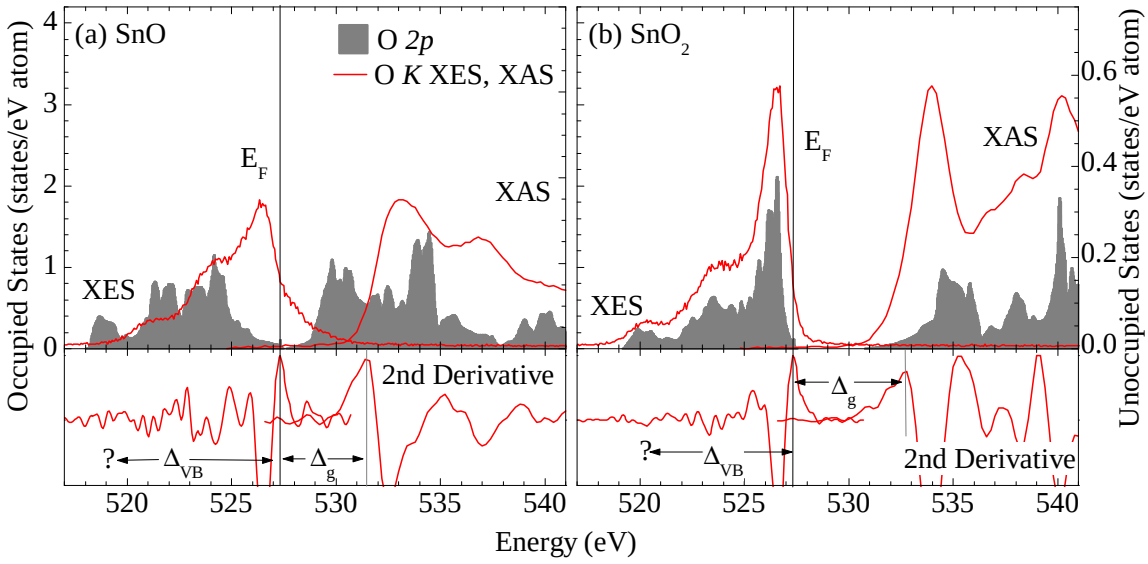

Figure 5.10: The calculated O $2p$ DOS and measured O K XES and XAS for (a) SnO and (b) SnO_2. The second derivatives of these spectra are shown in the bottom panels, this figure has the same style as Figure 5.3. Note how poorly the calculated DOS and measured XES spectrum in (a) line up when the peak in the second derivative of the O K XES is used to find the top of the valence band. This figure uses data published in Reference [17].

oxides, which interacted only weakly with the oxygen $2p$-states). The set of binary oxides formed with non-metal cations from period 5 (In, Sn, Sb, Te, and I) also contains systems where the cation is fully oxidized (i.e. In_2O_3, SnO_2, Sb_2O_5, and TeO_3), so my analysis of the valence and conduction bands of these types of systems can be continued to this set. There are also similar oxides with cations in a lower oxidation state (i.e. SnO, Sb_2O_3, TeO_2, I_2O_5) where the cation could contribute $5s^2$ states to the valence band. As an aside, these aspects are not innate to the period 5 cations, of course. There are analogous oxides with cations from periods 4 and 6 (that are sufficiently stable solids at ambient conditions to study with soft X-ray spectroscopy). I have studied these period 5 oxides mostly because they were the easiest to obtain and work with. These oxides were obtained from a commercial vendor in powder form (Alfa Aesar, 99.99% purity).

Using the peaks in the second derivative of the O K XES and XAS spectra is not particularly useful for several of these systems, as shown in Figure 5.10. For instance, the O K XES spectrum from both SnO and SnO_2 has weak low-energy structure that makes it impossible

to unambiguously find the peak in the second derivative representative of the bottom of the valence band. The same is true for the top of the valence band of SnO; using the peak in the second derivative to indicate the top of the valence band, as shown in Figure 5.10(a) clearly seriously misaligns the spectrum with the O $2p$-states. The second derivatives in the peaks of the O K XES and XAS of SnO_2, on the other hand, provide a rather good estimate of the band gap. These two systems show a key failing of the second derivative method; when the DOS has a very gradual slope towards the band edge (as is the case in SnO and SnO_2 at the bottom of the valence bands, and at SnO at the top of the valence band), no unambiguous peak in the second derivative can be identified. However without any prior knowledge of the electronic structure it can be difficult to determine whether the second derivative is appropriate for a given material. In my opinion, the second derivative method should still be used to analyse spectra if no other information about the electronic structure is available, but these caveats should be remembered.

The calculated DOS (using the PBE functional, but shifted to incorporate the mBJ band gap) and the calculated and measured O K XES and XAS (the latter calculation involves an explicit core hole) for In_2O_3, SnO_2, and Sb_2O_5 are shown in Figure 5.11. Although the cations in these systems should formally have no valence electrons (the cations are In^{3+}, Sn^{4+}, and Sb^{5+}), there is significant hybridization between the cation $5s$-states and the O $2p$-states at the bottom of the valence band (marked by the arrows in Figure 5.11(a)). This hybridization is real, because it is reproduced in the O K XES (both measured and calculated, as shown in Figure 5.11(b)) [17]. In fact, the calculated spectra for these compounds are in excellent agreement with the measured spectra. Because of this, the calculated spectra can be accurately aligned with the measured spectra. In this manner, once the calculated XES spectrum is aligned with the measured one, it is clear if the calculated band gap and core hole shift are inadequate to correctly align the calculated XAS with the measurements. The shift required to correct the alignment can then be used to correct the calculated band gap.

The calculated DOS (again using the PBE functional with the mBJ band gap) and the calculated and measured O K XES and XAS (again involving a core hole) for SnO, Sb_2O_3, TeO_2 are shown in Figure 5.12. In these systems the cations have a nominal valence state of $5s^2$, so we expect to see significant cation contribution to the valence band. In fact, the cation

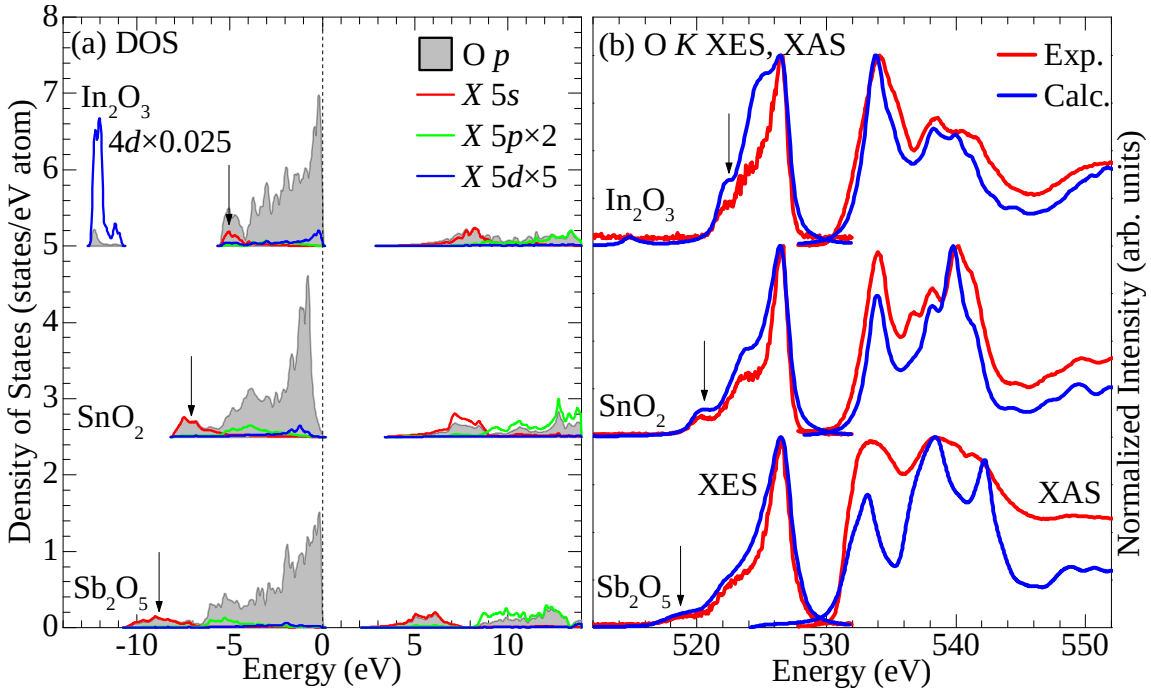

Figure 5.11: Electronic structure of period 5 oxides with a $5p^0$ ground state configuration. (a) The partial DOS calculated using the PBE functional with the mBJ band gap, (b) the calculated and measured O K XES (excited near 540 eV) and XAS (TFY mode). The arrows in (a) and (b) point out the $5s$-O $2p$ hybridized states at the bottom of the valence band in each oxide. This figure is reproduced in part with permission from Reference [17], Copyright 2012 American Chemical Society.

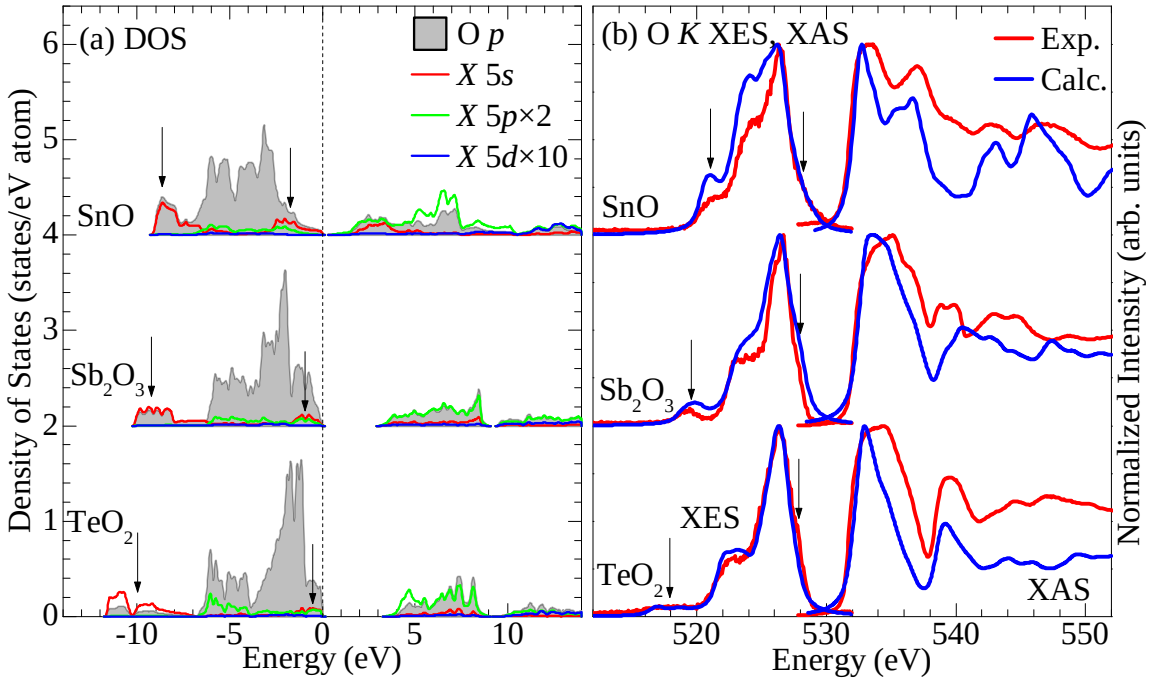

Figure 5.12: Electronic structure of period 5 oxides with a $5p^2$ ground state configuration. (a) The partial DOS calculated using the PBE functional with the mBJ band gap, (b) the calculated and measured O K XES (excited near 540 eV) and XAS (TFY mode). The arrows in (a) and (b) point out the $5s$-O $2p$ hybridized states at the bottom and top of the valence band in each oxide. This figure is reproduced in part with permission from Reference [17], Copyright 2012 American Chemical Society.

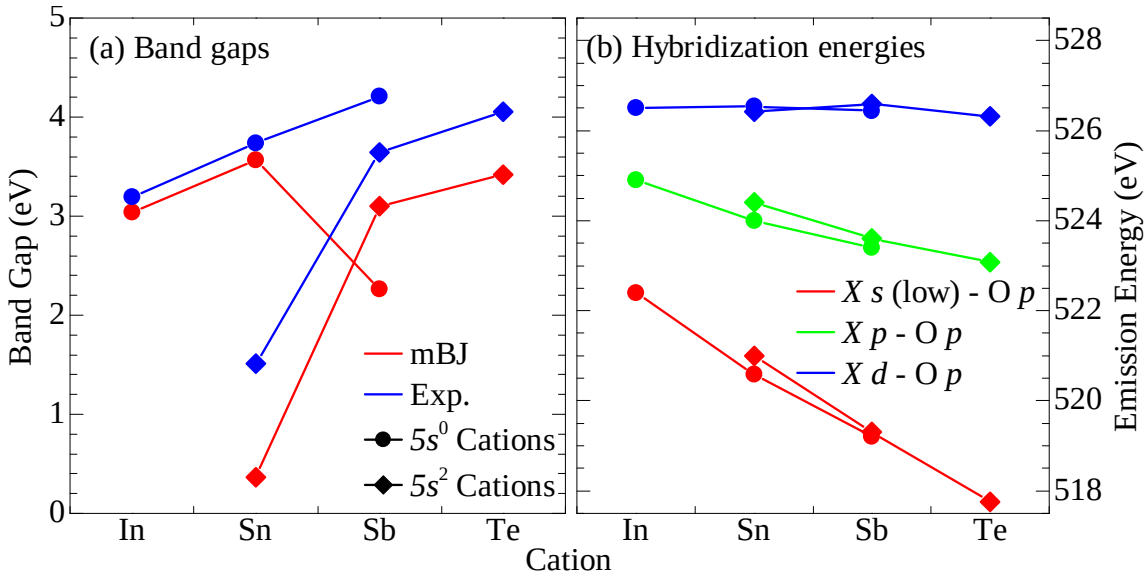

Figure 5.13: The band gaps and hybridization energies in the period 5 oxides. (a) The band gaps obtained from mBJ calculations and aligning the calculated and experimental spectra. (b) The energy centre points of the different cation and O $2p$ hybridization states. This figure is reproduced in part with permission from Reference [17], Copyright 2012 American Chemical Society.

$5s^2$ states are split: they are predominately found at both the top (in occupied antibonding states) and bottom (in bonding states) of the valence band, as shown by the arrows in Figure 5.12(a) [17]. The hybridization between the cation $5s$- and oxygen $2p$-states are again real, as shown in Figure 5.12(b) there is again excellent agreement between the measured and calculated spectra, and the hybridization features at the top and bottom of the valence band are visible (as shown by the arrows in Figure 5.12(b)).

As mentioned above, because the the calculated spectra for these compounds are so close to the measured ones, the band edges for each spectrum can be determined by aligning the calculated spectrum with the measured one. Combined with the calculated energy shift in the conduction band edge due to the core hole, one can obtain a semi-empirical estimate of the band gap the ground state and core hole-perturbed electronic structures by the following method:

1. We assume that the average interstitial potential (conveniently set as 0 Ryd for the internal energy scale in a WIEN2k calculation) is unaffected by the core hole potential;

in other words, the zero of the native WIEN2k energy scale is the same for both ground state and core hole-perturbed electronic structures. Because a good core hole calculation involves a large supercell, and only a single atom within this cell has the core hole vacancy, this is a reasonable assumption.

2. We then align the calculated (ground state) XES spectrum with the measured one. (This can be done visually, or perhaps by adjusting the energy shift of the calculated spectrum so the cross-correlation with the measured spectrum is maximized.) Once this is done we know where the top of the valence band (of the calculated spectrum, at least) is on the X-ray energy scale.

3. We then align the calculated (core hole perturbed) XAS spectrum with the measured one. Once this is done we know where the bottom of the (core hole perturbed) conduction band is on the X-ray energy scale, and can determine the difference between that and the top of the (ground state) valence band on the X-ray energy scale (Δ_X).

4. We then take the calculated Fermi levels (relative to the average interstitial potential, as noted above) and band gaps from the core hole perturbed (E_F^{ch} E_G^{gs}, respectively) and the ground state (E_F^{gs} and E_G^{gs}, respectively) calculations.

5. The core hole shift is then $\delta_{ch} = (E_F^{ch} + E_G^{ch}) - (E_F^{gs} + E_G^{gs})$. This is the shift in the onset of the conduction band caused by the core hole perturbation.

6. The new semi-empirical band gap (Δ_G) is then the core hole shift subtracted from the difference between the aligned XES and XAS spectra; $\Delta_G = \Delta_X - \delta_{ch}$.

Because of the core hole perturbation, as previously noted, the gap between an XES and XAS spectrum will always be smaller than the calculated gap. In fact, assuming the calculated core hole shifts are accurate (or at least not over estimated), the gaps calculated with the mBJ exchange correlation functional are all slightly too small, as shown in Figure 5.13(a). Assessing the accuracy of the calculated and semi-empirical gaps is troublesome because there is considerable discrepancy in the band gaps of these systems reported in the literature [17], but the suggested gaps shown in Figure 5.13(a) are reasonable.

Another potential problem with using XES and XAS spectra to estimate band gaps should be mentioned: even in perfect crystals, many structures have multiple inequivalent sites of the same atomic species, and the binding energy of (for example) the $1s$ core state may not necessarily be the same for each inequivalent site. Indeed, the binding energies for a given core state of a particular atom at different inequivalent sites calculated with WIEN2k can differ by a tenth of an eV or so even if the local environment for all sites is quite similar (and, of course, for sites with considerably different bonding environments the binding energies can differ by a much greater amount). Since an XES or XAS measurement samples *all* these sites (weighted by multiplicity, of course), in a very real sense there is not a single "valence band edge" or "conduction band edge" in the spectra; the energy of a band edge will be different for each inequivalent site, and likely impossible to distinguish in a spectrum. This effect can be corrected, at least approximately, by modifying the method outlined above to include adding the maximum binding energy difference to the semi-empirical band gap to represent the fact that the "top of the valence band" in the XES spectrum will be due to the tightest-bound site, while the "bottom of the conduction band" in the XAS spectrum will be due to the weakest-bound site. This assumes, however, that the core hole shifts for each site will be the same — so in general care must be taken when attempting to use this method to accurately determine the band gap.

A final point of interest in these materials is that the central energy for the bonding cation $5s$-, $5p$-, and $5d$-states in the valence band is independent of the oxidation state, as shown in Figure 5.13(b). (Note that the antibonding cation $5s$-states in SnO, Sb_2O_3, and TeO_2 are omitted.) This is an interesting result; the cation hybridizations in the valence band depend largely on the cation species, not the cation valence state.

5.4 Concluding Remarks

Determining the band gap of a material from XES and XAS spectra is a challenging task, and while the second derivative method is an easy approach to obtain a first estimate of the band gap, it will fail to properly determine the band edges in materials in which the DOS has a very gradual rise in intensity after the edge. Secondly, no matter what the method, a

purely empirical approach to determining the band gap from XES and XAS spectra will only work if the core hole perturbation has a negligible effect on the edge of the conduction band (as probed by XAS). Attempting to calculate the influence of the core hole perturbation, and in general replicate the shape of the XES and XAS spectra, is the best approach to determining the band gap. For the relatively simple binary oxides discussed herein, this is straightforward, but for more complicated systems or heterostructures the computational requirements to accurately compute the influence of a core hole may be quite demanding.

On the other hand, O K XES and XAS spectra do provide an excellent probe of hybridization features within the valence and conduction bands, and interestingly, the approximate energy of cation s,p,d — O $2p$ hybridization features within the valence band tend to follow atomic-like rules [15], and seem to be rather independent of cation valency [17].

Chapter 6

Band Gap Engineering in Ternary Oxides

As mentioned in the previous chapter, TiO_2 and ZnO are currently being studied to improve their performance in photocatalysts, photovoltaics, and other optoelectronic applications [70, 71, 78]. Despite the promise of these materials, they each have drawbacks which reduce their effectiveness in optoelectronics. One possible route for improving the properties of these binary oxides is to investigate ternary oxides that ideally preserve the best aspects of the electronic structure of the binary oxide while avoiding some of the shortcomings. In particular, the band gap of TiO_2 and ZnO is the largest shortcoming of these materials for optoelectronic purposes; in both materials it is too large (3.0 – 3.2 for TiO_2 [104, 105] and 3.3 – 3.4 eV for ZnO [78, 106, 107]) to efficiently use of the solar spectrum. Therefore finding a ternary oxide with a smaller band gap is a major focus of this research.

This chapter details my research into band gap engineering in ternary oxides using DFT and X-ray spectroscopy. I have studied materials based on TiO_2 and lone pair oxide percursors (Sn_2TiO_4, $PbTiO_3$, $Bi_4Ti_3O_{12}$, and $Bi_2Ti_4O_{11}$) and the ternary material based on TiO_2 and ZnO precursors ($ZnTiO_3$). These findings are also reported in my published work on the subject, see References [18, 19].

6.1 Lone Pair — Titanium Ternary Oxides

Rutile TiO_2 is an almost ideal photocatalyst for generating hydrogen: it is cheap, corrosion resistant, and has a band gap that straddles the reduction potential of water [70, 71, 108]. The process of splitting water with TiO_2 is very simple: a TiO_2 electrode can absorb light, creating electron-hole pairs, as long as the energy of the light exceeds the band gap of TiO_2 (i.e. $h\nu > E_g$ fwhere ν is the frequency of the light and E_g is the band gap of TiO_2). If the electrode is

immersed in water, the holes generated in the TiO_2 can transfer to water molecules, breaking them apart (denoting a hole by h^+, the reaction is $4h^+ + 2H_2O \rightarrow 4H^+ + O_2$) [70]. Under an applied voltage (around 5 V) the electrons created in the photoexcited TiO_2 electrode can be driven out into a metal electrode, and transfer to the H^+ making hydrogen gas [70].

The key to this process is efficiently creating electron-hole pairs through the absorption of light. Unfortunately, the band gap of TiO_2 is in the ultraviolet energy range, and therefore only a small portion of the solar spectrum is energetic enough to excite the electron-hole pairs. To efficiently harness the solar spectrum the band gap needs to be reduced to 2.2 eV or less [109]. It should be mentioned that water splitting can also be realized by anatase TiO_2 (the other common phase of TiO_2), however this system has an even larger band gap than rutile TiO_2 [105]. Therefore, in this research, I have focussed on rutile TiO_2 exclusively.

The titanium in TiO_2 is nominally Ti^{4+}, with a $3d^0$ valence state, so the conduction band is dominated by these empty Ti $3d$-states. Since the conduction band energy is only slightly greater than the reduction potential of water [110], ternary oxides whose conduction bands are dominated by Ti $3d^0$ states are a good starting point in the search for an appropriate photocatalyst with a smaller band gap.

An interesting class of candidate materials are ternary oxides involving Ti^{4+} and "lone pair" cations, like Sn^{2+}, Pb^{2+}, and Bi^{3+}. These cations are called "lone pair" cations because historically it was believed that the ns^2 states did not participate in chemical bonding [111], and although it is now known that this is not the case [17, 112–114], the name is still often used. As discussed in Section 5.3, antibonding cation $5s$- and O $2p$-states form the tops of the valence bands in SnO, Sb_2O_3, and TeO_2; a similar phenomenon occurs in PbO and Bi_2O_3 [17, 113, 114]. This raises the question: If the valence band in a lone pair binary oxide is defined by the cation ns^2 states, and the conduction band in TiO_2 is defined by the Ti $3d^0$ states, then are these features preserved in the ternary compound?

6.2 Lead Titanates

Several ternary oxides containing lone pair cations and Ti^{4+} are readily available. The most notable one is the perovskite $PbTiO_3$, which is widely used as a piezoelectric crystal when

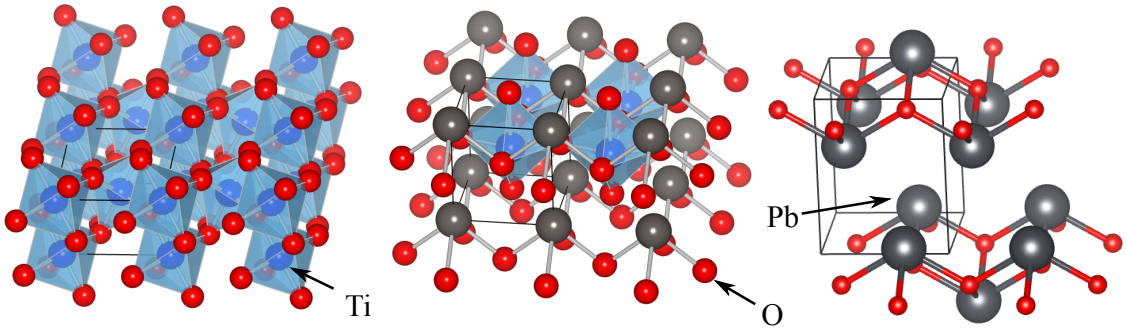

Figure 6.1: Crystal structures of (left to right): rutile TiO_2 (from Reference [117]), perovskite $PbTiO_3$ (from Reference [116]), and litharge PbO (from Reference [118]). A single unit cell is outlined for each system. These, and all other crystal structures shown herein, were drawn with VESTA [119].

alloyed with $PbZrO_3$ [115]. The structure of this system [116] features the same Ti^{4+} — 6 O^{2-} octahedra as found in rutile TiO_2 [117], and the same Pb^{2+}-capped — 4 O^{2-} square pyramids as found in litharge PbO [118], as shown in Figure 6.1. If the bulk electronic structure of $PbTiO_3$ is only weakly dependent on long range order, and is dominated by the atomic arrangement of nearest neighbours, then we can predict that it will be close to a superposition of the electronic structures of TiO_2 and PbO [18].

Indeed, this hypothesis is supported by the calculated electronic structure of TiO_2, PbO, and $PbTiO_3$, as shown in Figure 6.2(a). Like litharge SnO (refer back to Figure 5.12), the bottom and top of the valence band of PbO is defined by hybridized Pb $6s$ — O $2p$ bonding and antibonding states, respectively. The bulk of the O $2p$-states are in the middle of the valence band, the dominant cation states in this region are Pb $6p$-states. As expected, the only significant hybridization in TiO_2 is between the Ti $3d$- and O $2p$-states. Despite being nominally Ti^{4+}, there are some Ti $3d$-states in the valence band, these are mostly at the bottom of the valence band, identifying strong Ti — O bonding. The conduction band, however, is definitely dominated by Ti $3d$-states throughout (note that the conduction band Ti $3d$-states in Figure 6.2(a) have been reduced in intensity by a factor of 3 for clarity). These features in the electronic structures of PbO and TiO_2 are also found in the electronic structure of $PbTiO_3$, as shown in Figure 6.2(a). Like PbO, the valence band of $PbTiO_3$ has bonding Pb $6s$-, O $2p$-states at the very bottom of the valence band, and antibonding Pb

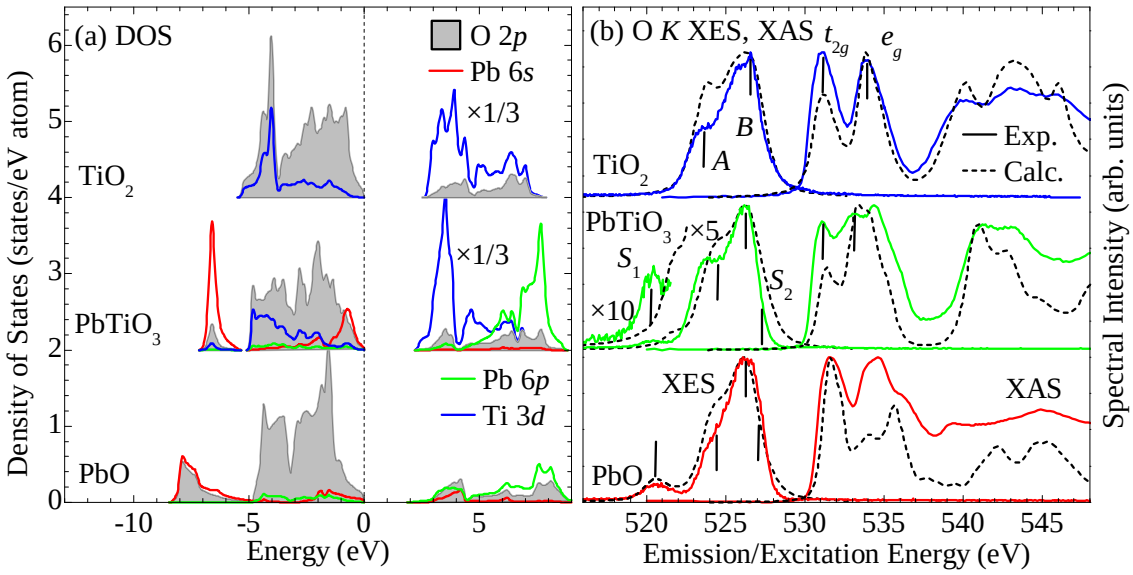

Figure 6.2: Electronic structure of TiO_2, PbO, and $PbTiO_3$: (a) The calculated DOS, the conduction band Ti $3d$-states have been scaled by a factor of 1/3 for clarity. The top of the valence band is at 0 eV. (b) The calculated and measured O K XES (excited near 540 eV) and XAS spectra (TFY mode). The various spectral features are labelled. This figure is adapted from data published in Reference [18] and newly calculated core hole perturbed XAS spectra.

$6s$-, O $2p$-states at the top of the valence band. The middle of the valence band has some Pb $6p$-states, as in PbO, but the dominant hybridization is between bonding Ti $3d$-, O $2p$-states as in TiO_2. Like TiO_2, the conduction band of $PbTiO_3$ is dominated by Ti $3d$-states, with Pb $6p$-states becoming significant at 8 eV and above, as shown in Figure 6.2(a). While the subtle shape of the valence and conduction bands of $PbTiO_3$ is obviously dependent on the crystal structure, the general features and distribution of states in the electronic structure of $PbTiO_3$ can be predicted by a simple superposition of the electronics structures of TiO_2 and PbO.

The measured O K-edge XES and XAS spectra of these compounds (all are powders purchased from Alfa Aesar, 99.9% purity) are in rather good agreement with the calculated spectra, as shown in Figure 6.2(b), suggesting that the calculated electronic structure is fairly accurate. Note that a $3 \times 3 \times 3$ supercell was used to calculated the influence of the core hole on these materials; my previously published work used the ground state XAS spectra [18].

As expected, the O K XES spectra of PbO and $PbTiO_3$ shows the bonding and antibonding Pb $6p$ — O $2p$ hybridizations, labelled S_1 and S_2, respectively, in Figure 6.2. The S_1 feature is somewhat weaker in intensity and at somewhat lower energies in the O K XES spectrum of $PbTiO_3$ than was predicted by the calculation, but it is still clearly present. As suggested by the calculated DOS, all O K XES spectra have a low energy shoulder (labelled A in Figure 6.2) that is due to Ti $3d$, Pb $6p$ — O $2p$ hybridization in the valence band, and all spectra have a main peak (labelled B in Figure 6.2(b)) due to the bulk of the O $2p$-states. As an aside, note that the calculated O K XES spectrum of PbO is in very good agreement with the measured spectrum; this shows that spin-orbit coupling (from the heavy Pb cation) in the valence band (which was not accounted for in these calculations) is not significant to the bulk electronic structure.

The calculated core hole perturbed XAS spectra are in reasonable agreement with the measured XAS spectra, as shown in Figure 6.2(b). The O K XAS spectrum of TiO_2 is dominated by two major features near the edge of the conduction band; since the local environment of Ti is nearly octahedral, these can be labelled as O $2p$ hybridization with t_{2g} and e_g symmetry $3d$-states [76]. The measured O K XAS spectrum of PbO also has two rather prominent features near the edge of the conduction band; these are very close to the energies of the features in the XAS spectrum of TiO_2 although obviously are due to completely different hybridizations. These features are repeated in the calculated O K XAS spectrum of PbO, although there is definitely a discrepancy in the relative intensities. Finally, the near-edge shape of the measured O K XAS of $PbTiO_3$ has three rather minor peaks on a broad background while the calculated XAS spectrum has only two clear peaks in this region.

To analyse the XAS spectra of these systems in more detail, the XAS spectra calculated from both the ground state and core hole perturbed states are shown in Figure 6.3 along with the appropriate DOS. It is immediately clear in Figure 6.3 that the XAS spectra calculated from the ground state conduction band are very similar in shape to the XAS spectra calculated from the core hole perturbed conduction band. In general the core hole perturbation has two effects on the XAS spectrum: the intensity of the lowest energy peaks is increased relative to the higher energy features, and the spectrum is shifted to lower energies. The

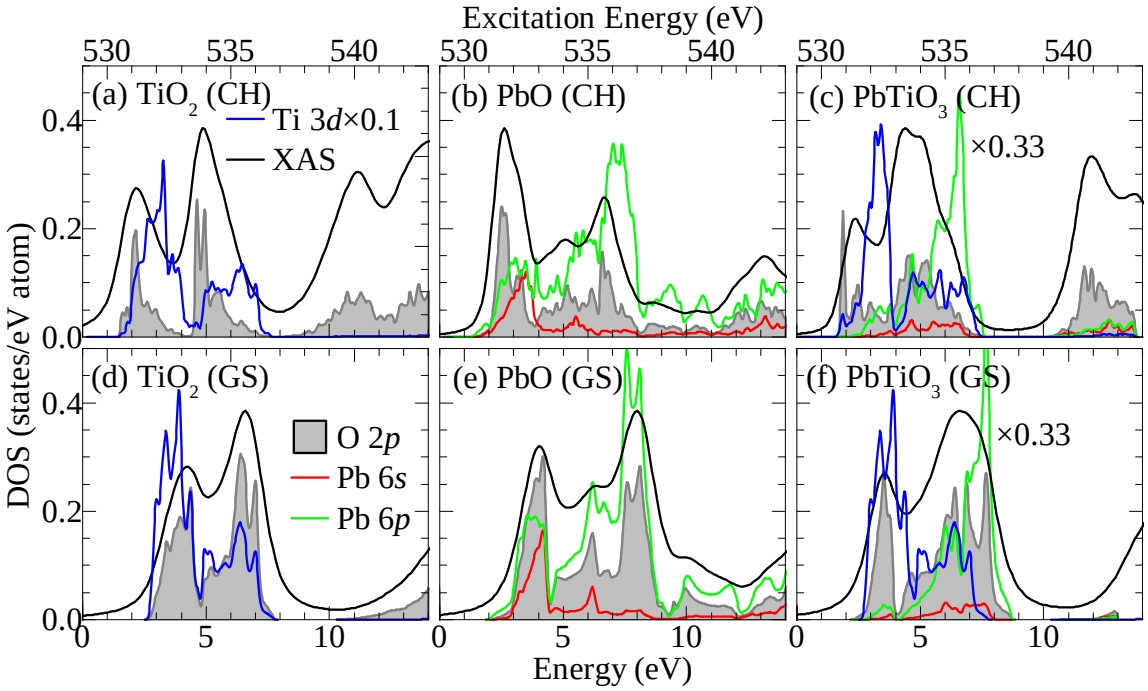

Figure 6.3: The calculated O K XAS spectra and partial DOS from a core hole perturbed calculation ("CH", panels (a-c)) and a ground state calculation ("GS", panels (d-g)) for: (a,d) TiO_2, (b,e) PbO, and (c,f) $PbTiO_3$. Note in the core hole perturbed cases the O $2p$ DOS shown here is only from the perturbed atom; all other partial DOSes have been averaged over the unit cell.

influence of the core hole on the XAS spectrum of TiO_2 is rather dramatic, as shown in Figure 6.3 (a); the local O $2p$-states are localized in energy to two rather narrow-band states immediately below the energy of the two main Ti $3d$ features (the t_{2g} and e_g bands, which are relatively unaffected by the O $1s$ core hole, as was expected due to the localization of the perturbation). This is in contrast to the ground state conduction band, shown in Figure 6.3(d), where the O $2p$-states are weighted towards the high-energy side of the main Ti $3d$ t_{2g} and e_g bands.

Likewise, in PbO, as shown in Figure 6.3 (b), the core hole perturbation localizes the near-edge O $2p$-states into a rather narrow band that is at lower energies than the corresponding states in the ground states DOS, shown in Figure 6.3 (e). The core hole perturbation causes the hybridizations higher up in the conduction band to be shifted to slightly lower energies, but otherwise not significantly affected. Since the measured XAS spectrum for PbO (refer back to Figure 6.2) has slightly different fine structure after the first near-edge peak than the calculated XAS spectrum, it is possible that the core hole perturbation has a greater influence on the O $2p$ — Pb $6p$ hybridized states than is predicted by the calculated spectrum.

The behaviour of the core hole perturbation in $PbTiO_3$ is as expected (see Figure 6.3(c,g)); there is a combination of greater localization (in energy) of O $2p$-states at the low energy side of the Ti $3d$ bands (as in TiO_2, see Figure 6.3(a)), and a general shift of the O $2p$-states to lower energies. Note that the crystal structure of $PbTiO_3$ has two oxygen sites, and the ground state WIEN2k calculation suggests that the binding energies of $1s$-states at these two sites differs by about 0.11 eV. This complicates the core hole perturbed DOS, because the core hole perturbation was calculated separately for each site, but the resulting XAS spectra and DOS were added together in Figure 6.3(c). This is why the extremely sharp O $2p$ DOS feature in Figure 6.3(c) at about 2 eV seems misaligned with the calculated XAS; when the appropriate binding energy and core hole shift is taken into account this feature actually contributes to the XAS spectrum peak at 531.4 eV. The XAS spectrum shown in Figure 6.3(c) is the sum of the two separate spectra from each site (weighted by the multiplicity of each site), after each spectrum has been shifted by the appropriate difference in Fermi levels and binding energies. The DOS, on the other hand, has just been weighted by the multiplicity of each site and shifted by the appropriate difference in Fermi levels; so it is

expected that the XAS does not perfectly align with the DOS. The XAS has been shifted to resemble what is actually measured (i.e. relative to the O $1s$ binding energy), the perturbed DOS cannot be measured relative to the Fermi level directly. For the XAS calculated from the ground state, shown in Figure 6.3(f), this difference in binding energies has been taken into account but since there is no core hole perturbation in this calculation the Fermi levels are consistent for all sites, and therefore the agreement between spectrum and DOS is much closer.

As previously mentioned, the near-edge of the measured XAS spectrum of $PbTiO_3$, shown in Figure 6.2, has three features on a broad background, but the calculated XAS spectrum (whether core hole perturbed or ground state) basically has only two features in this region. One possible explanation is that the perturbative effect on the O $2p$ — Pb $6p$ hybridized states is miscalculated (as I suggested was the case for PbO, as well). The first two features in the measured XAS spectrum would then be O $2p$-states localized at the bottom of the Ti $3d$ t_{2g} and e_g bands, as in TiO_2, the third higher energy feature would be from O $2p$ — Pb $6p$ hybridized states.

6.3 Tin Titanates

Since SnO is isostructural to PbO, and has a smaller band gap, it seems reasonable to expect that a tin titanate perovskite could be synthesized that would be analogous to $PbTiO_3$. In fact, it was the search for such a material that started my involvement in this research; my collaborator Prof. Nobihiro Kumada (University of Yamanashi, Kofu, Japan) was attempting to synthesize $SnTiO_3/SnZrO_3$ to see if it could act as a replacement piezoelectric for $PbTiO_3/PbZrO_3$; since although the latter is already widely used commercially it would still be preferable to find a less toxic replacement for lead in these compounds. This search lead to the accidental synthesis of Sn_2TiO_4 [120], and the initial research focussed on the structure and synthesis of Sn_2TiO_4 as a possible gateway to a perovskite $SnTiO_3$, not on the properties or potential applications of Sn_2TiO_4 itself [120, 121], although the possibility of using Sn_2TiO_4 as a test case for band gap engineering in lone pair — d^0 materials was soon investigated [122]. Despite this interest, most of the research into band gap engineering

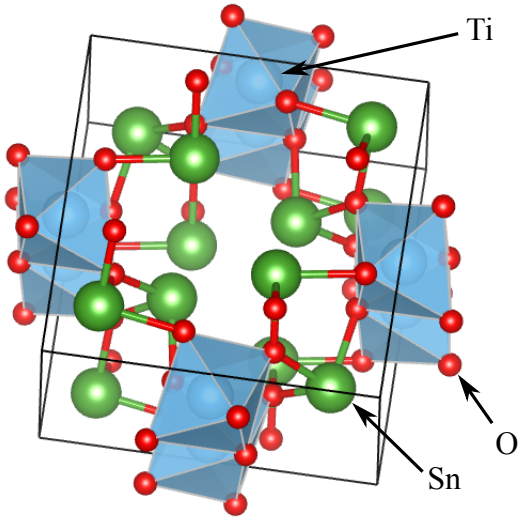

Figure 6.4: Crystal structures of Sn_2TiO_4 (from Reference [120]). A single unit cell is outlined. Note that SnO is isostructural to PbO, shown in Figure 6.1 (the structure of SnO is from Reference [123]).

was conducted by strictly theoretical methods, so it was appropriate for me to study these materials with X-ray spectroscopy.

Sn_2TiO_4 has a rather large unit cell with the $P4_2/mbc$ space group, as shown in Figure 6.4. Like $PbTiO_3$, Sn_2TiO_4 contains the same Ti^{4+} — 6 O^{2-} octahedra as TiO_2, and Sn^{2+} capped square pyramids based with 4 O^{2-} as found in litharge SnO [123]. However while the larger scale structure of $PbTiO_3$ was layered, Sn_2TiO_4 has channels running through it; the empty hemisphere required for stabilization of the lone pair Sn $5s^2$ states faces into these channels. Despite these structural differences, the electronic structure of Sn_2TiO_4 is quite similar to that of $PbTiO_3$, and is again close to a superposition of the electronic structures of SnO and TiO_2, as shown in Figure 6.5. The valence bands of SnO and Sn_2TiO_4 are sandwiched between bonding (at the bottom) and antibonding (at the top) Sn $5s$ — O $2p$-states, as in PbO and $PbTiO_3$, while the conduction band of Sn_2TiO_4 features the same two Ti $3d$ t_{2g} and e_g bands as TiO_2. Single crystals of Sn_2TiO_4 were generously provided by Prof. Nobuhiro Kumada (Interdisciplinary Graduate School of Medicine and Engineering, University of Yamanashi, Kofu, JP), and the crystal structure was verified by XRD by members of Prof. Kumada's research group [120].

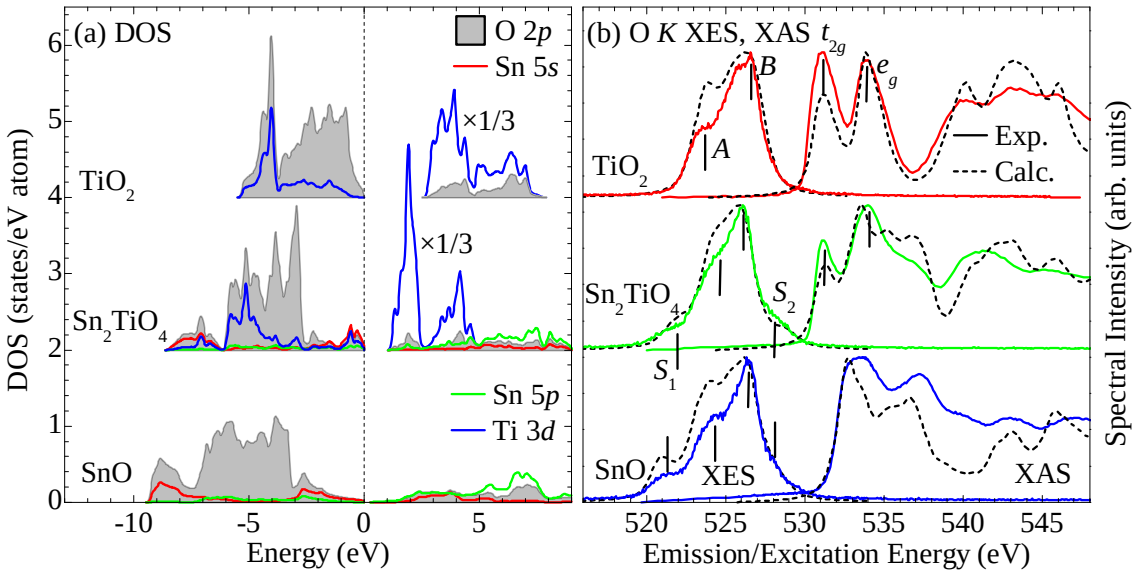

Figure 6.5: Electronic structure of TiO_2, SnO, and Sn_2TiO_4: (a) The calculated DOS. (b) The O K XES (excited near 540 eV) and XAS (TFY mode) spectra. This figure is organized the same as Figure 6.2, and is adapted from data published in Reference [18].

The calculated XES spectrum of Sn_2TiO_4 is in good agreement with the measured XES spectrum, as are the previously discussed spectra of SnO and TiO_2 (SnO powder purchased from Alfa Aesar, 99.9% purity). As in the case of the lead, titanium oxides, the hybridized states responsible for each of the main features of the experimental XES spectrum can be identified with the aid of the calculated electronic structure; the bonding Sn $5s$ — O $2p$ hybridization is responsible for feature S_1, the Sn $5p$, Ti $3d$ — O $2p$ hyridization within the valence band is responsible for feature A, the main O $2p$-states are feature B, and the antibonding Sn $5s$ — O $2p$ hybridization is feature S_2. For a more detailed discussion of the hybridizations in the electronic structure see Reference [18].

Interestingly, the XAS spectrum for Sn_2TiO_4 calculated from the ground state electronic structure is in quite good agreement with the measured XAS spectrum, as shown in Figure 6.5(b). The calculated (mBJ) band gap also puts the XAS spectrum in the right place relative to the measurement; once the calculated XES spectrum is aligned with the measured spectrum, if the exact same shift is applied to the calculated XAS spectrum it lines up with the measured spectrum as shown in Figure 6.5(b). However this does not preclude the

possibility that the actual band gap should be larger, since the measured XAS spectra could occur at lower energies due to a core hole shift; and indeed my calculations suggest that Sn_2TiO_4 has a core hole shift of about 0.4 eV.

6.4 Bismuth Titanates

The third class of ternary oxides that I have studied are those based on Bi^{3+}. There are two readily available candidate materials, $Bi_2Ti_4O_{11}$ and $Bi_4Ti_3O_{12}$ (there are actually many Bismuth titanate polymorphs; these two were the ones I was able to easily obtain). The former material is an antiferromagnet that exhibits some photocatalytic activity [124], crystallizes in the $C2/c$ spacegroup, and has 6 inequivalent oxygen sites [125]. The latter material is ferroelectric [126] and crystallizes in either the $B2cb$ space group or the $B1a1$ space group [127, 128]. Electronic structure calculations suggest there is very little difference between the calculated DOS of the $B2cb$-phase $Bi_4Ti_3O_{12}$ and the high-temperature $I4/mmm$-phase $Bi_4Ti_3O_{12}$ [126], so I only bothered to calculate the DOS from the $B2cb$ phase. Since neither $B2cb$ nor $B1a1$ are standard space groups, the actual structure I used was a simplified transform of $B1a1$, given in Table 6.1. This structure has 12 inequivalent oxygen sites. The structures of Bi_2O_3 and the bismuth titanates are shown in Figure 6.6. While the structures of the bismuth titanates are much more complex than the other lone pair-Ti^{4+} ternary oxides, they have the same local structure: the Ti^{4+} are at the centre of 6 O^{2-} octahedra, and the Bi^{3+} are coordinated by 3 O^{2-} and these Bi^{3+} have a the vacant hemisphere characteristic of lone pair cations.

The calculated DOS and measured and calculated O K XES and XAS spectra for these materials are shown in Figure 6.7. $Bi_2Ti_4O_{11}$ and Bi_2O_3 powders were obtained from Alfa Aesar (99.9% purity), while $Bi_4Ti_3O_{12}$ powders were generously provided by Dr. Alexei Belik (National Institute for Materials Science, Tsukuba, JP), members of Dr. Belik's research group verified the crystal structure of $Bi_4Ti_3O_{12}$ with XRD and found it was consistent with other reports found in the literature [126].

As with the other ternary oxides, the electronic structure of $Bi_2Ti_4O_{11}$ and $Bi_4Ti_3O_{12}$ resembles a superposition of the electronic structures of Bi_2O_3 and TiO_2. Importantly, the

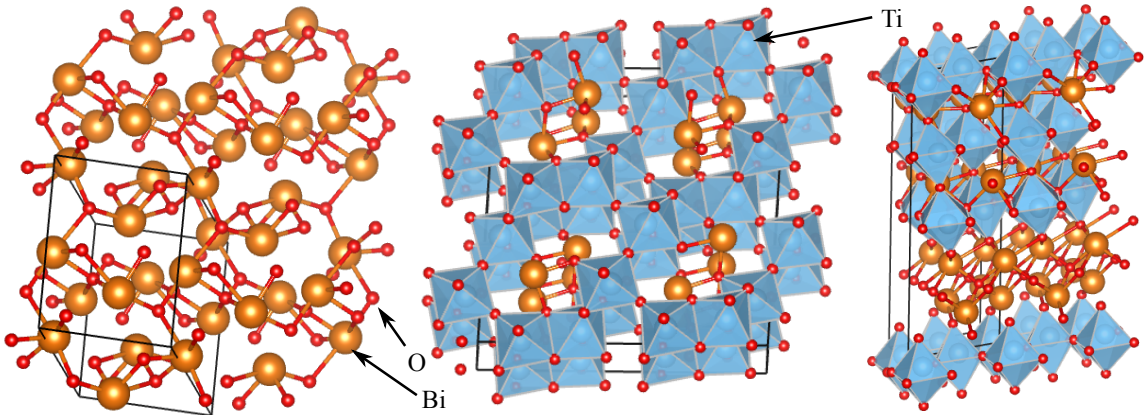

Figure 6.6: Crystal structures of (left to right): α-phase Bi_2O_3 (from Reference [129]), α-phase $Bi_2Ti_4O_{11}$ (from Reference [125]), and $Bi_4Ti_3O_{12}$ (see text, structure adapted from References [127] and [128]). A single unit cell is outlined for each system.

Table 6.1: Crystal structure of $Bi_4Ti_3O_{12}$. The space group is Pc, the lattice constants are $a = 5.45$ Å, $b = 16.64$ Å, and $c = 5.41$ Å. The lattice angles are $\alpha = 90.0°$, $\beta = 90.0°$, and $\gamma = 80.6°$. All positions are in the $2a$ Wyckoff site, and given in fractional coordinates.

Atom	x	y	z	Atom	x	y	z
Bi_1	0.2425	0.6088	0.2477	O_4	0.8176	0.755	0.9679
Bi_2	0.3916	0.3208	0.2707	O_5	0.1535	0.2456	0.9929
Bi_3	0.1105	0.8762	0.2523	O_6	0.0288	0.8586	0.6913
Bi_4	0.9648	0.1660	0.2315	O_7	0.3894	0.723	0.526
Ti_1	0.2551	0.4856	0.7504	O_8	0.1573	0.2444	0.4942
Ti_2	0.1343	0.742	0.7513	O_9	0.6474	0.6224	0.1795
Ti_3	0.0	0.0	0.7498	O_{10}	0.8055	0.3784	0.3084
O_1	0.9409	0.1044	0.7941	O_{11}	0.4999	0.5192	0.53
O_2	0.7712	0.965	0.0159	O_{12}	0.4349	0.4946	0.0541
O_3	0.7059	0.9888	0.5336				

bonding and antibonding Bi 6s-states define the bottom and top of the valence bands, respectively, and the unoccupied Ti 3d-states define the onset of the conduction bands of $Bi_2Ti_4O_{11}$ and $Bi_4Ti_3O_{12}$. The calculated XES spectra are also quite close to the measured XES spectra, as shown in Figure 6.7, although the calculated XAS seems to overestimate the intensity and energy of the O 2p— Bi 6p hybridization at the bottom of the valence band in $Bi_4Ti_3O_{12}$. The calculated XAS spectra shown here for Bi_2O_3, $Bi_2Ti_4O_{11}$, and $Bi_4Ti_3O_{12}$ were calculated from the ground state conduction band, no core hole perturbation was considered. This is mainly because the bismuth titanates have so many inequivalent sites and such low symmetry crystal structures that calculating the core hole perturbed XAS is probably not worth the effort — even using a large cluster like Westgrid it would take a week or two to obtain the core hole perturbed XAS spectrum from each site; and the ground state unoccupied DOSes already exhibit the same basic features as the measured XAS spectra. The measured XAS spectra of $Bi_2Ti_4O_{11}$ and $Bi_4Ti_3O_{12}$ have two sharp peaks in the near-edge region that are very close in energy to the peaks in the XAS spectrum of TiO_2; it is reasonable to expect — as has been the case for $PbTiO_3$ and Sn_2TiO_4 — that the first of these peaks is due to localized O 2p-states at the low energy side of the Ti 3d t_{2g} band, while the second peak is spread out somewhat due to both localized O 2p-states at the low energy side of the Ti 3e_g band and a core hole perturbed distortion of the ground state Bi 6p — O 2p-states.

One possible problem with this analysis is that the calculated ground state XAS spectrum of Bi_2O_3 bears very little resemblance to the measured XAS spectrum, as shown in Figure 6.7. The measured XAS spectrum of Bi_2O_3 is rather similar to the measured XAS spectrum of PbO, as shown in Figure 6.2, but while both the core hole perturbed and ground state calculated XAS spectrum for PbO has a sharp near-edge peak similar to that in the measured spectrum, there is no such fine structure in the ground state calculated XAS spectrum of Bi_2O_3. This is somewhat unsettling, because the ground state calculated XES spectrum of Bi_2O_3 (see Figure 6.7) is in rather good agreement with the measured spectrum, arguably just as good as the agreement between the calculated and measured XES spectra of PbO (see Figure 6.2).

In fact, including a core hole perturbation does not remedy the situation, as shown in Figure 6.8, and even including the spin-orbit interaction on the valence states of Bi (which

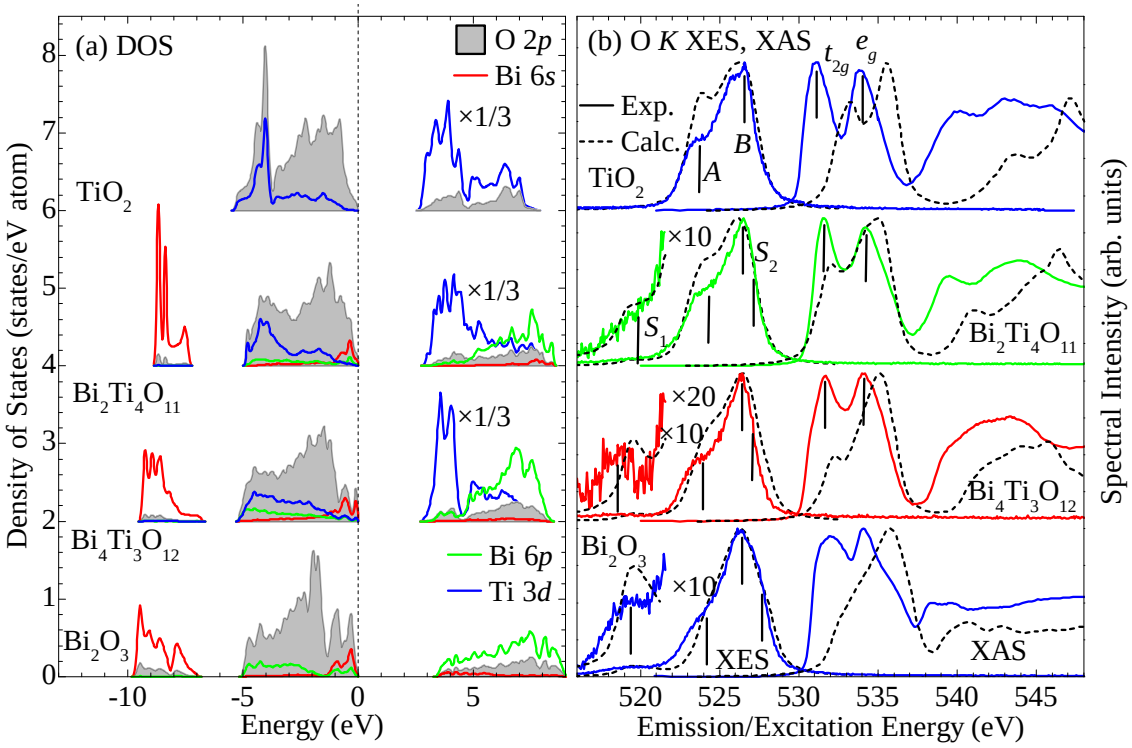

Figure 6.7: Electronic structure of TiO_2, Bi_2O_3, $Bi_2Ti_4O_{11}$ and $Bi_4Ti_3O_{12}$: (a) The calculated DOS. (b) The O K XES (excited near 540 eV) and XAS spectra (TFY mode). This Figure is organized the same as Figure 6.5, and is adapted from data published in Reference [18].

one might expect are necessary, since Bi is a rather heavy element) does not improve the agreement between the calculated and measured spectra. (Although one could argue that the XES spectrum calculated by including the spin-orbit interaction is in slightly better agreement with the measured spectrum — note the more clearly resolved shoulder in the "mBJ+so" calculated XES spectrum in Figure 6.8 — than the spectrum calculated without the spin-orbit interaction.) Unless the crystal structure used in the calculation is completely different from that of the actual sample that was measured — unlikely, in my opinion, given the agreement between the calculated and measured XES — I do not have a good explanation for the discrepancy. The core hole perturbation does not seem to have a very large impact on the band gap of Bi_2O_3; as shown in Figure 6.8 the difference between the ground state and core hole perturbed band gaps is a reduction of only about 0.2 eV in a gap that is originally about 3.4 eV. In fact all calculated gaps, even the gap calculated with the PBE function (which is expected to significantly underestimate the true band gap) are larger than the estimated gap using the peaks in the second derivatives of the XES and XAS spectra. Unless the core hole effect is significantly more influential than calculated; the measured XAS cannot be reconciled with the calculated XAS. The band gap estimated with the second derivatives is also significantly smaller than the optical gap reported in the literature (of 2.91 eV [130]), although that measurement was rather old and the authors also report an indirect band gap of 2.15 eV estimated from temperature dependent conductivity measurements [130], which is very close to the second derivative estimated gap of about 2.2 eV. Ultimately I think it is best to rely on the calculated band gaps, given the consistency between different techniques; it is easier to attribute the low band gap estimates from the XAS and conductivity measurements to some empirical error (or phase impurity, etc.) than to explain why all these calculations significantly *overestimate* the band gap of Bi_2O_3. It should also be mentioned that the electronic structure of Bi_2O_3 has previously been fairly extensively studied by X-ray spectroscopy [114], and these measurements are essentially the same as mine.

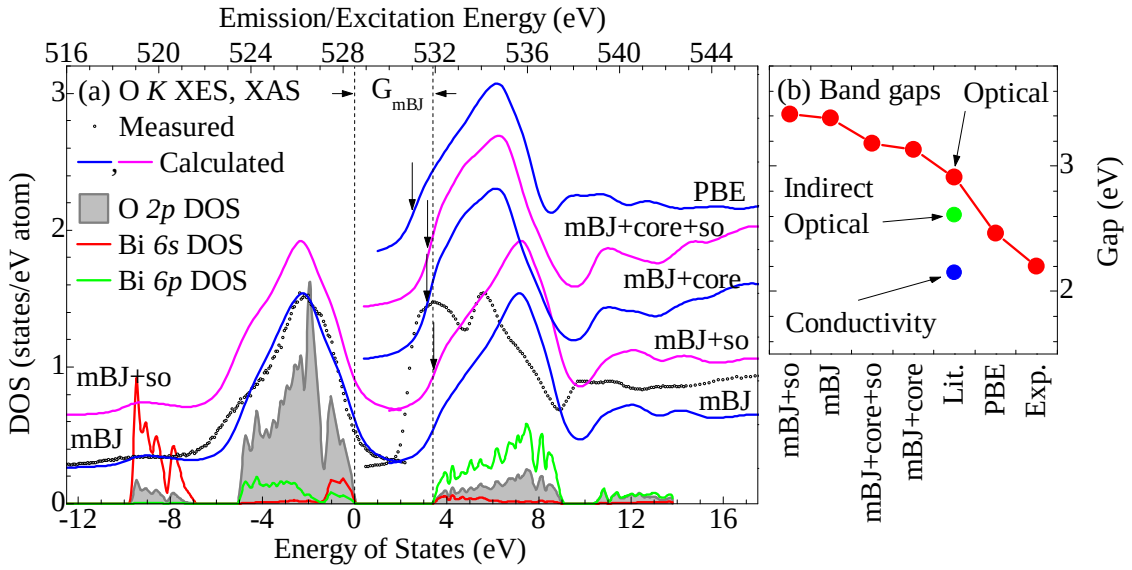

Figure 6.8: Electronic structure of Bi_2O_3: (a) The ground state electronic structure (calculated with the mBJ functional) of Bi_2O_3 and the measured O *K* XES and XAS spectra, compared to the spectra calculated with the PBE or mBJ functional, including spin-orbit interaction within the valence band (so) and a core hole perturbation (core). (b) The band gaps for each calculation, the band gap obtained from the literature [130], and the gap estimated from the peaks in the second derivatives of the XES and XAS spectra.

6.5 Trends in the Band Gaps

All of the ternary oxides studied herein have electronic structures that are very similar to a simple superposition of the electronic structures of their "precursor" binary oxides; the lone pair binary oxide (SnO, PbO, or Bi_2O_3) and TiO_2. Consistent with my starting hypothesis, the spectral features (taken from the experimental XES and XAS spectra, with guidance from the calculated spectra) labelled in Figures 6.2, 6.5, and 6.7 of the ternary oxides are at a logical progression in energy relative to those in the precursor binary oxides, as shown in Figure 6.9. The energy of the bonding lone pair — O $2p$ feature (labelled S_1) in the ternary oxides is very material dependent; there is little consistent trend relative to the energy of the S_1 feature in the corresponding lone pair binary oxide. In contrast, however, the antibonding lone pair — O $2p$ feature (labelled S_2) progresses to lower energies in the ternary oxide compared to the lone pair binary oxide; and this feature gets closer in energy to the main O $2p$ XES feature (labelled B) in TiO_2 as the ternary oxide has a greater proportion of TiO_2 as a fraction of the formula unit. The near-edge XAS spectral feature (labelled t) of the ternary oxides is close to that in the XAS spectrum of TiO_2; certainly in the XAS spectrum of $PbTiO_3$ and Sn_2TiO_4, this feature has practically the same energy as that in the spectrum of TiO_2. While this does not appear to be the case in the bismuth titanates, these systems have far more inequivalent sites (6 for $Bi_2Ti_4O_{11}$ and 12 for $Bi_4Ti_3O_{12}$) with a relatively wide range of binding energies (the WIEN2k ground state calculation suggests the O $1s$ binding energies are spread over a range of 0.4 eV for $Bi_2Ti_4O_{11}$ and 0.7 eV for $Bi_4Ti_3O_{12}$). Even if the core hole perturbation is exactly the same for all of these sites the electronic structure features observed in the XAS should still be spread over the range of binding energies. It is therefore not unexpected that the spectra of the bismuth titanates does not perfectly fall within this type of analysis.

The band gaps of these ternary and binary oxides estimated from the peaks in the second derivatives of the measured O K XES and XAS spectra, calculated with WIEN2k using the mBJ functional, estimated by semi-empirically aligning the calculated and measured spectra and accounting for the core hole shift, and found from the literature (mostly optical, although the aforementioned "indirect optical" and electrical conductivity band gap estimates

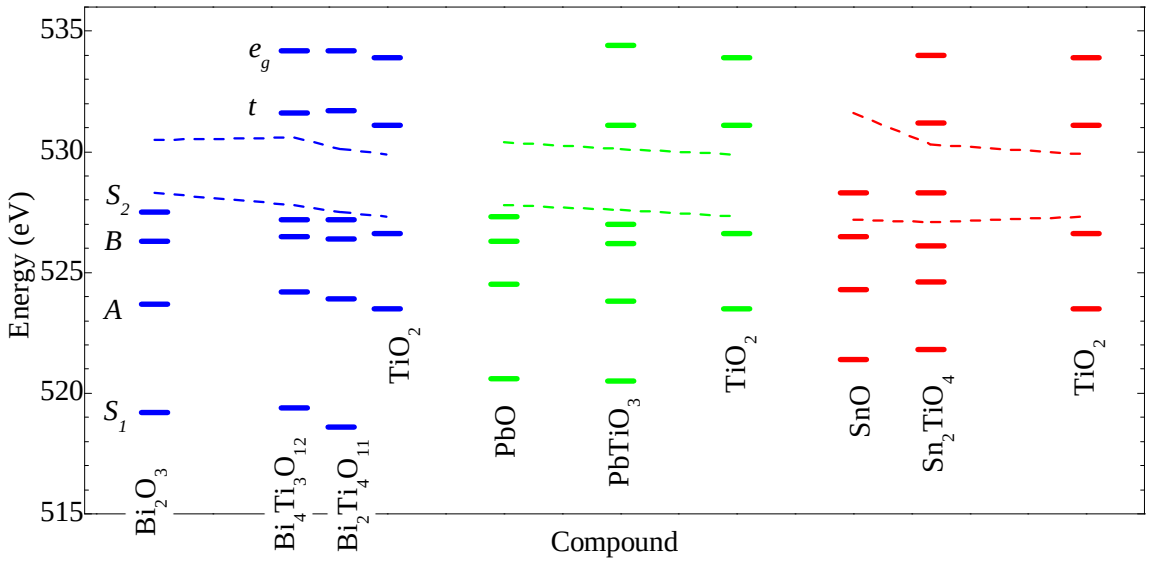

Figure 6.9: The energy of the spectral features labelled in Figures 6.5, 6.2, and 6.7. The horizontal spacing of the ternary oxides relative to the binary oxides is based on the "fraction" of the binary oxides that make up the ternary oxide. The dotted lines indicate the peaks in the second derivative of the O K XES (lower energy line) and XAS (higher energy line). This figure is adapted from data published in Reference [18].

for Bi_2O_3 are also shown) are shown in Figure 6.10. The problem with using the second derivative method to estimate the band gap of SnO was mentioned previously in Section 5.3. It is clear from Figure 6.10(a) that this is also a problem with Sn_2TiO_4 for the very same reason (the antibonding Sn 5s-states at the top of the valence band have a very gradual slope towards the band edge, making it difficult to unambiguously detect the appropriate peak in the second derivative). For the other materials, the second derivative, semi-empirical, and calculated band gaps are all in reasonable agreement; the largest discrepancy is the previously mentioned band gap of Bi_2O_3.

Determining the correct band gaps for these systems is important, because if the formula unit of these ternary oxides is rewritten as a mixture of the precursor binary oxides: (lone pair binary oxide)$_{1-x}$(TiO_2)$_x$ — for example Sn_2TiO_4 would be $(SnO)_{2/3}(TiO_2)_{1/3}$ — then, when the band gaps of these systems are plotted as a function of x (the "TiO_2 fraction"), the band gaps of the ternary oxides fall almost exactly on the straight line connecting the band gap of the lone pair binary oxide with the band gap of TiO_2, as shown in Figure 6.10(b). Therefore,

if these calculated gaps can be trusted, intermediate stoichiometries of these ternary oxides could be designed to obtain a particular band gap.

This approach seems legitimate, because the semi-empirical estimates of the band gaps also are approximately linear in terms of the "TiO_2 fraction", as shown in Figure 6.10(c) (note that since no core hole calculations were performed for the bismuth titanates, the gaps here are rather the second derivative estimates, and consequently have larger estimated errors). Finally, although there is a somewhat large discrepancy between the calculated and semi-empirical band gap of SnO, both are well below 2.2 eV, and therefore I expect a tin titanate could be designed to have the appropriate band gap to act as an efficient solar-powered photocatalyst for hydrogen production in water. (Of course Sn_2TiO_4 may already be the appropriate candidate to fulfil that role.)

6.6 Post Transition Metal — Titanium Ternary Oxides

A second way of possibly engineering the band gap of TiO_2 is to introduce cations with full d^{10} shells. The previous approach, creating ternary oxides composed of lone pair cations and d^0 metals, worked because the former largely defined the edges of the valence band while the latter defined the edge of the conduction band. A similar approach might be expected to work for full d^{10} cations, because the full d^{10} shell forms a separated and largely chemically inert band at the bottom of the valence band (refer back to Section 5.2), and p-d repulsion between the oxygen $2p$ and cation full shell d^{10} states may be expected to drive the valence band of the ternary oxide higher in energy (consequently reducing the band gap) [135].

With this in mind, I have studied the electronic structure of $ZnTiO_3$ [19]. $ZnTiO_3$ is a perovskite ceramic with potential applications in catalysis and nonlinear optics [136], and is just one of many stoichiometries of zinc titanates [137]. There is also $CdTiO_3$ [138] and $HgTiO_3$ [139] — to complete the range of post transition metal oxides — but unfortunately $ZnTiO_3$ was the only sample I had available to me at the time. $ZnTiO_3$ exists in both a cubic perovskite and a rhombohedral ilmenite structure [140, 141], the latter is the most interesting to me because it has the closest structural resemblance to rutile TiO_2, while the Ti^{4+} octahedra in the former have a long range order closer to that in anatase TiO_2 [142].

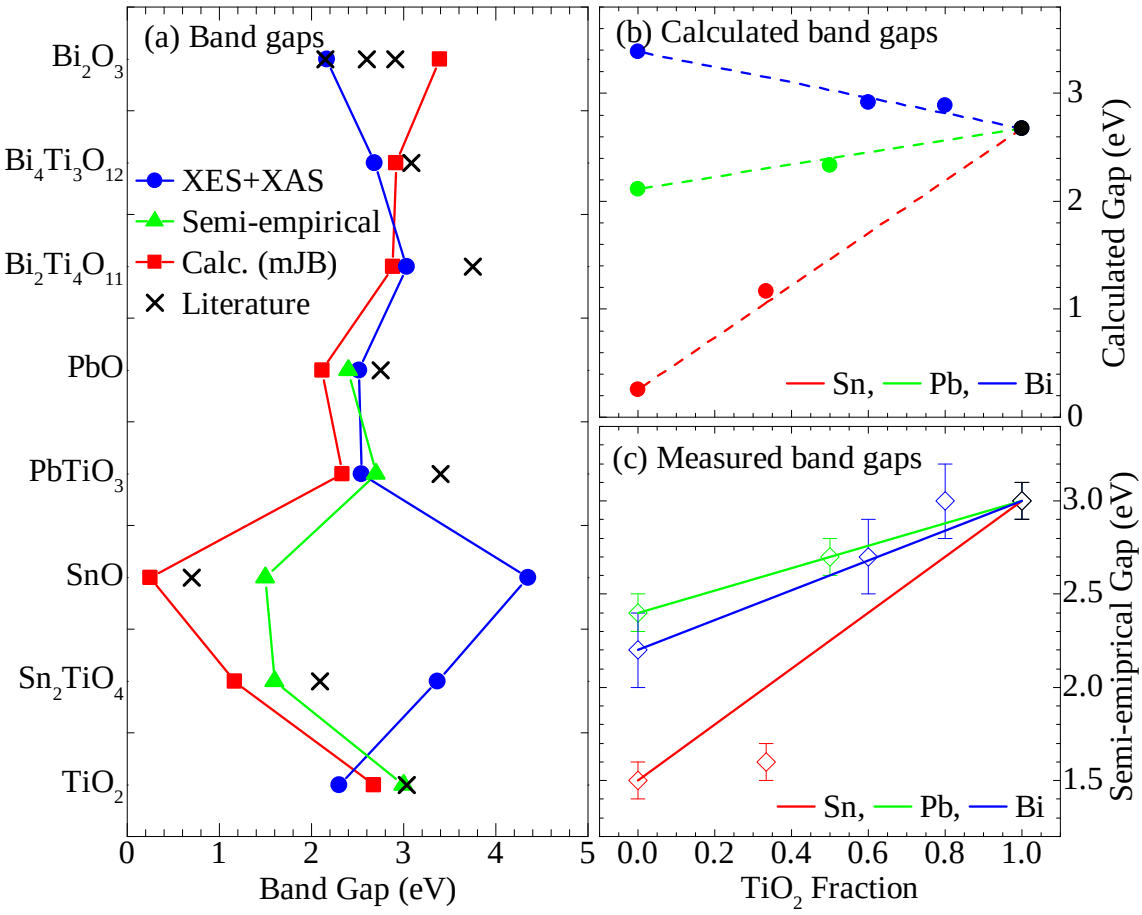

Figure 6.10: The band gaps of the lone pair — Ti $3d^0$ oxides. (a) Direct comparison of the band gaps estimated using the second derivative method, the band gaps estimated using a semi-empirical alignment of measured and calculated spectra, the calculated band gaps, and the measured optical gaps from the literature (see References [104, 122, 124, 130–134]). (b) The calculated band gaps of these materials plotted as a function of TiO_2 content, note how they are almost linear. (c) The band gaps estimated using the semi-empirical alignment method (or the second derivative method for the bismuth titanates) plotted as a function of TiO_2 content, these are almost linear as well. This figure uses some data published in Reference [18].

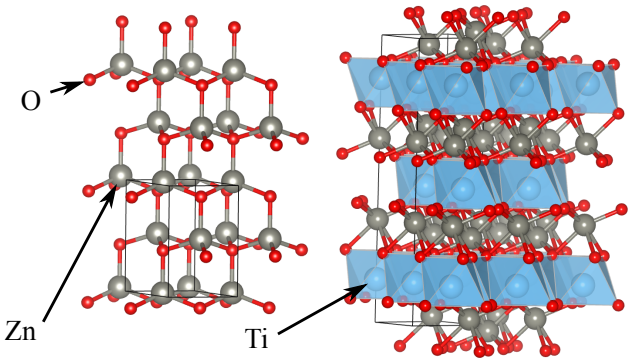

Figure 6.11: Crystal structures of (left to right): wurzite ZnO (from Reference [94]) and ilmenite $ZnTiO_3$ (from Reference [141]). A single unit cell is outlined for each system.

Ilmenite $ZnTiO_3$ was generously provided by Dr. Aleksandra Wypych, Dr. Izabela Bobowska, and Ms. Agnieszka Opasinska (Dept. of Molecular Chemistry, Technical University of Lodz, Lodz, PL), they also verified the crystal structure using XRD [143].

The crystal structure of $ZnTiO_3$ is shown in Figure 6.11, note the planar arrangement of TiO_6 octahedra similar to rutile TiO_2 (see Figure 6.1). The Zn cations are sandwiched between these planes of TiO_6 octahedra; while the Zn sites in $ZnTiO_3$ do have the same three-fold symmetry as those in ZnO, the Zn in $ZnTiO_3$ is coordinated by 6 oxygen atoms instead of the 4 in ZnO. For a lone pair cation the similarity in local structure was crucial to preserving the important bonding/antibonding ns^2 states (indeed, one of the challenges with incorporating Sn^{2+} in ternary oxides lies with ensuring it does not increase its coordination environment and become Sn^{4+} [122]). However, since the important contribution from Zn is the full $3d^{10}$ shell, which is insensitive to the local environment, the increase in Zn coordination should not be a problem.

The presence of Zn raises the same computational problems as with ZnO (refer back to Section 5.2); the Zn $3d^{10}$ shell will not be properly localized at the bottom of the valence band when the electronic structure is calculated with LDA or a GGA functional. Guided by my previous work on ZnO (refer back to Section 5.2), in addition to the basic calculations with the PBE and mBJ exchange correlation functionals, I also performed calculations with the hybrid functional LSDA+αHF (with the same mixing of $\alpha = 0.35\%$ as previously used

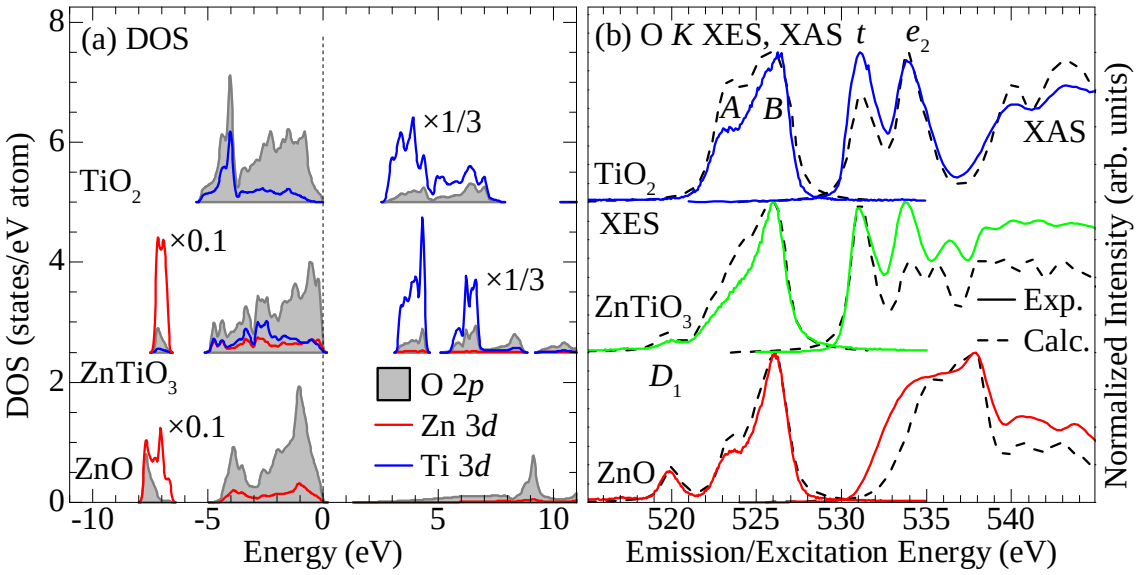

Figure 6.12: Electronic structure of TiO_2, ZnO, and $ZnTiO_3$: (a) The calculated DOS. (b) The O K XES (excited near 540 eV) and XAS spectra (TFY mode). This Figure is organized the same as Figure 6.5, and is adapted from data published in Reference [19].

for ZnO) and both PBE and mBJ with an on-site Hubbard potential of $U = 8$ eV. As with ZnO, the LSDA+αHF, PBE+U, or mBJ+U functionals were necessary to properly localize the Zn $3d^{10}$ states. The electronic structure of TiO_2, $ZnTiO_3$, and ZnO (the latter two both calculated using the PBE+U functional) is shown along with the measured and calculated O K XES and XAS spectra in Figure 6.12. Again the DOS of $ZnTiO_3$ has the same basic features as the DOS of ZnO and TiO_2; both ZnO and $ZnTiO_3$ have a localized Zn $3d^{10}$ shell at the bottom of the valence band with minimal hybridization with O $2p$-states. There is a also secondary feature near the bottom of the valence band (just above the $3d^{10}$ shell) due to bonding between O $2p$ and Zn or Ti $3d$-states, and finally the conduction bands of both TiO_2 and $ZnTiO_3$ are dominated by the same two Ti $3d$ t_{2g} and e_g bands.

The calculated spectra are very close to the measured spectra, as shown in Figure 6.12 (the ZnO powder was the same as that used in Section 5.1, 99.9% purity). Note that the calculated XAS for $ZnTiO_3$ and ZnO were conducted by perturbing the simple PBE functional with a core hole; because the conduction bands calculated for these materials are almost exactly the same no matter which functional was used, I stuck with the most computationally simple

functional for the more intensive super-cell core hole calculations.

However despite these similarities in the DOS, the idea of using these materials for band gap engineering almost totally breaks down: the semi-empirical band gap of TiO_2 is 3.0±0.1 eV (refer back to Figure 6.10), the semi-empirical gap of ZnO is 3.5±0.1 eV (refer back to Figure 5.9), while the semi-empirical band gap for $ZnTiO_3$ is 3.8±0.1 eV; larger than both of the band gaps of the precursor oxides. These band gap estimates seem to be quite accurate; as previously mentioned the band gap of TiO_2 has been reported to be 3.03 eV [104], the band gap of ZnO has been reported to be 3.4 eV [107], while the band gap of $ZnTiO_3$ has been reported to be 3.75 eV [144].

Interestingly (or maddeningly, depending on your perspective), the band gaps estimated from the peaks in the second derivatives of the O K XES and XAS spectra suggest that the band gap engineering scheme works: the second derivative band gap estimates are 2.6±0.2 eV for TiO_2 (refer back to Figure 6.10), 3.4±0.2 eV for ZnO (refer back to Figure 5.9), and 3.0±0.2 eV for $ZnTiO_3$ [19]. This naively suggests that the band gap of $ZnTiO_3$ is halfway between the band gaps of ZnO and TiO_2, as suggested by my band gap engineering scheme for lone pair ternary oxides. However this occurs because there is a rather large core hole shift in $ZnTiO_3$ (of about 0.8 eV), a core hole shift of about 0.4 eV in TiO_2, and a negligible core hole shift in ZnO (< 0.1 eV) [19]. The influence of $3d^{10}$ and $3d^0$ cations on the electronic structure in a ternary oxide is therefore more complicated than the influence of ns^2 and $3d^0$ cations. This does not preclude the possibility that $CdTiO_3$ or $HgTiO_3$ might have band gaps lower than TiO_2 (since the gaps of CdO and HgO are smaller than those of TiO_2, refer back to Figure 5.9), just that it might be unwise to assume this to be the case [19]. The toxicity of Cd and Hg would probably preclude their widespread use as photocatalysts.

Thus far my actual research results have focussed exclusively on oxygen K XES and XAS spectra. Although many of the heavy cations in the binary and ternary oxides lack interesting core levels in the soft X-ray range (i.e. those with the appropriate angular momentum to select the interesting valence or conduction states, as governed by the dipole selection rules, and those with a sufficiently large X-ray cross-section to permit acquisition of a good spectrum), certainly the Ti $L_{2,3}$ level is both within the soft X-ray range and appropriate for measuring the Ti $3d$-states, and it is fair to ask why these spectra have not been considered in my

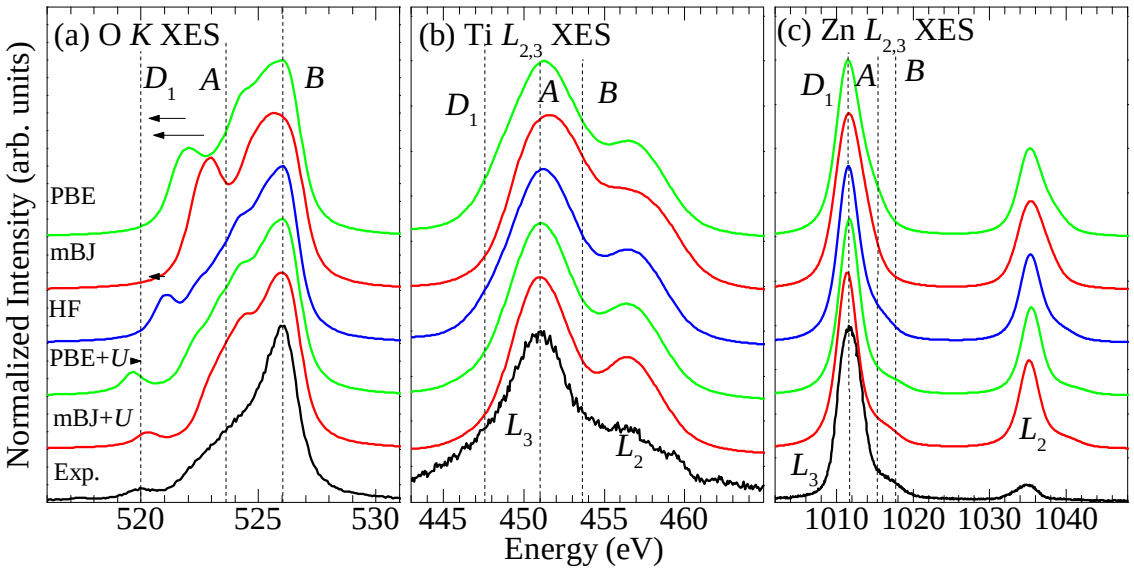

Figure 6.13: XES spectra of $ZnTiO_3$: (a) O K, (b) Ti $L_{2,3}$, and (c) Zn $L_{2,3}$. Both measured spectra and spectra calculated using a variety of exchange correlation functionals are shown. The on-site Hubbard potential $U = 8$ eV for Zn $3d$-states, and the hybrid functional (HF) was the LSDA+αHF function with a mixing of $\alpha = 35\%$, again only for Zn $3d$-states.

analysis.

$ZnTiO_3$ is perhaps the most ideal ternary oxide discussed herein to study with X-ray spectroscopy because all of the interesting valence and conduction band states, namely the O $2p$, Ti $3d$, and Zn $3d$-states can be studied by soft X-ray spectroscopy. The XES spectra of $ZnTiO_3$ for these edges is shown in Figure 6.13 along with the XES spectra calculated using the various exchange-correlation functionals. The spectral features labelled in Figure 6.12 have been reproduced in Figure 6.13 as well. This figure shows the utility of the O K XES spectrum over the Ti $L_{2,3}$ XES and Zn $L_{2,3}$ XES spectra; the top of the valence band in the former is obscured by the overlapping L_2 band (and the L_2 band is of weaker intensity making the top of this band difficult to unambiguously determine), while the lifetime broadening of the relatively intense $3d^{10}$ shell obscures any other hybridizations in the latter. It is therefore difficult to determine which calculation provides the best electronic structure; it is quite clear from the O K XES that only the electronic structure calculated with PBE+U or mBJ+U functionals provides the proper localization of the Zn $3d^{10}$ shell (feature D_1 in Figure 6.13),

because the O K XES only probes the relatively weak O $2p$ *hybridization* with the Zn $3d^{10}$ shell, these states do not overwhelm the spectra as they do in the Zn $L_{2,3}$ XES.

6.7 Concluding Remarks

From my study of several ternary oxides ($PbTiO_3$, Sn_2TiO_4, $Bi_2Ti_4O_{11}$, and $Bi_4Ti_3O_{12}$), it seems that the band gaps of ternary oxides that involve lone pair cations (Sn^{2+}, Pb^{2+}, Sb^{3+}, Bi^{3+}, Te^{4+}, etc.) and d^0 metals (Ti^{4+}, Zr^{4+}, Mo^{6+}, etc.) can be predicted by a simple weighted average of the band gaps of the binary lone pair and metal oxides precursors, when the ternary oxide formula unit is expressed as a fraction of these two oxides. For example, $PbTiO_3$ can be rewritten as $(PbO)_{1/2}(TiO_2)_{1/2}$ so the predicted band gap for $PbTiO_3$ is $E_G^{PbTiO_3} = \frac{1}{2}E_G^{PbO} + \frac{1}{2}E_G^{TiO_2}$. This occurs because the lone pair cation has a strong influence on the valence band, forming bonding and antibonding cation ns^2 — O $2p$ hybridizations at the bottom and top of the valence bands, respectively, while having only a rather weak influence on the edge of the conduction band, while the d^0 metal has a very weak influence on the valence band but dominates the bottom of the conduction band with unoccupied d-states. The DOS of the ternary oxide is therefore very close to a simple weighted sum of the DOSes for each precursor binary oxide; the gap is linear in the relative "concentrations" of the precursor oxides because one influences the valence band while the other influences the conduction band, both somewhat independently.

On the other hand, the band gaps of ternary oxides involving full d^{10} shell metals (Zn, Cd, Hg) and d^0 metals cannot be predicted in such a simple manner, even though the d^{10} metal does dominate the valence band and contributes very little to the conduction band.

Chapter 7

Electronic Structure of Layered Pnictides

Layered pnictides are materials whose structure is composed of planar arrangements of transition metals (Cr, Mn, Fe, Co, Ni, Cu, Zn) and pnictides (P, As, Sb), with charge-balancing cations (Li, Na, K, Ca, Sr, Ba, etc.) or rare-earth/oxygen pairs (LaO, EuO, GdO, SmO, etc.). The crystal structures of these materials were studied decades ago [2, 145], but over the last 6 years there has been an immense surge of interest in these materials.

Driven by the success of high-T_c cuprate superconductors, in which the phenomenon of superconductivity seemed to be linked to copper-oxide planes, Prof. Hosono's research group (Tokyo Institute of Technology, Yokohama, Japan) began searching for superconductivity in other layered materials, and in 2006 they discovered superconductivity at $T_c = 3.2$ K in LaOFeP [146]. Because of the rather low transition temperature this discovery alone did not gain much attention, although it was pointed out that despite the layered structure, the Fe^{2+} in LaOFeP was tetrahedrally coordinated, suggesting the Fe $3d_{xy}$,$3d_{xz}$,$3d_{yz}$ orbitals formed the Fermi level, rather than the Cu $3d_{x^2-y^2}$ orbitals in the square-planar coordinated Cu^{2+} in cuprate superconductors [146]. Just over a year later, however, the same group discovered superconductivity at $T_c = 26$ K in $La(O_{1-x}F_x)FeAs$ [147], and interest in the field sky-rocketed.

One of the early questions in iron pnictide research was whether the Fe $3d$-states were correlated in the same manner as the Cu $3d$ in the cuprates [148], i.e. a large on-site Coulomb interaction manifesting as a Hubbard-like potential U [51]. Driven initially by theoretical studies, this question naturally prompted many contradictory answers: there were claims that the on-site Coulomb correlation effects were large [149], moderate [150, 151], and weak [152]. Because X-ray spectroscopy provides a direct probe of the Fe $3d$-states, my research provided an experimental probe of the correlation strength in these pnictides.

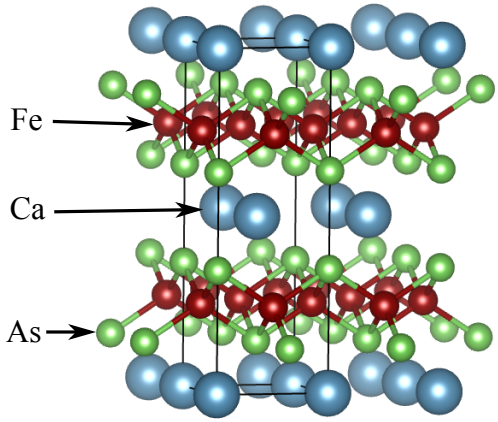

Figure 7.1: The crystal structure of $CaFe_2As_2$. A single unit cell is outlined in black, the crystal structure used is from Reference [154].

This chapter details my research on iron, manganese, and copper pnictides. These findings are also reported in my published work on the subject, see References [10, 20–23, 153].

7.1 Electronic Structure of $CaFe_2As_2$

The layered iron pnictide $CaFe_2As_2$ was one of the first pnictides I studied. Like many iron pnictides, $CaFe_2As_2$ undergoes a phase transition from a tetragonal to an orthorhombic phase at 170 K [154], if this phase is suppressed via doping or hydrostatic pressure (2 – 10 kbar) superconductivity with T_c between 10 and 20 K can be realized [155]. $CaFe_2As_2$ is a typical iron arsenide superconductor, and is an interesting material to study with X-ray spectroscopy because both the Fe $3d$-states and the Ca $3d$-states can be probed with soft X-ray spectroscopy. Examining the Ca $3d$-states might give insight into whether the Ca is simpy acting as a charge balancing cation, or whether it has an influence on the Fermi level. The behaviour of Ca in $CaFe_2As_2$ is likely similar to that of Sr in $SrFe_2As_2$ and Ba in $BaFe_2As_2$, but the latter two elements are not conducive to measuring the $4d$- or $5d$-states with soft X-ray spectroscopy.

At room temperature, $CaFe_2As_2$ has a tetragonal crystal structure with the $I4/mmm$ symmetry group, as shown in Figure 7.1. $CaFe_2As_2$ has a first-order phase transition to an orthorhombic $Fmmm$ structure below 170 K, similar phase transitions (at various tempera-

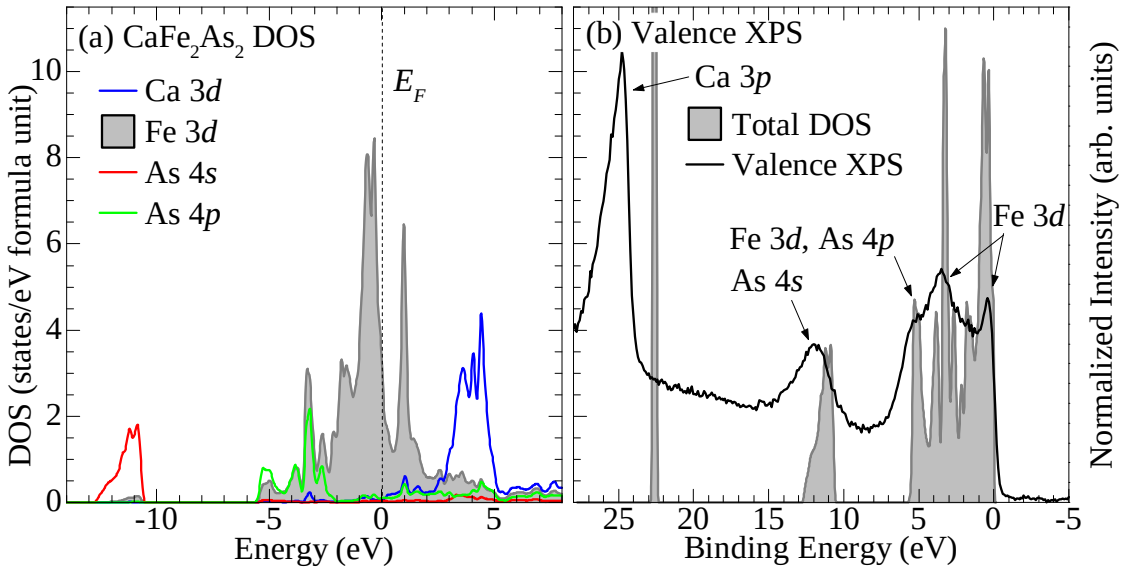

Figure 7.2: The DOS of $CaFe_2As_2$: (a) The partial DOSes which contribute significantly to the valence and conduction bands; the Ca and Fe $3d$-states and the As $4s$,$4p$-states. All other symmetries contribute only a few percent or less to the total intensity. (b) The total DOS compared to the measured XPS spectrum, this allows the states responsible for the peaks in the XPS spectrum to be identified. This figure is adapted from data published in Reference [21].

tures) occur in $BaFe_2As_2$ and $SrFe_2As_2$ [154]; but I did not investigate this phase. Although it is possible to perform X-ray spectroscopy measurements below 170 K, the bulk electronic structure is not significantly affected by these sort of minor phase transitions [156], and certainly not within the resolution of X-ray spectroscopy measurements.

The calculated electronic structure of $CaFe_2As_2$ is shown in Figure 7.2(a). Like almost all iron pnictides, $CaFe_2As_2$ is a "bad metal" with no separation between the valence and conduction bands. The electronic structure is also typical of most iron arsenides; the Fe $3d$-states provide the dominant contribution to the valence band and lower conduction band, the As $4s$-states are localized some 12 eV below the Fermi energy (E_F) and are only weakly hybridized with other states, and the As $4p$ — Fe $3d$ bonding states are between -2 and -5 eV relative to E_F. Finally, the Ca $3d$-states only become significant rather deep into the conduction band, some 3 eV above E_F [21].

The synthesis laboratory of Prof. Paul Canfield (Ames Laboratory, Ames, IA) was able to

make excellent quality single crystals of $CaFe_2As_2$. These crystals were grown with the "self flux" technique, and the structure was verified with XRD by members of Prof. Canfield's research group (see References [154, 157] for more details on purity and structure characterization). Because of the crystal quality, these samples could therefore be cleaved in vacuum and high quality XPS measurements could be obtained. As shown in Figure 7.2(b), the XPS measurements (courtesy of Dr. Anna Buling, University of Osnabrück, Osnabrück, Germany) are in quite good agreement with the calculated DOS, although the calculated DOS does underestimate the binding energy of the Ca $3p$ shell by 2 eV or so, and seems to underestimate the binding energy of the As $4s$-states by perhaps as much as 1 eV.

It should be stressed that the calculated DOS was performed using the simple PBE GGA functional; I did not add any additional on-site potential (through a Hubbard U) to the Fe sites, or attempt to treat the Fe $3d$-states with any hybrid functionals (i.e. with the LSDA+HF+α functional, or something similar). The DOS calculated from the generic DFT method seems quite adequate to explain the observed spectra.

As mentioned above, the Ca and Fe $3d$-states can be probed with Ca and Fe $L_{2,3}$ XES, respectively. However there are very few occupied Ca $3d$-states (as seen in the calculated DOS in Figure 7.2(a)) and the inherent life-time broadening in a (non-resonant) XES spectrum increases with energy, so the relatively high energy Fe $2L_{2,3}$ spectra may be too broad to identify features in the DOS. While for the binary and ternary oxides discussed in Chapters 5 and 6 I was content to calculate the XES and (core-hole perturbed) XAS spectra to directly compare to the measured spectra, for $CaFe_2As_2$ I tried to curve-fit the measured XES spectra to identify the underlying DOS features, and largely ignored the XAS spectra. At the time, my reasoning was as follows:

1. The valence band of $CaFe_2As_2$ is only about 5 eV wide, and the lifetime broadening at the Fe L_3 XES spectrum is at least 0.5 eV [158], and the instrumental broadening is about 0.7 eV; therefore due to these relatively large broadening factors the natural width of the spectrum will be considerably greater than the actual valence band width, and a wide range of possible DOSes could be broadened to resemble the measured spectrum.

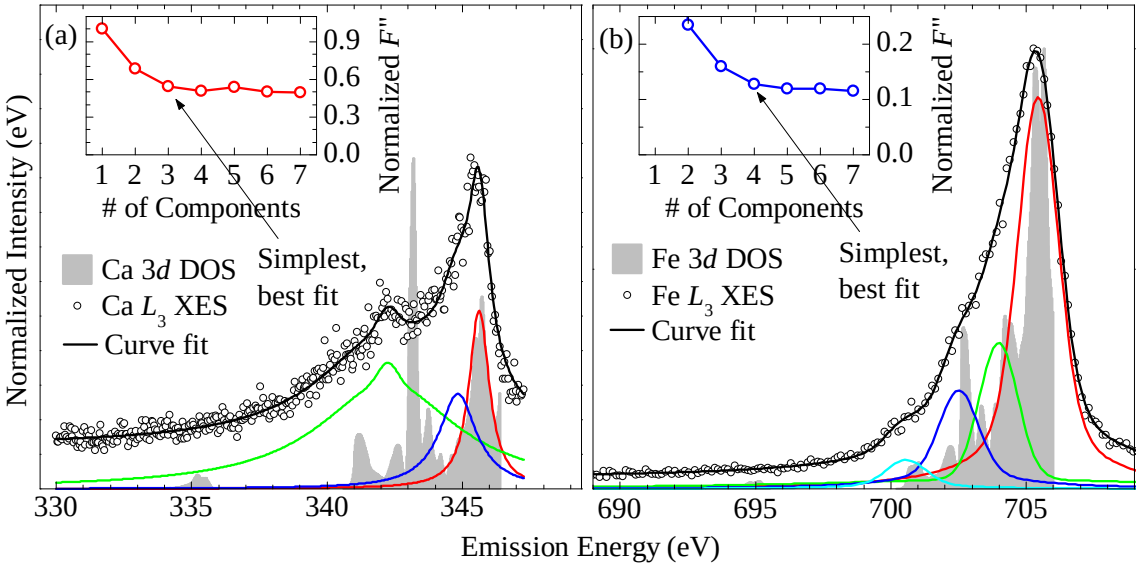

Figure 7.3: The XES spectra of $CaFe_2As_2$: (a) The Ca L_3 spectrum (excited at 360 eV), compared to the Ca $3d$ DOS. (b) The Fe L_3 spectrum (excited at 730 eV), compared to the Fe $3d$ DOS. In each plot the spectrum has been curve fit with pseudo-Voigt components; the insets show the how the "goodness of fit" depends on the number of pseudo-Voigt components. This figure is adapted from data published in Reference [21].

2. The perturbation by the Fe $2p$ core hole is significant [62]; the core hole perturbed calculation may be too distorted from the ground state conduction band to be of much use.

With this in mind I attempt to "deconvolute" the Ca and Fe L_3 XES spectra by fitting them with several pseudo-Voigts. The pseudo-Voigts were just a superposition of a Gaussian and a Lorentzian profile:

$$f_V = A\left(\eta f_G + (1-\eta)\, f_L\right) \tag{7.1}$$

$$f_G = \frac{1}{\sqrt{2\pi}\sigma}\exp\left(-\frac{(x-\mu)^2}{2\sigma^2}\right) \tag{7.2}$$

$$f_L = \frac{1}{\pi}\left(\frac{\frac{\Gamma}{2}}{(x-\mu)^2+\left(\frac{\Gamma}{2}\right)^2}\right), \tag{7.3}$$

where A was the amplitude of the pseudo-Voigt peak, η was the mixing fraction of Gaussian and Lorentzian components, μ was the centre point of the pseudo-Voigt peak, and σ and

Γ were the Gaussian profile standard deviation and the Lorentz profile half-width at half-maximum, respectively. The Gaussian standard deviation σ was set so the full-width at half-maximum of the Gaussian component matched the experimental broadening (which was not material specific), but all other parameters were varied in a non-linear least-squares fitting routine.

The relevant question now is: how many pseudo-Voigt components are appropriate? Clearly one can obtain perfect agreement by fitting one pseudo-Voigt per data point in the measured spectrum, but that fit is meaningless. To try to eliminate as much bias as possible, I performed several pseudo-Voigt fits of the Ca and Fe L_3 XES spectra with between 1 and 7 components (for multicomponent fits the variables A, η, σ, Γ, and μ were independent for each component). The quality of the fit was estimated by the quantity:

$$F'' = \sqrt{\sum_i \left(f_{exp.}(E_i) - f_{fit}(E_i)\right)^2} \tag{7.4}$$

For each spectrum a plateau was reached in the quality of fit parameter F'' with increasing number of components; in the case of the Ca L_3 XES spectrum 3 pseudo-Voigt components provided a significantly better fit than 2 components, but increasing to 4 or higher did not improve F'', while for the Fe L_3 XES spectrum 4 pseudo-Voigt coponents were necessary to reach the plateau in quality of fit. These fits — the "simplest, best fits" — and the raw spectrum are shown in Figure 7.3.

Apart from the two obvious features in the Ca L_3 XES spectrum in Figure 7.3(a), the experimental data is too noisy (again this is due to the fact that Ca has almost no occupied $3d$-states) to determine whether the third peak is meaningful (i.e. is it identifying a DOS feature that is not present in the calculated DOS, or is it just a consequence of the asymmetry of the main peak at 345.5 eV?), but the four pseudo-Voigt components in the Fe L_3 XES spectrum all line up within 0.5 eV of a local peak in the Fe $3d$ DOS. This process is therefore somewhat useful in analysing XES spectra [10, 20, 21].

In view of my later research, I should point out that I later found that my second argument listed above was wrong; because the iron pnictides are metallic the core hole perturbation cannot shift the edge of the conduction band to lower energies (there is no band gap to reduce, all states below the conduction band edge are already full), and apart from an increase in

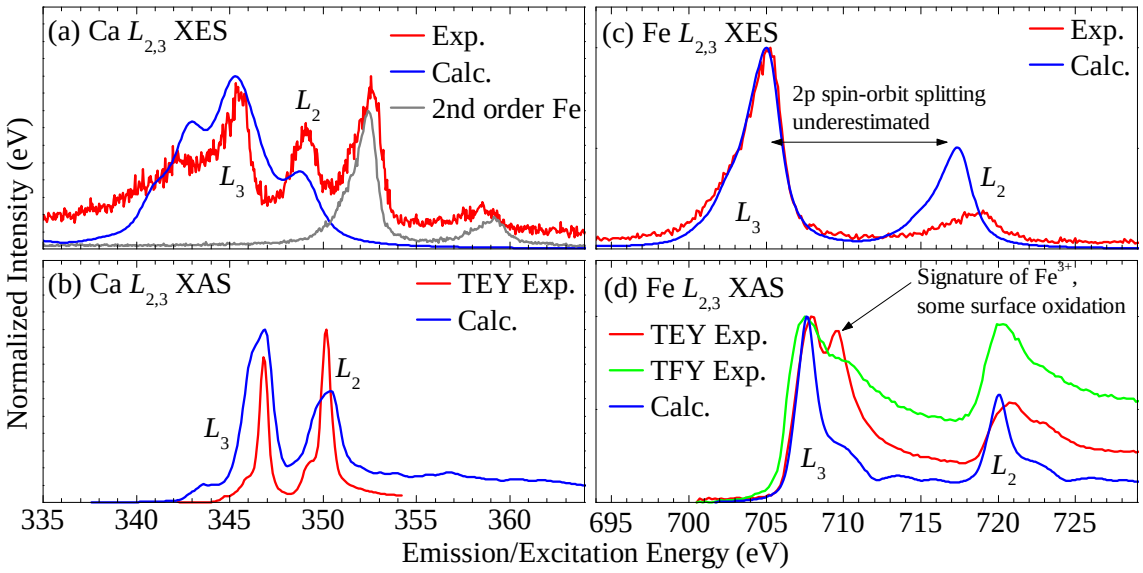

Figure 7.4: The calculated and measured spectra of $CaFe_2As_2$: (a) The Ca $L_{2,3}$ XES spectra (note the presence of a second-order Fe $L_{2,3}$ spectrum), (b) the Ca $L_{2,3}$ XAS spectra, (c) the Fe $L_{2,3}$ XAS spectra, and (d) the Fe $L_{2,3}$ XAS spectra.

the intensity of the near edge features the XAS calculated from the ground state electronic structure is often sufficient to explain the measured spectra. However my early work on iron pnictides was hampered by a second problem: the surfaces were often oxidized so TEY mode Fe $L_{2,3}$ XAS was not useful (rather, those measurements all showed a mixed-valent Fe-oxide) and the TFY mode Fe $L_{2,3}$ XAS suffered from considerable self-absorption.

Therefore, despite my original arguments, using the ground state electronic structure to calculate the XES and XAS spectra is still useful. The Ca $L_{2,3}$ XES and XAS are not very useful probes of the electronic structure of $CaFe_2As_2$, as mentioned above. The calculated and measured Ca $L_{2,3}$ XES and XAS spectra are shown in Figure 7.4(a) and (b), respectively. Note how the calculated spectrum has the same features as the measured Ca $L_{2,3}$ XES and XAS spectra, although the relative widths and intensities are not completely correct. I should point out that DFT is not expected to reproduce the correct relative intensities of the L_2 and L_3 bands. The calculated Fe $L_{2,3}$ XES and XAS spectra are in much better agreement with the measured spectra, as shown in Figure 7.4(c) and (d), respectively. In fact, the calculated XES spectrum is almost exactly the same as the measured XES, while the relative L_2 and

L_3 intensities are incorrect and the $2p$ spin-orbit splitting is somewhat underestimated, these inaccuracies are somewhat expected with DFT. The Fe $L_{2,3}$ XAS spectrum calculated from the ground state electronic structure *could* be in excellent agreement with the true XAS spectrum, but since the measured TEY XAS spectrum shows signs of surface oxidation (as noted in Figure 7.4(d)) and the intensity of the Fe L_3 band is suppressed in the TFY XAS spectrum due to self-absorption, it is difficult to directly compare the calculated and measured spectra.

Ultimately I think that both curve-fitting — especially in a manner where the number of components is selected based on some quantitative gauge of fit quality, rather than at the whim of the person conducting the fitting — and calculating the XES and XAS from the electronic structure are suitable approaches to analyzing the measured XES and XAS spectra of iron pnictides.

7.2 Transition Metal Substitution in $BaFe_2As_2$

As might be expected, the layered pnictide $BaFe_2As_2$ (also referred to as Ba122) has quite similar properties to $CaFe_2As_2$. It has basically the same crystal structure (see Figure 7.1), again undergoes a phase change to an orthorhombic form at moderately low temperature (around 140 K [159]), and likewise requires doping or hydrostatic pressure to suppress the phase transition and exhibit superconductivity [159, 160].

Something interesting occurs when Ba122 is doped with transition metals, however. While substituting Fe with a modest fraction of Co, Ni, or Cu (in the range of 5-10% substitution) can suppress the phase transition, superconductivity is only realized after substitution with Co and Ni, and not after substitution with Cu [159]. Early studies presented a rather confusing picture: $BaFe_2As_2$ doped with Co (Ba122:Co) seems to follow the predictions of a simple rigid band model (where the Co is assumed to simply contribute electrons to the Fermi level) [161, 162], Ba122:Ni does not [159]. Later DFT studies suggested that *all* the substituted transition metals were isovalent with Fe [163], in other words neither Co, Ni, nor Cu substitutions should contribute additional states to the Fermi level. This picture is supported by Mössbauer measurements that suggest no change in the localized $3d$ shell [164],

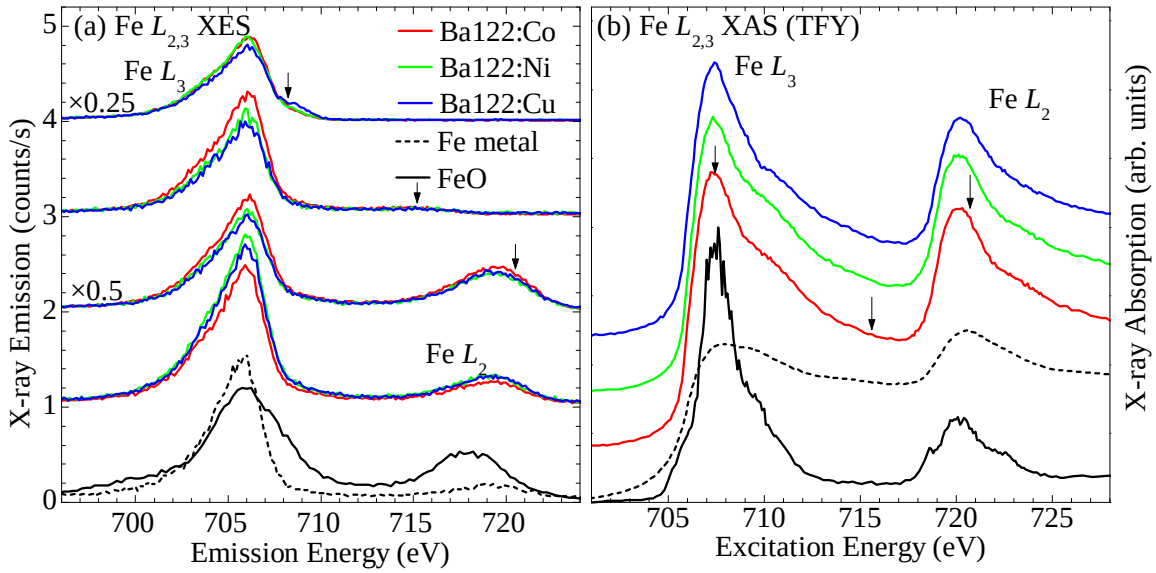

Figure 7.5: The measured Fe $L_{2,3}$ spectra of doped Ba122: (a) The Fe $L_{2,3}$ XES spectra (the arrows denote the excitation energy for the resonantly excited spectra, the non-resonant spectra were excited at 745 eV), (b) the Fe $L_{2,3}$ XAS spectra (TFY mode, except for FeO which was IPFY mode). For both (a) and (b) reference spectra of Fe metal and FeO are provided. This figure is adapted from one published in Reference [22].

but contradicts Hall effect measurements suggesting an increase in the free carriers near the Fermi level [165–167].

Naturally I think the prescription for this conundrum is studying these materials with soft X-ray spectroscopy. Glib remarks aside, there is a good reason for this: $L_{2,3}$ XAS is eminently suited to determining the $3d$-shell occupancy of transition metals [168]. Before proceeding with my findings, I should note that it has been pointed out that "doping" is probably the wrong word to describe these systems; "doping" is usually used in semiconductor physics to identify additives that increase or decrease the number of carriers and therefore "substitution" may be a better word [163]. However for the purposes of this discussion I will use the term "doping" to be equivalent in meaning to the word "substitution", mostly because that is the terminology I used in my paper on the subject (see Reference [22]).

The Fe $L_{2,3}$ XES spectra of Ba122:M (M = Co, Ni, Cu) are shown in Figure 7.5. As one would expect there is practically no difference between the spectra of Ba122 doped with different transition metals, while there are some small differences in absolute intensity these

are more likely due to slightly different surface conditions. The Fe $L_{2,3}$ XES of Ba122:M is almost the same as that of $CaFe_2As_2$ (refer back to Figure 7.4), and also quite close to that of Fe metal. In fact, resonantly excited XES spectra show no evidence of multiplet structure or other energy-loss features commonly associated with correlated materials [168]. The lack of inelastic scatter features in the resonant XES spectra is perhaps even better evidence than the agreement between the non-resonant XES spectra and the electronic structure calculated with a GGA functional [169], and even in the non-resonant regime note that the Fe $L_{2,3}$ XES of FeO (a typical strongly correlated oxide [170]) is broader and has more structure than that of the spectra of Fe metal or the iron pnictides. All together this presents rather good evidence that iron pnictides are not strongly correlated materials [20–22, 169].

These Ba122:M samples were excellent quality single crystals (provided by Prof. Paul Canfield, Ames Laboratory, Ames, IA; again the crystal structure of these samples was measured using XRD by members of Prof. Canfield's research group [171]) and for this system I had learned from my mistakes with $CaFe_2As_2$ and I cleaved these samples under N_2 directly before inserting them into the vacuum chamber on the SGM beamline. Because of this I managed to acquire Fe $L_{2,3}$ XAS spectra without any significant oxygen contamination, as shown in Figure 7.5(b), despite the samples being rather old (about a year and a half) at the time of measuring. (The best Fe $L_{2,3}$ XAS of Ba122 is probably that in Reference [169], but my measurements are in good agreement with the one published therein; note the lack of the Fe^{3+} feature indicative of oxidation that is present in Figure 7.4(d).) Like the XES spectra, the XAS spectra of Ba122:M are rather featureless and similar to the XAS spectrum of Fe metal, and is quite different from the sharp multiplet features present in the XAS spectrum of FeO. Note that the TFY spectrum of Fe metal is shown here because my Fe foil had significant surface oxidation, and this spectrum suffers from significant self-absorption. A much better Fe measurement in TEY mode can be found in Reference [169] (Fe foil from Alfa Aesar, 99.99% purity). The FeO XAS spectrum is courtesy of Robert Green, on FeO powder (from Alfa Aesar, 99.5% purity).

The main advantage of studying these systems with X-ray spectroscopy is of course that one can probe the electronic structure local to a particular species of atom. In this case, the most interesting (and important) spectroscopic findings ought to lie with the doped sites,

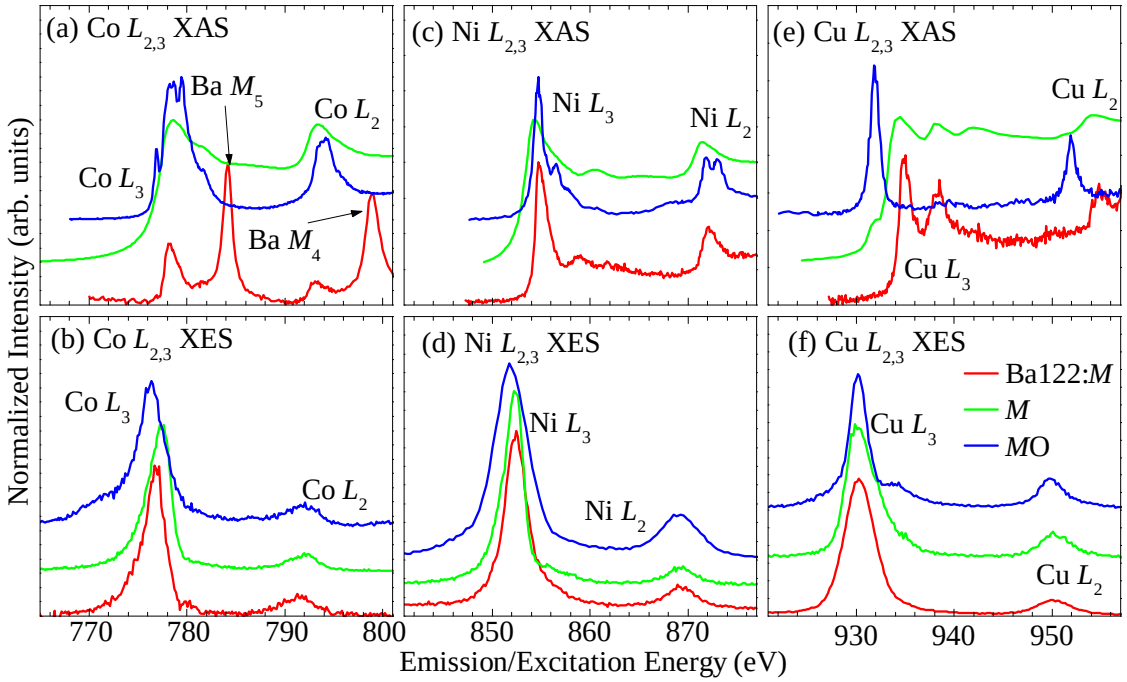

Figure 7.6: The measured $L_{2,3}$ spectra of the doped metals in Ba122: (a) the Co $L_{2,3}$ XAS spectra, (b) The Co $L_{2,3}$ XES spectra (excited at 800 eV), (c) the Ni $L_{2,3}$ XAS spectra, (d) The Ni $L_{2,3}$ XES spectra (excited at 890 eV), (e) the Cu $L_{2,3}$ XAS spectra, and (f) The Cu $L_{2,3}$ XES spectra (excited at 960 eV). For each case a reference spectrum from the appropriate metal (M) and metal monoxide (MO) are provided. All XAS spectra were acquired in TFY mode, except for the metal monoxide spectra (which were acquired in TEY mode). This figure is adapted from one published in Reference [22].

since these are the ones that define whether the system is superconducting (Ba122:Co, Ni) or not (Ba122:Cu). The $L_{2,3}$ XES and XAS for the doped sites is shown in Figure 7.6, along with the spectrum from the appropriate metal and metal monoxide. All of the doped XAS spectra were measured in bulk sensitive TFY mode; because the concentration of dopants was rather low self-absorption in these spectra was minimal. In fact, self-absorption in the TFY mode spectra is actually advantageous for the spectrum from Ba122:Co; because the Ba $M_{4,5}$ absorption edges unfortunately almost coincide with the Co $L_{2,3}$ absorption edges, by taking the spectrum in TFY mode the Ba $M_{4,5}$ fluorescence will be suppressed by self-absorption allowing the Co $L_{2,3}$ XAS to be more visible (see Figure 7.6(a)). Since the Ba site has negligible occupied $5p$ or $4f$-states, there is negligible Ba $M_{4,5}$ emission (see Figure 7.6(b)).

For all of the doped metals it is clear that the spectra from Ba122:M are much closer to those of the appropriate pure metal (all metal foils from Alfa Aesar, 99.99% purity) than the strongly correlated metal monoxide (all powders from Alfa Aesar, 99.5% purity), this shows that the doped transition metals do not act as localized impurities (in the Anderson impurity model sense) that create an on-site Coulomb potential or Hubbard U. However the doped transition metals affect the electronic structure of Ba122, it seems they do so more as making the doped material effectively an alloy of FeAs-MAs, rather than providing a local perturbing potential.

Secondly, the usefulness of X-ray spectroscopy in probing these doped sites is immediately clear in the case of the Cu $L_{2,3}$ XAS spectra of Ba122:Cu, shown in Figure 7.6(e): because $L_{2,3}$ XAS probes transitions between the $2p$- and unoccupied $3d$,$4s$-states, there is a huge difference between the spectrum of Cu metal and CuO. The latter has a $3d^9$ valence state, and this single unoccupied $3d$ state creates a massive resonance peak in the $L_{2,3}$ XAS spectrum. On the other hand the former has a $3d^{10}4s^1$ valence state, and with a full $3d$ shell there are no unoccupied $3d$-states for the XAS transition to probe; only the relatively distributed $4s$-states contribute to the XAS spectrum and consequently the XAS of Cu metal lacks the sharp features found in the $L_{2,3}$ XAS spectra of most other transition metals (the ones that do have empty $3d$-states). Comparing the XAS spectrum of Ba122:Cu to that of Cu metal and CuO, it is clear that the Cu dopants in Ba122:Cu *can not* have a 2+ valency, at best it

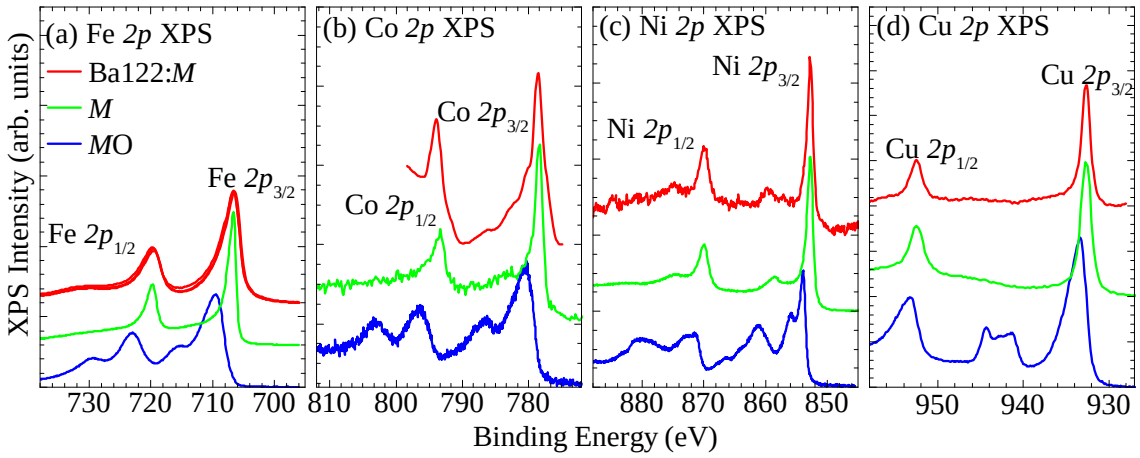

Figure 7.7: The measured metal $2p$ XPS spectra of doped Ba122: (a) Fe $2p$, (b) Co $2p$, (c) Ni $2p$, and (d) Cu $2p$. For each case a reference spectrum of the appropriate metal (M) and metal monoxide (MO) are provided. Note that for brevity the Fe $2p$ XPS spectra for each of the doped Ba122 samples are the same colour and superimposed in panel (a), it should be clear that all spectra are essentially the same. This figure is adapted from one published in Reference [22].

can be 1+ since no resonance with an unoccupied $3d$ state appears in the XAS spectrum [22].

Even the Cu^{1+} in Cu_2O has a rather large resonance XAS peak (larger than that seen in the spectrum of Ba122:Cu in Figure 7.6(e)), since "partial" $3d$ holes are created through hybridizing with oxygen [172]. Unfortunately the XAS onset in Cu_2O is at the same energy as that in Cu metal [173], so the possibility of Cu^{1+} in Ba122:Cu cannot be completely ruled out. But it is quite clear that Cu^{2+} is not present in Ba122:Cu, and therefore *if* the transition metals are isovalent substitutions, then Fe^{2+} may not be present either. I believe that it is more appropriate to refer to the FeAs plane as entirely metallic, with no formal valency for either the Fe or the As, rather than the conventional chemistry notation of $Fe^{2+}As^{3-}$.

Core level XPS spectroscopy is also a useful technique for determining on-site correlation strength [170]. The metal $2p$ XPS spectra of the Ba122:M samples and the relevant pure metals and metal monoxides are shown in Figure 7.7 (these spectra were measured by our collaborator Dr. Anna Buling, University of Osnabrück, Osnabrück, Germany). Again the spectra from Ba122:M are much closer to that of the appropriate metal rather than the metal monoxide; in particular the spectra from Ba122:M lack the large satellite features that are

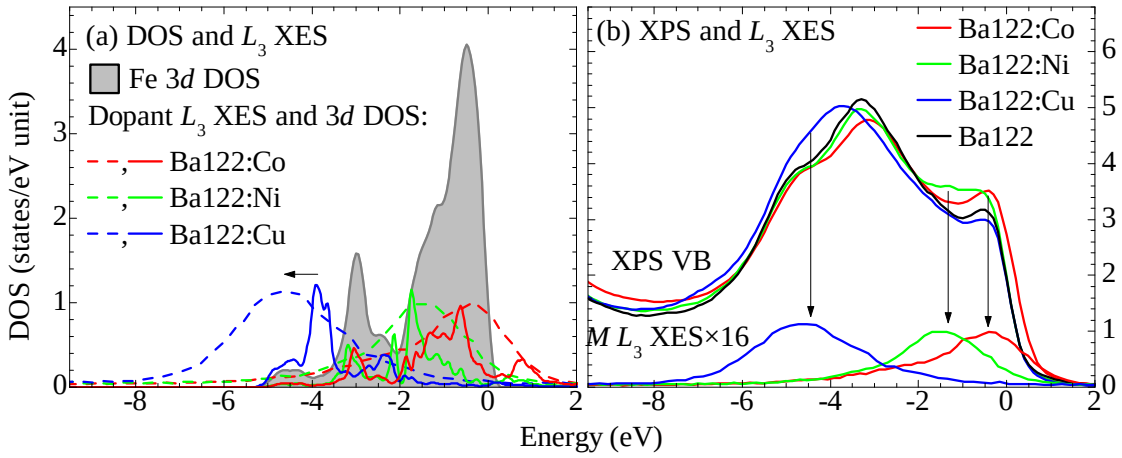

Figure 7.8: Valence band structure of doped Ba122: (a) The calculated DOS (solid lines) and doped metal L_3 XES (dotted lines), note how the calculated DOS overestimates the energy of the Cu 3d-states. (b) The measured XPS spectra and doped metal L_3 XES, note how the measured XPS spectra has features connected with the doped states. This figure is adapted from one published in Reference [22].

indicative of a strongly correlated system [170].

Finally, the XES and XAS measurements of the doped sites in Ba122:M should facilitate reconstructing the location of these states in the valence and conduction bands. Although it is easy to calculate the electronic structure of these systems, it is tricky to show that the calculation gets the doped states "right" without resorting to XES; the most common approach of using valence XPS will fail because the contribution from the small number of dopants will not be clearly visible. Even simply measuring the XES is problematic; how should these spectra be aligned with spectra from other edges within the valence band, if the states responsible for the spectra are too few to provide noticeable hybridization features in the other spectra? One can certainly use core level XPS spectra to get the binding energy, but even this has an error of an eV or so; for systems like Ba122 that have a valence band only 5 eV wide this can be problematic.

For Ba122, I think an easy solution is to align the edges of the XAS measurements for each metal site. Because Ba122 is metallic, the core hole perturbation cannot reduce the energy of the conduction band onset, and due to hybridization this onset should be the same for each site [22]. Using this approach I can align the Co, Ni, and Cu L_3 XES with the calculated

DOS, as shown in Figure 7.8(a). (The Fe L_3 XES spectra are omitted, since they agree with the calculated DOS in the same case as in $CaFe_2As_2$.) Using this approach, the Co and Ni L_3 XES suggests that the Co and Ni $3d$-states are close to where the DFT calculation predicts they should be (although perhaps the DFT calculation places the Co $3d$ some few tenths of an eV too deep in the valence band), but the Cu L_3 XES reveals that the Cu $3d$-states in Ba122:Cu are right at the bottom of the valence band, about 1 eV lower than predicted by the DFT calculation. Encouragingly, this method of aligning the XES with the electronic structure is supported by the valence XPS spectra; as shown in Figure 7.7(b) a weak local maxima occurs in each of the valence XPS spectra local to the placement of the L_3 XES.

From this analysis the difference between Ba122:Cu and Ba122:Co,Ni is clear: the Cu has a valency of 1+ (at most), and the full $3d^{10}$ shell is located at the very bottom of the valence band and is probably relatively chemically inert (somewhat similar to the $3d^{10}$ shell in ZnO and $ZnTiO_3$, refer back to Sections 5.2 and 6.6). It is also probable that the Fe, Co, and Ni are also not fully 2+, although since a valency of 0+, 1+, or 2+ has no impact on the filling of the $3d$ shell in these elements this is difficult to prove. In any event, Cu contributes quite differently to the electronic structure of Ba122 than Co and Ni, so it is not unreasonable that superconductivity is exhibited in Ba122:Co and Ba122:Ni but not Ba122:Cu.

7.3 Electronic Structure of Copper Pnictides

Following from the discussion of Ba122:Cu, the general influence of Cu on the electronic structure of layered pnictides is worth further study. It is obvious from the existence of cuprate superconductors that copper does not impede superconductivity in general, and even in layered pnictides $LiCu_2P_2$ exhibits superconductivity at $T_c = 3.7$ K [174]. There are several copper pnictides that are structurally analogous to iron pnictides, such as $BaCu_2As_2$ and $SrCu_2As_2$ — which, apart from replacing Fe with Cu, have the same structure as their FeAs-counterparts, shown in Figure 7.1 — and some early theoretical work on these systems suggested that the Cu was monovalent with a chemically inert $3d^{10}$ [175]. Recently several of these copper pnictides were re-examined (like most layered pnictides, their structure and synthesis methods had been known for several decades, but their electronic structure was

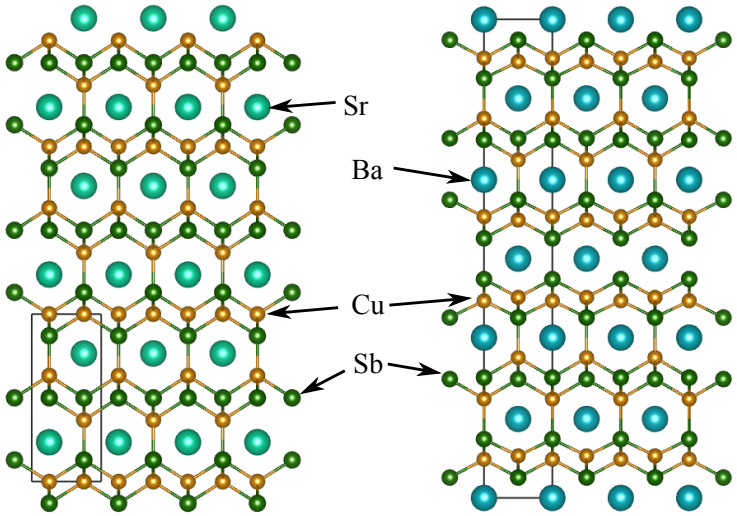

Figure 7.9: Crystal structures of (left to right): $SrCu_2Sb_2$ and $BaCu_2Sb_2$. The a axis of both structures is directly out of the page, a single unit cell is outlined for each system. Note there are two types of CuSb planes, in contrast to CuAs or FeAs structures. In $SrCu_2Sb_2$ the plane stacking is ABABAB, while in $BaCu_2Sb_2$ the plane stacking is ABAABA. The crystal structures are from Reference [177].

largely unknown) and their electronic and thermal properties were measured; as expected no superconductivity was found [176, 177].

I thought it would be useful to study some copper pnictides with soft X-ray spectroscopy; it would be possible to directly compare the Cu $L_{2,3}$ XES and XAS spectra from these systems with that from Ba122:Cu, and it would be possible to verify whether these copper pnictides were indeed Cu^{1+} systems. To that end I was able to obtain polycrystalline pieces of $SrCu_2As_2$, $SrCu_2(As_{0.84}Sb_{0.16})_2$, $SrCu_2Sb_2$, $BaCu_2Sb_2$, and $CaCu_{1.7}As_2$ and measure Cu $L_{2,3}$ XES and XAS spectra. I also calculated the electronic structure of these materials with WIEN2k (using the simple PBE exchange-correlation functional) using the crystal structures determined with XRD [176, 177]. The copper pnictide samples were graciously provided by Prof. David Johnston and Dr. Vivek Anand, at Iowa State University, Ames, IA (grown with the "self flux" technique, and the crystal structure was verified by XRD by members of Prof. Johnston's research group [176, 177]). The reference copper foil and CuO powders were the same as those used as references in Section 7.2 (Alfa Aesar, foil was 99.99% purity, the powder was 99.5% purity).

$SrCu_2As_2$ and $CaCu_2As_2$ are isostructural to $CaFe_2As_2$ (refer back to Figure 7.1). It turns out that $CaCu_2As_2$ is actually copper deficient [178], so for the calculated electronic structure I used a $2 \times 2 \times 1$ supercell and removed 2 Cu atoms (resulting in a $P4_2/mmc$ structure) to make $CaCu_{1.75}As_2$. I should note that the Cu vacancies in $CaCu_{1.7}As_2$ are random [177], while obviously they are ordered in the structure used in my DFT calculation. However the same is true for the core holes when calculating the core hole perturbed XAS, and these calculations tend to do a reasonable job of reproducing experimental data. Therefore, for a sufficiently large unit cell, I do not think that long range order shows any observable effects in the calculated XES or XAS spectrum (this does not include resonant X-ray scattering features, however).

The crystal structures of the copper antimonides are slightly different. In these compounds there are two types of CuSb planes; one with a central plane of Cu coordinated with 4 Sb atoms above and below the central plane (this is the structure that all layered metal arsenides have, refer back to Figure 7.1), and one with a central plane of Sb coordinated with 4 Cu atoms above and below the central plane (this is basically the inverse of the regular metal arsenide plane structure). Secondly, the stacking of these planes depends on the cation. As shown in Figure 7.9, $SrCu_2Sb_2$ has an alternating "ABAB" type of vertical arrangement of the planes (here "vertical" refers to along the c axis of the unit cell), while $BaCu_2Sb_2$ has an alternating "ABAABA" arrangement of these CuSb planes. This raises another question relevant to X-ray spectroscopy: will these two different Cu sites have different local electronic structures? The local symmetry of the Cu site changes considerably between the two types of CuSb planes, if the Cu $3d$-states are chemically active (and certainly if the Cu is divalent) then perhaps the Cu L_3 XES spectrum of (for example) $SrCu_2As_2$ will be quite different from that of $SrCu_2Sb_2$.

However, despite the structural differences, the DOS of the copper antimonides is quite similar to the DOS of the copper arsenides, as shown in Figure 7.10. Like the iron arsenides previously discussed, the Sb $5s$ or As $4s$-states form a separate band some 10 eV or so below the Fermi level. In the case of $SrCu_2(As_{1.875}Sb_{0.125})_2$ the Sb $5s$ and As $4s$-states are hybridized in this region. The Sb $5p$ or As $4p$-states hybridize with the Cu $3d$-states at the bottom of the main valence band, around -6 eV, again like the As $4p$ and Fe $3d$-states in

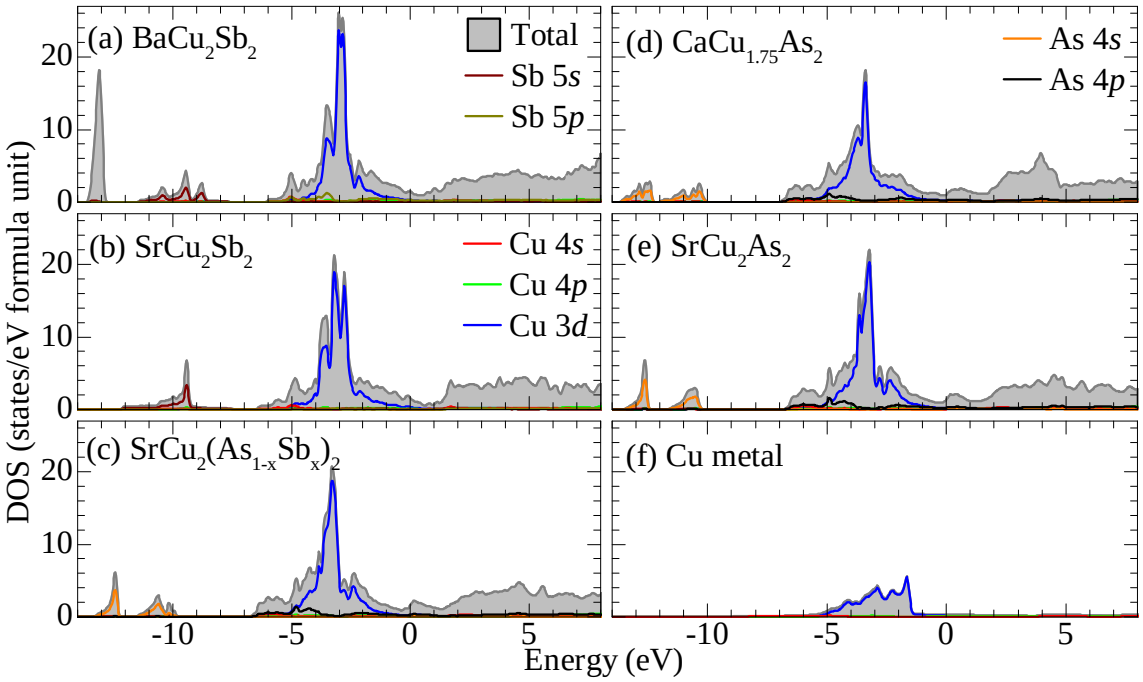

Figure 7.10: DOS of the copper pnictides: (a) $BaCu_2Sb_2$, (b) $SrCu_2Sb_2$, (c) $SrCu_2(As_{1-x}Sb_x)_2$ for $x = 0.125$, (d) $CaCu_{1.75}As_x$, (e) $SrCu_2As_2$, and (f) Cu metal for reference. Note that the vertical axis scale is consistent for each panel. The Fermi level is at 0 eV. This figure is adapted from one that will be published in our forthcoming paper [23].

the iron arsenides. However like the Cu $3d$-states in Ba122:Cu, the Cu $3d$-states in these copper pnictides are located some 3 eV below the Fermi level, and in general the number of states at the Fermi level in a copper pnictide is considerably smaller than in a comparable iron pnictide. These Cu $3d$-states of copper pnictides do seem to form a narrow-band full shell, and they are limited to a smaller energy range than in copper metal, despite the similar d-shell occupancy.

The distribution of Cu $3d$-states in the valence band of $SrCu_2As_2$ is not appreciably different (in terms of peak intensity or band width) than that in $SrCu_2Sb_2$, despite the latter having two inequivalent Cu sites with rather different local geometries. For that matter, the Cu $3d$ DOS in $BaCu_2As_2$ is more or less the same as the Cu $3d$ DOS in both strontium materials; certainly one could expect the two to be the same within the resolution of a Cu L_3 XES spectrum.

Indeed, the measured and calculated Cu L_3 XES spectra of these copper pnictides systems are quite similar to one another, and the calculated spectra are in good agreement with the measured spectra, as shown in Figure 7.11. Like the previously mentioned L_3 XES spectra from Fe, Co, Ni, and Cu in Ba122:X, the Cu L_3 XES spectra from copper pnictides are almost exactly the same as the spectrum from copper metal. The Cu $3d^{10}$ shell present in copper pnictides provides an interesting counterpoint to the Zn $3d^{10}$ shell present in ZnO and $ZnTiO_3$; the properties of the former seem quite adequately predicted by the PBE exchange-correlation functional, while the properties of the latter required an on-site Coulomb potential or a hybrid functional to reproduce the correct distribution. These differences are perhaps especially surprising given the fact that the Cu $3d^{10}$ shell has a smaller binding energy than the Zn $3d^{10}$ shell. (Certainly the PBE functional was sufficient to localize the In $4d^{10}$ in In_2O_3, refer back to Section 5.3.)

The Cu L_3 XAS spectra shown in Figure 7.11 were measured in surface sensitive TEY mode, since surface oxidation would lead to some Cu^{2+}, the XAS of which has a characteristic sharp pre-edge peak, it is clear that these samples were almost entirely free of surface oxidation. Only a very small amount of surface Cu^{2+} is present in the spectra of $SbCu_2Sb_2$, $SrCu_2(As_{0.84}Sb_{0.16})_2$, $SrCu_2As_2$, and Ca $Cu_{1.7}As_2$, as shown by the arrows in Figure 7.11. The XAS spectra calculated from the ground state electronic structure is in rather good agree-

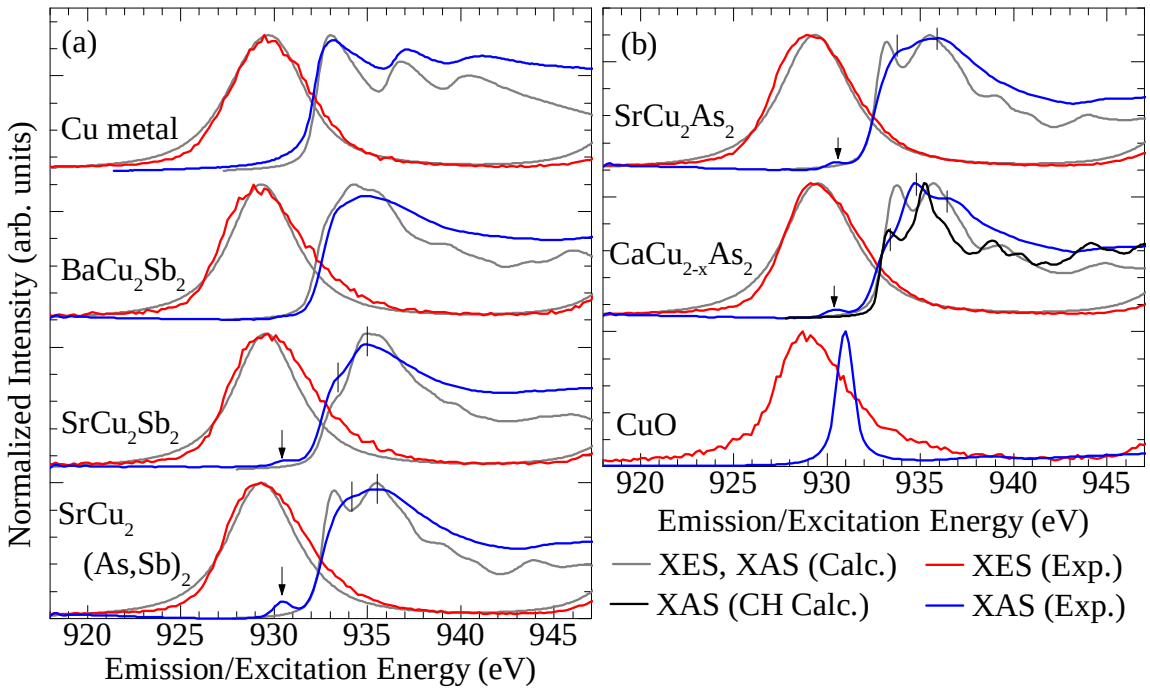

Figure 7.11: Measured and calculated Cu L_3 XES (excited at 1000 eV) and XAS spectra of the copper pnictides. The label $SrCu_2(As,Sb)_2$ refers to $SrCu_2(As_{1-x}Sb_x)_2$, for $x = 0.16$ in the measured spectra, and $x = 0.125$ for the calculated spectra. For $CaCu_{2-x}As_2$, $x = 0.3$ in the measured spectra and $x = 0.25$ in the calculated spectra. All XAS spectra were measured in TEY mode, note a trace amount of surface oxidation in the XAS spectra of $SrCu_2Sb_2$, $SrCu_2(As_{1-x}Sb_x)_2$, $SrCu_2As_2$, and $CaCu_{2-x}As_2$, noted by arrows. All XAS spectra were calculated from the ground state DOS except for $CaCu_{2-x}As_2$, here there is also a XAS spectrum of stoichiometric $CaCu_2As_2$ calculated with a core hole perturbation. This figure is adapted from one that will be published in our forthcoming paper [23].

ment with the measured XAS spectra in the cases of Cu metal, $BaCu_2Sb_2$, and $SrCu_2Sb_2$. For $SrCu_2(As_{0.84}Sb_{0.16})_2$ and $SrCu_2As_2$ the calculated XAS spectrum has two sharp peaks in the pre-edge, these features are at least qualitatively present in the measured XAS spectrum as a shoulder and a peak (denoted by the vertical lines in Figure 7.11).

For $CaCu_{1.7}As_2$ the agreement between the measured and calculated Cu L_3 spectrum is perhaps the worst; the near-edge of the measured spectrum has one peak and two shoulders (denoted by the vertical lines in Figure 7.11) while the spectrum calculated from the ground state electronic structure has two peaks in this region, quite similar to the calculated XAS spectrum of $SrCu_2As_2$. There are two likely causes for the discrepancy between the calculated and measured spectra of $CaCu_{1.7}As_2$: The core hole perturbation could cause greater distortion in this system than in the other copper pnictides, or the implicit ordering of the Cu vacancies in the calculated spectrum (an ordering which is not present in the actual sample) could have a significant effect on the conduction band. The former argument is easier to test than the latter; to that end I calculated the core hole perturbed XAS for stoichiometric $CaCu_2As_2$. My assumption here was that the local perturbation from a core hole was more significant than a vacant site that could be no closer than the second coordination shell. This spectrum is shown in Figure 7.11, and it is much closer to the measured XAS spectrum than the one calculated from the ground state electronic structure. While the features in the core hole perturbed calculated XAS spectrum are perhaps a bit too sharp, and the relative intensities are not quite correct, the general shape is in good agreement with the measured XAS spectrum. In a sense this supports the idea that the core hole effect is more significant in systems with lighter cations (Ca compared to Sr or Ba, As compared to Sb) that was mentioned in Chapter 5.

The measured Cu L_3 XAS spectra also suggest that describing Cu as monovalent may be an overstatement. As previously mentioned for Ba122:Cu (refer back to Section 7.2), the Cu L_3 XAS of Cu_2O also has a sharp $3d$ resonance peak at the same energy as the onset in Cu metal [173], and while the Cu L_3 XAS spectrum of Ba122:Cu did have a reasonably sharp peak in the near edge region that could be the spectral signature of Cu^{1+}, the Cu L_3 XAS spectra from these copper pnictides clearly do not have any features of the required sharpness or intensity. Like copper metal, the Cu L_3 XAS spectrum of a copper pnictide is

entirely due to unoccupied Cu $4s$-states. Of course one cannot rule out the possibility that Cu^{1+} — As^{2-} bonding has less hybridization than Cu^{1+} — O^{2-} bonding, and that the cause of the $3d$ resonance in the XAS spectrum of Cu_2O is not applicable to a copper pnictide, but I think the Cu L_3 XAS of copper pnictides offers a strong argument that attaching a formal valency to any site in a metal pnictide layer is incorrect.

As a final observation on the X-ray spectra, it is worth mentioning that only the calculated XES spectra were individually aligned with the measured XES spectra in Figure 7.11; the calculated XAS spectra were shifted in the same manner as the XES spectra so agreement in the onset and energy of particular features in the calculated and measured XAS spectra is not necessarily guaranteed. (For the core hole perturbed XAS spectrum of $CaCu_{1.7}As_2$ the average interstitial potential was aligned with that in the ground state calculation, as described in Section 5.3.) In fact the calculated and measured XAS spectra in Figure 7.11 are in excellent alignment, this suggests that the calculated electronic structure accurately reproduces the binding energy of the Cu $3d^{10}$ shell. Recall that this is in contrast to the Cu $3d^{10}$ states in Ba122:Cu; in that system the calculated $3d^{10}$ states were about an eV or so higher in energy than the measured L_3 XES spectrum suggests. In general my research supports the original prediction that copper pnictides are typical *sp*-metals [175], since Ba122:Cu is not as "well-behaved" it may be fruitful to further study the electronic structure of the $Ba(Fe_{1-x}Cu_x)As_2$ family.

After this chapter was written, a manuscript based on the research discussed above was published in Physical Review B [23].

7.4 Magnetic Ordering in LiFeAs and LiMnAs

LiFeAs is a simple layered pnictide that is somewhat unusual because it naturally superconducts at around 18 K without needing doping, vacancies, or external pressure [179, 180]. LiFeAs also has no long range magnetic order [180]; for these reasons LiFeAs is a good "model compound" for studying the general phenomenon of superconductivity in layered pnictides.

I first studied LiFeAs and the related compound NaFeAs (with a $T_c = 9$ K [181]) with soft X-ray spectroscopy for the purposes of understanding the basic electronic structure [20],

a project which resulted in findings very similar to those described for $CaFe_2As_2$ in Section 7.1. These LiFeAs and NaFeAs samples were pressed pellets of powders made by sintering elemental powders, and the crystal structure was verified with XRD [1]. The synthesis and structural study was conducted by members of Prof. Simon Clarke's research group, Dept. of Chemsitry, University of Oxford, Oxford UK.

I recently acquired higher quality polycrystalline samples of LiFeAs, LiMnAs, and $Li(Fe_{0.95}Mn_{0.05})As$ (these samples were provided by Prof. Chang-Qing Jin, Chinese Academy of Sciences, Beijing, China, grown with the "self flux" method, the crystal structure was verified by XRD performed by members of Prof. Jin's research group [182]) and consequently obtained higher quality measurements of LiFeAs.

My main interest here was to compare the electronic structure of LiFeAs with that of LiMnAs. The electrical properties of LiMnAs are quite different from those of LiFeAs; while at ambient conditions the latter is a bad metal and an itinerant magnet [180], the former is an insulating (or at least semiconducting) antiferromagnet [183]. Systems like LiMnAs have recently been studied as possible spintronic materials [184], and while there has been some theoretical work done on the electronic structure of LiMnAs [185], there is little experimental data currently available. In this context I think it is useful to examine the electronic structure and magnetic ordering of LiFeAs and LiMnAs in more detail.

Both LiMnAs and LiFeAs have the same layered structure typically of all layered pnictides (both structures belong to the $P4/nmm$ spacegroup). The unit cell contains 2 transition metals sites, so to systematically investigate longer-ranged antiferromagnetic ordering in these systems I started with a $2 \times 2 \times 2$ supercell and initialized the spins of all the transition metal atoms independently. To simplify the possible structures, I assumed that magnetic coupling between the FeAs (or MnAs, as appropriate) layers was minimal, so I only considered the distinct orderings within a single 2×2 layer and either treated the second layer exactly the same, or with the spins completely reversed from that of the first layer. I describe the former arrangement as ferromagnetic (FM) order along the c axis (the total structure is still antiferromagnetic, of course), while I describe the latter arrangement as antiferromagnetic (AFM) order along the c axis.

For each 2×2 layer there are 8 transition metal sites, for in-plane AFM order there must

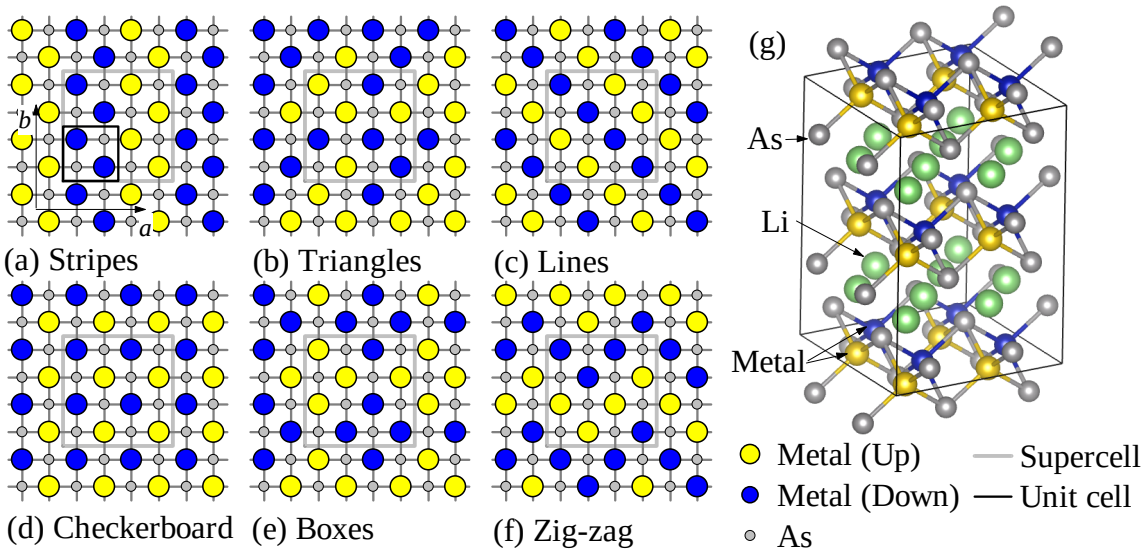

Figure 7.12: Possible antiferromagnetic orderings within a 2×2 plane: (a) through (f) the six unique orderings labelled by name. (g) a $2 \times 2 \times 2$ unit cell (of LiMnAs; LiFeAs is essentially the same) showing checkerboard with FM vertical order as an example.

be 4 "up" and 4 "down" sites. Therefore there are:

$$\begin{pmatrix} 8 \\ 4 \end{pmatrix} = \frac{8!}{4!(8-4)!} = 70 \tag{7.5}$$

total possible arrangements of atoms. However since origin of the supercell is arbitrary, as is the direction chosen for "up" there are much fewer than 70 distinct arrangements. Since any given structure is equivalent to a structure with all spins reversed (up $\leftrightarrow$ down), it is clear there can be no more than 35 distinct arrangements. In fact, after drawing out all the structures and tiling them, I have found only 6 distinct arrangements, as shown in Figure 7.12. In addition to the six in-plane AFM orderings, I also considered an in-plane FM order where all 8 sites had the same spin (which I call "sheets" order). This makes a total of 7 in-plane structures and 2 different plane stackings ("AA" stacking, resulting in the aforementioned FM order along the c axis, and "AB" stacking, resulting in the aforementioned AFM order along the c axis), or 14 different structures in total.

Hereafter the in-plane magnetic order will be referred to by the names given in Figure 7.12, while the c axis order will be called FM or AFM as appropriate. For each of these

Table 7.1: Spacegroups of magnetic ordering in LiFeAs and LiMnAs. The fundamental unit cell for both is $P4/nmm$, the lattice constants are in terms of the fundamental unit cell lattice constants (a, b, c). For the fundamental unit cell structure, see References [1] and [2]. For FM triangles, $\beta = 149.25°$ while for AFM triangles, $\beta = 130.04°$.

Structure	Spacegroup	Metal Sites	Lattice Constants
FM Sheets	$P4/nmm$	1	$a \times b \times c$
AFM Sheets	$P4/nmm$	2	$a \times b \times 2c$
FM Zig-zag	$Pma2$	4	$2a \times 2b \times c$
AFM Zig-zag	$Pma2$	8	$2a \times 2b \times 2c$
FM Boxes	$P4mm$	2	$2a \times 2b \times c$
AFM Boxes	$P4mm$	4	$2a \times 2b \times 2c$
FM Checkerboard	$P\bar{4}m2$	2	$a \times b \times c$
AFM Checkerboard	$P\bar{4}m2$	4	$a \times b \times 2c$
FM Lines	$Pccm$	2	$\sqrt{2}a \times \sqrt{2}b \times c$
AFM Lines	$Pccm$	4	$\sqrt{2}a \times \sqrt{2}b \times 2c$
FM Triangles	$C2$	6	$2\sqrt{2}a \times 2\sqrt{2}b \times c/\sin(\beta)$
AFM Triangles	$C2$	12	$2\sqrt{2}a \times 2\sqrt{2}b \times 2c/\sin(\beta)$
FM Stripes	$P2_1/m$	2	$2a \times b \times c$
AFM Stripes	$P2_1/m$	4	$2a \times b \times 2c$

structures I reduced the $2 \times 2 \times 2$ supercell as much as possible while still preserving the appropriate tiling (therefore the "FM sheets" order is the same as the spin-polarized single unit cell); this was done to both increase the speed of the calculations (by increasing the symmetry) and to maintain the magnetic ordering during the SCF cycle, while the spins were initialized to a certain magnetic order neither the direction nor the magnitude of the magnetic moments were constrained during the SCF cycle. The space groups and number of metal sites for each type of magnetic ordering is summarized in Table 7.1.

Some relevant parameters from each structure are presented in Figure 7.13. The most important parameter in determining the optimal magnetic ordering is the energy gain relative

to the non-magnetic structure, which I define as:

$$\Delta_E^i = \frac{E_{tot}^{NM}}{n^{NM}} - \frac{E_{tot}^i}{n^i} \tag{7.6}$$

where E_{tot}^x is the total energy (NM for the non-magnetic structure, i for the ith magnetic structure) and n^x is the number of formula units per unit cell in structure x. If a particular magnetic structure is more stable than the non-magnetic structure it should have a lower total energy per formula unit, so consequently the structure i with the largest Δ_E is the most stable.

As shown in Figure 7.13(a), the AFM lines structure is the most stable magnetic configuration for LiFeAs. It should be pointed out that the energy gains of the FM lines, FM and AFM zig-zag, and the AFM triangles structures are all within room-temperature (0.025 eV) of the FM lines structures, and the total energy gains are only 0.15 eV or less compared to the non-magnetic structure. Taken together this supports the experimental findings that LiFeAs has little long range magnetic order [179, 180], the energy gains shown in Figure 7.13(a) suggest that at room temperature a random distribution of antiferromagnetic domains, possibly with different internal orderings, is likely to exist and fluctuate over time in LiFeAs. I should also point out that the lines structure in DFT is often identified as the signature of spin density wave ordering [186], a key magnetic structure that typically manifests at low temperatures in layered pnictides and must be suppressed before superconductivity can be realized [187].

On the other hand, the magnetic structures in LiMnAs all provide much larger energy gains than those in LiFeAs, as shown in Figure 7.13(b), and it is clear that the checkerboard structure is the most stable. These calculations therefore support the experimental findings that LiMnAs is a well-ordered antiferromagnet [183]. There is very little difference between the AFM and FM c axis orderings for LiMnAs (and, in most cases, very little difference between AFM and FM in LiFeAs), this suggests that my assumption that there is very little magnetic coupling between the MnAs (or FeAs) layers, and therefore there is little value in explicitly considering other stacking arrangements along the c axis (for example, an alternating stacking of lines and boxes planes is possible, as are many others, but not likely to be physically realized). I should point out that the checkerboard magnetic structure in DFT

is often identified as a signature of Mott insulators, like the parent compounds for cuprate superconductors [188].

There is a relatively large amount of variation in the magnetic moments per Fe site in the LiFeAs structures, as shown in Figure 7.13(c) the average magnetic moments vary from 1.18 ± 0.04 μ_B/Fe for AFM sheets to 2.00 ± 0.06 μ_B/Fe for AFM lines, this variation is another indication of random or itinerant magnetic ordering or spin-density wave behaviour at finite temperatures in LiFeAs. Here the "margin or error" should be interpreted as the standard deviation of magnetic moments; since the magnetic moments were not fixed in the the DFT calculation, each transition metal site could have a slightly different moment. I should also point out that DFT calculations are known to overestimate magnetic moments in iron pnictides [186], so it is not unexpected that all of these values are significantly greater than the measured moment of 0.9 μ_B/Fe for LiFeAs [189]. All of the magnetic moments are quite similar in LiMnAs, as one would expect for a robust antiferromagnet; here the average magnetic moment (averaged across all LiMnAs structures) is 3.96 ± 0.04 μ_B/Mn. Because all the moments are essentially the same, I have omitted plotting the moments for LiMnAs as was done for LiFeAs in Figure 7.13(c).[1]

Finally, all LiFeAs structures predicted metallic behaviour (i.e. no band gap), again this is reassuring since LiFeAs is known to be a bad metal [152], while all LiMnAs structures except for the non-magnetic, FM and AFM sheets, and FM stripes structure have a non-zero band gap. The highest gap is 0.62 eV for the FM checkerboard structure, while the band gap of the lowest energy structure, AFM checkerboard, is 0.534 eV (the energy gain of the AFM checkerboard structure is only 1.41 meV better than the FM checkerboard structure, however), as shown in Figure 7.13(d). The band gap of LiMnAs has been reported to be between 0.39 eV and 0.81 eV, measured by scanning tunnelling microscopy [183], so my calculations are in reasonable agreement with experimental results.

The DOSes of the most stable magnetic structures for LiFeAs and LiMnAs (the AFM lines and AFM checkerboard orderings, respectively) is shown in Figure 7.14. Since both structures are antiferromagnetic, only the spin up DOS is shown in Figure 7.14(a), (b).

[1] I should also point out that I used the PBE exchange correlation functional for all of these calculations, which is known to overestimate magnetic moments [35]. I intend to recalculate these moments with the LDA functional, and also attempt to optimize the atomic positions.

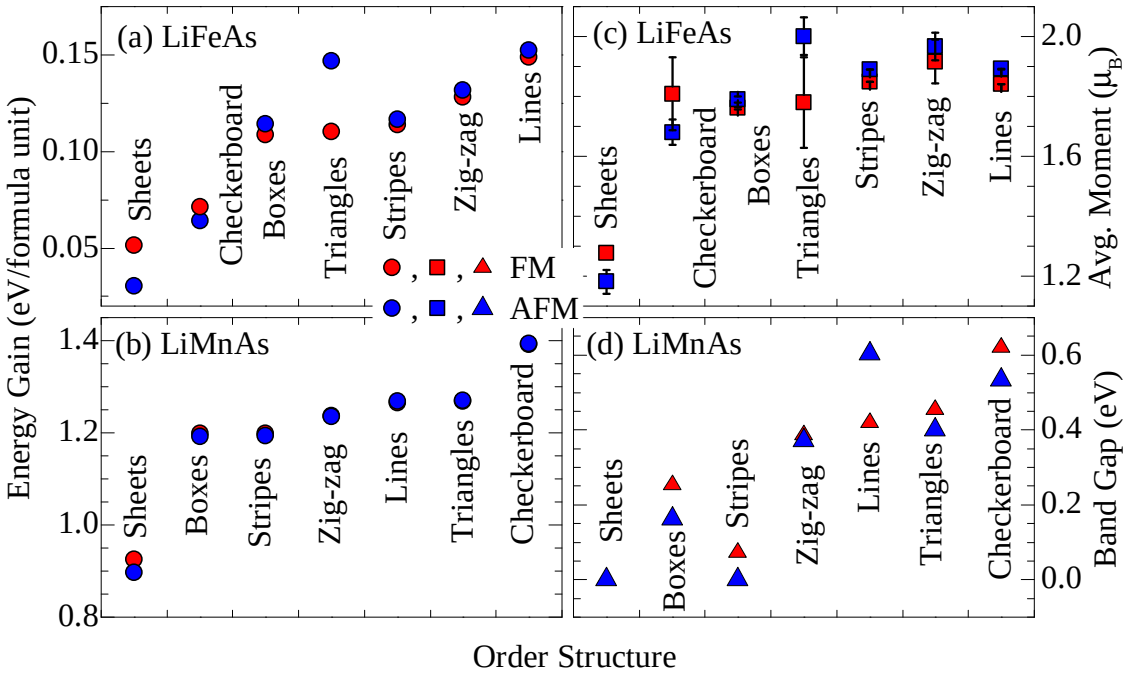

Figure 7.13: The energy gain (with respect to the non-magnetic case) for the different magnetic structures in (a) LiFeAs and (b) LiMnAs. (c) The average magnetic moment per Fe site in LiFeAs, the "error bars" indicate the standard deviation of the moments for each inequivalent Fe site. (d) The band gaps of the LiMnAs structures.

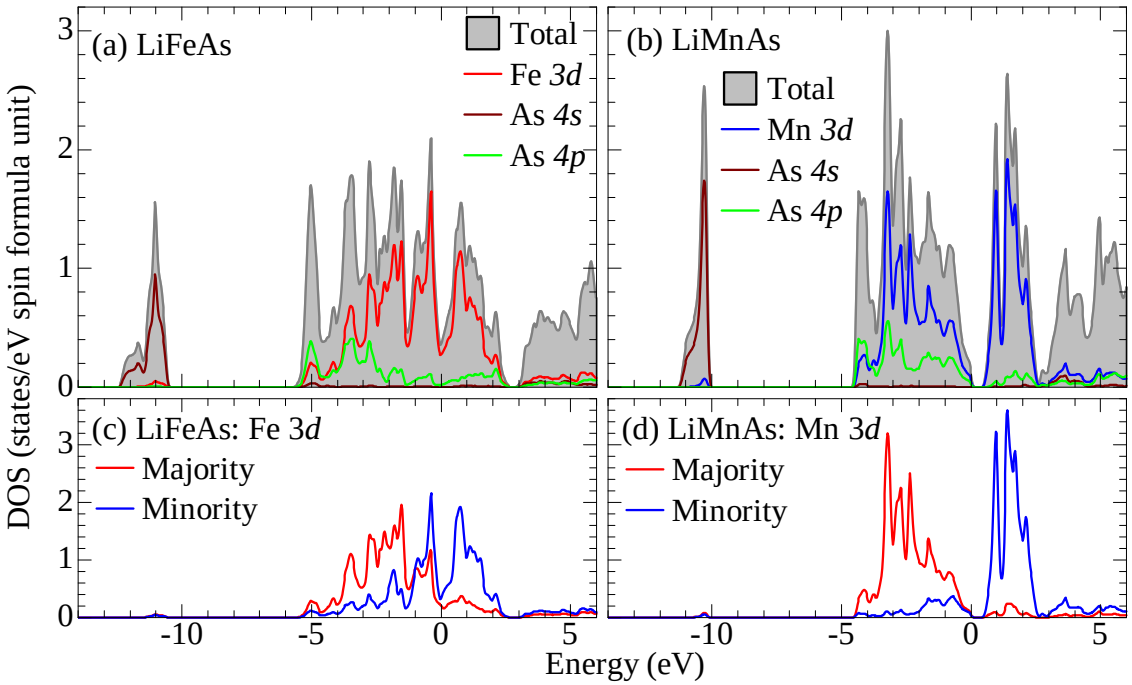

Figure 7.14: The average spin up DOSes of (a) LiFeAs (AFM lines order) and (b) LiMnAs (AFM checkerboard order). The transition metal spin separated $3d$ DOS is given for (c) LiFeAs and (d) LiMnAs.

Apart from the small band gap in LiMnAs, the electronic structures of both systems seem rather typical of all layered pnictides; there is an As $4s$ band some 10 eV or so below the Fermi energy, the main valence band is only about 5 eV wide, the As $4p$-states are hybridized with the transition metal $3d$-states at the bottom of the valence band, and the transition metal $3d$-states dominate near the top of the valence band. In LiMnAs, however, the bulk of the Mn $3d$-states is deeper in the valence band than the Fe $3d$-states in LiFeAs. The bandwidths in LiMnAs are also somewhat narrower than in LiFeAs; even the As $4s$ band is narrower in LiMnAs than in LiFeAs.

The Mn $3d$-states in LiMnAs have a much greater spin separation than the Fe $3d$-states in LiFeAs, as shown in Figure 7.14(c),(d). Of course this is due to the greater magnetic moment of Mn compared to Fe, and the fewer $3d$ electrons in Mn compared to Fe. Near the Fermi level, however, the two spin densities are essentially the same in LiMnAs; this may present challenges in using LiMnAs in spintronics.

Like all layered iron arsenides I have studied, the Fe $L_{2,3}$ XES and XAS spectra of LiFeAs are very similar to that of iron metal, and resonantly excited XES shows an almost depressing lack of fine structure or inelastic scatter. I was able to transfer the LiFeAs sample from a glass vial (where it had been sealed immediately after synthesis) into the beamline vacuum chamber without the surface becoming noticeably oxidized; as shown in Figure 7.15(a) the Fe $L_{2,3}$ XAS spectrum of LiFeAs, measured in surface sensitive TEY mode, does not show the two peak structure at the L_3 edge that is indicative of surface oxidation (this structure can be seen in the spectrum from $CaFe_2As_2$ in Figure 7.4(d)), and with the other pnictides, a ground state XAS calculation does a rather good job of reproducing the measured XAS spectrum. The non-resonant Fe $L_{2,3}$ XES spectrum is also reasonably reproduced by the calculated XES spectrum, and the resonantly-excited Fe $L_{2,3}$ XES spectra are very similar to those from other iron pnictides (refer back to Figure 7.5 and References [20–22, 169]), as shown in Figure 7.15(b). I should also point out that each XES spectrum can be scaled so the low energy side of the Fe L_3 bands align perfectly, as shown in Figure 7.15(c). In fact, as long as the excitation energy is above the Fe L_3 absorption threshold, the shape of the Fe L_3 XES spectrum is almost entirely insensitive to excitation energy. This behaviour has been previously noted in other iron pnictides, and is further evidence that there is no on-site Hubbard U potential, or any other strong local correlations [169].

Similarly, the Mn $L_{2,3}$ XAS spectrum of LiMnAs is very similar to that of manganese metal, and has none of the sharp fine structure associated with most manganites [168, 190–192], as shown in Figure 7.15(d). The Mn L_2 edge is, however, different from the L_3 edge, and this is not the case for pure Mn metal [193,194], so there is at least some ligand interaction at work here. However the Mn $L_{2,3}$ XAS calculated from the ground state electronic structure does a reasonable job of reproducing the shape of the Mn L_3 edge, and while I am not sure I can identify the correlation strength in LiMnAs at present, it certainly has weaker on-site correlations than any other Mn-ligand compound I have studied or seen in the literature.

The Mn $L_{2,3}$ XES spectra of LiMnAs (shown in Figure 7.15(e)) are also free from any prominent multiplet or charge-transfer features, unlike those from MnO [192]. The elastic scatter is surprisingly intense for some spectra, but generally these spectra are very reminiscent in shape of the Fe $L_{2,3}$ XES from LiFeAs, and like the spectra from LiFeAs, all of the Mn

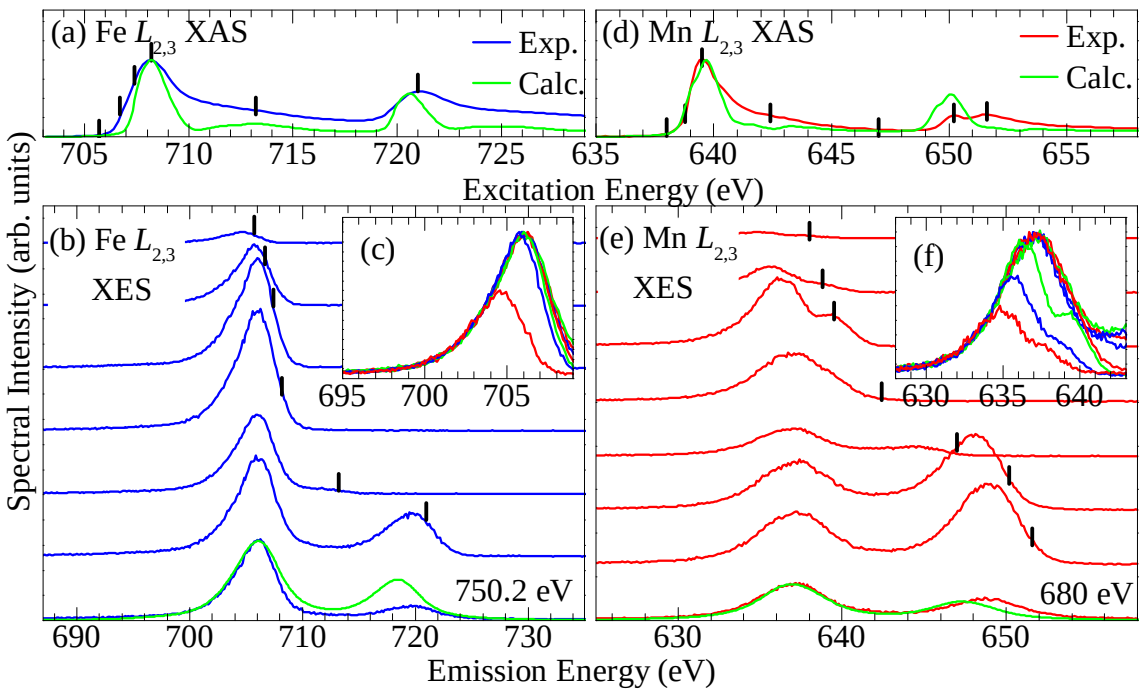

Figure 7.15: The X-ray spectra of LiFeAs: (a) Fe $L_{2,3}$ XAS, (b) Fe $L_{2,3}$ XES as measured, and (c) Fe $L_{2,3}$ XES spectra scaled to show the similarity in the low energy spectral shape, and for LiMnAs: (d) Mn $L_{2,3}$ XAS, (e) Mn $L_{2,3}$ XES as measured, and (f) Mn $L_{2,3}$ XES scaled to show similarity in low energy spectral shape. The black ticks show the appropriate excitation energy, or the energy is labelled (if off the scale of the plot). All XAS spectra were measured in TEY mode.

$L_{2,3}$ XES spectra of LiMnAs can be scaled so the low energy side of the Mn L_3 XES spectra align perfectly, as shown in Figure 7.15(f), ruling out the possibility of significant energy loss features in the XES spectra. Combined with the XAS spectrum mentioned above, it seems relatively clear that there is no significant on-site Hubbard U potential present in LiMnAs, which to me seems somewhat odd for a half-filled $3d$ metal in system with a finite band gap and Mott insulator-like antiferromagnetic ordering. There was some recent theoretical work suggesting that Hund's rule coupling is the significant correlation effect on layered pnictides, and further that half-shell filling should promote a Mott-like band gap [195], and I am hoping to work with Robert Green to calculate model Hamiltonian resonant XES spectra for LiMnAs to investigate the possibility of strong Hund's rule correlations in this system.

Finally, I would like to conclude this section by briefly reporting some of my preliminary

results from studying Li($Fe_{1-x}Mn_x$)As. For this system I simply took the LiFeAs structure with the AFM lines order and substituted one Fe site with Mn on each plane (the two Mn were substituted in opposite spin sites), making Li($Fe_{0.875}Mn_{0.125}$)As. One should obviously consider other (many other) possibilities. Since LiMnAs is isostructural to LiFeAs, and since DFT calculations suggest that magnetic moment of Mn is at least double that of Fe, a variety of structures should be calculated to test for the possibilities of Mn clustering, or long range magnetic coupling between Mn sites. This single calculation is sufficient only for a preliminary analysis.

The DOS of Li($Fe_{0.875}Mn_{0.125}$)As is shown in Figure 7.16(a). Naturally, the DOS is very similar to that of LiFeAs (refer back to Figure 7.14(a)). In particular note how the Mn $3d$-states are hybridized with the Fe $3d$-states throughout the valence band, although the natural valence band of LiMnAs is narrower than that of LiFeAs and the Mn $3d$-states in LiMnAs are weighted more towards the bottom of the valence band than in Li($Fe_{0.875}Mn_{0.125}$)As (refer back to Figure 7.14). The magnetic moment of Mn is also reduced to 2.0 μ_B/Mn, a bit larger than the magnetic moments of Fe (roughly 1.8 μ_B/Fe), and it is clear from the spin separated $3d$ DOS shown in Figure 7.16(b) that the large spin separation found in LiMnAs is not preserved in Li($Fe_{0.875}Mn_{0.125}$)As (or at least in *this structure* for Li($Fe_{0.875}Mn_{0.125}$)As).

Despite these differences in the electronic structures, the Mn $L_{2,3}$ XAS spectrum of Li($Fe_{0.95}Mn_{0.05}$)As is almost the same as that of LiMnAs, as shown in Figure 7.16(c). The DFT calculations suggest that Li($Fe_{0.95}Mn_{0.05}$)As is metallic; this is possibly reproduced in the XAS spectra since the onset of the Mn $L_{2,3}$ XAS spectrum of Li($Fe_{0.95}Mn_{0.05}$)As occurs perhaps as much as 0.5 eV lower than that in LiMnAs. This is close to the calculated band gap of LiMnAs, but one should be cautious: I have not yet investigated the effect of a core hole on the XAS spectrum of LiMnAs, and because LiMnAs has a band gap it is quite possible that a core hole can shift the onset of the conduction band.

The Mn $L_{2,3}$ XES spectra of Li($Fe_{0.95}Mn_{0.05}$)As are also almost the same as those of LiMnAs, as shown in Figure 7.16(d). Importantly, the peak of the Mn L_3 band is at slightly higher energies in Li($Fe_{0.95}Mn_{0.05}$)As compared to LiMnAs, this is expected since the latter has a greater weight of occupied Mn $3d$-states deeper in the valence band than Li($Fe_{0.95}Mn_{0.05}$)As. There is one very interesting feature in the non-resonant Mn L_3 XES

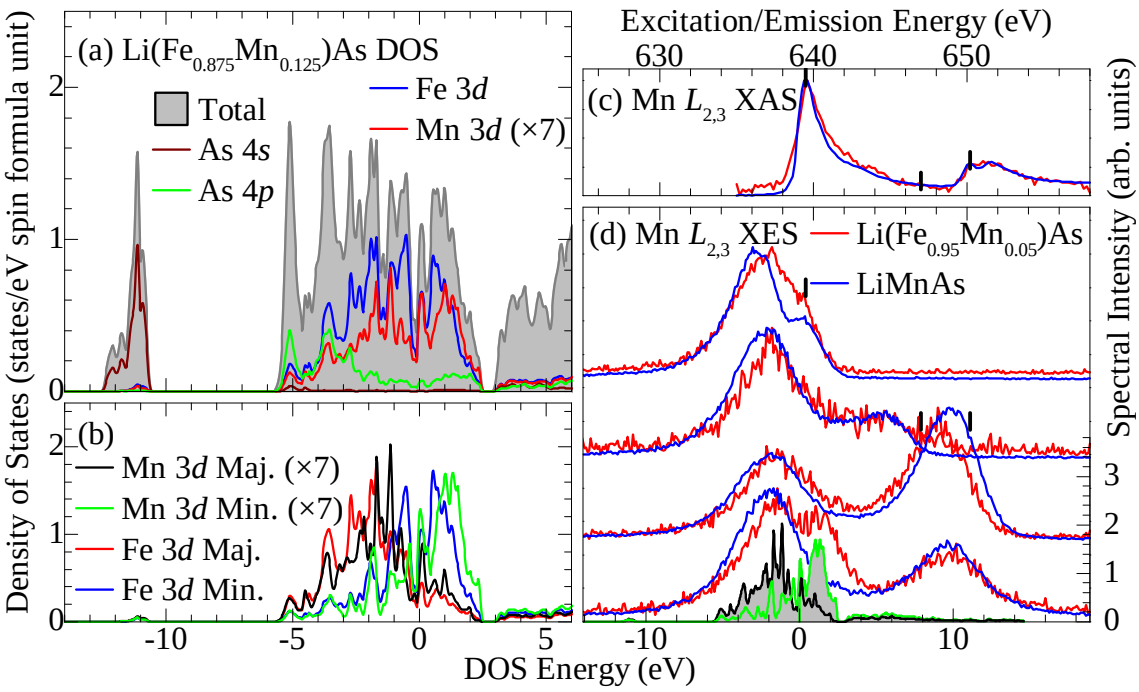

Figure 7.16: For synthesized $Li(Fe_{0.95}Mn_{0.05})As$ and calculated $Li(Fe_{0.875}Mn_{0.125})As$: (a) the average spin up DOS, (b) the Fe and Mn spin separated $3d$ DOS, (c) the Mn $L_{2,3}$ XAS spectrum (compared to that from LiMnAs), and (d) the Mn $L_{2,3}$ spectrum XES (compared to that from LiMnAs). In (d) the spin separated Mn $3d$ DOS has been replotted to show the reemission feature in the non-resonant Mn $L_{2,3}$ spectrum.

spectrum of $Li(Fe_{0.95}Mn_{0.05})As$ that is not present in that of LiMnAs; a very strong re-emission line that is due to states about 2 eV above the Fermi level. (Note the shoulder at high energies in the L_3 line in the lower-most spectrum of $Li(Fe_{0.95}Mn_{0.05})As$ in Figure 7.16(d)). A very similar re-emission feature has previously been observed in Heusler alloys, and was attributed to the existence of a "spin trap" that collected long-lifetime excited electrons [196]. This re-emission feature is in almost exact agreement in terms of alignment and relative intensity as the minority spin unoccupied Mn $3d$-states. My tentative hypothesis is that excited electrons (likely generated indirectly by Auger processes, but some from direct excitation on other Mn sites) will be trapped in the conduction band at regions local to these "defect-like" Mn sites in the LiFeAs lattice, and are therefore available to fill an Mn $2p_{3/2}$ core hole if that site subsequently absorbs and incoming X-ray. This type of behaviour has not been observed in any other transition metal substituted iron pnictide (certainly not the Ba122:Co,Ni,Cu studied in Section 7.2), and I hope to remeasure this system in an external magnetic field and with different polarizations of incident X-rays to further investigate this phenomenon.

7.5 Concluding Remarks

I have studied a wide range of layered iron pnictides with Fe $L_{2,3}$ XES and XAS: $CaFe_2As_2$ [21], LiFeAs and NaFeAs [20], $BaFe_2As_2$ doped with Co, Ni, and Cu [22], and a few more that I have not yet had time to publish (KFe_2As_2, $SrFe_2As_2$ doped with Ni), and in all cases the spectra are essentially the same as those from iron metal. In general, simple DFT calculations using the PBE GGA exchange-correlation functional adequately reproduce the DOS and appropriate XES and XAS spectra; often a core hole perturbation is not even necessary for the latter. Taken together this is pretty conclusive evidence that there are no strong *local* correlation effects (like an on-site Hubbard U potential) in layered iron pnictides; the metal $3d$-states are more accurately described by single-electron band structure wavefunctions (i.e. identified by crystal momenta quantum numbers) rather than single-electron orbital wavefunctions (i.e. identified angular momenta quantum numbers), and consequently multiplet splitting (which is dependent on LS coupling, and therefore on valence electrons being well

defined by specific orbitals) does not manifest in the X-ray spectra of layered iron pnictides.

Copper pnictides ($CaCu_{1.7}As_2$, $SrCu_2As_2$, $SrCu_2Sb_2$, $BaCu_2Sb_2$) are an even more extreme case; these have full $3d^{10}$ shells that are relatively chemically inert and certainly insensitive to local coordination geometry [23]. It is fairly clear that copper pnictides are relatively typical *sp* metals.

In general, metallic behaviour seems to be the norm for iron pnictides substituted with heavier transition metals (Co, Ni, Cu), but not for iron pnictides substituted with lighter transition metals. At least in the case of "fully Fe substituted" LiMnAs a finite band gap developes, a more rigid antiferromagnetic ordering is present, and at least some correlation effects are visible in the X-ray spectra. For partially substituted $Li(Fe_{0.95}Mn_{0.05})As$, the Mn "defect sites" may act as spin (or at least charge) traps for excited electrons, a behaviour that does not seem to manifest in Co, Ni, or Cu-substituted iron pnictides.

Chapter 8

Conclusions

8.1 Summary of Results

Hopefully it is clear by now that X-ray spectroscopy can provide very valuable information about the electronic structure of almost any material. Soft X-ray spectroscopy in particular has sufficient resolution to provide a wealth of information, and only requires the material to be vacuum compatible. I think it is important to emphasize the usefulness of XES, even in the non-resonant regime: these measurements provide atomic- and symmetry-specific probes of the *entire* valence bands, and give valuable insight into the deep bonding states as well as those close to the Fermi level. The accuracy of DFT in dealing with bonding states deep in the valence band is sometimes an aspect that is overlooked in theoretical studies that are supported by measurements that do not probe the full valence band, as an example there are a few relatively recent studies on ZnO available in the literature wherein the authors used a simple LDA (or GGA) exchange correlation functional [197, 198] — and it would take only a single look at a non-resonant O K XES spectrum to reveal how the Zn $3d^{10}$ states were improperly treated [15, 16].

At this point, XES and XAS are still most useful when combined with a theoretical calculation of the electronic structure (and, ideally, a theoretical calcualtion of the relevant XES and XAS spectra), as opposed to comparing with spectra from reference compounds only. From a purely empirical standpoint, specific types of bonding or antibonding (i.e. metal $3d$ — ligand $2p$) can be identified from the appropriate ligand XES spectrum when suitable related reference spectra are available; the O K XES spectrum of $ZnTiO_3$ can be readily interpreted when compared with that from ZnO and TiO_2, for example, [19] but electronic structure calculations are still needed for a full analysis, especially to distinguish whether

hybridization features truly are occupied antibonding orbitals or not [17].

If the core hole perturbation can be accurately calculated, the actual band gap (i.e. the appropriate correction factor for the typically underestimated band gap obtained from DFT) can be determined relatively accurately from a XES and XAS spectra from the same edge [17]. However without theoretical insight, estimating the band gap is subject to quite a bit of error; while empirical methods like using the peaks in the second derivative can often work quite well [15], there are other materials where this technique fails entirely [17], and it is difficult to recognize these cases without some other information about the electronic structure. Ultimately, a study of the electronic structure of a particular material is likely to yield better results if the X-ray spectra are part of a suite of spectra from related compounds (all with respect to the same absorption edge) rather than measuring spectra from multiple edges on the same compound.

Having mentioned these caveats, I have shown that the electronic structure, hybridization, bonding environment, and band gaps can be accurately deduced with XES and XAS spectra combined with DFT calculations for a wide range of materials [15–19]. For ternary lone pair-TiO_2 oxides, in particular, the band gap of intermediate phases can be predicted from the pure binary oxides [18]; this provides a road map for band gap engineering in potential photocatalysts. Finally, l have shown how the total valence band, including the electronic states from dopants can be reconstructed from experimental data; this lead to the conclusion that DFT was not accurately accounting for the $3d^{10}$ states from Cu substituted into $BaFe_2As_2$ [22].

8.2 Future Research

As mentioned in Chapters 6 and 7, there are several regions where the research conducted herein can be extended. In particular, there are many existing ternary oxides that contain lone pair cations and d^0 metals, and these systems should be studied with DFT calculations and soft X-ray spectroscopy to see if they too support the strategy for band gap engineering outlined in Section 6.5. For example, the ternary oxides $PbZrO_3$ and $BiVO_4$ are both commercially available (Alfa Aesar, for example) and have simple enough crystal structures that

studying these systems would be straightforward. There are also a large range of intermediate phases in the Bi_2O_3 — TiO_2 system, and $PbZrO_3$ can be easily alloyed with $PbTiO_3$. Studying these systems would be more challenging, since most intermediate phases would have large, low-symmetry unit cells, but these intermediate phases would provide a very powerful test of the strategy for band gap engineering.

The ZnO — TiO_2 is also quite rich in intermediate phases, and these could provide useful insight into the nature of the core hole perturbation in broad band systems. Given how the core hole perturbation provides a much greater distortion to the conduction band in ilmenite $ZnTiO_3$ than in either wurtzite ZnO or rutile TiO_2, it would be interesting to study what happens in rhombohedral $ZnTiO_3$ or intermediate phases like Zn_2TiO_4 or $Zn_2Ti_3O_8$ [199].

Finally, studying iron pnictides with soft X-ray spectroscopy may not provide much insight into the physics of these materials unless the experimental resolving power is high enough to detect magnetic scattering. The iron chalcogenides, on the other hand, show evidence of having stronger on-site correlations [10], and may be a more fruitful area to study with soft X-ray spectroscopy. The most promising area for future reseach, however, might lie with layered pnictides with transition metal substitutions that cross the boundary of a half-filled $3d$ shell (i.e. Mn substitution in LiFeAs, as mention in Section 7.4, or Fe, Co, Ni, or Cu substitution in LiMnAs).

References

[1] M. J. Pitcher, D. R. Parker, P. Adamson, S. J. C. Herkelrath, A. T. Boothroyd, Ri. M. Ibberson, M. Brunelli, and S. J. Clarke. Structure and superconductivity of LiFeAs. *Chem. Commun.*, 45:5918, 2008.

[2] V. G. Achenbach and H. Schuster. Ternare Verbindungen des Lithiums und Natriums mit Mangan und Elementen der 5. Hauptgruppe. *Z. anorg. allg. Chem.*, 475:9, 1981.

[3] N. W. Ashcroft and N. D. Mermin. *Solid State Physics*. Thomson Learning, Inc., 1976.

[4] H. W. B. Skinner. The Soft X-Ray Spectroscopy of Solids. I. K- and L-Emission Spectra from Elements of the First Two Groups. *Philos. T. R. Soc. A*, 239(801):95, 1940.

[5] H. M. O'Bryan and H. W. B. Skinner. The Soft X-Ray Spectroscopy of Solids. II. Emission Spectra from Simple Chemical Compounds. *P. Roy. Soc. A: Math. Phys.*, 176(965):229, October 1940.

[6] J. Slater. The Electronic Structure of Metals. *Rev. Mod. Phys.*, 6(4):209, 1934.

[7] L. G. Parratt. Electronic band structure of solids by x-ray spectroscopy. *Rev. Mod. Phys.*, 31(3):616, 1959.

[8] P. Hohenberg and W. Kohn. Inhomogeneous Electron Gas. *Phys. Rev.*, 136(3B):864, 1964.

[9] W. Kohn and L. J. Sham. Self-Consistent Equations Including Exchange and Correlation Effects. *Phys. Rev.*, 140(4A):1133, 1965.

[10] E. Z. Kurmaev, J. A. McLeod, N. A. Skorikov, L. D. Finkelstein, A. Moewes, M. A. Korotin, Yu. A. Izyumov, Y. L. Xie, G. Wu, and X. H. Chen. Structural models of $FeSe_x$. *J. Phys.: Condens. Matt.*, 21(43):435702, 2009.

[11] J. Kuneš, L. Baldassarre, B. Schächner, K. Rabia, C. A. Kuntscher, Dm. M. Korotin, V. I. Anisimov, J. A. McLeod, E. Z. Kurmaev, and A. Moewes. Metal-insulator transition in $NiS_{2-x}Se_x$. *Phys. Rev. B*, 81:035122, 2010.

[12] J. A. McLeod, A. Buling, E. Z. Kurmaev, P. V. Sushko, M. Neumann, L. D. Finkelstein, S.-W. Kim, H. Hosono, and A. Moewes. Spectroscopic characterization of a multiband complex oxide: Insulating and conducting cement $12CaO{\cdot}7Al_2O_3$. *Phys. Rev. B*, 85:045204, 2012.

[13] J. A. McLeod, E. Z. Kurmaev, P. V. Sushko, T. D. Boyko, I. A. Levitsky, and A. Moewes. Selective Response of Mesoporous Silicon to Adsorbants with Nitro Groups. *Chem. Eur. J.*, 18(10):2912, 2012.

[14] P. Blaha, K. Schwarz, G. K. H. Madsen, D. Kvasnicka, and J. Luitz. ***WIEN2k****, An Augmented Plane Wave + Local Orbitals Program for Calculating Crystal Properties*. Karlheinz Schwarz, Technische Universität Wien, Austria, 2001. ISBN 3-9501031-1-2.

[15] J. A. McLeod, R. G. Wilks, N. A. Skorikov, L. D. Finkelstein, M. Abu-Samak, E. Z. Kurmaev, and A. Moewes. Band gaps and electronic structure of alkaline-earth and post-transition-metal oxides. *Phys. Rev. B*, 81:245123, 2010.

[16] J. A. McLeod, R. J. Green, N. A. Skorikov, L. D. Finkelstein, M. Abu-Samak, E. Z. Kurmaev, and A. Moewes. Valence structure of alkaline and post-transition metal oxides. *Proc. SPIE*, 7940:79400R, 2011.

[17] J. A. McLeod, N. A. Skorikov, L. D. Finkelstein, E. Z. Kurmaev, and A. Moewes. Chemical Bonding and Hybridization in *5p* Binary Oxide. *J. Phys. Chem. C*, 116(45):24248, 2012.

[18] J. A. McLeod, R. J. Green, E. Z. Kurmaev, N. Kumada, A. A. Belik, and A. Moewes. Band-gap engineering in TiO_2-based ternary oxides. *Phys. Rev. B*, 85(19):195201, 2012.

[19] J. A. McLeod, A. Moewes, D. A. Zatsepin, E. Z. Kurmaev, A. Wypych, I. Bobowska, A. Opasinska, and S. O. Cholakh. Predicting the band gap of ternary oxides containing $3d^10$ and $3d^0$ metals. *Phys. Rev. B*, 86(19):195207, 2012.

[20] E. Z. Kurmaev, J. A. McLeod, N. A. Skorikov, L. D. Finkelstein, A. Moewes, Yu. A. Izyumov, and S. Clarke. Identifying valence structure in LiFeAs and NaFeAs with core-level spectroscopy. *J. Phys.: Condens. Matt.*, 21(34):345701, 2009.

[21] E. Kurmaev, J. McLeod, A. Buling, N. Skorikov, A. Moewes, M. Neumann, M. Korotin, Yu. Izyumov, N. Ni, and P. Canfield. Contribution of Fe3d states to the Fermi level of $CaFe_2As_2$. *Phys. Rev. B*, 80(5):054508, 2009.

[22] J. A. McLeod, A. Buling, R. J. Green, T. D. Boyko, N. A. Skorikov, E. Z. Kurmaev, M. Neumann, L. D. Finkelstein, N. Ni, A. Thaler, S. L. Bud'ko, P. C. Canfield, and A. Moewes. Effect of 3d doping on the electronic structure of $BaFe_2As_2$. *J. Phys.: Condens. Matt.*, 24(21):215501, 2012.

[23] J. A. McLeod, E. Z. Kurmaev, I. Perez, V. K. Anand, P. Kanchana Perera, D. C. Johnston, and A. Moewes. Electronic Structure of Copper Pnictides: Influence of Different Cations and Pnictogens. *Phys. Rev. B*, page 014508, 2013.

[24] H. Motz. Applications of the Radiation from Fast Electron Beams. *J. Appl. Phys.*, 22(5):527, 1951.

[25] J. A. McLeod. EXAFS study of amorphous selenium. Master's thesis, University of Saskatchewan, 2010.

[26] J. J. Jia, T. A. Callcott, J. Yurkas, A. W. Ellis, and F. J. Himpsel. First experimental results from EM / TENN / TULANE / LLNL / LBL beamline at the advanced light source undulator. *Rev. Sci. Instr.*, 66(2):1394, 1995.

[27] T. Regier, J. Paulsen, G. Wright, I. Coulthard, K. Tan, T. K. Sham, and R. I. R. Blyth. Comissioning of the Spherical Grating Monochromator Soft X-ray Spectroscopy Beamline at the Canadian Light Source. In *AIP Conf. Proc.*, volume 879, page 473, 2007.

[28] T. Regier, J. Krochak, T. K. Sham, Y. F. Hu, J. Thompson, and R. I. R. Blyth. Performance and capabilities of the Canadian Dragon: The SGM beamline at the Canadian Light Source. *Nucl. Instrum. Meth. A*, 582:93, 2007.

[29] B. L. Henke, E. M. Gullikson, and J. C. Davis. X-ray interactions: photoabsorption, scattering, transmission, and reflection at E=50-30000 eV, Z=1-92. *Atomic Data Nucl. Data*, 54(2):181, 1993. http://henke.lbl.gov/optical_constants/.

[30] M. Abbate, J. B. Goedkoop, F. M. F. de Groot, M. Grioni, J. C. Fuggle, S. Hofmann, H. Petersen, and M. Sacchi. Probing depth of soft x-ray absorption spectroscopy measured in total-electron-yield mode. *Surf. Interface Anal.*, 18(1):65, 1992.

[31] A. Achkar, T. Regier, H. Wadati, Y.-J. Kim, H. Zhang, and D. Hawthorn. Bulk sensitive x-ray absorption spectroscopy free of self-absorption effects. *Phys. Rev. B*, 83(8):081106(R), 2011.

[32] J. Bearden. X-ray wavelengths. *Rev. Mod. Phys.*, 39:78, 1967.

[33] L. J. P. Ament, M. van Veenendaal, T. P. Devereaux, J. P. Hill, and J. van den Brink. Resonant inelastic x-ray scattering studies of elementary excitations. *Rev. Mod. Phys.*, 83(2):705, 2011.

[34] S. Eisebitt and W. Eberhardt. Band structure information and resonant inelastic soft X-ray scattering in broad band solids. *J. Electron Spectrosc.*, 110-111(1-3):335, 2000.

[35] D. J. Singh and L. Nordström. *Planewaves, Pseudopotentials and the LAPW Method*, chapter 2,3,4,5. Springer, New York, New York, 2 edition, 2006.

[36] P. Ordejón, E. Artacho, and J. M. Soler. Self-consistent order-N density-functional calculations for very large systems. *Phys. Rev. B*, 53:R10441, 1996.

[37] J. M. Soler, E. Artacho, J. D. Gale, A. García, J. Junquera, P. Ordejón, and D. Sánchez-Portal. The SIESTA method for ab initio order- N materials simulation. *J. Phys.: Condens. Matter*, 14(11):2745, 2002.

[38] R. M. Martin. *Electronic Structure: Basic Theory and Practical Methods*, chapter 2, 6, 7, 8. Cambridge University Press, Cambridge, 2004.

[39] D. S. Sholl and J. A. Steckel. *Density Functional Theory: A Practical Introduction*, chapter 1. John Wiley & Sons, Inc., Hoboken, New Jersey, 2009.

[40] S. Cottenier. *Density Functional Theory and the family of (L)APW-methods: a step-by-step introduction*. Instituut voor Kern-en Stralingsfysica, K. U. Leuven, Belgium, 2004. ISBN 90-807215-1-4.

[41] F. Herman, J. P. Van Dyke, and I. B. Ortenburger. Improved statistical exchange approximation for inhomogeneous many-electron systems. *Physical Review Letters*, 22:807, 1969.

[42] A. D. Becke. Density-functional exchange-energy approximation with correct asymptotic behaviour. *Physical Review A*, 38:3098, 1988.

[43] J. P. Perdew and Y. Wang. Accurate and simple analytic representation of the electron-gas correlation energy. *Physical Review B*, 45:13244, 1992.

[44] J. P Perdew, K. Burke, and M. Ernzerhof. Generalized Gradient Approximation Made Simple. *Phys. Rev. Lett.*, 77:3865, 1996.

[45] P. Dufek, P. Blaha, and K. Schwarz. Applications of Engel and Vosko's generalized gradient approximation in solids. *Phys. Rev. B*, 50:7279, 1994.

[46] A. D. Becke and E. R. Johnson. A simple effective potential for exchange. *J. Chem. Phys.*, 124(22):221101, 2006.

[47] F. Tran and P. Blaha. Accurate Band Gaps of Semiconductors and Insulators with a Semilocal Exchange-Correlation Potential. *Phys. Rev. Lett.*, 102:226401, 2009.

[48] J. E. Jaffe and A. C. Hess. Hartree-Fock study of phase changes in ZnO at high pressure. *Phys. Rev. B*, 48(11):7903, 1993.

[49] V. I. Anisimov, J Zaanen, and O. K. Andersen. Band theory and Mott insulators: Hubbard U instead of Stoner I. *Phys. Rev. B*, 44(3):943, 1991.

[50] F. Tran, P. Blaha, K. Schwarz, and P. Novák. Hybrid exchange-correlation energy functionals for strongly correlated electrons: Applications to transition-metal monoxides. *Phys. Rev. B*, 74:155108, 2006.

[51] V. I. Anisimov, F Aryasetiawan, and A. I. Lichtenstein. First-principles calculations of the electronic structure and spectra of strongly correlated systems: the LDA+U method. *J. Phys: Condens. Matt.*, 9:767, 1997.

[52] O. K. Andersen. Linear methods in band theory. *Phys. Rev. B*, 12(8):3060, 1975.

[53] J. J. Sakurai and J. Napolitano. *Modern Quantum Mechanics*, chapter 5, page 365. Addison-Wesley, San Francisco, CA, 2nd edition, 1994.

[54] E. Merzbacher. *Quantum Mechanics*, chapter 5, page 497. John Wiley & Sons, Inc., Hoboken, NJ, 3rd edition, 1998.

[55] E. McGuire. K-shell Auger transition rates and flurescence yields for elements Be-Ar. *Physical Review*, 185(1):1, 1969.

[56] J. Valjakka, J. Utriainen, T. Åberg, and J. Tulkki. Direction-dependent initial-state relaxation in oxygen K x-ray emission. *Physical Review B*, 32:6892, 1985.

[57] R. D. Cowan. *The theory of atomic structure and spectra*, chapter 4,5. University of California Press, Berkeley, CA, 1981.

[58] I. P. Grant. Relativistic calculation of atomic structures. *Advances in Physics*, 19(82):747, 1970.

[59] A. Neckel, K. Schwarz, R. Eibler, P. Rastl, and P. Weinberger. Elektronische Struktur und Valenzbandspektren einiger metallischer Hartstoffe. *Mikrochim. Act., Suppl.*, 6:257, 1975.

[60] K. Schwarz, A. Neckel, and J. Nordgren. On the x-ray emission spectra from FeAl. *J. Phys. F: Met. Phys.*, 9(12):2509, 1979.

[61] K. Schwarz and E. Wimmer. Electronic structure and x-ray emission spectra of YS in comparison with NbO. *J. Phys. F: Met. Phys.*, 10:1001, 1980.

[62] E. Kurmaev, R. Wilks, A. Moewes, L. Finkelstein, S. Shamin, and J. Kuneš. Oxygen x-ray emission and absorption spectra as a probe of the electronic structure of strongly correlated oxides. *Phys. Rev. B*, 77(16):165127, 2008.

[63] P. J. W. Weijs, M. T. Czyźyk, J. F. Van Acker, W. Speier, J. B. Goedkoop, H. van Leuken, H. J. M. Hendix, R. A. de Groot, G. van der Laan, K. H. J. Buschow, G. Wiech, and J. C. Fuggle. Core-hole effects in the x-ray-absorption spectra of transition-metal silicides. *Phys. Rev. B*, 41(17):11899, 1990.

[64] V. Mauchamp, M. Jaouen, and P. Schattschneider. Core-hole effect in the one-particle approximation revisited from density functional theory. *Phys. Rev. B*, 79(23):235106, 2009.

[65] P. Skytt, P. Glans, D. C. Mancini, J.-H. Guo, N. Wassdahl, J. Nordgren, and Y. Ma. Angle-resolved soft-x-ray fluorescence and absorption study of graphite. *Phys. Rev. B*, 50:10457, 1994.

[66] J. A. Carlisle, E. L. Shirley, E. A. Hudson, L. J. Terminello, T. A. Callcott, J. J. Jia, D. L. Ederer, R. C. C. Perera, and F. J. Himpsel. Probing the graphite band structure with resonant soft-X-ray fluorescence. *Phys. Rev. Lett.*, 74(7):1234, 1995.

[67] F. Acke and I. Panas. Promoting Effects of Na and Fe Impurities on the Catalytic Activity of CaO in the Reduction of NO by CO and H_2. *J. Phys. Chem. B*, 102:5127, 1998.

[68] M. C. Paganini, M. Chiesa, P. Martino, and E. Giamello. EPR Study of the Surface Basicity of Calcium Oxide. 1. The CaONO Chemistry. *J. Phys. Chem. B*, 106:12531, 2002.

[69] V. R. Choudhary, A. M. Rajput, and A. S. Mamman. NiO-Alkaline Earth Oxide Catalysts for Oxidative Methane-to-Syngas Conversion: Influence of Alkaline Earth Oxide on the Surface Properties and Temperature-Programmed Reduction/Reaction by H_2 and Methane. *J. Catal.*, 178:576, 1998.

[70] A. Fujishima and K. Honda. Electrochemical Photolysis of Water at a Semiconductor Electrode. *Nature*, 238:37, 1972.

[71] R. Asahi, T. Morikawa, T. Ohwaki, K. Aoki, and Y. Taga. Visible-light photocatalysis in nitrogen-doped titanium oxides. *Science*, 293:269, 2001.

[72] K. Hashimoto, H. Irie, and A. Fujishima. TiO_2 Photocatalysis: A Historical Overview and Future Prospects. *Jpn. J. Appl. Phys.*, 44:8269, 2005.

[73] M. Imada, A. Fujimori, and Y. Tokura. Metal-insulator transitions. *Rev. Mod. Phys.*, 70(4):1039, 1998.

[74] J. Zaanen, G. A. Sawatzky, and J. W. Allen. Bandgaps and Electronic Structure of Transition-Metal Compounds. *Phys. Rev. Lett.*, 55(4):418, 1985.

[75] G. A. Sawatzky and J. W. Allen. Magnitude and Origin of the Band Gap in NiO. *Phys. Rev. Lett.*, 53(24):2339, 1984.

[76] F. M. F. de Groot, M. Grioni, J. C. Fuggle, J. Ghijsen, G. A. Sawatzky, and H. Petersen. Oxygen 1s x-ray-absorption edges of transition-metal oxides. *Phys. Rev. B*, 40(8):5715, 1989.

[77] D. M. Bagnall, Y. F. Chen, Z. Zhu, T. Yao, S. Koyama, M. Y. Shen, and T. Goto. Optically pumped lasing of ZnO at room temperature. *Appl. Phys. Lett.*, 70(17):2230, 1997.

[78] Ü. Özgür, Ya. I. Alivov, C. Liu, A. Teke, M. A. Reshchikov, S. Doğan, V. Avrutin, S.-J. Cho, and H. Morkoc. A comprehensive review of ZnO materials and devices. *J. Appl. Phys.*, 98:041301, 2005.

[79] Y. Azzaz, S. Kacimi, A. Zaoui, and B. Bouhafs. Electronic properties and stability of ZnO from computational study. *Physica B: Condensed Matter*, 403:3154, 2008.

[80] X. Liu, C. Li, S. Han, J. Han, and C. Zhou. Synthesis and electronic transport studies of CdO nanoneedles. *Appl. Phys. Lett.*, 82(12):1950, 2003.

[81] C. H. Champness and C. H. Chan. Optimization of CdO layer in a Se:CdO photovoltaic cell. *Solar Energy Mater. Solar Cells*, 37:72, 1995.

[82] F. A. Benko and F. P. Koffyberg. Quantum efficiency and optical transitions of CdO photoanodes. *Solid State Commun.*, 57:901, 1986.

[83] H. L. Hartnagel, A. L Dewar, A. K. Jain, and C. Jagadish. *Semiconducting Transparent Thin Films*. IOP Publishing, Bristol, 1995.

[84] C. Kilic and A. Zunger. Origins of Coexistence of Conductivity and Transparency in SnO_2. *Phys. Rev. Lett.*, 88:095501, 2002.

[85] B. J. Ingram, G. B. Gonzalez, D. R. Kammler, M. I. Bertoni, and T. O. Mason. Chemical and Structural Factors Governing Transparent Conductivity in Oxides. *J. Electroceram.*, 13:167, 2004.

[86] M.-M. Bagheri-Mohagheghi and M. Shokooh-Saremi. The effect of high acceptor dopant concentration of Zn^{2+} on electrical, optical and structural properties of the In_2O_3 transparent conducting thin films. *Semicond. Sci. Technol.*, 18:97, 2003.

[87] L. F. J. Piper, A. DeMasi, S. W. Cho, K. E. Smith, F. Fuchs, F. Bechstedt, C. Körber, A. Klein, D. J. Payne, and R. G. Egdell. Electronic structure of In_2O_3 from resonant x-ray emission spectroscopy. *Appl. Phys. Lett.*, 94:022105, 2009.

[88] P. D. C. King, T. D. Veal, F. Fuchs, Ch. Y. Wang, D. J. Payne, A. Bourlange, H. Zhang, G. R. Bell, V. Cimalla, O. Ambacher, R. G. Egdell, F. Bechstedt, and C. F. McConville. Band gap, electronic structure, and surface electron accumulation of cubic and rhombohedral In_2O_3. *Phys. Rev. B*, 79:205211, 2009.

[89] Y. N. Xu and W. Y. Ching. Electronic, optical, and structural properties of some wurtzite crystals. *Phys. Rev. B*, 48:4335, 1993.

[90] R. M. Hazen. Effects of temperature and pressure on the cell dimension and X-ray temperature factors of periclase. *American Mineralogist*, 61:266, 1976.

[91] G. Fiquet, P. Richet, and G. Montagnac. High-temperature thermal expansion of lime, periclase, corundum and spinel. *Physics and Chemistry of Minerals*, 27:103, 1999.

[92] R. W. G. Wyckoff. *Crystal Structures 1.* Interscience Publishers, New York, New York, 2 edition, 1963.

[93] M. Bär, S. Nishiwaki, L. Weinhardt, S. Pookpanratana, O. Fuchs, M. Blum, W. Yang, J. D. Denlinger, W. N. Shafarman, and C. Heske. Depth-resolved band gap in $Cu(In,Ga)(S,Se)_2$ thin films. *Appl. Phys. Lett.*, 93(24):244103, 2008.

[94] K. Kinhara and G. Donnay. Anharmonic thermal vibrations in ZnO. *Can. Mineral.*, 23:647, 1985.

[95] J. Zhang. Room-temperature compressibilities of MnO and CdO: further examination of the role of cation type in bulk modulus systematics. *Phys. Chem. Min.*, 26(8):644, 1999.

[96] K. Aurivillius. Least-Squares Refinement of the Crystal Structures of Orthorhombic HgO and of Hg_2O_2NaI. *Acta Chem. Scand.*, 18:1305, 1964.

[97] A. V. Emeline, G. V. Kataeva, V. K. Ryabchuk, and N. Serpone. Photostimulated Generation of Defects and Surface Reactions on a Series of Wide Band Gap Metal-Oxide Solids. *J. Phys. Chem. B*, 103:9190, 1999.

[98] U. Schönberger and F. Aryasetiawan. Bulk and surface electronic structures of MgO. *Phys. Rev. B*, 52:8788, 1995.

[99] R. C. Whited, C. J. Flaten, and W. C. Walker. Exciton thermoreflectance of MgO and CaO. *Solid State Commun.*, 13:1903, 1973.

[100] A. S. Rao and R. J. Kearney. Logarithmic Derivative Reflectance Spectra of BaO and SrO. *Phys. Stat. Sol. (b)*, 95:243, 1979.

[101] W. H. Strewlow and E. L. Cook. Compilation of Energy Band Gaps in Elemental and Binary Compound Semiconductors and Insulators. *J. Phys. Chem. Ref. Data*, 2:163, 1973.

[102] T. K. Subramanyam, S. Uthanna, and B. Srinivasulu Naidu. Preparation and characterization of CdO films deposited by dc magnetron reactive sputtering. *Mater. Lett.*, 35(3-4):214, 1998.

[103] P.-A. Glans, T. Learmonth, K. Smith, J. Guo, A. Walsh, G. Watson, F. Terzi, and R. Egdell. Experimental and theoretical study of the electronic structure of HgO and Tl_2O_3. *Phys. Rev. B*, 71(23):235109, 2005.

[104] J. Pascual, J. Camassel, and H. Mathieu. Resolved Quadrupolar Transition in TiO_2. *Phys. Rev. Lett.*, 39(23):1490, 1977.

[105] H. Tang, H. Berger, P. E. Schmid, and F. Lévy. Optical properties of anatase (TiO_2). *Solid State Commun.*, 92:267, 1994.

[106] V. Srikant and D. R. Clarke. On the optical band gap of zinc oxide. *J. Appl. Phys*, 83:5447, 1998.

[107] C. Klingshirn. The Luminescence of ZnO under High One- and Two-Quantum Excitation. *Phys. Stat. Sol.*, 71:547, 1975.

[108] R. Sharma, P. P. Das, M. Misra, V. Mahajan, J. P. Bock, S. Trigwell, A. S. Biris, and M. K. Mazumder. Enhancement of the photoelectrochemical conversion efficiency of nanotubular TiO_2 photoanodes using nitrogen plasma assisted surface modification. *Nanotechnology*, 20:075704, 2009.

[109] D. Y. C. Leung, X. Fu, C. Wang, M. Ni, M. K. H. Leung, X. Wang, and X. Fu. Hydrogen Production over Titania-Based Photocatalysts. *ChemSusChem*, 3:681, 2010.

[110] A. L. Linsebigler, G. Lu, and J. T. Yates. Photocatalysis on TiO_n Surfaces: Principles, Mechanisms, and Selected Results. *Chem. Rev.*, 95(3):735, 1995.

[111] L. E. Orgel. The stereochemistry of B subgroup metals. Part II. The inert pair. *J. Chem. Soc.*, page 3815, 1959.

[112] A. Walsh and G. W. Watson. Influence of the anion on lone pair formation in Sn(II) monochalcogenides: a DFT study. *J. Phys. Chem. B*, 109(40):18868, 2005.

[113] A. Walsh and G. W. Watson. The origin of the stereochemically active Pb(II) lone pair: DFT calculations on PbO and PbS. *J. Solid State Chem.*, 178(5):1422, 2005.

[114] A. Walsh, G. Watson, D. Payne, R. Edgell, J. Guo, P.-A. Glans, T. Learmonth, and K. Smith. Electronic structure of the α and δ phases of Bi_2O_3: A combined ab initio and x-ray spectroscopy study. *Phys. Rev. B*, 73(23):235104, 2006.

[115] H. P. Savakus, K. A. Klicker, and R. E. Newnham. PZT-epoxy piezoelectric transducers: A simplified fabrication procedure. *Mat. Res. Bul.*, 16:677, 1985.

[116] A. M. Glazer and S. A. Mabud. Powder profile refinement of lead zirconate titanate at several temperatures. II. Pure $PbTiO_3$. *Acta Cryst. B*, 34:1065, 1978.

[117] R. J. Swope, J. R. Smyth, and A. C. Larson. H in rutile-type compounds: I. Single-crystal neutron and X-ray diffraction study of H in rutile. *Am. Mineral.*, 80:448, 1995.

[118] P. Boher, P. Garnier, J. R. Gavarri, and A. W. Hewat. Monoxyde quadratique PbOα(I): Description de la transition structurale ferroélastique. *J. Solid State Chem.*, 57:343, 1985.

[119] K. Momma and F. Izumi. *VESTA3* for three-dimensional visualization of crystal, volumetric and morphology data. *J. Appl. Cryst.*, 44(6):1272, 2011.

[120] N. Kumada, Y. Yonesaki, T. Takei, N. Kinomura, and S. Wada. Preparation and crystal structure of a new tin titanate containing Sn^{2+}; Sn_2TiO_4. *Mater. Res. Bull.*, 44:1298, 2009.

[121] S. Ohara, H. Takizawa, and Y. Hayashi. Solid-state Synthesis of Sn_2TiO_4: A New Synthetic Strategy for Direct Synthesis of Sn^{2+} Compounds Using Microwave Irradiation. *Chem. Lett.*, 39(4):364, 2010.

[122] C. R. A. Catlow, Z. X. Guo, M. Miskufova, S. A. Shevlin, A. G. H. Smith, A. A. Sokol, A. Walsh, D. J. Wilson, and S. M. Woodley. Advances in computational studies of energy materials. *Phil. Trans. R. Soc. A*, 368:3379, 2010.

[123] X. Wang, F. X. Zhang, I. Loa, K. Syassen, M. Hanfland, and Y.-L. Mathis. Structural properties, infrared reflectivity, and Raman modes of SnO at high pressure. *phys. stat. sol. (b)*, 241(14):3168, 2004.

[124] T. Kidchob, L. Malfatti, D. Marongiu, S. Enzo, and P. Innocenzi. Sol-Gel Processing of $Bi_2Ti_2O_7$ and $Bi_2Ti_4O_{11}$ Films with Photocatalytic Activity. *J. Am. Ceram. Soc.*, 93(9):2897, 2010.

[125] V. Kahlenberg and H. Böhm. The structures of α- and β-$Bi_2Ti_4O_{11}$. *Acta Cryst. B*, 51:11, 1995.

[126] Y. Noguchi, T. Goto, M. Miyamama, A. Hoshikawa, and T. Kamiyama. Ferroelectric distortion and electronic structure in $Bi_4Ti_3O_{12}$. *J. Electroceram.*, 21:49, 2008.

[127] K. R. Chakraborty, S. N. Achary, S. J. Patwe, P. S. R. Krishna, A. B. Shinde, and A. K. Tyagi. Low temperature neutron diffraction studies on $Bi_4Ti_3O_{12}$. *Ceram. International*, 33:601, 2007.

[128] Y.-I. Kim and M. K. Jeon. Combined structural refinement of $Bi_4Ti_3O_{12}$ using X-ray and neutron powder diffraction data. *Mater. Lett.*, 58:1889, 2004.

[129] G Malmros. The Crystal Structure of α-Bi_2O_3. *Acta Chem. Scand.*, 24:384, 1970.

[130] H. Gobrecht, S. Seeck, H.-E. Bergt, A. Märtens, and K. Kossmann. Über Untersuchungen an Wismutoxid-Aufdampfschichten. I. Herstellung sowie elektrische und optische Eigenschaften. *phys. stat. sol.*, 33:599, 1969.

[131] Y. Ogo, H. Hiramatsu, K. Nomura, H. Yanagi, T. Kamiya, M. Hirano, and H. Hosono. p-channel thin-film transistor using p-type oxide semiconductor, SnO. *Appl. Phys. Lett.*, 93:032113, 2008.

[132] W. L. Warren, J. Robertson, D. Dimos, B. A. Tuttle, G. E. Pike, and D. A. Payne. Pb displacements in Pb(Zr,Ti)O_3 perovskites. *Phys. Rev. B*, 53(6):3080, 1996.

[133] R. C. Keezer, D. L. Bowmand, and J. H. Becker. Electrical and Optical Properties of Lead Oxide Single Crystals. *J. Appl. Phys.*, 39(4):2062, 1968.

[134] H. Zhang, G. Chen, and X. Li. *Solid State Ionics*, 180:1599, 2009.

[135] A. Schleife, F. Fuchs, J. Furthmüller, and F. Bechstedt. First-principles study of ground- and excited-state properties of MgO, ZnO, and CdO polymorphs. *Phys. Rev. B*, 73:245212, 2006.

[136] C. Ye, Y. Wang, Y. Ye, J. Zhang, and G. H. Li. Preparation and photoluminescence of undoped $ZnTiO_3$ thin films. *J. Appl. Phys.*, 106:033520, 2009.

[137] F. H. Dulin and D. E. Rase. Phase Equilibria in the System ZnO-$TiO_2$4. *J. Am. Ceram. Soc.*, 43(3):125, 1960.

[138] S. A. Mayén-Hernández, J. Santos-Cruz, G. Torres-Delgado, R. Castanedo-Pérez, J. Márquez-Marín, J. G. Mendoza-Alvarez, and O. Zelaya-Angel. $CdTiO_3$ thin films prepared by solgel method using a simpler route. *Surf. Coat. Tech.*, 200(11):3567, 2006.

[139] Y. J. Shan, Y. Inaguma, H. Tetsuka, T. Nakamura, and L. J. Gauckler. Synthesis and Phase Transition of $HgTiO_3$. *Ferroelectrics*, 337(1):71, 2006.

[140] O. Yamaguchi, M. Morimi, H. Kawabata, and K. Shimizu. Formation and Transformation $ZnTiO_3$. *J. Am. Ceram. Soc.*, 70:C97, 1987.

[141] W.-J. Yin, S.-H. Wei, M. M. Al-Jassim, and Y. Yan. Origin of the diverse behavior of oxygen vacancies in ABO_3 perovskites: A symmetry based analysis. *Phys. Rev. B*, 85:201201(R), 2012.

[142] U. Steinike and B. Wallis. Formation and Structure of Ti — Zn-Oxides. *Cryst. Res. Technol.*, 32:187, 1997.

[143] I. Bobowska, A. Opasinska, A. Wypych, and P. Wojciechowski. Synthesis and dielectric investigations of $ZnTiO_3$ obtained by a soft chemistry route. *Mat. Chem. Phys.*, 134(1):87, 2012.

[144] C. Ye, S. S. Pan, X. M. Teng, H. T. Fan, and G. H. Li. Preparation and optical properties of nanocrystalline thin films in the ZnO-TiO_2 system. *Appl. Phys. A*, 2008:375, 90.

[145] W. Bronger, P. Müller, R. Höppner, and H.-U. Schuster. Zur Charakterisierung der magnetischen Eigenschaften von NaMnP, NaMnAs, NaMnSb, NaMnBi, LiMnAs und KMnAs über Neutronenbeugungsexperimente. *Z. anorg. allg. Chem.*, 539:175, 1986.

[146] Y. Kamihara, H. Hiramatsu, M. Hirano, R. Kawamura, H. Yanagi, T. Kamiya, and H. Hosono. Iron-based layered superconductor: LaOFeP. *J. Am. Chem. Soc.*, 128(31):10012, 2006.

[147] Y. Kamihara, T. Watanabe, M. Hirano, and H. Hosono. Iron-based layered superconductor $La[O_{1-x}F_x]FeAs$ (x = 0.05-0.12) with T_c = 26 K. *J. Am. Chem. Soc.*, 130(11):3296, 2008.

[148] L. Petit, A. Svane, Z. Szotek, and W. Temmerman. First-principles study of rare-earth oxides. *Phys. Rev. B*, 72(20):205118, 2005.

[149] L. Hozoi and P. Fulde. Correlated Electrons in Fe-As Compounds: A Quantum Chemical Perspective. *Phys. Rev. Lett.*, 102(13):136405, 2009.

[150] M. Aichhorn, L. Pourovskii, V. Vildosola, M. Ferrero, O. Parcollet, T. Miyake, A. Georges, and S. Biermann. Dynamical mean-field theory within an augmented plane-wave framework: Assessing electronic correlations in the iron pnictide LaFeAsO. *Phys. Rev. B*, 80(8):085101, 2009.

[151] M. M. Qazilbash, J. J. Hamlin, R. E. Baumbach, Lijun Zhang, D. J. Singh, M. B. Maple, and D. N. Basov. Electronic correlations in the iron pnictides. *Nat. Phys.*, 5(9):647, 2009.

[152] D. J. Singh and M.-H. Du. Density Functional Study of $LaFeAsO_{1-x}F_x$: A Low Carrier Density Superconductor Near Itinerant Magnetism. *Phys. Rev. Lett.*, 100(23):237003, 2008.

[153] A. Lukoyanov, S. Skornyakov, J. McLeod, M. Abu-Samak, R. Wilks, E. Kurmaev, A. Moewes, N. Skorikov, Yu. Izyumov, L. Finkelstein, V. Anisimov, and D. Johrendt. Correlation effects in Ni3d states of LaNiPO. *Phys. Rev. B*, 81(23):235121, 2010.

[154] N. Ni, S. Nandi, A. Kreyssig, A. Goldman, E. Mun, S. Budko, and P. Canfield. First-order structural phase transition in $CaFe_2As_2$. *Phys. Rev. B*, 78(1):014523, 2008.

[155] M. Torikachvili, S. Budko, N. Ni, and P. Canfield. Pressure Induced Superconductivity in $CaFe_2As_2$. *Phys. Rev. Lett.*, 101(5):057006, 2008.

[156] T. Yildirim. Strong Coupling of the Fe-Spin State and the As-As Hybridization in Iron-Pnictide Superconductors from First-Principle Calculations. *Phys. Rev. Lett.*, 102(3):0370030, 2009.

[157] A. I. Goldman, D. N. Argyriou, B. Ouladdiaf, T. Chatterji, A. Kreyssig, S. Nandi, N. Ni, S. L. Bud'ko, P. C. Canfield, and R. J. McQueeney. Lattice and magnetic instabilities in $CaFe_2As_2$: A single-crystal neutron diffraction study. *Phys. Rev. B*, 78:100506, 2008.

[158] E. J. McGuire. Atomic L-Shell Coster-Kronig, Auger, and Radiative Rates and Flourescence Yields for Na-Th. *Phys. Rev. A*, 3:587, 1971.

[159] P. C. Canfield, S. L. Bud'ko, N. Ni, J. Q. Yan, and A. Kracher. Decoupling of the superconducting and magnetic/structural phase transitions in electron-doped $BaFe_2As_2$. *Phys. Rev. B*, 80:060501(R), 2009.

[160] C. W. Chu and B. Lorenz. High pressure studies on Fe-pnictide superconductors. *Physica C*, 469:385, 2009.

[161] A. F. Kemper, C. Cao, P. J. Hirschfeld, and H.-P. Cheng. Effects of cobalt doping and three-dimensionality in $BaFe_2As_2$. *Phys. Rev. B*, 80:104511, 2009.

[162] E. M. Bittar, C. Adriano, T. M. Garitezi, P. F. S. Rosa, L. Mendonca-Ferreira, F. Garcia, G. de M. Azevedo, P. G. Pagliuso, and E. Granado. Co-Substitution Effects on the Fe Valence in the $BaFe_2As_2$ Superconducting Compound: A Study of Hard X-Ray Absorption Spectroscopy. *Phys. Rev. Lett.*, 107:267402, 2011.

[163] H. Wadati, I. Elfimov, and G. A. Sawatzky. Where Are the Extra d Electrons in Transition-Metal-Substituted Iron Pnictides? *Phys. Rev. Lett.*, 105:157004, 2010.

[164] A. Khasanov, S. C. Bhargava, J. G. Stevens, J. Jiang, J. D. Weiss, E. E. Hellstrom, and A. Nath. Mössbauer studies of the superconducting cobalt/nickel-doped $BaFe_2As_2$. Whither go the injected electron(s)? *J. Phys.: Condens. Matter*, 23:202201, 2011.

[165] F. Rullier-Albenque, D. Colson, A. Forget, and H. Alloul. Hall Effect and Resistivity Study of the Magnetic Transition, Carrier Content, and Fermi-Liquid Behavior in $Ba(Fe_{1-x}Co_x)_2As_2$. *Phys. Rev. Lett.*, 103:057001, 2009.

[166] N. P. Butch, S. R. Saha, X. H. Zhang, K. Kirshenbaum, R. L. Greene, and J. Paglione. Effective carrier type and field dependence of the reduced- T_c superconducting state in $SrFe_{2x}Ni_xAs_2$. *Phys. Rev. B*, 81:024518, 2010.

[167] L. Fang, H. Luo, P. Cheng, Z. Wang, Y. Jia, G. Mu, B. Shen, I. I. Mazin, L. Shan, C. Ren, and H.-H. Wen. Roles of multiband effects and electron-hole asymmetry in the superconductivity and normal-state properties of $Ba(Fe_{1-x}Co_x)_2As_2$. *Phys. Rev. B*, 80:140508, 2009.

[168] F. M. F de Groot. Multiplet effects in X-ray spectroscopy. *Coordin. Chem. Rev.*, 249:31, 2005.

[169] W. L. Yang, A. P. Sorini, C.-C. Chen, B. Moritz, W.-S. Lee, F. Vernay, P. Olalde-Velasco, J. D. Denlinger, B. Delley, J.-H. Chu, J. G. Analytis, I. R. Fisher, Z. A. Ren, J. Yang, W. Lu, Z. X. Zhao, J. van den Brink, Z. Hussain, Z.-X. Shen, and T. P. Devereaux. Evidence for weak electronic correlations in iron pnictides. *Phys. Rev. B*, 80:014508, 2009.

[170] G. Lee and S.-J. Oh. Electronic structures of NiO, CoO, and FeO studied by 2p core-level x-ray photoelectron spectroscopy. *Phys. Rev. B*, 43:14674, 1991.

[171] N. Ni, S. L. Bud'ko, A. Kreyssig, S. Nandi, G. E. Rustan, A. I. Goldman, S. Gupta, J. D. Corbett, A. Kracher, and P. C. Canfield. Anisotropic thermodynamic and transport properties of single-crystalline $Ba_{1-x}K_xFe_2As_2$ (x=0 and 0.45). *Phys. Rev. B*, 78:014507, 2008.

[172] J. Hu, D. Payne, R. Egdell, P.-A. Glans, T. Learmonth, K. Smith, J. Guo, and N. Harrison. On-site interband excitations in resonant inelastic x-ray scattering from Cu_2O. *Phys. Rev. B*, 77(15):155115, 2008.

[173] M. Grioni, J. F. van Acker, M. T. Czyžyk, and J. C. Fuggle. Unoccupied Electronic structure and core-hole effects in the x-ray-absorption spectra of Cu2O. *Phys. Rev. B*, 45:3309, 1992.

[174] J.-T. Han, J.-S. Zhou, J.-G. Cheng, and J. B. Goodenough. A New Pnictide Superconductor without Iron. *J. Am. Chem. Soc.*, 132(3):908, 2010.

[175] D. J. Singh. Electronic structure of $BaCu_2As_2$ and $SrCu_2As_2$: sp-band metals. *Phys. Rev. B*, 79(15):153102, 2009.

[176] V. K. Anand and D. C. Johnston. Observation of a phase transition at 55 K in single-crystal $CaCu_{1.7}As_2$. *Phys. Rev. B*, 86(21):214501, 2012.

[177] V. K. Anand, P. Kanchana Perera, Abhishek Pandey, R. J. Goetsch, A. Kreyssig, and D. C. Johnston. Crystal growth and physical properties of $SrCu_2As_2$, $SrCu_2Sb_2$, and $BaCu_2Sb_2$. *Phys. Rev. B*, 85(21):214523, 2012.

[178] I. Pilchowski and A. Mewis. Ternäre BaAl4-Varianten. Darstellung und Struktur von CaCu2As2, Ca2Cu6P5 und Ba2Cu3P4. *Z. anorg. allg. Chem.*, 581(1):173, 1990.

[179] C. W. Chu, F. Chen, M. Gooch, A. M. Guloy, B. Lorenz, B. Lv, K. Sasmal, Z. J. Tang, J. H. Tapp, and Y. Y. Xue. The synthesis and characterization of LiFeAs and NaFeAs. *Physica C*, 469(9-12):326, 2009.

[180] M. Wang, M. Wang, H. Miao, S. V. Carr, D. L. Abernathy, M. B. Stone, X. C. Wang, L. Xing, C. Q. Jin, X. Zhang, J. Hu, T. Xiang, H. Ding, and P. Dai. Effect of Li-deficiency impurities on the electron-overdoped LiFeAs superconductor. *Phys. Rev. B*, 86(14):144511, 2012.

[181] D. R. Parker, M. J. Pitcher, P. J. Baker, I. Franke, T. Lancaster, S. J. Blundell, and S. J. Clarke. Structure, antiferromagnetism and superconductivity of the layered iron arsenide NaFeAs. *Chem. Commun.*, 16:2189, 2009.

[182] X Wang, Q Liu, Y Lv, W Gao, L Yang, R Yu, F Li, and C Jin. The superconductivity at 18 K in LiFeAs system. *Solid State Commun.*, 148(11-12):538, 2008.

[183] A. P. Wijnheijmer, X. Martí, V. Holý, M. Cukr, V. Novák, T. Jungwirth, and P. M. Koenraad. Scanning tunneling microscopy reveals LiMnAs is a room temperature antiferromagnetic semiconductor. *Appl. Phys. Lett.*, 100(11):112107, 2012.

[184] Z. Deng, C. Q. Jin, Q. Q. Liu, X. C. Wang, J. L. Zhu, S. M. Feng, L. C. Chen, R. C. Yu, C. Arguello, T. Goko, F. Ning, J. Zhang, Y. Wang, A. A. Aczel, T. Munsie, T. J. Williams, G. M. Luke, T. Kakeshita, S. Uchida, W. Higemoto, T. U. Ito, B. Gu, S. Maekawa, G. D. Morris, and Y. J. Uemura. Li(Zn,Mn)As as a new generation ferromagnet based on a I-II-V semiconductor. *Nat. Commun.*, 2:422, 2011.

[185] T. Jungwirth, V. Novák, X. Martí, M. Cukr, F. Máca, A. Shick, J. Mašek, P. Horodyská, P. Němec, V. Holý, J. Zemek, P. Kužel, I. Němec, B. Gallagher, R. Campion, C. Foxon, and J. Wunderlich. Demonstration of molecular beam epitaxy and a semiconducting band structure for I-Mn-V compounds. *Phys. Rev. B*, 83(3):035321, 2011.

[186] I. I. Mazin and M. D. Johannes. A key role for unusual spin dynamics in ferropnictides. *Nat. Phys.*, 5(2):141, 2008.

[187] D. J. Singh. Electronic structure and doping in $BaFe_2As_2$ and LiFeAs: Density functional calculations. *Phys. Rev. B*, 78(9):094511, 2008.

[188] P. A. Lee, N. Nagaosa, and X.-G. Wen. Doping a Mott insulator: Physics of high-temperature superconductivity. *Rev. Mod. Phys.*, 78:17, 2006.

[189] H. Gretarsson, A. Lupascu, Jungho Kim, D. Casa, T. Gog, W. Wu, S. R. Julian, Z. J. Xu, J. S. Wen, G. D. Gu, R. H. Yuan, Z. G. Chen, N.-L. Wang, S. Khim, K. H. Kim, M. Ishikado, I. Jarrige, S. Shamoto, J.-H. Chu, I. R. Fisher, and Young-June Kim. Revealing the dual nature of magnetism in iron pnictides and iron chalcogenides using x-ray emission spectroscopy. *Phys. Rev. B*, 84:100509, 2011.

[190] S. P. Cramer, F. M. F. DeGroot, Y. Ma, C. T. Chen, F. Sette, C. A. Kipke, D. M. Eichhorn, M. K. Chan, and W. H. Armstrong. Ligand field strengths and oxidation states from manganese L-edge spectroscopy. *J. Am. Chem. Soc.*, 113(21):7937, 1991.

[191] D.-Yong Cho, S.-J. Oh, Dong Kim, A. Tanaka, and J.-H. Park. Investigation of local symmetry effects on the electronic structure of manganites: Hexagonal $YMnO_3$ versus orthorhombic $LaMnO_3$. *Phys. Rev. B*, 79(3):035116, 2009.

[192] G. Ghiringhelli, M. Matsubara, C. Dallera, F. Fracassi, A. Tagliaferri, N. Brookes, A. Kotani, and L. Braicovich. Resonant inelastic x-ray scattering of MnO: $L_{2,3}$ edge measurements and assessment of their interpretation. *Phys. Rev. B*, 73(3):035111, 2006.

[193] L. A. J. Garvie and A. J. Craven. High-resolution parallel electron energy-loss spectroscopy of Mn $L_{2,3}$-edges in inorganic manganese compounds. *Phys. Chem. Min.*, 21(4):191, August 1994.

[194] Y. Yonamoto, T. Yokoyama, K. Amemiya, D. Matsumura, and T. Ohta. Magnetism of an ultrathin Mn film on Co(100) and the effect of oxidation studied by x-ray magnetic circular dichroism. *Phys. Rev. B*, 63(21):214406, 2001.

[195] L. de Medici, J. Mravlje, and A. Georges. Janus-Faced Influence of Hunds Rule Coupling in Strongly Correlated Materials. *Phys. Rev. Lett.*, 107(25):256401, 2011.

[196] M. Yablonskikh, Yu. Yarmoshenko, V. Grebennikov, E. Kurmaev, S. Butorin, L.-C. Duda, J. Nordgren, S. Plogmann, and M. Neumann. Origin of magnetic circular dichroism in soft x-ray fluorescence of Heusler alloys at threshold excitation. *Phys. Rev. B*, 63(23):235117, 2001.

[197] J. Li, S.-H. Wei, S.-S. Li, and J.-B. Xia. Design of shallow acceptors in ZnO: First-principles band-structure calculations. *Phys. Rev. B*, 74(8):081201(R), 2006.

[198] D. Karmakar, S. Mandal, R. Kadam, P. Paulose, A. Rajarajan, T. Nath, A. Das, I. Dasgupta, and G. Das. Ferromagnetism in Fe-doped ZnO nanocrystals: Experiment and theory. *Phys. Rev. B*, 75(14):144404, 2007.

[199] S. F. Bartram and R. A. Slepetys. Compound Formation and Crystal Structure in the System ZnO-TiO_2. *J. Am. Ceram. Soc.*, 44(10):493, 1961.

Appendix A

Copyright from Published Work

As mentioned in the relevant sections, some of the data reported herein has been published in academic journals prior to the completion of this thesis. Some of the figures found herein are similar to those from a previously published paper that I authored or co-authored, however all figures in this thesis have been at least slightly modified (and many extensively modified) from their previously published form. The figures present in this thesis are all permitted by the copyright agreements from the journals in question.

For reference, these copyright agreements are given below.

A.1 Physical Review B Copyright Agreement

The transfer of copyright agreement for Physical Review B can be found online at: `http://prb.aps.org/authors/transfer-of-copyright-agreement`. This agreement holds for References [15, 18, 19, 21, 23].

The agreement reads as follows:

> Copyright to the unpublished and original article submitted by the author(s), the abstract forming part thereof, and any subsequent errata (collectively, the "Article") is hereby transferred to the American Physical Society (APS) for the full term thereof throughout the world, subject to the Author Rights (as hereinafter defined) and to acceptance of the Article for publication in a journal of APS. This transfer of copyright includes all material to be published as part of the Article (in any medium), including but not limited to tables, figures, graphs, movies, other multimedia files, and all supplemental materials. APS shall have the right to register copyright to the Article in its name as claimant, whether separately or as part of the journal issue or other medium in which the Article is included. The author(s), and in the case of a Work Made For Hire, as defined in the U.S. Copyright Act, 17 U.S.C. §101, the employer, shall have the following rights (the "Author Right"):
>
> 1. All proprietary rights other than copyright, such as patent rights.
> 2. The nonexclusive right, after publication by APS, to give permission to third parties to republish print versions of the Article or a translation thereof, or excerpts therefrom, without obtaining permission from APS, provided the APS-prepared version is not used for this purpose, the Article is not republished in another journal, and the third party does not charge a fee. If the APS version is used, or the third party republishes in a publication or product charging a fee for use, permission from APS must be obtained.

3. The right to use all or part of the Article, including the APS-prepared version without revision or modification, on the author(s)' web home page or employer's website and to make copies of all or part of the Article, including the APS-prepared version without revision or modification, for the author(s)' and/or the employer's use for educational or research purposes.

4. The right to post and update the Article on free-access e-print servers as long as files prepared and/or formatted by APS or its vendors are not used for that purpose. Any such posting made or updated after acceptance of the Article for publication shall include a link to the online abstract in the APS journal or to the entry page of the journal. If the author wishes the APS-prepared version to be used for an online posting other than on the author(s)' or employer's website, APS permission is required; if permission is granted, APS will provide the Article as it was published in the journal, and use will be subject to APS terms and conditions.

5. The right to make, and hold copyright in, works derived from the Article, as long as all of the following conditions are met: (a) at least one author of the derived work is an author of the Article; (b) the derived work includes at least ten (10) percent of new material not covered by APS's copyright in the Article; and (c) the derived work includes no more than fifty (50) percent of the text (including equations) of the Article. If these conditions are met, copyright in the derived work rests with the authors of that work, and APS (and its successors and assigns) will make no claim on that copyright. If these conditions are not met, explicit APS permission must be obtained. Nothing in this Section shall prevent APS (and its successors and assigns) from exercising its rights in the Article.

6. If the Article was prepared under a U.S. Government contract, the government shall have the rights under the copyright to the extent required by the contract.

All copies of part or all of the Article made under any of the Author Rights shall include the appropriate bibliographic citation and notice of the APS copyright. By signing this Agreement, the author(s), and in the case of a Work Made For Hire, the employer, jointly and severally represent and warrant that the Article is original with the author(s) and does not infringe any copyright or violate any other right of any third parties, and that the Article has not been published elsewhere, and is not being considered for publication elsewhere in any form, except as provided herein. If each author's signature does not appear [below], the signing author(s) represent that they sign this Agreement as authorized agents for and on behalf of all authors who have the legal right to transfer copyright and that this Agreement and authorization is made on behalf of the same. The signing author(s) (and, in the case of a Work Made For Hire, the signing employer) also represent and warrant that they have the full power to enter into this Agreement and to make the grants contained herein.

A.2 The Journal of Physics: Condensed Matter Copyright Agreement

The transfer of copyright agreement for the Journal of Physics: Condensed Matter can be found online at: `http://authors.iop.org/atom/help.nsf/0/F20EC7D4A1A670AA80256F1C0053EEFF?OpenDocument`. This agreement holds for References [20, 22].

The agreement reads as follows:

1. IOP Publishing Limited ("IOP") agrees to publish"the Article" written by "the Named Authors" in the the Journal of Physics: Condensed Matter ("the Journal")
2. Transfer of Copyright Agreement
   (a) On acceptance for publication the undersigned author(s) ("Author") of the Article assigns exclusively to IOP worldwide copyright in the Article for the full term and for all media and formats in all material published as part of the Article, which expression includes but is not limited to the text, abstract, tables, figures, graphs, video abstracts and other multimedia content but excludes any other item referred to as supplementary material. For the avoidance of doubt, copyright does not subsist in any fundamental data underlying the Article and nothing in this Agreement is intended to limit access to or use of such data.
   (b) If any of the Named Authors are UK Government employees, on acceptance for publication the Author shall grant IOP a royalty free exclusive licence for the full term of copyright for all media and formats to do in relation to the Article all acts restricted by copyright worldwide.
   (c) On acceptance for publication the Author shall grant IOP a royalty free non-exclusive licence for the full term of copyright for all media and formats to do in relation to any supplementary material not deemed to be part of the Article all acts restricted by copyright worldwide.
3. Author Rights
   (a) IOP grants the Named Authors the rights specified in 3(b), 3(c) and 3(d). All such rights must be exercised for non-commercial purposes, if possible should display citation information and IOP's copyright notice, and for electronic use best efforts must be made to include a link to the online abstract in the Journal. Exercise of the rights in 3(c) and 3(d) additionally must not use the final published IOP format but the Named Author's own format (which may include amendments made following peer review, but not any editing, typesetting or other changes made by IOP) (the "Accepted Manuscript").
   (b) The rights are:
      i. To make copies of the Article (all or part) for teaching purposes;
      ii. To include the Article (all or part) in a research thesis or dissertation;

iii. To make oral presentation of the Article (all or part) and to include a summary and/or highlights of it in papers distributed at such presentations or in conference proceedings; and

iv. All proprietary rights other than copyright.

(c) The additional rights are to:

i. Use the Accepted Manuscript (all or part) without modification in personal compilations of a Named Author's own works (provided not created by a third party publisher); and

ii. Include the Accepted Manuscript (all or part) on a Named Author's own personal website

(d) In addition to the above, no sooner than 12 months from the date of first publication of the Article, the Named Authors may:

i. Include the Accepted Manuscript (all or part) on websites of the institution (including its repository) where a Named Author worked when research for the Article was carried out; and

ii. Include the Accepted Manuscript (all or part) on third party websites including e-print servers, but not on other publisher's websites.

4. Signature

(a) In signing this Agreement the Author represents and warrants that the Article is the original work of the Named Authors, it has not been published previously in any form (other than as permitted under 3(b)(ii), 3(c) and 3(d) which fact has been notified to IOP Publishing Ltd in writing), all Named Authors have participated sufficiently in the conception and writing of the Article, have received the final version of the Article, agree to its submission and take responsibility for it, and submission has been approved as necessary by the authorities at the establishment where the research was carried out.

(b) The Author warrants that he/she signs this Agreement as authorised agent for all Named Authors and has the full power to enter into this Agreement and to make the grants it contains, that the Article has not been and will not be submitted to another publisher prior to withdrawal or rejection, it does not infringe any third party rights, it contains nothing libellous or unlawful, all factual statements are to the best of the Author's knowledge true or based on valid research conducted according to accepted norms, and all required permissions have been obtained in writing.

(c) All Named Authors assert their moral rights.

(d) Each of the Named Authors consents to the publication and processing by IOP of their email addresses.

A.3 The Journal of Physical Chemistry C Copyright Agreement

The transfer of copyright agreement for the Journal of Physical Chemistry C can be found online at: http://pubs.acs.org/paragonplus/copyright/jpa_form_a.pdf. This agreement holds for Reference [17].

The portion of this agreement relevant to the present circumstances reads as follows:

1. Copyright
   (a) Submitted Work: The Corresponding Author, with the consent of all coauthors, hereby transfers to the ACS the copyright ownership in the referenced Submitted Work, including all versions in any format now known or hereafter developed. If the manuscript is not accepted by ACS or withdrawn prior to acceptance by ACS, this transfer will be null and void.
   (b) Supporting Information: The copyright ownership transferred to ACS in any copyrightable[1] Supporting Information accompanying the Submitted Work is nonexclusive. The Author and the ACS agree that each has unlimited use of Supporting Information. Authors may use or authorize the use of material created by the Author in the Supporting Information associated with the Submitted or Published Work for any purpose and in any format.
2. Permitted Uses by Author(s)
   (a) Reuse/Republication of the Entire Work in Theses or Collections:
      i. Authors may reuse all or part of the Submitted, Accepted or Published Work in a thesis or dissertation that the Author writes and is required to submit to satisfy the criteria of degree-granting institutions. Such reuse is permitted subject to the ACS' "Ethical Guidelines to Publication of Chemical Research" (http://pubs.acs.org/ethics); the Author should secure written confirmation (via letter or email) from the respective ACS journal editor(s) to avoid potential conflicts with journal prior publication/embargo policies. Appropriate citation of the Published Work must be made. If the thesis or dissertation to be published is in electronic format, a direct link to the Published Work must also be included using the ACS Articles on Request author-directed link (see http://pubs.acs.org/page/policy/articlesonrequest/index.html).
      ii. Authors also may reuse the Submitted, Accepted, or Published work in printed collections that consist solely of the Author's own writ-

[1] Title 17 of the United States Code defines copyrightable material as "original works of authorship fixed in any tangible medium of expression" (Chapter 1, Section 102). To learn more about copyrightable material see "Frequently Asked Questions about Copyright" on the Publications Division website, at http://pubs.acs.org/page/copyright/learning_module/module.html.

ings; if such collections are to be posted online or published in an electronic format, please contact ACS at copyright@acs.org to inquire about terms for licensed electronic use.

(b) Reuse of Figures, Tables, Artwork, and Text Extracts in Future Works:

i. Authors may reuse figures, tables, artwork, illustrations, text extracts of up to 400 words, and data from the Author's Submitted, Accepted, or Published Work in which the ACS holds copyright for teaching or training purposes, in presentations at conferences and seminars, in subsequent scholarly publications of which they are an Author, and for posting on the Author's personal website, university networks, or primary employer's institutional websites, and conference websites that feature presentations by the Author(s) provided the following conditions are met:

- Appropriate citation to the Published Work is given
- Modifications to the presentation of previously published data in figures and tables are noted and distinguished from any new data not contained in the Published Work, and
- Reuse is not to illustrate news stories unrelated to the Published Work
- Web posting by the Author(s) is for non-commercial purposes.

ii. To reuse figures, tables, artwork, illustrations, and text from ACS Published Works in general, ACS requests that interested parties use the Copyright Clearance Center Rightslink service. For information see http://pubs.acs.org/page/copyright/rightslink.html General ACS permission information can be found at http://pubs.acs.org/page/copyright/permissions.html.

The right to reproduce these data in my thesis was confirmed via email by editor Prof. Kenneth Jordan (jphyschm@pitt.edu). More information is available at: http://pubs.acs.org/userimages/ContentEditor/1218205107465/dissertation.pdf.

A.4 SPIE Proceedings Copyright Agreement

The transfer of copyright agreement for SPIE Proceedings can be found online at: http://spie.org/x1125.xml. This agreement holds for Reference [16].

The portion of this agreement relevant to the present circumstances reads as follows:

> Information for authors reproducing their own SPIE material As stated in the SPIE Transfer of Copyright agreement, authors, or their employers in the case of works made for hire, retain the following rights:
>
> - All proprietary rights other than copyright, including patent rights.
> - The right to make and distribute copies of the Paper for internal purposes.
> - The right to use the material for lecture or classroom purposes.

- The right to prepare derivative publications based on the Paper, including books or book chapters, journal papers, and magazine articles, provided that publication of a derivative work occurs subsequent to the official date of publication by SPIE.

Thus, authors may reproduce figures and text in new publications. The SPIE source publication should be referenced.

The right to reproduce these data in my thesis was confirmed via email by Karen Thomas (`karent@spie.org`) on behalf of Eric Pepper, the Director of Publications for SPIE.

Appendix B

Basis Sets used in WIEN2k

This appendix explicitly derives the coefficients used in the basis sets for WIEN2k. For more details see References [14, 35, 38–40].

In WIEN2k, the electronic states are denoted by band indices n, a set of points within the first Brillouin zone $\{\vec{k}\}$, and a set of reciprocal lattice vectors $\{\vec{G}\}$. Each atomic site t has a an atomic sphere radius r_{MT}^t, while the unit cell has a volume V.

Each band n and k-point $\vec{k}$ is defined by a wavefunction $\psi_{\vec{k}}^n(\vec{r})$. These wavefunctions are composed of a basis of trial wavefunctions as follows:

$$\psi_{\vec{k}}^n(\vec{r}) = \sum_{\vec{G}} c_{\vec{G}}^{n,\vec{k}} \phi\left(\vec{r}, \vec{G}, \vec{k}, n\right),$$

where $c_{\vec{G}}^{n,\vec{k}}$ is a scaling constant and $\phi\left(\vec{r}, \vec{G}, \vec{k}, n\right)$ is a known eigenfunction of some complete basis.

B.1 APW Basis

For the Augmented Planewave (APW) basis, the trial functions are as follows:

$$\phi_{APW}\left(\vec{r}, \vec{G}, \vec{k}, n\right) = \begin{cases} \frac{1}{\sqrt{V}} \exp\left(i\left(\vec{k}+\vec{G}\right)\cdot\vec{r}\right), & \vec{r} \in I \\ \sum_{\ell,m} A_{\ell m}^{t,\vec{k}+\vec{G}} u_\ell^t\left(r', E^{n\vec{k}}\right) Y_{\ell m}(\hat{r}'), & \vec{r} \in r_{MT}^t \end{cases},$$

where $\vec{r}' = \vec{r} - \vec{r}_t$, I denotes interstitial space, and $\vec{r} \in r_{MT}^t$ indicates that $\vec{r}$ is within the atomic sphere radius r_{MT}^t of atomic nuclei t. The coefficients $A_{\ell m}^{t,\vec{k}+\vec{G}}$ are chosen to match the planewave at the sphere boundary, by using the planewave expansion:

$$\begin{aligned} \frac{1}{\sqrt{V}} \exp\left(i\vec{K}\cdot\vec{r}\right) &= \frac{4\pi}{\sqrt{V}} \exp\left(i\vec{K}\cdot\vec{r}_t\right) \sum_{\ell m} i^\ell j_\ell(Kr') Y_{\ell m}^\dagger\left(\hat{K}\right) Y_{\ell m}(\hat{r}') \\ \Rightarrow A_{\ell m}^{t,\vec{K}} &= \frac{4\pi}{\sqrt{V}} i^\ell \exp\left(i\vec{K}\cdot\vec{r}_t\right) \frac{j_\ell\left(Kr_{MT}^t\right)}{u_\ell^t\left(r_{MT}^t, E^{n\vec{k}}\right)} Y_{\ell m}^\dagger\left(\hat{K}\right) \end{aligned}$$

Note that the APW functions are discontinuous in the first derivative at the sphere boundary, however the total many-body wavefunction is smooth and continuous everywhere [40]. As mentioned in Section 3.4, since the APW basis relies on the eigenfunction energy $E^{n\vec{k}}$, and the complete APW wavefunction is needed to define the electron density that is required to solve for the eigenfunction energy $E^{n\vec{k}}$, the APW basis requires more diagonalizations to obtain and is therefore slower to converge. Consequently the APW basis is almost never used.

B.2 LAPW Basis

For the Linearized Augmented Planewave (LAPW) basis, the trial functions are as follows:

$$\phi_{LAPW}\left(\vec{r},\vec{G},\vec{k},n\right) = \begin{cases} \frac{1}{\sqrt{V}}\exp\left(i\left(\vec{k}+\vec{G}\right)\cdot\vec{r}\right), & \vec{r}\in I \\ \sum_{\ell,m}\left(A_{\ell m}^{t,\vec{k}+\vec{G}}u_\ell^t\left(r',E_\ell^t\right)+B_{\ell m}^{t,\vec{k}+\vec{G}}\dot{u}_\ell^t\left(r',E_\ell^t\right)\right)Y_{\ell m}\left(\hat{r}'\right), & \vec{r}\in r_{MT}^t \end{cases}$$

In this case rather than using the specific energy eigenvalues $E_{\vec{k}}^n$ to define the radial portion of the wavefunction inside the atomic sphere, an atomic-specific and angular momentum dependent set of energies E_ℓ^t are used instead. The LAPW basis comes from using a Taylor expansion of $u_\ell^t(r,E)$ around E_ℓ^t, and for this reason the energy derivative $\frac{\partial}{\partial E}u_\ell^t(r,E) = \dot{u}_\ell^t(r,E)$ is not normalized, and is orthogonal to $u_\ell^t(r,E)$.

The coefficients $A_{\ell m}^{t,\vec{K}}$, $B_{\ell m}^{t,\vec{K}}$ are chosen by making the LAPW function match the planewave in both value and derivative at the sphere boundary:

$$\begin{aligned} \frac{1}{\sqrt{V}}\exp\left(i\vec{K}\cdot\vec{r}\right) &= \frac{4\pi}{\sqrt{V}}\exp\left(i\vec{K}\cdot\vec{r}_t\right)\sum_{\ell m}i^\ell j_\ell\left(Kr'\right)Y_{\ell m}^\dagger\left(\hat{K}\right)Y_{\ell m}\left(\hat{r}'\right) \\ \frac{1}{\sqrt{V}}\frac{\partial}{\partial r'}\exp\left(i\vec{K}\cdot\vec{r}\right) &= \frac{4\pi}{\sqrt{V}}\exp\left(i\vec{K}\cdot\vec{r}_t\right)\sum_{\ell m}i^\ell \frac{\partial}{\partial r'}j_\ell\left(Kr'\right)Y_{\ell m}^\dagger\left(\hat{K}\right)Y_{\ell m}\left(\hat{r}'\right) \\ \Rightarrow \frac{4\pi}{\sqrt{V}}i^\ell\exp\left(i\vec{K}\cdot\vec{r}_t\right)j_\ell\left(Kr_{MT}^t\right)Y_{\ell m}^\dagger\left(\hat{K}\right) &= A_{\ell m}^{t,\vec{k}+\vec{G}}u_\ell^t\left(r_{MT}^t,E_\ell^t\right)+B_{\ell m}^{t,\vec{k}+\vec{G}}\dot{u}_\ell^t\left(r_{MT}^t,E_\ell^t\right) \\ \Rightarrow \frac{4\pi}{\sqrt{V}}i^\ell\exp\left(i\vec{K}\cdot\vec{r}_t\right)j_\ell'\left(Kr_{MT}^t\right)Y_{\ell m}^\dagger\left(\hat{K}\right) &= A_{\ell m}^{t,\vec{k}+\vec{G}}u_\ell^{t\prime}\left(r_{MT}^t,E_\ell^t\right)+B_{\ell m}^{t,\vec{k}+\vec{G}}\dot{u}_\ell^{t\prime}\left(r_{MT}^t,E_\ell^t\right) \end{aligned}$$

$$\begin{aligned} \text{or :} \quad \alpha j_\ell &= Au_\ell+B\dot{u}_\ell \\ \alpha j_\ell' &= Au_\ell'+B\dot{u}_\ell' \\ \text{so that} \quad \alpha j_\ell\dot{u}_\ell' &= Au_\ell\dot{u}_\ell'+B\dot{u}_\ell\dot{u}_\ell' \\ \alpha j_\ell'\dot{u}_\ell &= A\dot{u}_\ell u_\ell'+B\dot{u}_\ell\dot{u}_\ell' \\ A\left(u_\ell\dot{u}_\ell'-\dot{u}_\ell u_\ell'\right) &= \alpha\left(j_\ell\dot{u}_\ell'-j_\ell'\dot{u}_\ell\right) \\ \text{and} \quad \alpha j_\ell u_\ell' &= Au_\ell u_\ell'+B\dot{u}_\ell u_\ell' \\ \alpha j_\ell' u_\ell &= Au_\ell u_\ell'+Bu_\ell\dot{u}_\ell' \\ B\left(\dot{u}_\ell u_\ell'-u_\ell\dot{u}_\ell'\right) &= \alpha\left(j_\ell u_\ell'-j_\ell' u_\ell\right) \end{aligned}$$

The normalization condition for $\dot{u}_\ell^t\left(r,E_\ell^t\right)$ so that it is a true Taylor expansion of $u_\ell^t(r,E)$, i.e. $u_\ell^t(r,E) = u_\ell^t(r,E_\ell^t)+(E-E_\ell^t)\dot{u}_\ell^t(r,E_\ell^t)$ requires that:

$$\left(r_{MT}^t\right)^2\left(u_\ell^t\left(r_{MT}^t,E_\ell^t\right)\dot{u}_\ell^{t\prime}\left(r_{MT}^t,E_\ell^t\right)-\dot{u}_\ell^t\left(r_{MT}^t,E_\ell^t\right)u_\ell^{t\prime}\left(r_{MT}^t,E_\ell^t\right)\right)=-1,$$

so we therefore have:

$$\begin{aligned} A_{\ell m}^{t,\vec{K}} &= -\frac{4\pi\left(r_{MT}^t\right)^2}{\sqrt{V}}i^\ell\exp\left(i\vec{K}\cdot\vec{r}_t\right)\left(j_\ell\left(Kr_{MT}^t\right)\dot{u}_\ell^{t\prime}\left(r_{MT}^t,E_\ell^t\right)-j_\ell'\left(Kr_{MT}^t\right)\dot{u}_\ell^t\left(r_{MT}^t,\ell^t\right)\right)Y_{\ell m}^\dagger\left(\hat{K}\right) \\ B_{\ell m}^{t,\vec{K}} &= \frac{4\pi\left(r_{MT}^t\right)^2}{\sqrt{V}}i^\ell\exp\left(i\vec{K}\cdot\vec{r}_t\right)\left(j_\ell\left(Kr_{MT}^t\right)u_\ell^{t\prime}\left(r_{MT}^t,E_\ell^t\right)-j_\ell'\left(Kr_{MT}^t\right)u_\ell^t\left(r_{MT}^t,\ell^t\right)\right)Y_{\ell m}^\dagger\left(\hat{K}\right) \end{aligned}$$

B.3 LAPW+LO States

For localized states, local orbitals (LOs) are added to the LAPW basis as follows:

$$\phi^t_{\ell m,LO}\left(\vec{r}\right) = \begin{cases} 0, & \vec{r} \in I \\ \left(A^t_{\ell m} u^t_\ell\left(r', E^t_\ell\right) + B^t_{\ell m} \dot{u}^t_\ell\left(r', E^t_\ell\right) + C^t_{\ell m} u^t_\ell\left(r', E^{t,LO}_\ell\right)\right) Y_{\ell m}\left(\hat{r}'\right), & \vec{r} \in r^t_{MT} \end{cases}.$$

Since these wavefunctions are identically zero outside the atomic sphere, they do not connect to the planewaves and have no $\vec{k}$ or $\vec{G}$ dependence. These wavefunctions must be normalized, have zero value and zero slope outside the sphere. The coefficients $A^t_{\ell m}$, $B^t_{\ell m}$, and $C^t_{\ell m}$ are therefore:

$$\begin{aligned} 0 &= A u_\ell + B \dot{u}_\ell + C u_{\ell,2} \\ 0 &= A u'_\ell + B \dot{u}'_\ell + C u'_{\ell,2} \qquad \text{at } r' = r^t_{MT} \\ \Rightarrow A &= \left(\frac{\dot{u}_\ell u'_{\ell,2} - \dot{u}'_\ell u_{\ell,2}}{u_\ell \dot{u}'_\ell - u'_\ell \dot{u}_\ell}\right) C = -x_{ac} r^2_{MT} C \\ \Rightarrow B &= -\left(\frac{u_\ell u'_{\ell,2} - u'_\ell u_{\ell,2}}{u_\ell \dot{u}'_\ell - u'_\ell \dot{u}_\ell}\right) C = x_{bc} r^2_{MT} C \\ \text{and} \quad 1 &= \int r^2 dr \left(A u_\ell + B \dot{u}_\ell + C u_{\ell,2}\right)^2 \\ &= \int r^2 dr \left(A^2 u^2_\ell + B^2 \dot{u}^2_\ell + C^2 u^2_{\ell,2} + 2AB u_\ell \dot{u}_\ell + 2AC u_\ell u_{\ell,2} + 2BC \dot{u}_\ell u_{\ell,2}\right) \\ &= A^2 + B^2 \int r^2 dr \dot{u}^2_\ell + C^2 + 2AC \int r^2 dr u_\ell u_{\ell,2} + 2BC \int r^2 dr \dot{u}_\ell u_{\ell,2} \\ \Rightarrow \frac{1}{C^2} &= \left(x_{ac} r^2_{MT}\right)^2 + \left(x_{bc} r^2_{MT}\right)^2 \int r^2 dr \dot{u}^2_\ell + 1 - 2\left(x_{ac} r^2_{MT}\right) \int r^2 dr u_\ell u_{\ell,2} \\ &\quad + 2\left(x_{bc} r^2_{MT}\right) \int r^2 dr \dot{u}_\ell u_{\ell,2} \end{aligned}$$

B.4 APW+lo States

For quasi-localized states, WIEN2k uses the technique of adding local orbitals (los) to energy-independent APW functions. These states consist of a mixture of two basis functions, the normal $\vec{k}$,$\vec{G}$-dependent APW functions with a fixed energy E^t_ℓ rather than the eigenvalue $E^n_{\vec{k}+\vec{G}}$:

$$\begin{aligned} \phi_{APW+lo}\left(\vec{r}, \vec{G}, \vec{k}, n\right) &= \begin{cases} \frac{1}{\sqrt{V}} \exp\left(i\left(\vec{k}+\vec{G}\right)\cdot\vec{r}\right), & \vec{r} \in I \\ \sum_{\ell,m} A^{t,\vec{k}+\vec{G}}_{\ell m} u^t_\ell\left(r', E^t_\ell\right) Y_{\ell m}\left(\hat{r}'\right), & \vec{r} \in r^t_{MT} \end{cases} \\ A^{t,\vec{K}=\vec{k}+\vec{G}}_{\ell m} &= \frac{4\pi}{\sqrt{V}} i^\ell \exp\left(i\vec{K}\cdot\vec{r}_t\right) \frac{j_\ell\left(K r^t_{MT}\right)}{u^t_\ell\left(r^t_{MT} E^t_\ell\right)} Y^\dagger_{\ell m}\left(\hat{K}\right), \end{aligned}$$

and a local orbital (lo) for particular atoms and angular momenta:

$$\phi^t_{\ell m,lo}\left(\vec{r}\right) = \begin{cases} 0, & \vec{r} \in I \\ \left(A^t_{\ell m} u^t_\ell\left(r', E^t_\ell\right) + B^t_{\ell m} \dot{u}^t_\ell\left(r', E^t_\ell\right)\right) Y_{\ell m}\left(\hat{r}'\right), & \vec{r} \in r^t_{MT} \end{cases}.$$

Here the choice of E_ℓ^t for the lo is the same as for the APW, above. The coefficients $A_{\ell m}^t$ and $B_{\ell m}^t$ are chosen such that the lo is normalized and has zero value (but not zero slope) at the sphere boundary:

$$\begin{aligned} 0 &= Au_\ell + B\dot{u}_\ell \qquad \text{at } r_{MT}^t \\ \Rightarrow A &= \left(\frac{\dot{u}_\ell}{u_\ell}\right) B \\ 1 &= \int r^2 dr \left(Au_\ell + B\dot{u}_\ell\right)^2 \\ &= A^2 + B^2 \int r^2 dr \dot{u}_\ell^2 \\ \Rightarrow \frac{1}{B^2} &= \left(\frac{\dot{u}_\ell}{u_\ell}\right)^2 + \int r^2 dr \dot{u}_\ell^2 \end{aligned}$$

B.5 APW+lo+LO States

For localized states that are somewhat coincident in energy with states already described by the APW+lo basis, and additional local orbital (LO) is added with an additional energy parameter, just as with the LAPW basis, as follows:

$$\phi_{\ell m,LO}^t\left(\vec{r}\right) = \begin{cases} 0, & \vec{r} \in I \\ \left(A_{\ell m}^t u_\ell^t\left(r', E_\ell^t\right) + C_{\ell m}^t u_\ell^t\left(r', E_\ell^{t,LO}\right)\right) Y_{\ell m}\left(\hat{r}'\right), & \vec{r} \in r_{MT}^t \end{cases} .$$

These wavefunctions are slightly different from LAPW+LO wavefunctions in that they do not depend on the energy derivative of the radial wavefunction $\dot{u}_\ell\left(r\right)$). The coefficients $A_{\ell m}^t$ and $C_{\ell m}^t$ are chosen such that the LO is normalized and has zero value (but not zero slope) at the sphere boundary:

$$\begin{aligned} 0 &= Au_\ell + Cu_{\ell,2} \qquad \text{at } r_{MT}^t \\ \Rightarrow A &= \left(\frac{u_{\ell,2}}{u_\ell}\right) C \\ 1 &= \int r^2 dr \left(Au_\ell + Cu_{\ell,2}\right)^2 \\ &= A^2 + 2AC \int r^2 dr u_\ell u_{\ell,2} + C^2 \\ \Rightarrow \frac{1}{C^2} &= \left(\frac{u_{\ell,2}}{u_\ell}\right)^2 + 2\left(\frac{u_{\ell,2}}{u_\ell}\right) \int r^2 dr u_\ell u_{\ell,2} + 1 \end{aligned}$$

Appendix C

Integrals of Three Spherical Harmonics

An integral of three spherical harmonics over all solid angles occurs quite often in solid state quantum mechanics, and it can conveniently be expressed in terms of Wigner 3j symbols [57]:

$$\begin{aligned}\Omega\left(\ell_1 m_1, \ell_2 m_2, \ell_3 m_3\right) &= \iint Y^{\dagger}_{\ell_1 m_1}(\hat{r}) Y_{\ell_2 m_2}(\hat{r}) Y_{\ell_3 m_3}(\hat{r}) \sin\theta d\theta d\phi \\ &= (-1)^{-m_1}\sqrt{\frac{(2\ell_1+1)(2\ell_2+1)(2\ell_3+1)}{4\pi}}\begin{pmatrix} \ell_1 & \ell_2 & \ell_3 \\ 0 & 0 & 0 \end{pmatrix} \\ &\quad \times \begin{pmatrix} \ell_1 & \ell_2 & \ell_3 \\ -m_1 & m_2 & m_3 \end{pmatrix}.\end{aligned}$$

The Wigner 3j symbols, of the form:

$$\begin{pmatrix} \ell_1 & \ell_2 & \ell_3 \\ m_1 & m_2 & m_3 \end{pmatrix},$$

have an analytic solution, although explicitly calculating the solution for arbitrary sets of ℓ and m is tedious. There are several important restrictions on the sets of ℓ and m, however: the 3j symbol is identically zero unless $m_1 + m_2 + m_3 = 0$, $\ell_i + \ell_j \geq \ell_k$ for i, j, k as any permutation of the indices $1, 2, 3$ [57]. For the special case when $m_1 = m_2 = m_3 = 0$, the 3j symbol is identically zero unless $\ell_1 + \ell_2 + \ell_3$ is an even integer [57]. Finally the 3j symbol is always real.

From these properties of the 3j symbol, we know that the integral of three spherical harmonics, $\Omega\left(\ell_1 m_1, \ell_2 m_2, \ell_3 m_3\right)$, obeys these properties:

1. The set of ℓ and m is constrained: $\Omega\left(\ell_1 m_1, \ell_2 m_2, \ell_3 m_3\right) = 0$ unless $m_1 + m_2 + m_3 = 0$, $\ell_i + \ell_j \geq \ell_k$ for i, j, k as any permutation of the indices $1, 2, 3$, and $\ell_1 + \ell_2 + \ell_3$ is an even integer.

2. Cyclic permutations are identical: $\Omega\left(\ell_1 m_1, \ell_2 m_2, \ell_3 m_3\right) = \Omega\left(\ell_2 m_2, \ell_3 m_3, \ell_1 m_1\right)$ $= \Omega\left(\ell_3 m_3, \ell_1 m_1, \ell_2 m_2\right)$.

3. Self-adjoint: $\Omega\left(\ell_1 m_1, \ell_2 m_2, \ell_3 m_3\right) = \Omega^{\dagger}\left(\ell_1 m_1, \ell_2 m_2, \ell_3 m_3\right)$.

These 3j symbols also obey a useful orthogonality relation [57]:

$$\sum_{m_1, m_2} \begin{pmatrix} \ell_1 & \ell_2 & \ell_3 \\ m_1 & m_2 & m_3 \end{pmatrix}\begin{pmatrix} \ell_1 & \ell_2 & \ell_4 \\ m_1 & m_2 & m_4 \end{pmatrix} = \frac{\delta_{\ell_3,\ell_4}\delta_{m_3,m_4}}{2\ell_3+1} \tag{C.1}$$

Using the properties of Wigner 3j symbols we can simply several expressions consisting of partial sums over the product of several integrals of three spherical harmonics; these occur in the expressions for transitions between different single-particle electronic states.

The first expression is the following:

$$\begin{aligned}
\sum_{m_1,m} \Omega\left(\ell_1 m_1, \ell m, \ell_2 m_2\right) \Omega\left(\ell_1 m_1, \ell m, \ell_3 m_3\right) &= \sum_{m_1,m} (-1)^{-m_1} \sqrt{\frac{(2\ell_1+1)(2\ell+1)(2\ell_2+1)}{4\pi}} \\
&\quad \times \begin{pmatrix} \ell_1 & \ell & \ell_2 \\ 0 & 0 & 0 \end{pmatrix} \begin{pmatrix} \ell_1 & \ell & \ell_2 \\ -m_1 & m & m_2 \end{pmatrix} \\
&\quad \times (-1)^{-m_1} \sqrt{\frac{(2\ell_1+1)(2\ell+1)(2\ell_3+1)}{4\pi}} \\
&\quad \times \begin{pmatrix} \ell_1 & \ell & \ell_3 \\ 0 & 0 & 0 \end{pmatrix} \begin{pmatrix} \ell_1 & \ell & \ell_3 \\ -m_1 & m & m_3 \end{pmatrix} \\
&= \frac{1}{4\pi}(2\ell_i+1)(2\ell+1)\sqrt{(2\ell_2+1)(2\ell_3+1)} \\
&\quad \times \begin{pmatrix} \ell_1 & \ell & \ell_2 \\ 0 & 0 & 0 \end{pmatrix} \begin{pmatrix} \ell_1 & \ell & \ell_3 \\ 0 & 0 & 0 \end{pmatrix} \\
&\quad \times \sum_{m_1,m} \begin{pmatrix} \ell_1 & \ell & \ell_2 \\ -m_1 & m & m_2 \end{pmatrix} \begin{pmatrix} \ell_1 & \ell & \ell_3 \\ -m_1 & m & m_3 \end{pmatrix} \\
&= \frac{1}{4\pi}(2\ell_1+1)(2\ell+1) \begin{pmatrix} \ell_1 & \ell & \ell_2 \\ 0 & 0 & 0 \end{pmatrix}^2 \delta_{\ell_2,\ell_3}\delta_{m_2,m_3} \\
&= W(\ell_1,\ell,\ell_2)\delta_{\ell_2,\ell_3}\delta_{m_2,m_3} \qquad \text{(C.2)}
\end{aligned}$$

The second expression is:

$$\begin{aligned}
&\sum_{m_1 m_2 m_3 m_4 m_5} \Omega\left(\ell_1 m_1, \ell_2 m_2, \ell_5 m_5\right) \Omega\left(\ell_3 m_3, \ell_5 m_5, \ell_7 m_7\right) \Omega\left(\ell_1 m_1, \ell_6 m_6, \ell_4 m_4\right) \Omega\left(\ell_2 m_2, \ell_3 m_3, \ell_4 m_4\right) \\
&\quad = \sum_{m_1 m_2 m_3 m_4 m_5} \Omega\left(\ell_1 m_1, \ell_2 m_2, \ell_5 m_5\right) \Omega\left(\ell_3 m_3, \ell_5 m_5, \ell_6 m_6\right) \Omega\left(\ell_1 m_1, \ell_6 m_6, \ell_4 m_4\right) \\
&\qquad \times \Omega\left(\ell_2 m_2, \ell_3 m_3, \ell_4 m_4\right) \delta_{\ell_6,\ell_7}\delta_{m_6,m_7} \qquad \text{(C.3)}
\end{aligned}$$

This can be demonstrated by numerically calculating the sum; an analytic proof would be too tedious to be worthwhile.

Finally, Wigner 3j symbols with $m_1 = m_2 = m_3 = 0$ have a relatively compact analytic solution, given by: [57]

$$\begin{pmatrix} \ell_1 & \ell_2 & \ell_3 \\ 0 & 0 & 0 \end{pmatrix} = (-1)^L \sqrt{\frac{(2L-2\ell_1)!(2L-2\ell_2)!(2L-2\ell_3)!}{(2L+1)!}} \frac{L!}{(L-\ell_1)!(L-\ell_2)!(L-\ell_3)!}.$$

For X-ray dipole transitions, where $\ell_2 = 1$, we know from the properties of Wigner 3j symbols given above that for an arbitrary ℓ_1 (i.e. the known core level angular momentum), and $\ell_2 = 1$, the Wigner 3j symbol will be zero unless $\ell_3 = \ell_1 \pm 1$ (this is the only way we can have $|\ell_1 - 1| \leq \ell_3 \leq \ell_1 + 1$ and the sum $\ell_1 + 1 + \ell_3$ be an even integer), so we can simplify

this expression to:

$$\begin{aligned}
\begin{pmatrix} \ell_1 & 1 & \ell_1+1 \\ 0 & 0 & 0 \end{pmatrix} &= (-1)^{\ell_1+1}\sqrt{\frac{2(2\ell_1)!}{(2\ell_1+3)!}}\frac{(\ell_1+1)!}{(\ell_1)!} \\
&= (-1)^{\ell_1+1}\sqrt{\frac{2}{(2\ell_1+1)(2\ell_1+2)(2\ell_1+3)}}(\ell_1+1) \\
\begin{pmatrix} \ell_1 & 1 & \ell_1+1 \\ 0 & 0 & 0 \end{pmatrix}^2 &= \frac{2(\ell_1+1)^2}{(2\ell_1+1)(2\ell_1+2)(2\ell_1+3)} \\
&= \frac{\ell_1+1}{(2\ell_1+1)(2\ell_1+3)}, \qquad \text{and} \\
\begin{pmatrix} \ell_1 & 1 & \ell_1-1 \\ 0 & 0 & 0 \end{pmatrix} &= (-1)^{\ell_1}\sqrt{\frac{2(2\ell_1-2)!}{(2\ell_1+1)!}}\frac{\ell_1!}{(\ell_1-1)!} \\
&= (-1)^{\ell_1}\sqrt{\frac{2}{(2\ell_1-1)(2\ell_1)(2\ell_1+1)}}\ell_1 \\
\begin{pmatrix} \ell_1 & 1 & \ell_1-1 \\ 0 & 0 & 0 \end{pmatrix}^2 &= \frac{2\ell_1^2}{(2\ell_1-1)(2\ell_1)(2\ell_1+1)} \\
&= \frac{\ell_1}{(2\ell_1-1)(2\ell_1+1)}.
\end{aligned}$$

Therefore:

$$\begin{aligned}
W(\ell_1,1,\ell_1-1) &= \frac{3}{4\pi}\left(\frac{\ell_1}{2\ell_1+1}\right), \text{ and} \\
W(\ell_1,1,\ell_1+1) &= \frac{3}{4\pi}\left(\frac{\ell_1+1}{2\ell_1+3}\right)
\end{aligned}$$

Appendix D

X-ray Transitions in WIEN2k

As mentioned in Section 4.2, X-ray transitions from a core level to a band state (or vice versa) can be evaluated entirely within the r_{MT} sphere of the particular atomic site, since the core wavefunction is zero outside this region. Without loss of generality, for the derivations herein I will treat the initial state as a core level state and the final state as a band state (in band n with momentum $\vec{k}$):

$$\begin{aligned} \psi_i &= u_{\ell_c}(r,E)Y_{\ell_c m_c}(\hat{r}) \\ \psi_f &= \sum_{\ell m} f_{\ell m}^{n\vec{k}}(r,E)Y_{\ell m}(\hat{r}), \end{aligned}$$

Strictly speaking, this just defines an absorption transition, but the end result is symmetric under the exchange $\psi_i \leftrightarrow \psi_f$ so the end result works for emission transitions as well. Since all of these derivations are within the Schödinger picture of quantum mechanics, there are no operators used to create or annihilate particles. Therefore one must know beforehand which states are unoccupied and occupied, and restrict the calculation to the appropriate states (i.e. occupied core levels and unoccupied conduction band states for X-ray absorption, unoccupied core levels and occupied valence band states for X-ray emission).

D.1 X-ray Transitions in the APW Formalism

Within the APW basis (refer back to Section B.1) we have the following for the band states:

$$\psi_f = \sum_{\ell m} a_{\ell m}^{n\vec{k}} u_\ell(r, E^{n\vec{k}})Y_{\ell m}(\hat{r})$$

We also need to sum across the core level magnetic moment m_c, since that is not a good quantum number (i.e. can not be experimentally selected), and we therefore have the X-ray transition intensity at a given band and crystal momentum of:

$$\begin{aligned} I^{n\vec{k}}(h\nu) &= \sum_{m_c}\sum_{qq'} Y_{1q}^{\dagger}(\hat{e})Y_{1q'}(\hat{e}) \sum_{\ell m}\sum_{\ell' m'} \left(a_{\ell' m'}^{n\vec{k}}\right)^{\dagger} a_{\ell m}^{n\vec{k}} \int r^2 dr u_{\ell_c}(r,E_c) r u_\ell(r,E^{n\vec{k}}) \\ &\quad \times \int (r')^2 dr' u_{\ell_c}(r',E_c) r' u_{\ell'}(r',E^{n\vec{k}}) \Omega(\ell_c m_c, 1q, \ell m)\Omega(\ell_c m_c, 1q', \ell' m')\delta(E^{n\vec{k}} - E_c - h\nu). \end{aligned}$$

As mentioned in Section 4.2, when using unpolarized light or a polycrystalline sample, we can integrate $\hat{e}$ over a full sphere, and this introduces a factor of $\delta_{qq'}$. Subsequently we can sum over the spherical harmonic terms, which introduce factors of $\delta_{\ell\ell'}$ and $\delta_{mm'}$, so the expression is reduced to:

$$I^{n\vec{k}}(h\nu) = \sum_{\ell}\left(\sum_m \left|a_{\ell m}^{n\vec{k}}\right|^2\right)\left[\int r^2 dr u_{\ell_c}(r,E_c) r u_\ell(r,E^{n\vec{k}})\right]^2 W(\ell_c,1,\ell)\delta(E^{n\vec{k}} - E_c - h\nu).$$

Since we cannot observe the intensity from a specific band or crystal momentum, we should sum over the former (restricting ourselves to occupied or unoccupied bands, for XES or XAS, respectively) and integrate over the latter:

$$\begin{aligned} I(h\nu) &= \sum_{\ell} \rho_{\ell}(h\nu + E_c) \left[\int r^2 dr u_{\ell_c}(r, E_c) r u_{\ell}(r, h\nu + E_c) \right]^2 W(\ell_c, 1, \ell) \\ \text{where} \qquad \rho_{\ell}(E) &= \sum_{m} \sum_{n} \int dV_k \left| a_{\ell m}^{n\vec{k}} \right|^2 \delta(E^{n\vec{k}} - E) \end{aligned}$$

Since $u_\ell(r, E)$ is only dependent on the energy, not the band or crystal momentum, we were justified in replacing $u_\ell(r, E^{n\vec{k}})$ with $u_\ell(r, h\nu + E_c)$, to avoid including it in the summation over bands and integral over crystal momentum. This is done because the X-ray intensity is now the product of some transition matrix element $\left[\int r^2 dr u_{\ell_c}(r, E_c) r u_\ell(r, E)\right]^2 W(\ell_c, 1, \ell)$ and the local, partial, DOS $\rho_\ell(E)$ [59, 60].

D.2 X-ray Transitions in the Mixed Basis Formalism

As mentioned in Section 3.4, the APW basis is almost never used in WIEN2k. Rather, each state is either a LAPW or APW+lo state (refer back to Sections B.2 and B.4) and may also include local orbitals (LAPW+LO, Section B.3 or APW+lo+Lo, Section B.5). For both LAPW+LO or APW+lo+LO the band state (where there are $j = 1...n_\ell$ LOs for state ℓ) is defined as:

$$\psi_f = \sum_{\ell m} \left(a_{\ell m}^{n\vec{k}} u_\ell(r, E_\ell) + b_{\ell m}^{n\vec{k}} \dot{u}_\ell(r, E_\ell) + \sum_j c_{\ell m}^j u_\ell(r, E_\ell^j) \right) Y_{\ell m}(\hat{r}),$$

where the definitions of $a_{\ell m}^{n\vec{k}}$, $b_{\ell m}^{n\vec{k}}$, and $c_{\ell m}^j$ depend on whether the state is an APW or LAPW state, and whether or not it has one or more LOs (if not, the $c_{\ell m}^j = 0$).

In this case the radial integral is no longer separable into a transition matrix part and a density of states part. Although the integration is greatly simplified because there are only a few radial wavefunctions for each ℓ (rather than one for every energy, as was the case with the APW formalism), the square of the integral mixes the various $a_{\ell m}^{n\vec{k}}$, $b_{\ell m}^{n\vec{k}}$, and $c_{\ell m}^j$ coefficients.

Because of the partial DOS is an observable, it should not depend on the choice of basis set. Therefore the APW method outlined in Section D.1 should be applicable for calculating non-polarized XES and XAS spectra, even when using the partial DOS calculated with

WIEN2k's mixed basis set. The implicit argument here is:

$$\begin{aligned}\left|a^{n\vec{k}}_{\ell m;(\mathrm{APW})}(r,E^{n\vec{k}})\right|^2 &= \left|a^{n\vec{k}}_{\ell m}\right|^2+\left|b^{n\vec{k}}_{\ell m}\right|^2\int r^2dr\dot{u}^2_\ell(r,E_\ell)+\sum_j\left|c^j_{\ell m}\right|^2\\ &+\left(a^{n\vec{k}}_{\ell m}\left(b^{n\vec{k}}_{\ell m}\right)^\dagger+\left(a^{n\vec{k}}_{\ell m}\right)^\dagger b^{n\vec{k}}_{\ell m}\right)\int r^2dru_\ell(r,E_\ell)\dot{u}_\ell(r,E_\ell)\\ &+\sum_j\left(a^{n\vec{k}}_{\ell m}\left(c^j_{\ell m}\right)^\dagger+\left(a^{n\vec{k}}_{\ell m}\right)^\dagger c^j_{\ell m}\right)\int r^2dru_\ell(r,E_\ell)u_\ell(r,E^j_\ell)\\ &+\sum_j\left(b^{n\vec{k}}_{\ell m}\left(c^j_{\ell m}\right)^\dagger+\left(b^{n\vec{k}}_{\ell m}\right)^\dagger c^j_{\ell m}\right)\int r^2dr\dot{u}_\ell(r,E_\ell)u_\ell(r,E^j_\ell)\\ &+\sum_{j\neq j'}\left(c^j_{\ell m}\left(c^{j'}_{\ell m}\right)^\dagger+\left(c^j_{\ell m}\right)^\dagger c^{j'}_{\ell m}\right)\int r^2dru_\ell(r,E^j_\ell)u_\ell(r,E^{j'}_\ell),\end{aligned}$$

(where it is assumed that all regular solutions to the radial Dirac equation $u_\ell(r,E)$ are normalized over the atomic sphere) which is reasonable since the charge density at a given band n and crystal momentum $\vec{k}$ should not depend on the choice of basis set. In fact, the APW method outlined in Section D.1 might be *preferable* to explicitly calculating the X-ray transitions from the LAPW basis because the former assures of a smoothly varying transition matrix, and will be more accurate at high energies (in the conduction band) or low energies (in the valence band) that are far from the single energy points E_ℓ used in the mixed basis set.

The difference between an X-ray spectrum calculated with the APW method outlined in Section D.1 and the explicit calculation using the mixed basis is shown in Figure D.1. Note how the amplitude of the "LAPW" spectrum (here "LAPW" is used as a shorthand for "mixed LAPW+LO and APW+lo+LO basis") varies rather erratically with respect to the Cu $3d$ DOS in the valence band, while the behaviour of the "APW" spectrum (here "APW" is used as a shorthand for "using APW transition matrix elements and WIEN2k partial DOS") is much smoother. Note also how the APW $4s$ part smoothly increases in the conduction band, while the LAPW $4s$ part is close to the partial DOS throughout. These differences may be ascribed to the fact that WIEN2k uses the APW+lo basis set for the Cu $3d$ states, and the lo is centred in the middle of the valence band, while the Cu $4s$ states have no localized orbital (lo or LO) in the valence or conduction regions. This mixed basis set has been converged to a ground state charge density (i.e. expectation value of the wavefunction), not an X-ray transition intensity (i.e. overlap of the wavefunction with a core wavefunction and the dipole operator); hence when the basis set is used to calculate the X-ray transitions explicitly, there are regions of anomalous intensity depending on whether a localized orbital (lo or LO) is "switched on" or not.

However when the X-ray intensity depends on polarization dependence, the $\ell'\neq\ell$, $m'\neq m$ cross terms are not always zero, so the transition is not always proportional to some partial DOS, and consequently the polarized X-ray spectra may need to be calculated explicitly from the wavefunction in the original (mixed) basis set.

Since RXES using the Kramers-Heisenberg formula (refer back to Section 4.4) is just the $\vec{k}$-dependent product of an XES and an XAS spectrum, it is fairly straightforward to obtain

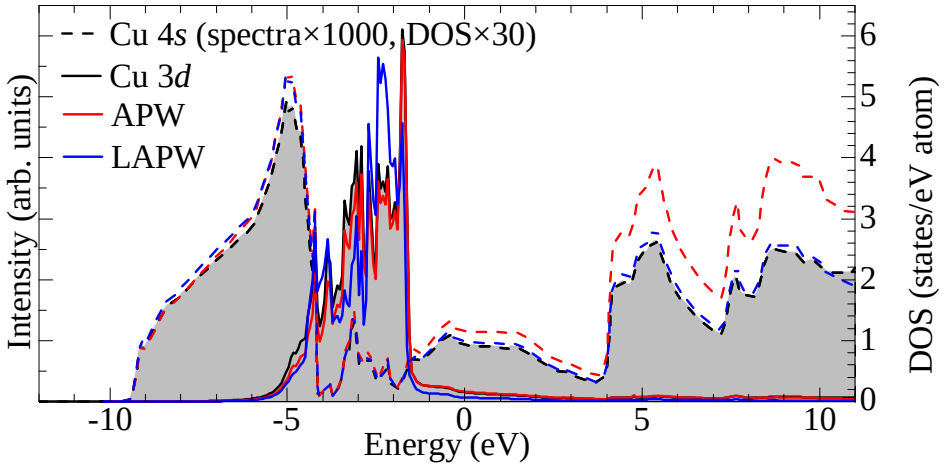

Figure D.1: A Cu L_3 unbroadened X-ray spectra (with no distinction between occupied and unoccupied) calculated with the partial DOS and the APW transition matrix elements (labelled as "APW"), and explicitly from the mixed LAPW+LO and APW+lo+LO wavefunctions (labelled as "LAPW"), compared to the calculated partial DOS. The X-ray spectrum ℓ_c+1 and ℓ_c-1 parts, probing the Cu $3d$ and $4s$ states, respectively, are shown separately.

a RXES spectrum using the APW or mixed basis methods.